

Departamento de Ingeniería civil Escuela Politécnica Superior

# The Application of Differential Synthetic Aperture Radar Interferometry Dataset for Validation, Characterization and Flood Risk Analysis in Land Subsidence-Affected Areas

María Inés Navarro Hernández

Thesis submitted in fulfilment of the requirements for the degree of DOCTOR OF PHILOSOPHY AT THE UNIVERSITY OF ALICANTE INTERNATIONAL DOCTORAL MENTION.

Ph.D. in MATERIALS, STRUCTURES AND SOIL ENGINEERING: SUSTAINABLE CONSTRUCTION

Directed by:

Dr. Javier Valdés Abellán

Dr. Roberto Tomás Jover

Alicante, Spain

May 2024

This research is funded by the PRIMA Programme supported by the European Union (Grant agreement 1924), project RESERVOIR.



Doctoral thesis presented by María Inés Navarro Hernández, in the form of a compilation of publications, in accordance with the provisions of the internal regulations of the doctoral school (University of Alicante Governing Council of December 17, 2013, modified by University of Alicante Governing Council of April 26, 2018, BOUA of April 26, 2018, and University of Alicante Governing Council of July 30, 2019, and University of Alicante Governing Council of September 29, 2020, BOUA of October 16, 2020), for the obtaining of the Doctoral degree from the University of Alicante under the supervision of Dr. Javier Valdés Abellán and Dr. Roberto Tomás Jover.

Bº. Doctoral Thesis supervisors

Javier Valdés Abellán Roberto Tomás Jover

**Doctoral** candidate

María Inés Navarro Hernández
Alicante, May 2024

#### **Abstract**

This interdisciplinary doctoral dissertation addresses land subsidence in different and diverse study cases in the world, employing advanced techniques and methodologies to measure their magnitude and comprehensively explore its causes, and implications. Investigating areas such as the San Luis Potosi metropolitan area, Alaşehir-Sarıgöl sub-basin (ASSB) in Türkiye, and the Alto Guadalentín Valley in Spain, the research unveils critical insights into the complex dynamics of subsidence phenomena. Utilizing advanced remote sensing techniques like Persistent Scatterer Interferometry (PSI) and Coherent Pixels Technique (CPT), the study assesses subsidence rates and correlates them with factors such as trace faults, groundwater extraction, and soft soil thickness. Validation methodologies were developed and proposed to the scientific community on the first stage, integrating Global Navigation Satellite System (GNSS) benchmarks, enhance the reliability of Differential Synthetic Aperture Radar Interferometry (DInSAR) measurements, ensuring a robust foundation for subsequent analyses. The research aims to contribute to the understanding of land subsidence and contribute to create a decision-support framework to mitigate the phenomenon while addressing specific research objectives within each identified topic of inquiry.

The research topic 1 includes the "DInSAR for monitoring land subsidence in overexploited aquifers". In the San Luis Potosi metropolitan area (Mexico), the application of CPT technique reveals intriguing correlations between trace faults, land subsidence, and groundwater extraction. Specifically, areas in the municipality of Soledad de Graciano Sánchez exhibit subsidence values ranging between -1.5 and -3.5 cm/year, while in San Luis Potosi, values range from -1.8 to -4.2 cm/year. The validation of CPT results against five Global Navigation Satellite System (GNSS) benchmarks establishes a robust correlation of 0.986, underlining the reliability of DInSAR-derived deformations. Additionally, in regions like the Alaşehir-Sarıgöl sub-basin (Türkiye), where water stress is heightened due to intensive agricultural irrigation, the study explores the roles of tectonic activity and groundwater withdrawal in land subsidence. Utilizing the P-SBAS algorithm, 98 Sentinel-1 SAR images in ascending orbits and 123 in descending orbits were analysed, covering the period from 2016 to 2020. Independent Component Analysis was applied to distinguish long-term displacements from seasonal variations in the DInSAR time series data. Displacement rates of up to -6.40 cm/year were identified, thus, the proposed P-SBAS algorithm facilitates the monitoring of displacement, revealing direct correlations between DInSAR displacement and critical factors like aquitard layer compaction. These findings contribute valuable insights into the dynamic interactions shaping overexploited aguifers.

The research topic 2, developing parallelly to topic 1, consists of the "Validation of DInSAR data applied to land subsidence areas". Addressing the imperative for validation methodologies in subsidence assessments, a systematic approach introduces statistical analyses and classification schemes. This methodology is designed to validate and refine DInSAR data, enhancing the reliability of subsidence assessments. By normalizing Root Mean Square Error (RMSE) parameters with the range and average of *in-situ* deformation values and employing the squared Pearson correlation coefficient (R²), a classification scheme is established. This scheme facilitates the acceptance/rejection of DInSAR data for further analyses through the application of automatic analysis supported by a Matlab © code, ensuring a more accurate representation of land subsidence phenomena.

The research topic 3 covers the exploitation of DInSAR data for assessing flooding potential and determining characteristic parameters of aquifer systems. The first one is "Impact of land subsidence on flood patterns". The study in the Alto Guadalentín Valley, a region experiencing extreme flash floods jointly with high-magnitude land subsidence, integrates flood event models, Differential interferometric SAR (DInSAR) techniques, and 2D hydraulic flow models. Through Synthetic Aperture Radar (SAR) satellite

images and DInSAR, land subsidence's magnitude and spatial distribution are quantified. The results demonstrate significant changes in water surface elevation between the two 1992 and 2016 temporal scenarios, leading to a 2.04 km² increase in areas with water depths exceeding 0.7 m. These outcomes, incorporated into a flood risk map and economic flood risk assessment, underscore the pivotal role of land subsidence in determining inundation risk and its socio-economical implications. The research offers a valuable framework for enhancing flood modelling by considering the intricate dynamics of land subsidence. The second application of DInSAR data is about the "Automatic calculation of skeletal storage coefficients in aquifer systems". In response to the need for automating data analysis for specific storage coefficients in aquifer systems, a MATLAB© application is introduced. This application streamlines the correlation between piezometric levels and ground deformation, significantly reducing analysis time and mitigating potential human interpretation errors. The developed application integrates temporal groundwater level series from observation wells and ground deformation data measured by *in-situ* or remote sensing techniques (e.g., DInSAR). Through the automatic construction of stress-strain curves, the application contributes to the estimation of skeletal storage coefficients, offering a valuable tool for evaluating aquifer system behaviours.

This comprehensive research, guided by the complexities of these three distinct research topics, yields detailed insights and methodological advancements. By integrating diverse datasets and employing advanced techniques, this dissertation offers a multidimensional understanding of land subsidence dynamics and provides a robust foundation for sustainable groundwater management globally.

**Keywords:** Land subsidence, groundwater withdrawal, Sentinel-1, DInSAR, Coherent Pixel Technique, PSBAS, Validation, Independent component Analysis, Flood hazard mapping, HEC-RAS, 2D flow models, Risk evaluation, Stress-Strain curves, Storage coefficient, MATLAB.

#### Resumen

Esta tesis doctoral interdisciplinaria aborda la subsidencia del terreno en diferentes y diversos casos de estudio en todo el mundo, empleando técnicas y metodologías avanzadas para medir su magnitud y explorar exhaustivamente sus causas e implicaciones. Al investigar áreas como el área metropolitana de San Luis Potosí, la subcuenca de Alaşehir-Sarıgöl (ASSB) en Turquía y el Valle del Alto Guadalentín en España, la investigación reveló ideas críticas sobre la dinámica compleja de los fenómenos de subsidencia. Utilizando técnicas avanzadas de teledetección como la Interferometría de Radar de Apertura Sintética Persistente (PSI) y la Técnica de Píxeles Coherentes (CPT), el estudio evaluó las tasas de subsidencia y las correlacionó con factores como trazas de fallas activas, extracción de aguas subterráneas y espesor del suelo blando. Se desarrollaron y propusieron metodologías de validación a la comunidad científica en la primera etapa, integrando puntos de referencia del Sistema Global de Navegación por Satélite (GNSS), mejorando la fiabilidad de las mediciones de Interferometría Diferencial de Radar de Apertura Sintética (DInSAR), asegurando así una base sólida para análisis posteriores. La investigación tiene como objetivo contribuir a la comprensión de la subsidencia del terreno y crear un marco de apoyo en la toma de decisiones para mitigar el fenómeno, abordando objetivos de investigación específicos dentro de cada línea de investigación identificada.

La línea de investigación 1 incluye "DInSAR para monitoreo de la subsidencia del suelo en acuíferos sobreexplotados". En el área metropolitana de San Luis Potosí (México), la aplicación de la técnica CPT reveló que existe una correlación entre la subsidencia y las trazas de las fallas activas, así mismo como con la extracción de aguas subterráneas. Específicamente, algunas áreas del municipio de Soledad de Graciano Sánchez mostraron valores de subsidencia que oscilan entre -1.5 y -3.5 cm/año, mientras que, en San Luis Potosí, los valores van desde -1.8 hasta -4.2 cm/año. La validación de los resultados de CPT frente a cinco puntos de referencia del Sistema Global de Navegación por Satélite (GNSS) estableció una correlación sólida de 0.986, subrayando la fiabilidad de las deformaciones derivadas de DInSAR. Además, en regiones como la subcuenca de Alaşehir-Sarıgöl (Turquía), donde el estrés hídrico se ve aumentado debido al riego agrícola intensivo, el estudio explora el impacto de la actividad tectónica y la extracción de aguas subterráneas en la subsidencia del terreno. Utilizando el algoritmo P-SBAS, se analizaron 98 imágenes SAR de Sentinel-1 en órbitas ascendentes y 123 en órbitas descendentes, cubriendo el período de 2016 a 2020. Se aplicó Análisis de Componentes Independientes para separar los hundimientos a largo plazo de variaciones estacionales en los datos de series temporales de DInSAR. Se identificaron tasas de hundimiento de hasta -6.40 cm/año, por lo tanto, el algoritmo P-SBAS propuesto facilitó el monitoreo del desplazamiento, revelando correlaciones directas entre el desplazamiento de DInSAR y factores críticos como la compactación de la capa de acuitardo. Estos hallazgos contribuyen con valiosas aportaciones sobre las interacciones dinámicas que dan forma a los acuíferos sobreexplotados.

La línea de investigación 2, fue desarrollada en paralelo con la línea 1, y consiste en la "Validación de datos de DInSAR aplicados a áreas de subsidencia del terreno". Abordando la necesidad de metodologías de validación al momento de evaluar la subsidencia, a través de un enfoque sistemático que introduce análisis estadísticos y esquemas de clasificación. Esta metodología está diseñada para validar y refinar datos de DInSAR, mejorando la fiabilidad de las mediciones de la subsidencia. Al normalizar los parámetros de Error Cuadrático Medio (RMSE) con el rango y el promedio de los valores de deformación in situ, combinado con el coeficiente de correlación de Pearson al cuadrado (R²), se establece un esquema de clasificación. Este esquema facilita la aceptación/rechazo de los datos de DInSAR para análisis posteriores mediante la aplicación de análisis automático, el cual está soportado por un código de Matlab, que asegura una estimación más precisa de los fenómenos de subsidencia del terreno.

La línea de investigación 3 incluye la aplicación y/o explotación de datos de DInSAR para evaluar el potencial de inundaciones y determinar parámetros característicos de sistemas acuíferos. El primer caso en donde se aplican los datos DInSAR es en el "Impacto de la subsidencia del suelo en los patrones de inundación". El área de estudio corresponde al valle del Alto Guadalentín, una región que experimenta inundaciones repentinas extremas junto con subsidencia del suelo de gran magnitud, integra modelos de eventos de inundaciones, técnicas DInSAR diferencial y modelos de flujo hidráulico 2D. A través de imágenes satelitales de Radar de Apertura Sintética (SAR) y DInSAR, se cuantificó la magnitud y distribución espacial de la subsidencia del terreno. Los resultados demostraron cambios significativos en la elevación de la superficie del agua entre los dos escenarios temporales de 1992 y 2016, lo que lleva a un aumento de 2.04 km² en áreas con profundidades de agua que exceden los 0.7 m. Estos resultados, incorporados en un mapa de riesgo de inundaciones y una evaluación económica del riesgo de inundaciones, subrayan el papel fundamental de la subsidencia del suelo en la determinación del riesgo de inundación y sus implicaciones socioeconómicas. La investigación ofrece un marco valioso para mejorar la modelización de inundaciones al considerar la dinámica intrincada de la subsidencia del terreno. La segunda aplicación de datos de DInSAR consiste en el "Cálculo automático de coeficientes de almacenamiento en sistemas acuíferos". En respuesta a la necesidad de automatizar el análisis de datos para coeficientes de almacenamiento específicos en sistemas acuíferos, se desarrolló una aplicación MATLAB. Esta aplicación simplifica la correlación entre los niveles piezométricos y la deformación del suelo, reduciendo significativamente el tiempo de análisis y mitigando posibles errores de interpretación humana. La aplicación desarrollada integra series temporales de niveles de agua subterránea de pozos de observación y datos de deformación del suelo medidos por técnicas in situ o de teledetección (por ejemplo, DInSAR). A través de la construcción automática de curvas de esfuerzo-deformación, la aplicación contribuye a la estimación de los coeficientes de almacenamiento, ofreciendo una herramienta valiosa para evaluar los comportamientos de los sistemas acuíferos.

Esta investigación integral, guiada por las complejidades de estas tres de investigación, ofrece ideas detalladas y avances metodológicos. Al integrar conjuntos de datos diversos y emplear técnicas avanzadas, esta tesis doctoral ofrece una comprensión multidimensional de la dinámica de la subsidencia del terreno y proporciona una base sólida para la gestión sostenible de las aguas subterráneas a nivel mundial.

**Palabras clave:** Subsidencia del terreno, extracción de aguas subterráneas, Sentinel-1, DInSAR, Técnica de Píxeles Coherentes, PSBAS, Validación, Análisis de Componentes Independientes, Cartografía de peligro de inundación, HEC-RAS, Modelos de flujo 2D, Evaluación de riesgos, Curvas de esfuerzo-deformación, Coeficiente de almacenamiento, MATLAB.

### Acknowledges

Quiero empezar extendiendo mis más sinceras palabras de agradecimientos a mis directores, Javier Valdés y Roberto Tomás, por su apoyo constante y sus valiosos comentarios a lo largo de este proceso, con quienes he compartido una excelente experiencia de lo que es el trabajo en equipo. La dedicación y compromiso de ambos ha sido fundamental para el desarrollo y éxito de todas las tareas de investigación que llevamos a cabo durante los últimos tres años. Como profesionales y personas ambos son naturalmente diferentes, pero se complementan a la perfección, así que me llevo de ellos también el gran ejemplo que dan de su calidad humana y lo importante que es crear sinergias dentro de ambiente de trabajos sanos para sacar adelante con éxito los proyectos que se emprendan. Gracias por la confianza que depositaron en mí y por alentarme a seguir en este camino.

También quiero expresar gratitud a mi mamá y a mi familia (en Colombia y en México), por su apoyo y amor incondicional a lo largo de los años. A mis amigos de toda la vida en Colombia, a los nuevos amigos que me ha dado el doctorado en la UA (Ángel, Panpan, Xiaojie, Hengyi, Dian...), a quienes me acogieron en Pavía (Laura, Michelle, Giulia...), a Lala y Jose que nunca me han dejado sola en Alicante, y a Poli por todo el amor inagotable a través de las décadas.

Además, deseo agradecer a todas las personas que han hecho parte de este proceso académico, a Claudia Meisina por recibirme en la Universidad de Pavía y asesorarme durante mi estancia. A todos los profes de la UA que hacen parte del RESERVOIR (Conchi, Adri, Juanma) y al resto del personal del departamento de ingeniería civil, así como también a todos los compañeros de RESERVOIR con quienes hemos colaborado en publicaciones científicas.

Gracias al proyecto RESERVOIR (Grant agreement 1924) por su financiación a través de la Universidad de Alicante, por brindarme la oportunidad de llevar a cabo esta investigación y proporcionar los recursos necesarios. También me gustaría extender mis agradecimientos a los revisores externos Claudia Meisina y Matteo del Soldato por el tiempo y criterio que se han tomado para evaluar esta tesis doctoral, por sus comentarios y correcciones que han contribuido a mejorar esta memoria.

Este trabajo no habría sido posible sin el apoyo y la colaboración de todas estas personas, y estoy profundamente agradecida por su contribución a mi investigación.

# Table of Content

res revia FIRS	tions T PA Dduct Stru Back 1. 2. State	RT	12 14 15 16 16 16 19 20
FIRS Intro 1. 2. 1.2. 1.2. 1.2. 3.	tions T PA Oduct Stru Back 1. 2. State	RT	14 15 16 16 16 16 19 20
Intro 1. 2. 1.2. 1.2. 1.2. 3.	T PA oduct Stru Back 1. 2. 3.	cture of the PhD thesis	15 16 16 16 19 20
Intro 1. 2. 1.2. 1.2. 3.	Stru Back 1. 2. State	cture of the PhD thesis	16 16 16 19 20
1. 2. 1.2. 1.2. 1.2. 3.	Stru Back 1. 2. 3. Stat	cture of the PhD thesis	16 16 16 19 20
2. 1.2. 1.2. 1.2. 3. 4.	Back 1. 2. 3. Stat	OlnSAR for monitoring land subsidence in overexploited aquifers	16 16 19 20
1.2. 1.2. 1.2. 3.	1. 2. 3. State	DInSAR for monitoring land subsidence in overexploited aquifers  Validation of DInSAR data applied in land subsidence areas  Applications of DInSAR dataement of the problem	16 19 20
1.2. 1.2. 3. 4.	2. 3. Stat	Validation of DInSAR data applied in land subsidence areas.  Applications of DInSAR dataement of the problem	19 20
1.2. 3. 4.	3. Stat	Applications of DInSAR data	20
3. 4.	Stat	ement of the problem	
4.			21
	Нур	adh acta and altitudina	
5.		otnesis and objectives	22
	Justi	fication of the thematic unit and publications	22
6.	Con	gress related to the thesis	24
7.	Othe	er publications	25
1.7.	1.	Papers in progress of publication	25
1.7.	2.	Participation in papers not related to the thesis	26
1.7.	3.	Congress not-related to the thesis	26
Sett	ings (	of the study areas	29
1.	San	Luis Potosí valley	29
2.	East	ern Gediz river basin	30
3.	Alto	Guadalentín aquifer	30
4.	Mur	cia city	31
5.	Tert	iary detritic aquifer of Madrid	31
6.	Sout	thern Yangtse Delta, China	32
7.	Nort	th China Plain (Beijing city)	32
Met	hodo	logy	34
1.	Fund	damentals of DInSAR technique	34
3.1.	1.	The Coherent Pixel Technique (CPT)	36
3.1.2.		P-SBAS	36
2.	DInS	SAR data processing	36
3.2.	1.	San Luis Potosí valley	36
3.2.	2.	Eastern Gediz River basin	37
3.	Prin	cipal and independent components analysis	37
	5. 7. 1.7.: 1.7.: 1.7.: Sett 1. 2. 3. Met 1. 3.1.: 3.1.: 3.2.: 3.2.:	5. Justi 6. Cong 7. Other 1.7.1. 1.7.2. 1.7.3. Settings of 1. San 2. East 3. Alto 4. Mur 5. Tert 6. Sout 7. Nort Methodo 1. Fund 3.1.1. 3.1.2. 2. DInS 3.2.1. 3.2.2.	4. Hypothesis and objectives 5. Justification of the thematic unit and publications 5. Congress related to the thesis 7. Other publications 1.7.1. Papers in progress of publication 1.7.2. Participation in papers not related to the thesis 1.7.3. Congress not-related to the thesis Settings of the study areas 1. San Luis Potosí valley 2. Eastern Gediz river basin

	3.4.	Valid	dation methodology: ValInSAR	37	
	3.4	l.1.	Pre-processing	37	
	3.4	1.2.	Step 1: Ingestion	38	
	3.4	1.3.	Step 2: Processing	39	
	3.5.	Floo	d modelling in Alto Guadalentín	39	
	3.5	5.1.	Input data	39	
	3.5	5.2.	Model setup	40	
	3.5	5.3.	Hazard and risk evaluation	41	
	3.6.	Stre	ss-strain application	41	
	3.6	5.1.	Plotting the stress-strain curves	41	
	3.6	5.2.	Extraction of the $\mathit{Ske}$ and $\mathit{Skv}$ parameters from stress-strain curves	41	
4.	Re	sults		43	
	4.1.	DIns	SAR data for monitoring land subsidence	43	
	4.1	L.1.	CPT and P-SBAS results	43	
	4.1	L.2.	Validation of DInSAR results	43	
	4.1	L.3.	PCA/ICA results	45	
	4.2.	Vall	nSAR results	45	
	4.2	2.1.	Definition of buffer areas	45	
	4.2	2.2.	Velocity validation	46	
	4.2	2.3.	Time series validation	47	
	4.3.	Floo	d modelling results	47	
	4.3	3.1.	Water depth results	47	
	4.3	3.2.	Velocity results	49	
	4.3	3.3.	Flood hazard classification and economic damage estimation	50	
	4.4.	Calc	ulation of skeletal storage coefficient results	51	
5.	Dis	cussio	n	55	
	5.1.	DIns	SAR data for monitoring land subsidence	55	
	5.1	L.1. Re	ationship between land subsidence and soft soil thickness	55	
	5.1.2. Relationship between land subsidence and groundwater extraction				
	5.1	L.3. Rel	ationship between land subsidence and active faults	59	
	5.2.	Reco	ommended accuracies for validation of DInSAR data	61	
	5.3.	Floo	d modelling in Alto Guadalentín	62	
	5.4.	Calc	ulation of skeletal storage coefficient discussion	63	
6.	Со	nclusio	ons	67	
7.	Fu	ture re	search	78	
8.	Re	ferenc	es	79	

igures
Figure 2.1 Localization of the study areas
Figure 3.1 Geometry of the DInSAR image acquisition for a zero baseline. (Blanco-Sánchez, 2009) 34
Figure 3.2 General flowchart of the methodology
Figure 3.3 (a) Distribution of PS/DS around the in-situ benchmark A and equispaced buffer rings. (b)
Dispersion analysis for different buffer sizes in order to find the optimal value. (c) . Deformation rate
computation from time series
Figure 3.4 Cumulative land subsidence after the integration of all InSAR data for the 1992-2016 period.
The modelling area, mesh used for the refinement region and boundary inflow and outflow sections are
also plotted in the map
Figure 4.1 (a) LOS displacements rates for the metropolitan area of SLPV, (b) LOS displacement rates the ASSB
Figure 4.2 Validation of DInSAR dataset: (a) Correlation plot between CGNSS and CPT time series data in
SLP. (b) Correlation plot between SALH CGNSS and P-SBAS time series data in ASSB. Continued lines
·
represent the 1:1 line, and dotted lines parallel to the 1:1 line represent the ± 1 cm/error
Figure 4.3 FastICA results in ASSB: (a) ICs eigenvector time series compared with seasonal cumulative
rainfall (blue), (b) IC1 score map, (c) IC2 score map, (d) IC3 score map
Figure 4.4 Dispersion analysis for different buffer size in order to find the optimal value. The dotted line
ndicates the optimal buffer size. (a) results for CSK dataset in Alto Guadalentín aquifer. (b) results for
Sentinel-1 dataset in Alto Guadalentín aquifer. (c) results for ENVISAT dataset in Murcia. (d) results for
Sentinel-1 dataset in San Luis Potosí
Figure 4.5 Correlation plot and statistics values (cm/year) for the velocity validation. (a) Levelling
penchmark vs ENVISAT for Alto Guadalentín aquifer. (b) Extensometers vs ENVISAT for Murcia and (c)
Continuous GNSS vs Sentinel-1 for San Luis Potosí Valley. Continued lines represent the 1:1 line, and
dotted lines parallel to the 1:1 line represent the ± 1 cm error46
igure 4.6 Time series validation for the comparison between DInSAR observations and in-situ
echniques. (a) LORC CGNSS station with CSK observations. (b) V-3 extensometer with Envisat
observations in Murcia. (c) TNSL station with Sentinel-1 observations in San Luis Potosí
Figure 4.7 Water depth map for the (a) 1992 and (b) 2016 scenarios48
Figure 4.8 Comparison between water depths in 1992 and 2016 along cross sections A-A' and B-B'.48
Figure 4.9 Water flow velocity map for the (a) 1992 and (b) 2016 scenarios. The black squares denote
he flooded area with changes49
Figure 4.10 Differences in the (a) water depth and (b) velocity between the 1992 and 2016 scenarios.
This corresponds to a zoom-in of the black square plotted in figure 4.950
Figure 4.11 (a) Hazard risk map for the 1992 and (b) 2016 scenarios. The black squares denote the
looded area with changes50
Figure 4.12 Number of (a) rural and (b) urban cadastral units affected by different flood hazard risks
under the 1992 and 2016 scenarios51
Figure 4.13 Stress-strain curves results from the Southern Yangtse Delta. (A-B) Second confined aquifer;
C-D) Second aquitard layer. (E-F) Third aquitard layer
Figure 4.14 Stress-strain curves results from the Second aquifer layer of the Plain of Beijing: (A) elastic
component of subsidence. (B) inelastic component of subsidence (second layer aquifer)53
Figure 4.15 Stress-strain curves results from North China plain. (A) elastic component of subsidence in
he Second layer - Pinggezhuang station; (B) inelastic component of subsidence in the Second layer -

nelastic component of subsidence in the third layer - Tianzhu station53
igure 4.16 Stress-strain curves results from wells CA-3 and CA-4 placed in the Madrid Tertiary aquifer- ystem54
igure 5.1 Soft soil thickness map of the San Luis Potosí valley55
igure 5.2 Deformation rate values along the section P1–P6 in San Luis Potosí56
igure 5.3 Relationship between soft soil thickness and land subsidence in Gediz basin: (a) Soft soil
hickness map derived from boreholes. (b) Vertical component of LOS displacement rate. (c) Correlation
lot between soft soil thickness and vertical displacement rate. (d) Comparison between IC1 and LOS
lisplacement at two locations with high soft soil thickness and land displacements: (e) time series
omparison at zone 1. (f) Time series comparison at zone 2
igure 5.4 (a) Static level evolution of the San Luis Potosi valley for the 2007–2017 period. (b) and (c)
riezometric level evolution and deformation time series measured by CPT for two wells in SLPV. The
ocation of the wells is shown in (a). Blue points and dashed blue line represent the measured values
nd the general trend of static water level, respectively58
igure 5.5 Relationship between seasonality and piezometric head evolution in Gediz basin: (a) spatial
listribution of groundwater level evolution from 2016 to 2018 and (b) IC2 map score
igure 5.6 IC2 components in two selected wells of Gediz basin: (a) IC2 and piezometric head time series
t the well 55129. (b) IC2 and piezometric head time series at the well 22043
igure 5.7 Deformation rate map derived by CPT covering (a) the Aeropuerto fault zone, coloured lines
epresent sections across the trace fault. (b) Land subsidence sections D-D', E-E', F-F', and G-G' along
he Aeropuerto fault. (c) the San José del terremoto fault
igure 5.8 Relationship between active faults and land subsidence: (a) Rate displacement map covering
arıgöl fault influence area in Gediz basin. (b) Analysis of vertical displacement sections A-A', B-B', C-C'
nd D-D' along the Sarıgöl fault trace
igure 5.9 (a) Thresholds proposed for DInSAR validation using velocity values. (b) Accuracy thresholds
roposed for DInSAR validation using displacement time series. Letters from A to F correspond to the
catterplots in Figure 5.10
igure 5.10 Correlation plot for time series validation due to accuracy categorization in Figure 5.9. (a)
orrelation between LORC station and CSK observations in Alto Guadalentín. (b) Correlation between
RCA station and Sentinel-1 observations in Alto Guadalentín. (c) Correlation between TNSL station and
entinel-1 in San Luis Potosí. (d) Correlation between Ei-6 extensometer and ENVISAT observations in
Aurcia. (e) Correlation between Ei-1 extensometer and ENVISAT observations in Murcia. (f) Correlation
etween extensometer and ENVISAT observations in Murcia. Continued lines represent the 1:1 line, and
otted lines parallel to the 1:1 line represent the ± 1 cm error62
igure 5.11 . Comparison graphic of the different storage coefficients calculated in the Southern Yangtse
igure 5.12 Comparison graphic of the different storage coefficients calculated in the North China Plain.
igure 5.13 Comparison between the elastic storage coefficients calculated by the MATLAB application
nd the coefficients calculated by Béjar-Pizarro et al. (2017)65

#### **Abbreviations**

ASSB: Alaşehir-Sarıgöl sub-basin CPT: Coherent pixel technique DEM: Digital elevation model

DInSAR: Differential Interferometry synthetic aperture radar

DSM: Digital surface model

GEP: Geohazard Exploitation Platform GNSS: Global navigation satellite system

IWS: Interferometric Wide Swath

ICA: Independent Component Analysis

IC: Independent component IDW: Inverse Distance Weighting IGN: Instituto Geológico Nacional LiDAR: Light Detection and Ranging

LOS: Line-of-sight

Max-e: Maximum difference

MD: Mean difference

Min-e: Minimum difference NRMSE1: Normalized RMSE 1 NRMSE2: Normalized RMSE2

PCA: Principal Component Analysis

PS: Persistent scatterers

PSI: Persistent Scatterer Interferometry P-SBAS: Parallel Small Baseline Subset

RMSE: Root Mean Square Error SAR: Synthetic Aperture Radar SCI: Science Citation Index SD: Standard Deviation

SLP: San Luis Potosí

SLPV: San Luis Potosí Valley

SRTM: Shuttle Radar Topography Mission TDAM: The Tertiary Detritic Aquifer of Madrid

# I. FIRST PARTGeneral synthesis

#### 1. Introduction

#### 1.1. Structure of the PhD thesis

This thesis follows the format prescribed by the University of Alicante's Doctoral School for dissertations presented as a compendium of publications, meeting the regulations set by the University's Governing Council in 2013. It adheres to the requirement of providing a synthesis in one of the official languages of the Valencian Community, summarizing objectives, hypotheses, presented works, and thematic unit justification. The synthesis includes a concise overview of obtained results, discussions, and final conclusions, aiming to precisely convey the thesis content. The thesis is divided into two parts: an initial section focusing on the overall synthesis and a subsequent section incorporating contributed publications, specifically, articles published in indexed journals.

This thesis is organized around three key research topics. The initial part explores the current understanding of each research topic, outlines associated problems, presents hypotheses, and establishes specific objectives. It then explains the significance of the work and justifies the thematic unity of the articles presented in the final part of the thesis. The second section provides a brief overview of study locations in Spain, Türkiye, and China. It describes the geological features of these areas and emphasizes the characteristics of the studied aquifers, detailing the historical evolution of groundwater extraction over recent decades. The third section discusses the research methodologies employed for each research topic. Subsequently, specific findings and their implications are presented and discussed for each research focus. This approach facilitates an in-depth exploration of unique results within each research topic.

The synthesis concludes by summarizing key conclusions from the collective body of work. This structured presentation ensures a coherent narrative in alignment with the central themes of three four research areas: 1. Differential Interferometric Synthetic Aperture Radar (DInSAR) for monitoring land subsidence in overexploited aquifers. 2. Validation of DInSAR data applied to land subsidence areas. 3. Applications of DInSAR data: Flood modelling and Automatic calculation of specific storage coefficients in aquifer systems.

#### 1.2. Background by research topics.

#### 1.2.1. DInSAR for monitoring land subsidence in overexploited aquifers.

Subsidence refers to the gradual sinking or settling of the Earth's surface over a broad area, driven by natural or human-induced factors (Herrera-García et al., 2021). Although rarely fatal, it can cause significant material damage. The American Geological Institute's glossary describes it as the gradual downward settling of the Earth's solid surface, mainly caused by natural geological processes or human activities like resource extraction and saturation of porous deposits (Tomas et al., 2011; Zermeña et al., 2005). Human intervention, particularly in populated areas relying on groundwater, is a primary trigger for subsidence. The phenomenon gained attention in the 20th century with population growth and increased water consumption, leading to intensive aquifer exploitation. Today, subsidence involves geological risks, prompting authorities worldwide to develop technologies for its identification and mitigation (Declercq et al., 2017).

Land subsidence driven predominantly by groundwater extraction is observed in major cities worldwide. San Joaquin Valley in Central California, marked by extensive agriculture, experiences subsidence linked to hydrocompaction, oil extraction, and tectonic adjustments, with a significant event recorded in 1972 (Bolger et al., 2011; Poland et al., 1984). China faces subsidence in coastal regions, flat areas, and valleys due to rapid urbanization, affecting over 45 cities with economic losses exceeding \$100 million annually, primarily attributed to groundwater extraction (Hu et al., 2004). Tehran, Iran, grapples with subsidence resulting from extensive groundwater extraction for agriculture, domestic, and industrial use,

experiencing a subsidence rate of 42 cm/year (Mahmoudpour et al., 2013). Bologna, Italy, witnesses' subsidence post-World War II tied to groundwater extraction, notably impacting historical buildings, intensified by economic growth and exacerbating natural subsidence due to tectonic movements and sediment compaction (Darini, 2007). This overview provides a comprehensive perspective on the diverse causes, hydrogeological settings, and socio-economic impacts associated with land subsidence globally.

There are two types of subsidence: natural subsidence and anthropogenic subsidence. Natural subsidence refers to slow and small-scale movements on the Earth's surface associated with internal geological processes, occurring over geological time scales (thousands of millions of years). It can be induced by tectonic processes, natural consolidation of soils and erosive processes. On the other hand, anthropogenic subsidence, also known as exogenous subsidence, involves surface deformation processes related to natural or human-induced compaction (Darini, 2007). It includes subtypes triggered by activities like mineral extraction in underground galleries, tunnel construction, extraction of fluids (water, oil, or gas) from underground reservoirs, and the decline of the water table due to prolonged droughts. Subsidence caused by the construction of underground structures or mining galleries, especially in coal mines, is one subtype of anthropogenic subsidence. Another subtype is subsidence due to compaction, influenced by factors such as load, drainage, vibration, fluid extraction, and hydrocompaction. Natural subsidence occurs over geological time frames and has not historically caused serious effects. In contrast, anthropogenic subsidence, driven by various human activities, can lead to surface deformations and poses potential risks (Darini, 2007).

This doctoral thesis focuses on subsidence due to the extraction of groundwater from detrital aquifers. The connection between subsidence and groundwater extraction was first established by Fuller (1908), and since then, interest in studying the mechanisms and effects of subsidence associated with piezometric head declines has substantially increased (Garzón, 2011). Aquifers, geological formations capable of storing and transmitting water, can be confined, unconfined, or semiconfined. The extraction of water from aquifers leads to a decline in piezometric levels, leading to a decrease in pore-water pressure and an increase in effective stresses on the terrain, resulting in subsidence. However, the process is more complex for confined aquifers, as water extraction does not lead to porosity drainage. Instead, it reduces interstitial pressure, lowering the piezometric level and triggering consolidation and porosity reduction, which translates into surface subsidence (Maliva, 2004). The theories of Terzaghi provide insights into the water release and consolidation processes in confined aquifers, respectively (Burbey, 2001). The relationship between changes in groundwater levels and the compression of aquifer systems is explained by this principle of effective stress According to Terzaghi, when fluid pressure decreases, as in the case of lowered groundwater levels, the support previously provided by pore-fluid pressure is transferred to the aquifer systems skeleton, causing compression. Conversely, when porefluid pressure increases, such as during groundwater recharge, the skeleton expands. This alternating compression and expansion of the skeleton occur as pore-fluid pressure fluctuates with aquifer discharge and recharge (Galloway et al., 1999). The fully recoverable deformation results in seasonal, reversible displacements of the land surface, commonly observed in response to seasonal changes in groundwater withdrawal. The preconsolidation stress represents the maximum level of past stressing of a skeletal element. If the load on the aquitard skeleton exceeds this stress, the aquitard may undergo significant, permanent rearrangement, leading to irreversible compaction. This compaction results in a permanent reduction of pore volume in the aquitard, contributing to subsidence. In confined aquifer systems with large-scale over-exploited, the volume of water derived from irreversible aquitard compaction is roughly equal to the volume of subsidence. This represents a one-time mining of stored groundwater and a permanent reduction in the aquifer system's storage capacity. Aquitards, being less permeable than aquifers, may experience slow vertical drainage into adjacent pumped aquifers, lagging behind changes in water levels (D. Galloway et al., 1999).

The drainage of a free aquifer may not follow Terzaghi's consolidation theory, yet subsidence occurs due to the loss of interstitial hydrostatic pressure and increased stress on the solid fraction of the soil, leading to reorganization and greater compaction. Subsidence in locations with rapid sinkings often occurs in compressible or intermediate deposits, such as alluvial or lacustrine deposits, lahars, or sandstones, suggesting consolidation of deep compressible strata, either due to pumping of confined aquifers or local geological variations (Chaussard et al., 2014).

In Mexico, where over 60 % of the population relies on groundwater extraction, several cities in the central region face the consequences of this practice. San Luis Potosí is one such city experiencing declines in piezometric water levels since 1971, with subsidence studied over the last two decades, revealing structural damage to homes, roads, and historical buildings. This has resulted in significant economic impacts, prompting an in-depth investigation into the causes and their correlation with groundwater exploitation. The identification of vulnerable areas is considered a valuable tool for the territorial planning of affected municipalities (Figueroa-Miranda et al., 2018). The metropolitan area of San Luis Potosí and Soledad de Graciano Sánchez currently faces significant subsidence issues in the state of San Luis Potosí. A comprehensive study conducted in 2006 focused on the historic centre of the city, revealing structural damages in prominent buildings such as the Mask Museum, Regional Museum of San Luis Potosí, Church of the Holy Spirit, and Federico Silva Museum, all attributed to differential settlements due to soil faults. Geophysical studies identified three types of faults—vertical, horizontal, and step faults—linked to factors like declining piezometric levels, granular material consolidation, and basin bedrock irregularities (Herrera-Pérez, 2012). Economic repercussions of subsidence were analysed, identifying 1982 properties at risk, with 282 already experiencing structural damage. The drainage and water supply network also suffered, with 22 identified "faults" concentrated in the northeast, causing an estimated monetary impact of \$2.5 million. A monitoring network of 74 wells intercepting the aquifer highlighted a decreasing piezometric water level range from 95 to 155 m by 1998, with an observed drawdown fluctuating between 0.5 and 4.0 m in the triennial period from 1995 to 1998.

Additionally, Türkiye, located in the complex tectonic zone of the Anatolian microplate in the eastern Mediterranean, experiences significant deformations and seismic activity due to interactions with Eurasia, Africa, and Arabia plates (Tatar et al., 2012). This has led to a horst and graben structure in the Menderes massif, with tectonic valleys in western Türkiye, predominantly filled with detrital materials, facing considerable land subsidence. Studies over the past two decades have observed faults along the grabens, revealing that normal faults induce structural damage through differential subsidence (Imamoglu et al., 2022). Beyond tectonic influences, other factors contributing to land subsidence include overexploitation of aquifers due to intensive agriculture and anthropogenic activities. The eastern Gediz River Basin, a western Turkish tectonic valley, has developed economic activities like agriculture, animal husbandry, industry, geothermal fields, and mining. Groundwater, the primary water source, faces increasing pressure due to these activities, making the Gediz valley one of Türkiye's most stressed basins (Duru et al., 2018).

Various methods are employed to measure ground deformations, ranging from traditional approaches involving pore pressure and topographic changes to modern techniques like Global Navigation Satellite System (GNSS) and remote sensing, with Differential Interferometric Synthetic Aperture Radar (DInSAR) being a prominent technology (Tomás et al., 2014). DInSAR offers high-resolution, day-and-night, weather-independent, wide-coverage, and accurate measurements of surface changes, making it cost-effective for detecting and monitoring regional-scale surface subsidence with centimetre to millimetre precision. DInSAR has been extensively used globally to study settlements resulting from groundwater withdrawal, particularly in areas heavily reliant on groundwater reserves (Hu et al., 2019).

Numerous studies, have applied DInSAR techniques for evaluating ground deformation. Examples include monitoring subsidence rates in Bangkok using Radarsat-1 images (Aobpaet et al., 2010), the Coherent Pixels Technique for studying land subsidence in Murcia (Spain), Gardanne (France), and St. Lazare Railway Station (Paris), and studying the Guadalentín Valley (Spain) and Delta municipality region (Greece) using ENVISAT/ASAR and ERS 1/2 images, respectively (Duque et al., 2007; Raspini et al., 2014; Rigo et al., 2013). In Iran, ENVISAT images were used to map land subsidence in Yazd province (Amighpey & Arabi, 2016). Myanmar's Yangon exhibited subsiding rates of 120 mm/year, as identified by Sentinel-1 images (Horst et al., 2018). Tehran's accumulated settlements of 39.6 cm during 2014-2017 were monitored using ENVISAT-ASAR, Sentinel 1, and GPS observations (Foroughnia et al., 2019). Notably, many InSAR studies in Mexico, particularly in Mexico City, Valle de Toluca, Morelia, and Mexicali, utilize different satellite images and approaches (Castellazzi et al., 2016). For instance, in San Luis Potosí a DInSAR study using Sentinel-1 images for 2014-2019 indicated subsidence values of up to 13.4 cm in certain areas, approximately 2.6 cm/year (Tristán et al., 2020). Despite the significant impact of subsidence, there are limited studies on its monitoring and diagnostic origin in the San Luis Potosí Valley (SLPV), with few utilizing InSAR techniques to date (Tristán et al., 2020). In the eastern Gediz river basin, previous geodetic studies using InSAR and GPS measured subsidence rates, with the Sarıgöl fault showing cumulative vertical displacement of -60 to -85 cm from 2000 to 2010 (Koca et al., 2011). GPS benchmarks from 2013 to 2015 indicated a maximum displacement rate of -90 mm/year along the Sarigöl fault (Poyraz et al., 2019). InSAR monitoring from May 2014 to November 2015 identified a maximum displacement rate of -50 mm/year in the Line of Sight (LOS) direction. Collectively, these studies suggest that subsidence is not solely attributed to tectonic creep but can also result from land subsidence induced by groundwater extraction (Poyraz & Hastaoğlu, 2020).

The main objective of this research topic is to assess the effects of groundwater exploitation in the San Luis Potosí Valley on the subsidence phenomenon through a spatial analysis. As well as, to assess the impact of tectonic activity and groundwater extraction in the eastern Gediz River Basin on both land subsidence and the development of faults. Additionally, to establish a connection between subsidence and groundwater extraction practices while exploring other contributing factors, such as the thickness of soft soil layers.

#### 1.2.2. Validation of DInSAR data applied in land subsidence areas.

Validating measured displacement results is crucial when describing a new subsidence study area. This process not only establishes DInSAR as a reliable technique for such studies but also enhances the robustness of the derived conclusions. Currently, validation relies on discrete data from various techniques, lacking a unified and comprehensive methodology. The monitoring of land subsidence has relied on various geodetic techniques. Techniques such as levelling, borehole extensometers, continuous GNSS, GNSS benchmarks, and InSAR have been instrumental in measuring surface displacements. Levelling, with a resolution of 0.1-1.0 mm, provides vertical displacement data in a line-network arrangement on a monthly or annual basis (Awange, 2018). Borehole extensometers, boasting a resolution of 0.01-0.10 mm, offer continuous daily vertical displacement measurements at specific points. Continuous GNSS, with a resolution of 1-2 mm in both vertical and horizontal components, operates within networks or at specific points, providing continuous data. GNSS benchmarks, with a resolution of 8-15 mm, offer vertical and horizontal measurements monthly or annually in a network or point arrangement (Galloway & Burbey, 2011). Notably, DInSAR is exceptional at mapping large areas affected by land subsidence, over 10,000 km<sup>2</sup>, with a high density of point measurements and a resolution of approximately 5.0 mm, depending on ground characteristics, on a monthly or weekly basis (Prati et al., 2010). Each technique contributes uniquely to our understanding of subsidence patterns, offering various resolutions, displacement components, arrangements, and sample frequencies.

Monitoring methods involving on-site instruments, such as levelling or GNSS, face several drawbacks. These approaches offer point-based measurements, resulting in spatially limited observations, and are time-intensive with a high relative cost per measurement point (Tomás et al., 2014). Consequently, they may impede the identification of new subsidence areas beyond the instrumented site. In contrast, DInSAR serves as an effective monitoring technique to supplement these sparse measurements (Hu et al., 2019). However, it is essential to note that DInSAR data may not always align with deformation rates and subsidence time series obtained from *in-situ* monitoring strategies, necessitating a thorough comparison and validation before further analysis.

The objective of this research topic is to develop and assess a systematic approach for comparing DInSAR with various *in-situ* techniques through the utilization of a novel code named "ValInSAR". Additionally, the goal is to propose validation strategies applicable to any land subsidence product.

#### 1.2.3. Applications of DInSAR data

This section examines the background related to two examples of DInSAR data applications: Flood modelling considering land subsidence measured by DInSAR data and Automatic calculation of skeletal storage coefficients in aquifer systems.

Floods, resulting from intense rainfall surpassing soil infiltration capacity, are globally prevalent, causing substantial economic losses (Schumann, 2011). In SE Spain, with its semi-arid climate and distinctive geomorphology, floods pose a significant social and economic threat, leading to numerous deaths (Pujadas Ferrer, 2002). Climate change has heightened the frequency of extreme floods, and projections anticipate a doubling of such events in Europe by 2035 (Marchi et al., 2010). Settlements along alluvial fans face increased vulnerability, necessitating effective flood risk management strategies (Mihu-Pintilie et al., 2019). Advanced flood modelling using remote sensing data and sophisticated software has significantly improved risk assessment, enabling precise flood mapping that considers climate change effects. Various hydraulic models, including 1D, 2D, and 3D, are employed for flood event simulation, each with its advantages and computational demands (Cerri, 2017). Precision in hydraulic modelling relies on high-resolution digital terrain models obtained through remote sensing technologies like LiDAR and satellite data. The Alto Guadalentín valley exemplifies a region experiencing both intense land subsidence and flood events. Groundwater withdrawal has induced significant subsidence, leading to cumulative vertical displacements exceeding 1 m (Bonì et al., 2015). Despite high water flow rates, the valley's limited riverbed channels make it susceptible to floods, historically experiencing significant events with notable social and economic impacts. Recent flood patterns, observed in events like those in 1973 and 2012, indicate a potential link between gravel mining, aquifer overexploitation, and altered river dynamics (Gil-Meseguer et al., 2012). Integrating remote sensing technologies like DInSAR with hydraulic modelling enhances flood risk assessments, improving parameter accuracy and facilitating effective flood hazard management in complex terrains like the Alto Guadalentín valley.

On the other hand, the use of stress-strain curves provides a graphical representation of the correlation between ground displacement, resulting from aquifer-system compaction, and the temporal evolution of groundwater levels. These curves serve as a means to interpret the mechanical behaviour of either the entire aquifer system or specific layers within it. Additionally, valuable insights into hydrogeological variables, such as the storage coefficient, can be derived from this relationship. Despite the significant advantages and information conveyed by stress-strain curves, their analysis is commonly performed manually, lacking a well-defined, objective protocol. This manual approach proves to be laborious and time-consuming producing subjective results relies significantly on the researcher's interpretation, skills and expertise in analysing graphical data.

The preconsolidation pressure represents the maximum effective stress a soil has experienced throughout its geological history and is pivotal in distinguishing between elastic (recoverable) and inelastic (irreversible) deformations (Poland, 1984). In the context of land subsidence resulting from piezometric level fluctuations, the preconsolidation pressure in soils affected by groundwater withdrawal indicates the depth at which deformations become irreversible.

Terzagui's poroelasticity theory, established in 1925, relates water level fluctuations to the effective stress in the aquifer skeleton, revealing the elastic expansion or compression of the aquifer system based on changes in fluid pressure (Galloway & Hoffmann, 2007). From this bases, stress-strain curves, introduced by Riley (Riley, 1969), represent the relationship between land subsidence and piezometric level fluctuations, enabling estimation of the skeletal storage coefficient of compressible strata (Burbey, 2001). Aquifer systems can exhibit various mechanical behaviours, including elastic, elastoplastic, and viscoelasto-plastic responses, influenced by factors such as stratigraphy, pumping conditions, climate, and precipitation trends. Elastic behaviour is characterized by fully recoverable deformation, typical in aquifer-systems with seasonal groundwater level variations. Elastoplastic behaviour involves non-recoverable plastic deformation, observed even when stress remains within elastic limits. Irrecoverable deformation, indicating intense aquifer exploitation, results in a significant drop in groundwater levels, with stress-strain plots depicting clear temporal evolution and compaction. It is essential to acknowledge that aquifer system behaviour varies based on geological and hydrogeological conditions. Further research and field data are imperative to comprehensively characterize and understand the complexities of specific aquifer systems (Burbey, 2001; Zhang et al., 2007).

This last research topic aims to conduct rainfall-runoff simulations in the Alto Guadalentín valley, considering two scenarios: 1992 and 2016, to incorporate the cumulative subsidence observed in the region over that timeframe. Furthermore, presents a tool designed to automate the analysis of stress-strain curves, aiming to improve objectivity and streamline the analytical procedure. The application's performance has been evaluated using actual data from various aquifer systems globally impacted by land subsidence.

#### 1.3. Statement of the problem

The escalating challenge of land subsidence, exacerbated by extensive groundwater extraction, demands a detailed and region-specific understanding. This makes almost compulsory the identification and later analysis of those subsidence-affected regions with a lack of a clear and comprehensive analysis of the phenomenon. This is particularly true in the two pilot sites of San Luis Potosi and the eastern Gediz river. Within this paradigm, the development of DInSAR technology emerges as a fundamental tool for accurate and expansive subsidence monitoring.

The validation methodologies incorporated into the research become even more crucial in the context of subsidence monitoring. Rigorous validation against DInSAR-derived subsidence data, alongside field measurements, enhances the reliability of the measurements and underscores its potential as a robust tool for hydrogeological investigations.

Beyond subsidence analysis, the broader applications of this research extend to flood modelling, where the validated application can offer insights into potential flood risk areas in Alto Guadalentín. Furthermore, the calculation of the skeletal storage coefficient provides an additional layer of understanding for groundwater management practices in aquifer systems affected by land subsidence.

The significance of this research lies not only in advancing our understanding of aquifer behaviour and groundwater-induced subsidence but also in providing hydrogeologists and decision-makers with a systematic, validated, and versatile tool. By comprehensively addressing the specific challenges in San

Luis Potosi, the eastern Gediz River Basin, and Alto Guadalentín, this study aims to contribute valuable insights for sustainable water resource management, subsidence mitigation, and flood risk assessment.

#### 1.4. Hypothesis and objectives

The integration of advanced DInSAR techniques, validated through innovative methodologies such as the ValInSAR code, along with interdisciplinary applications including hydraulic modelling and stress-strain curve analysis, can contribute to the understanding and management of land subsidence. This research proposes that exploiting the power of DInSAR data, combined with complementary datasets and analytical tools, will not only enhance the accuracy of subsidence monitoring but also provide invaluable insights into the complex interrelation of geological, hydrological, and anthropogenic factors contributing to land subsidence. The outcomes are expected to provide practical applications in predicting subsidence trends, mitigating flood risks, and optimizing groundwater resource management strategies for sustainable urban development.

The general objective of this doctoral dissertation is to comprehensively investigate and understand the dynamics of land subsidence in diverse global contexts, employing advanced remote sensing techniques and methodologies. The research aims to measure subsidence magnitude, identify triggering factors, and explore implications, focusing on specific study areas such as the San Luis Potosi metropolitan area (Mexico), Alaşehir-Sarıgöl sub-basin (Türkiye), and the Alto Guadalentín Valley (Spain). Through the utilization of advanced techniques like PSBAS and CPT, the study assesses subsidence rates and establishes correlations with trace faults, groundwater extraction, and soft soil thickness. Additionally, the research aims to enhance the reliability of DInSAR measurements through the development and proposal of validation methodologies. To achieve the general objective, the following specific objectives were formulated:

- Conduct an analysis of the spatial distribution of subsidence and its evolution over time in historically overexploited aquifers.
- Develop and propose a methodology for the validation of DInSAR data using in-situ technologies.
- Predict the impact of land subsidence resulting from overexploitation of aquifer bodies on flood risk and infrastructure.
- Develop a methodology and application to automate stress-strain curves and calculate  $S_{ke}$  and  $S_{kv}$  coefficients in aquifer systems.

#### 1.5. Justification of the thematic unit and publications

The results obtained through this doctoral thesis were published in journals indexed in the Science Citation Index (SCI) by Clarivate Analytics. The Table 1.1 summarizes the impact factor of the journals that include the articles comprising this thesis as a compendium, as well as their position within different categories.

Table 1.1 Impact factor of the journals corresponding to the compendium. \*Values corresponding to 2022.

Journal	Year	Impact factor	JCR category	Rank by category	Quartile
Remote sensing	2020	4.8	Environmental	76/274	Q2
		_	sciences		
			Geosciences	27/200	Q1

#### **INTRODUCTION**

			Imaging science	8/29	Q2
			Remote sensing	10/32	Q2
Journal of selected	2022	5.5	Engineering electrical	58/275	Q1
topics in applied earth observations			Geography physical	6/49	Q1
and remote			Imagine science	6/28	Q1
sensing			Remote sensing	9/34	Q2
Water resource	2023*	4.3	Engineering civil	33/139	Q1
management			Water resources	25/103	Q1
Engineering	2023*	7.4	Engineering geological	1/41	Q1
geology			Geosciences	12/202	Q1

The publications comprising this thesis are listed below in the same order corresponding to the journals in which they were published in Table 1.1.

a) Navarro-Hernández, M. I., Tomás, R., Lopez-Sanchez, J. M., Cárdenas-Tristán, A., & Mallorquí, J. J. (2020). Spatial analysis of land subsidence in the San Luis potosi valley induced by aquifer overexploitation using the coherent pixels technique (CPT) and sentinel-1 insar observation. Remote Sensing, 12(22), 1–23. <a href="https://doi.org/10.3390/rs12223822">https://doi.org/10.3390/rs12223822</a>

This paper corresponds to one of the two papers that belong to the first research topic. This paper focuses on assessing the impact of groundwater withdrawal on land subsidence and fault development in the San Luis Potosi Valley (SLPV) by analysing 112 Sentinel-1 images spanning from 2014 to 2019. The processing involves the implementation of the Coherent Pixel Technique (CPT) to measure displacements and evaluate their correlation with various influencing factors, including piezometric levels and soft soil thickness. Additionally, the study explores the spatial distribution of shallow faults. The findings contribute valuable insights into the mechanisms driving land subsidence in the region and the aquifer system's response to variations in piezometric levels due to groundwater withdrawal in the SLPV. The paper provides details about the geographical and geological characteristics of the study area, as well as outlines the processing of Synthetic Aperture Radar (SAR) images and DInSAR techniques used in the analysis. The results obtained through the CPT method are presented along with validation, they indicate that subsidence in Soledad de Graciano Sánchez ranges mainly from -1.5 to -3.5 cm/year, while in San Luis Potosi, values vary from -1.8 to -4.2 cm/year. The observed correlation between fault traces, land subsidence, and groundwater extraction suggests that the subsidence is linked to faulting induced by groundwater withdrawal, aligning with the structural faults concealed beneath sediments.

b) Navarro-Hernández, M. I., Valdes-Abellan, J., Tomás, R., Lopez-Sanchez, J. M., Ezquerro, P., Bru, G., Boni, R., Meisina, C., & Herrera, G. (2022). ValInSAR: A systematic approach for the validation of Differential SAR Interferometry in land subsidence areas. IEEE Journal of Selected Topics in Applied Earth Observations and Remote Sensing, 15, 3650–3671. <a href="https://doi.org/10.1109/JSTARS.2022.3171517">https://doi.org/10.1109/JSTARS.2022.3171517</a>

This paper corresponds to the second research topic, focusing on the validation of the DInSAR data. This paper is motivated by the current lack of a systematic and standardized approach for validating and assessing the quality of DInSAR datasets in the context of land subsidence. Recognizing the importance of this gap, our aim is to contribute to the DInSAR-users' community by proposing a systematic methodology. This methodology is designed to evaluate differences between DInSAR and other *in-situ* 

techniques. Furthermore, we present a new open-source code, ValInSAR, to streamline the assessment process. The overarching objective is to provide recommendations for validation strategies applicable to a broad range of land subsidence products.

c) Navarro-Hernández, M. I., Valdes-Abellan, J., Tomás, R., Tessitore, S., Ezquerro, P., & Herrera, G. (2023). Analysing the Impact of Land Subsidence on the Flooding Risk: Evaluation Through InSAR and Modelling. Water Resources Management, 37(11), 4363–4383. https://doi.org/10.1007/s11269-023-03561-6

This paper corresponds to the third research topic, which focuses on the application of the DInSAR data. In this paper we conducted 2D Surface flow numerical simulations for the Alto Guadalentín valley, focusing on two scenarios (1992 and 2016), to unravel the impact of cumulative subsidence within the region on the water surface flow trends. Utilizing a 2D hydraulic model (HEC-RAS), we assessed changes in flood extent, water depth, velocity, and the subsequent economic damage. The scenarios were derived from the integration of high-resolution Light Detection and Ranging (LiDAR) Digital Surface Model (DSM) data (2.5 m) and satellite-based displacement measurements, incorporating cumulative subsidence data obtained through InSAR for the period 1992-2016. This innovative multidimensional approach involved analysing one of the many consequences of inefficient detrital aquifer management, integrating LiDAR DSM data analysis, hydraulic modelling, and satellite-based displacement estimation. We explored the impact of water overexploitation leading to the compaction of unconsolidated alluvial soils and subsequent subsidence, potentially changing flood patterns. This study explores into complex cause-effect mechanisms, providing a quantitative assessment of the economic impact of subsidence on flood-related damage.

d) Navarro-Hernández, M. I., Tomás, R., Valdes-Abellan, J., Bru, G., Ezquerro, P., Guardiola-Albert, C., Elçi, A., Batkan, E. A., Caylak, B., Ören, A. H., Meisina, C., Pedretti, L., & Rygus, M. (2023). Monitoring land subsidence induced by tectonic activity and groundwater extraction in the eastern Gediz River Basin (Türkiye) using Sentinel-1 observations. Engineering Geology, 107343. https://doi.org/10.1016/j.enggeo.2023.107343

This paper corresponds to the first research topic applied in the second study area. The objective of this study was to assess the impact of tectonics and groundwater extraction on land subsidence and fault evolution in the Alaşehir-Sarıgöl sub-basin. The study utilized the P-SBAS algorithm within the Geo-hazard Exploitation Platform to process Sentinel-1 SAR images spanning from 2016 to 2021. By combining P-SBAS with Independent Component Analysis (ICA), the research offers valuable insights into land subsidence mechanisms, emphasizing the application potential beyond the specific study area. The ICA technique demonstrates advantageous in identifying subsidence patterns and explaining their principal causes. DInSAR analysis revealed displacement rates reaching up to 6.40 cm/year, demonstrating a clear correlation between displacement and soft soil thickness. The study highlights aquitard layer compaction resulting from groundwater withdrawal and piezometric head depletion as the primary drivers of land subsidence. Despite challenges in distinguishing tectonic-induced displacements from those caused by soft soil compaction, the analysis identifies two spatiotemporal displacement trends: one associated with long-term, linear plastic compaction of the aquitard due to groundwater withdrawal and the other involving long-term displacements with seasonal rebounds triggered by yearly water level fluctuations.

#### 1.6. Congress related to the thesis.

**Navarro-Hernández, M. I.**, Guardiola-Albert, C., Valdes-Abellan, J., Ezquerro, P., Pla, C., Meisina, C., Bru, G., & Tomás, R.: Stakeholder perception for groundwater management from a subsidence point of view in the Guadalentín Valley (Spain), EGU General Assembly 2021, online, 19–30 Apr 2021, EGU21-9958, https://doi.org/10.5194/egusphere-egu21-9958, 2021.

**Navarro-Hernández, M. I.**, Cardenas Tristán, A., & Putri, Ratih. Geostatistical analysis of static level evolution between 1995-2005 and 2007-2017 in San Luis Potosí Aquifer, México. ICST 2021 – The 2nd Geoscience and Environmental Management Symposium, Conference paper, 17 November 2021.

**Navarro-Hernández, M. I.**, Tomás, R., Lopez-Sanchez, J. M., Cárdenas-Tristán, A., & Mallorquí, J. Determination of aquifer-system parameters in San Luis Potosí Valley (México) from space using PS-InSAR. Living Planet Symposium 2022, Bonn, Germany; 26 May 2022.

**Navarro-Hernández, M. I.**, Valdes-Abellan, J., Tomás, R., Tessitore, S., Ezquerro, P., & Herrera, G. Flood inundation mapping using 2-d streamflow hydraulic modeling and land subsidence data from InSAR observations in the Alto Guadalentin valley, Spain. EGU General Assembly 2022, Vienna, Austria, 23–27 May 2022, EGU22-3787, https://doi.org/10.5194/egusphere-egu22-3787, 2022.

**Navarro-Hernández, M.** I., Tomás, R., Valdes-Abellan, J., Bru, G., Ezquerro, P., Guardiola-Albert, C., Elçi, A., Batkan, E. A., Caylak, B., Hakan, Ö. A., Meisina, C., Pedretti, L., and Rygus, M.: Analysis of land subsidence caused by groundwater overexploitation in the Gediz River Basin based on Sentinel-1 observations, EGU General Assembly 2023, Vienna, Austria, 24–28 Apr 2023, EGU23-12338, https://doi.org/10.5194/egusphere-egu23-12338, 2023.

**Navarro-Hernández, M. I.**, Valdes-Abellan, J., Tomás, R., Lopez-Sanchez, J. M., Ezquerro, P., Bru, G., Bonì, R., Meisina, C. & Herrera, G. Methodology for the validation of DInSAR datasets used for monitoring land subsidence (2023). The 10th International Symposium on Land Subsidence (TISOLS). Delft, Netherlands.

**Navarro-Hernández, M.,** Pozo, S., Valdes-Abellan, J., and Tomás, R.: Automated analysis of strain-stress curves for aquifer system characterization, EGU General Assembly 2024, Vienna, Austria, 14–19 Apr 2024, EGU24-4174, https://doi.org/10.5194/egusphere-egu24-4174, 2024

#### 1.7. Other publications.

#### 1.7.1. Papers in progress of publication

**Navarro-Hernández, M. I.**, García. S., Valdes-Abellan, J. & Tomás, R., (2024). A New Stress-Strain Analysis Application for Aquifer Systems Characterization in Land Subsidence Affected Areas. (*In progress*)

This paper corresponds to the third research topic, focusing on the Application of the DInSAR data. This paper presents a novel application designed to automate the analysis of stress-strain curves, aiming to improve objectivity and streamline the analytical process. The application was tested using authentic data from diverse aquifers globally affected by land subsidence. It integrates temporal series of groundwater levels, typically derived from observation wells, and ground deformation data obtained through *in-situ* (e.g., borehole extensometer, levelling survey) or remote sensing techniques (e.g., DInSAR). The automated process constructs stress-strain curves, showcasing its functionality across various aquifer systems exhibiting distinct geomechanical behaviours. The study utilizes real-world examples to demonstrate the efficacy of the proposed application.

To summarize, it is important to remark that the central theme of this thesis is the study and monitoring of land subsidence in various aquifer systems around the world. As mentioned before, this phenomenon can be monitored through different geodetic techniques, but this work focuses on the application of DInSAR techniques using various algorithms (e.g., CPT, PSBAS). In the first research topic, two distinct cases have been studied: the San Luis Potosí valley and the eastern Gediz River Basin. Despite differing in some morphological and land-use characteristics, both areas comprise aquifers under hydrological stress

due to high demand for groundwater. Due to their similarities in soft soil thickness and tectonic basin type, they respond similarly to increased pore pressure due to piezometric declines.

After monitoring a specific area using DInSAR techniques, data validation becomes the first necessary step to increase reliability on results built with that data. Typically, *in-situ* techniques are employed for validation, but due to the lack of an established methodology in the scientific community, the second research topic develops and proposes a validation methodology through the creation of a MATLAB code. This code is used to validate one of the study areas from the first research topic. Once DInSAR data is processed and validated, it is possible to utilize these results by combining them with other technologies to explain and study phenomena related to subsidence. This led to the idea of analysing the impact of subsidence on flood risk in the Alto Guadalentín study area. By measuring and calculating changes over time, two different terrain models were reconstructed to quantify how subsidence can alter flooding patterns and assess the economic repercussions of these effects.

Finally, another application studied in this thesis involved using temporal DInSAR series combined with piezometric data in detrital aquifers to calculate storage coefficients. Going beyond established practices, a methodology for automating the calculation of these parameters was developed and proposed. These parameters provide crucial information for determining aquifer storage capacity and modelling subsidence in a specific study area.

#### 1.7.2. Participation in papers not related to the thesis

Other papers have been published during the doctoral studies in collaboration with different authors. While these papers may not be directly related to the specific objectives of the thesis, they significantly contribute to enrich the acquired knowledges.

Bonì, R., Teatini, P., Zoccarato, C., Guardiola-Albert, C., Ezquerro, P., Bru, G., Tomás, R., Valdes-Abellan, J., Pla, C., **Navarro-Hernández, M. I.**, Elçi, A., Çaylak, B., Ören, A. H., Shatanawi, K., Mohammad, A. H., Abu Hajar, H., Letterio, T., Genovesi, R., Hreisha, H., Al Mimi, Q. & Meisina, C. (2022). Stakeholders' Perspective on Groundwater Management in Four Water-Stressed Mediterranean Areas: Priorities and Challenges. Land, 11(5), 738. <a href="https://doi.org/10.3390/land11050738">https://doi.org/10.3390/land11050738</a>

Hu, L., **Navarro-Hernández, M. I.**, Liu, X., Tomás, R., Tang, X., Bru, G., Ezquerro, P., & Zhang, Q. (2022). Analysis of regional large-gradient land subsidence in the Alto Guadalentín Basin (Spain) using openaccess aerial LiDAR datasets. Remote Sensing of Environment, 280(March). <a href="https://doi.org/10.1016/j.rse.2022.113218">https://doi.org/10.1016/j.rse.2022.113218</a>

Tomás, R., Zeng, Q., Lopez-Sanchez, J. M., Zhao, C., Li, Z., Liu, X., **Navarro-Hernández, M. I.**, Hu, L., Luo, J., Díaz, E., Szeibert, W. T., Luis, J., Riquelme, A., Yu, C., Cano, M., & Pastor, J. (2023). Advances on the investigation of landslides by space-borne synthetic aperture radar interferometry. Geo-Spatial Information Science. <a href="https://doi.org/10.1080/10095020.2023.2266224">https://doi.org/10.1080/10095020.2023.2266224</a>

#### 1.7.3. Congress not-related to the thesis

Bonì, R., Teatini, P., Zoccarato, C., Guardiola-Albert, C., Ezquerro, P., Bru, G., Tomás, R., Valdes-Abellan, J., Pla, C., **Navarro-Hernández, M. I.**, Elçi, A., Çaylak, B., Ören, A. H., Shatanawi, K., Mohammad, A. H., Abu Hajar, H., Letterio, T., Genovesi, R., Hreisha, H., Al Mimi, Q. & Meisina, C. (2022). La perspectiva de los grupos implicados sobre el manejo de las aguas subterráneas en cuatro cuencas mediterráneas bajo estrés hídrico: Prioridades y desafíos. Congreso Nacional del Agua, Albatera, España.

Bru, G., Ezquerro, P., Guardiola-Albert, C., Béjar-Pizarro, M., Herrera, G., Tomás, R., **Navarro-Hernández, M. I.,** Meisina, C. & Boni, R. Towards aquifer deformation models integrating SAR remote sensing:

preliminary land subsidence results using GEP tools. the 23rd EGU General Assembly, held online 19-30 April, 2021, id. EGU21-12806

Hu, L., **Navarro-Hernández, M. I**., Liu, X., Tomás, R., Tang, X., Bru, G., Ezquerro, P., & Zhang, Q. Analysis of regional large-gradient land subsidence in the Alto Guadalentin Basin (Spain) using aerial DInSAR datasets. Living Planet Symposium 2022, Bonn, Germany; 26 May 2022

Bru, G., Ezquerro, P., Guardiola-Albert, C., Bejar-Pizarro, M., Herrera, G., Tomas, R., **Navarro-Hernandez, M. I.**, Lopez-Sanchez, J. M., Oren, A. H., Caylak, B., Elci, A., Shatanawi, S., Mohammad, A.H., Abu Hajar, H.A., Boni, R., Rygus, M., Pedretti, L. & Meisina, C. EXPLORING LAND SUBSIDENCE WITH A-DINSAR THEMATIC APPS OF THE GEOHAZARDS PLATFORM. Living Planet Symposium 2022, Bonn, Germany; 26 May 2022

Bru, G., Ezquerro, P., Guardiola-Albert, C., Bejar-Pizarro, M., Herrera, G., Tomas, R., **Navarro-Hernandez, M. I.**, Lopez-Sanchez, J. M., Oren, A. H., Caylak, B., Elci, A., Shatanawi, S., Mohammad, A.H., Abu Hajar, H.A., Boni, R. & Meisina, C. Land subsidence analysis caused by aquifer overexploitation using GEP tools: A-DInSAR on the cloud. En Proceedings 3rd Congress in Geomatics Engineering. Editorial Universitat Politècnica de València. 127-136. https://doi.org/10.4995/CiGeo2021.2021.12722

Bru, G., Portela, J.J., Ezquerro, P., **Navarro-Hernández, M. I.**, Staller, A., Béjar-Pizarro, M., Guardiola-Albert, C., Fernández-Merodo, J.A., López-Vinielles, J. L., Tomás, R & López-Sánchez, J. M. Imaging land subsidence in the Guadalentín River Basin (SE Spain) using Advanced Differential SAR Interferometry (2022). 5th Joint International Symposium on Deformation Monitoring (JISDM), 20-22 June 2022, Valencia, Spain DOI: http://doi.org/10.4995/JISDM2022.2022.13826

Valdes-Abellan, J., **Navarro-Hernández, M. I.**, Tomás, R., Tessitore, S., Ezquerro, P., & Herrera, G. (2022). Sobreexplotación de acuíferos, subsidencia y su impacto en el riesgo de inundación. El caso paradigmático del Valle del Alto Guadalentín. Congreso Nacional del Agua, Albatera, España.

Caylak, B., Oren, A. H., Elçi, A., Batkan, E. A., Guardiola-Albert, C., Bru, G., Ezquerro, P., Tomás, R. & **Navarro-Hernández, M. I**. Investigation of the relationship of land subsidence due to over-exploitation of groundwater with the variation in piezometric levels (2022). Conference: International Gediz and Aegean River Basins Symposium (GEDIZSYMP2022). Izmir, Türkiye

Meisina C, Pedretti L, Rygus M, Bonì R, Teatini P, Zoccarato C, Li Y, Guardiola-Albert C, Ezquerro P, Bru G, Tomás R, Valdes-Abellan J, Pla C, **Navarro-Hernández M**, Elçi A, Batkan EA, Çaylak B, Ören A, Shatanawi K, Hind Mohammad A, Abu Hajar H, Letterio T, Genovesi R, Hreisha H, Mimi Q. Sustainable Management of Groundwater by Earth Observation Technologies (2022). Conference: 39th IAHR World Congress, Granada, Spain. DOI: 10.3850/IAHR-39WC2521716X20221512.

Tomás, R., Valdes-Abellan, J., Pla, C., Pastor, J. L., **Navarro-Hernández, M. I.**, Cano, M., Riquelme, A. & Lopez-Sanchez, J. M. A scale-model experiment to enhance dissemination of land subsidence accompanying groundwater extraction (2023). The 10th International Symposium on Land Subsidence (TISOLS). Delft, Netherlands.

Meisina C, Pedretti L, Rygus M, Bonì R, Teatini P, Zoccarato C, Li Y, Guardiola-Albert C, Ezquerro P, Bru G, Tomás R, Valdes-Abellan J, Pla C, **Navarro-Hernández M**, Elçi A, Batkan EA, Çaylak B, Ören A, Shatanawi K, Hind Mohammad A, Abu Hajar H, Letterio T, Genovesi R, Hreisha H, Mimi Q. A-DInSAR analysis for the study of subsidence in water stressed Mediterranean areas (2023). The 10th International Symposium on Land Subsidence (TISOLS). Delft, Netherlands.

#### **INTRODUCTION**

Bonì, R., Teatini, P., Zoccarato, C., Minderhoud, P., Tosi, L., Béjar-Pizarro, M., Guardiola-Albert, C., Bru, G., Ezquerro, P., Herrera, G., Tomás, R. & **Navarro-Hernández, M. I**. Investigating land subsidence trend in the major coastal cities of Europe (2023). The 10th International Symposium on Land Subsidence (TISOLS). Delft, Netherlands

Pla, C., Valdes-Abellan, J., **Navarro-Hernandez, M. I**., Guardiola-Albert, C., Ezquerro, P., Bru, G., Elçi, A., Meisina, C., & Tomas, R.: Multicriteria decision-making approach as a strategy to deal with land subsidence in affected areas, EGU General Assembly 2023, Vienna, Austria, 24–28 Apr 2023, EGU23-11516, https://doi.org/10.5194/egusphere-egu23-11516, 2023.

Tomás, R., Zeng, Q., Lopez-Sanchez, J. M., Zhao, C., Li, Z., Chen, H., Liu, X., **Navarro-Hernández, M. I**., Hu, L., Luo, J., Reyes, C., Orlandi, D., Díaz, E., Pastor, J. L., Riquelme, A. & Cano, M. Application of Spaceborne SAR Interferometric to Geohazard Monitoring. 2023 Dragon 5 Symposium, Hohhot, Inner Mongolia, China, 11-15 September 2023.

# 2. Settings of the study areas

In this section, a brief description will be provided for all the study areas considered during the development of this doctoral thesis. The locations of the study areas are shown in Figure 2.1

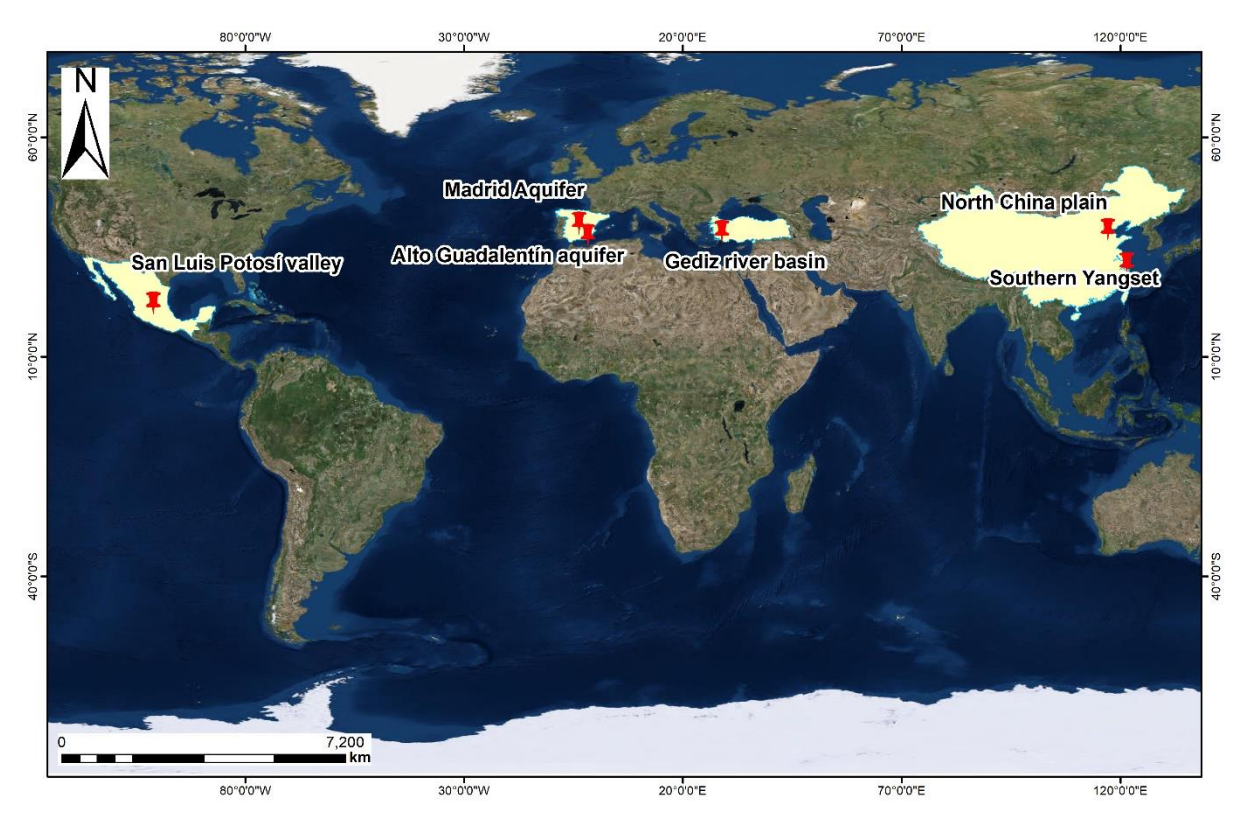


Figure 2.1 Localization of the study areas.

#### 2.1. San Luis Potosí valley

The San Luis Potosí (SLP) valley is situated in the Mexican central plateau, within the physiological province between the eastern Sierra Madre and the western Sierra Madre. The valley is located on a tectonic graben, which is the most significant faulting expression in the region. Geologically, the area originated from a tectonic basin bordered by N-S trending stepped faults. Over time, it accumulated alluvial, lacustrine, and pyroclastic sediments. The volcanic activity that produced pyroclastic material did not significantly alter the main relief features, allowing the hydrographic basins formed in the Tertiary period to persist. The rocks in the mountain ranges delineating the valley are of igneous and effusive origin from the Tertiary period, accompanied by pyroclastic material like ignimbrites, tuffs, and mainly rhyolitic breccias, forming the western boundary of the basin. This sequence of igneous rocks overlies marine sedimentary rocks from the Upper Cretaceous. Lithological well logs and geophysical surveys indicate that the granular materials filling the tectonic basin range from approximately 50 to 300 m in thickness, while the volcanic material's thickness varies between 400 and 500 m (CONAGUA, 2015).

Exploiting the SLP Valley aquifer system has revealed two distinct piezometric levels, indicating two hydrogeological units. The shallower unit comprises interconnected aquifers with common characteristics, behaving as semi-confined. Covering 230 km², mainly consisting of 4 to 60 m thick alluvial sediment, this aquifer's piezometric levels are shallower in urban areas and deeper towards the east, receiving natural recharge from runoff of the Sierra de San Miguelito (CONAGUA, 2015). The shallow aquifer consists of semi-consolidated gravel, sand, and silt, while the deep aquifer is

lithologically composed of volcanic rocks in a fractured medium (Noyola-Medrano et al., 2009). Separated by a low-permeability layer, the upper section of the deep aquifer, representing the tectonic basin's fill material, ranges from 100 to 150 m in depth and 100 to 200 m in thickness. The lower section consists of the fractured Portezuelo Latite, contributing granular material (Hergt et al., 2009). Igneous rocks do not act as confining layers due to a well-developed vertical fracture system, providing secondary permeability for water storage.

Since 1995, a drawdown cone has been present in San Luis Potosí, descending 25 meters more towards the north between 1995 and 2001. By 2005, 92 % of domestic water was sourced from groundwater, signifying a significant increase from 59 % in 1960. The accelerated groundwater extraction, reaching 4.1 m³/s in 2007 from 0.97 m³/s in 1970, resulted in an annual volume of 92.2 million m³ in 2006. Factors exacerbating the decline include rapid population growth, agricultural and industrial expansions, low permeability of lithological materials, low precipitation, high evaporation in semi-arid climates, erosion, deforestation, and impervious surfaces hindering water retention and infiltration (CONAGUA, 2015).

#### 2.2. Eastern Gediz river basin

The Eastern Gediz river basin, also known as the Alaşehir-Sarıgöl sub-basin (ASSB) is situated in western Anatolia. The graben exhibits a typical Mediterranean climate with dominant agricultural land use, primarily vineyards covering approximately 70 % of the cultivated surface. Main residential areas include Salihli, Alaşehir, Yeşilyurt, and Sarıgöl, with a population of over 250,000 inhabitants (Copernicus, 2018). The majority of groundwater in the basin (86.5 %) is utilized for agricultural irrigation, while 11.6 % is assigned for general water purposes, and only 1.5 % is allocated for drinking water purposes, emphasizing a predominant focus on irrigation within the water consumption pattern (Tonkul et al., 2019).

Geologically, this graben consists of metamorphic rocks in the basement and a sedimentary cover. The sedimentary fill is divided into Quaternary and Neogene basin materials, with the latter comprising sedimentary sequences of fluvial-alluvial, alluvial-fan, debris, and clay-rich layers (Üner & Dogan, 2021). The region is seismically active due to its location in the Aegean extension region, experiencing significant earthquakes in the past. The area is prone to seismic activity, with the Gediz graben being part of the Aegean horst-graben system. The Gediz detachment fault, a low-angle fault, is a crucial structural element separating Neogene sediments from the metamorphic basement. The area is also affected by E-W oriented high angle oblique active faults, contributing to the overall seismic activity (Poyraz et al., 2019).

The absence of good historical groundwater monitoring records in the study area has led to the use of an indirect method to assess the impact of human activities, particularly groundwater abstractions, on the quantity of groundwater. This represents one of the challenges in interpreting the main factors that may lead to subsidence.

#### 2.3. Alto Guadalentín aquifer

The Alto Guadalentín valley (SE Spain) where the city of Lorca is located, faces significant subsidence rates, reaching up to 10 cm/year due to prolonged aquifer system exploitation. The basin, part of the Spanish Mediterranean arc, has a climate with scarce rainfall (250 mm per year) and an annual mean temperature of ~18 °C, with a growing population, the depression exhibits a horst and graben structure, bounded by the active Alhama de Murcia fault to the north (Fernandez et al., 2018). Comprising two contiguous sub-basins, Alto and Bajo Guadalentín, the aquifer system rests on a basement of relatively impermeable Palaeozoic metamorphic complexes overlain by Miocene conglomerates and/or calcarenite series. The top layer consists of Pliocene-Quaternary, low-

permeability conglomerates, sand, silt, and clays accumulating to 300–900 m (Ezquerro et al., 2020). The aquifer-system, linked to Plio-Quaternary sediments, experiences recharge dependency on rainfall and irrigation. Recent studies revealed a significant layer of fine-grained sediments correlated with subsidence rates. Historical overexploitation since the 1960s–1970s led to increased overdraft and contamination, causing a continuous piezometric level decrease. The area also faced a prolonged drought from 1990 to 1995, impacting natural recharge. InSAR studies identified high subsidence rates and a delayed transient of nonlinear compaction due to the 1990–1995 drought (Ezquerro et al., 2020). As the groundwater depletion occurred before the 1988 declaration of temporary overexploitation, with continued decline due to pumping pressure and low rainfall. Previous works also established a relationship between groundwater changes, land subsidence, and compressible sediments thickness, emphasizing the complex interplay of geological and anthropogenic factors in the region.

#### 2.4. Murcia city

Murcia city, situated in the Vega Media of the Segura River basin in the eastern Betic Cordillera (SE Spain), has faced significant challenges since the 1990s due to groundwater extraction and soil consolidation from the upper gravel of the deep aquifer (Tessitore et al., 2016; Tomás et al., 2010). This basin is influenced by compressive stress since the Upper Miocene, bordered by active faults. The basin's recent sedimentary fill, comprising Pleistocene to Holocene materials, forms an aquifer system with shallow and deep units. The deep aquifer, below 30 m, consists of gravel, sand, marls, clay, and silts, characterized by high hydraulic conductivities. The shallow aquifer, within the first 30 m, comprises recent clay, silt, and sandy facies with low permeability. This geotechnical profile plays a vital role in groundwater resource exploitation and supports deep foundations in the region (Herrera et al., 2010). The groundwater extraction and soil consolidation have led to varying degrees of damage to buildings and urban structures (Bru et al., 2013). To comprehensively assess the impact, a meticulous study on land subsidence was conducted spanning from 1995 to 2005. Advanced technology, including images from ERS and ENVISAT sensors, coupled with advanced processing techniques like SPN and CPT, provided valuable insights into the evolving landscape. DInSAR results, derived from the mentioned technologies, revealed a deformation velocity of up to -5 mm/year during the specified period (Herrera et al., 2010). This comprehensive study area utilized data from fifteen strategically positioned in-situ borehole extensometers, covering the timeline from February 2001 to March 2007. Among these extensometers, five followed the incremental type, while the remaining ten were of the rod type. The rod extensometers were anchored at depths ranging between 10 and 20 m, providing a broad perspective on subsurface deformation (Pardo et al., 2013). In contrast, the incremental extensometers delivered precise deformation measurements at 1-meter depth intervals, contributing to a detailed understanding of the subsidence dynamics in the region (Tomás et al., 2010). This multifaceted approach, combining satellite-based observations and in-situ measurements, not only validated the DInSAR findings but also enriched the overall comprehension of the intricate interactions between groundwater dynamics, soil consolidation, and their repercussions on the urban landscape of Murcia city.

#### 2.5. Tertiary detritic aquifer of Madrid

The Tertiary Detritic Aquifer of Madrid (TDAM) is situated in the northwestern part of the Madrid basin, a tectonically influenced triangular basin spanning approximately 6000 km² (Béjar-Pizarro, Ezquerro, et al., 2017). It encompasses materials deposited in continental environments from Late Cretaceous to Upper Miocene, forming the detritic facies of the TDAM. Bounded by the Toledo Mountains to the south, Altomira Range to the southeast, and Central System Range to the northwest, the region is intersected by major rivers like Guadarrama, Manzanares, and Jarama. The TDAM,

characterized by elevation between 650 and 800 m a.s.l., constitutes a heterogeneous and anisotropic aquifer system with a multilayer structure and a thickness exceeding 3 km. Comprising metric sand lenses embedded in a low-permeability clay matrix, the aquifer's coarse fraction is predominantly arkosic sand, while the fine fraction consists of smectite, illite, and a low percentage of kaolinite (Béjar-Pizarro, Ezquerro, et al., 2017; Hernández-García & Custodio, 2004). The deposits result from the erosion of the northwest mountain range, displaying a spatially variable percentage of the fine fraction. The TDAM stores at least 20,000 Mm³ of groundwater, and a well-established network of 70 wells provides water to the city during drought periods (Llamas et al., 1996). Two extraction areas, the northern and southern fields, covering 500 km², have wells with depths between 300 and 700 m. From 1991 to 2011, these fields underwent five cycles of groundwater extraction and recovery, coinciding with drought periods. Previous studies have reported land deformation associated with groundwater level changes in the TDAM (Ezquerro et al., 2014). This study builds upon existing research by modelling groundwater levels across the extraction fields and mapping groundwater storage changes to identify regions affected by storage loss.

#### 2.6. Southern Yangtse Delta, China

The southern Yangtze Delta, situated within economically significant provinces in China, has experienced important subsidence attributed to intensified demand for groundwater driven by economic and industrial development. The aquifer system in this region is complex, consisting of Quaternary materials like gravel, sand, silty sand, silty clay, and clay, with a variable depth ranging from 250 to 310 m beneath Shanghai, occasionally exceeding 360 m. The aquifer system is comprised of five layers, featuring unconfined and confined aquifers separated by aquitard layers of lower permeability (Zhang et al., 2007). Land subsidence in this aquifer was initially reported in 1921, with groundwater extraction leading to displacements of around 24 mm/year. Subsequently, post-1949 when groundwater pumping intensified, displacements increased to 110 mm/year. Mitigation measures, including enhanced artificial recharge and relocating extraction to deeper confined aquifers, were implemented. Despite these efforts, the decline in piezometric levels persisted until the late 1990s. This resulted in the convergence of three cones of depression from different cities, forming a regional cone covering 7,000 km², causing water levels to drop by 87.7 m at the cone's centre. By 2000, the maximum cumulative subsidence in the area had reached 2.8 m (Xue et al., 2008).

#### 2.7. North China Plain (Beijing city)

Beijing, recognized as one of the world's most densely populated cities, faces significant subsidence risks, particularly in its expansive delta region. This plain consists of sediments derived from fluvial and alluvial processes, forming a well-defined aquifer system. The aquifer comprises five confined layers separated by low-permeability strata, with the upper three layers being extensively exploited for domestic and industrial water supply (Zhang et al., 2014). Notably, the Pinggezhuang and Tianzhu extensometer stations to the south of Beijing provide valuable insights. Tianzhu, experiencing substantial groundwater extraction since 2004, is situated at the confluence of alluvial fans from the Wenyu and Chaobai rivers. In contrast, Pinggezhuang, characterized by one of the highest subsidence rates in Beijing, records up to 24 mm/year, and is located over the alluvial fan of the Chaobai River. These regions exhibit sedimentary deposits from the Paleogene to the Quaternary period, with Pinggezhuang recording 380 m of Quaternary material and Tianzhu covering over 500 m of aquifer thickness due to the intersection of two alluvial fans (Li et al., 2022). Long-term groundwater overexploitation, especially from 2004 to 2010, caused a considerable decline in piezometric levels, reaching up to 30 meters in both phreatic and confined aquifers. This decline led to sediment compaction and extensive land subsidence, with the region experiencing cumulative subsidence of up to 600 mm from 1955 to 2009. Monitoring through borehole extensometers, initiated in 2004 and

#### **SUTDY AREAS**

2008, revealed the deepest monitoring reaching approximately 250 meters, with a reference point established at a bedrock depth of 900 meters. Additionally, a Permanent Scatterer Interferometry study from June 2003 to January 2010 measured the largest annual land subsidence at 52 mm/year, with a maximum cumulative subsidence of 342 mm. These findings highlight the complex interaction between groundwater exploitation, sedimentary characteristics, and land subsidence in Beijing's critical deltaic region (Zhu et al., 2020).

# 3. Methodology

Figure 3.2 provides a summarized overview of the methodology applied in this thesis through a flowchart. It is divided into blocks that outline the steps followed for each of the methodologies in the three research topics: DInSAR for monitoring land subsidence, Validation of DInSAR data applied in land subsidence and Applications of DInSAR data.

#### 3.1. Fundamentals of DInSAR technique

InSAR is a technique employed to reconstruct the topography of a scene observed by a radar sensor by combining two SAR images acquired from different positions (Blanco-Sánchez et al., 2008). Meanwhile, DInSAR technique aims to cancel or minimize interferometric phase terms to extract those related to terrain deformation (Mora, 2003), Figure 3.1 shows a schematic of the DInSAR configuration. Assuming that displacement is how the height has changed between two images, its expression is as follows:

$$\varphi_{def} = \frac{4\pi}{\lambda} \cdot \rho$$

It is important to consider that the deformation included in the phase is in the range direction, as it is only possible to measure movements in the Line of Sight (LOS) direction (Blanco-Sánchez, 2009). Taking into account that the components of the interferometric phase are:

$$\Delta \varphi = \Delta \varphi_{flat} + \Delta \varphi_{def} + \Delta \varphi_{topo} + \Delta \varphi_{atm} + \Delta \varphi_{noise}$$

where  $\Delta \varphi$  is the total interferometric phase,  $\Delta \varphi_{flat}$  is the flat-earth component due to range distance difference between pixels,  $\Delta \varphi_{def}$  is the relative displacement,  $\Delta \varphi_{topo}$  is the topographic component,  $\Delta \varphi_{atm}$  is a phase component related to the atmospheric phase screen and  $\Delta \varphi_{noise}$  comprises the errors due to different decorrelation sources (Declercq et al., 2017). To calculate the deformation, it is necessary to isolate the topographic term  $\Delta \varphi_{topo}$  from equation which is done through a known topography. There are various alternatives for this, but the most common is to use an external Digital Elevation Model (DEM) to synthesize the topographic term in the equation. However, it is likely that the used DEM contains inaccuracies or errors. Therefore, the topography would not be completely cancelled, giving rise to a new term depending on the inaccuracies of the DEM, known as DEM error or  $\varepsilon$  (Blanco-Sánchez, 2009). Now the expression of the interferometric phase would be as follows:

$$\Delta \varphi = \Delta \varphi DEM_{error} + \Delta \varphi_{def} = \frac{4\pi}{\lambda}.\frac{B_n}{r_0 sin\theta}.\Delta \varepsilon + \frac{4\pi}{\lambda}.\rho$$

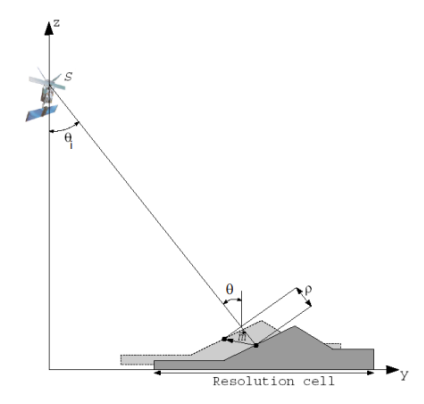


Figure 3.1 Geometry of the DInSAR image acquisition for a zero baseline (Blanco-Sánchez, 2009).

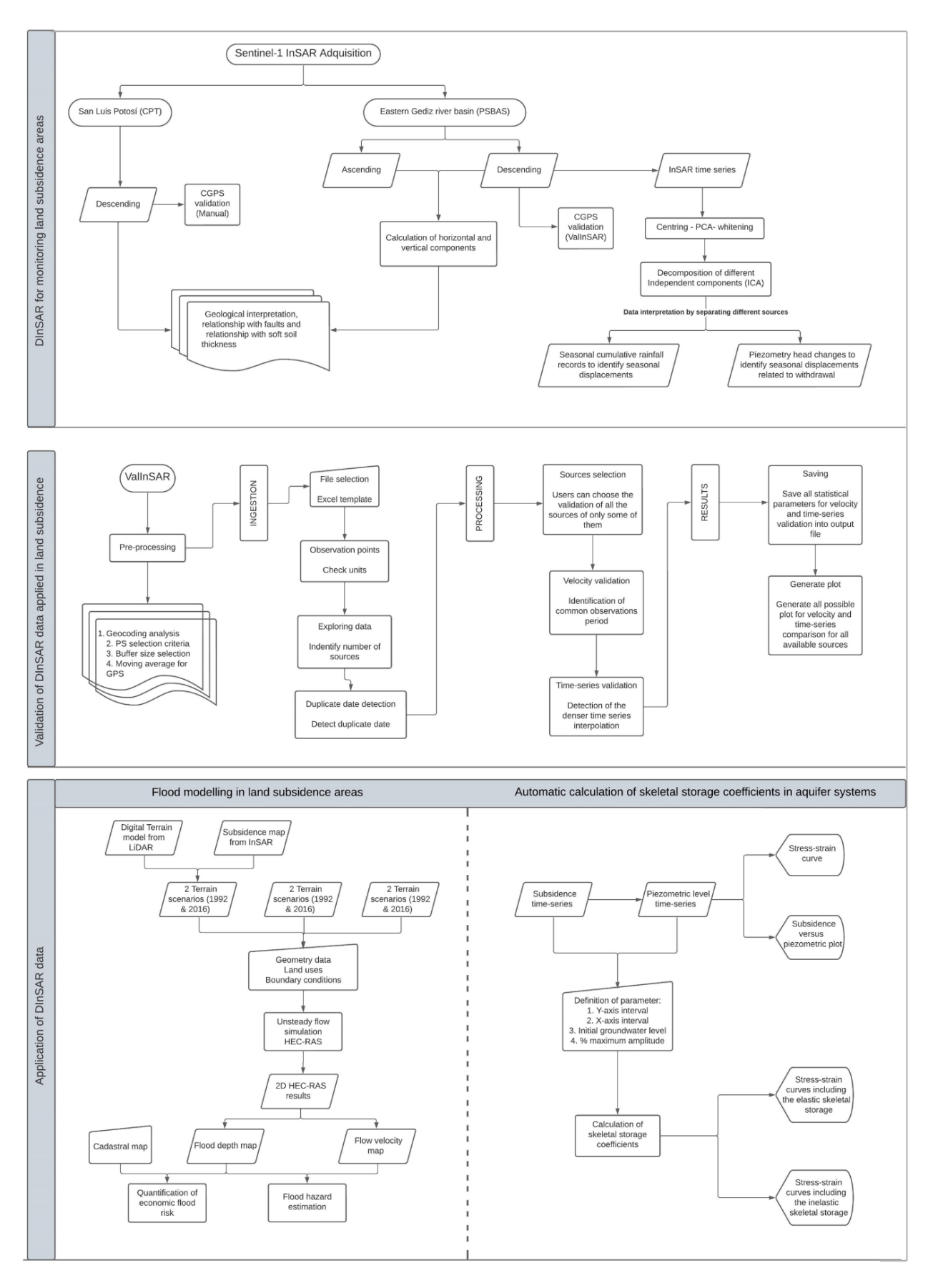


Figure 3.2 General flowchart of the methodology.

Nevertheless, DInSAR does not overcome certain limitations associated with interferogram phase, including temporal decorrelation, spatial decorrelation, and atmospheric delay (Hooper, 2008). Consequently, in the last two decades, more sophisticated algorithms have been devised to tackle these challenges, with examples being the Permanent Scatters (PS) and Small Baseline Subset (SBAS) techniques (Minh et al., 2020). In this thesis, specifically, CPT has been implemented to analyse subsidence in the San Luis Potosí Valley, and PSBAS has been applied to study the phenomenon in the eastern Gediz river basin, which are described below.

#### 3.1.1. The Coherent Pixel Technique (CPT)

The Coherent Pixels Technique (CPT), developed at the Universitat Politècnica de Catalunya, is an advanced DInSAR algorithm designed to discern both linear and non-linear movements in a series of differential interferograms and coherence images. It addresses challenges such as DEM error and atmospheric artifacts (Duque et al., 2007). CPT isolates the deformation term from interferograms by optimizing selection based on temporal and spatial baselines, ensuring high-quality pixel selection, estimating linear deformation and DEM error, and then extracting the non-linear deformation term (Blanco-Sánchez et al., 2008). This method employs a systematic approach involving coherence evaluation, linear model adjustment, and application of temporal and spatial filters to separate atmospheric artifacts from the non-linear deformation phase. The algorithm enhances the detection of pixels, minimizes data processing, and provides valuable insights into deformation characteristics (Blanco-Sánchez et al., 2008).

#### 3.1.2. P-SBAS

SBAS, an Advanced DInSAR technique, minimizes temporal and geometric decorrelation and noise effects, providing centimetre to millimetre accuracy in deformation velocity maps and displacement time series (De Luca et al., 2018). By using a multi-reference interferogram network with short temporal and perpendicular baselines, SBAS reduces noise and ensures high coherence. The Parallel SBAS (P-SBAS) version optimally utilizes distributed high-performance computing infrastructure, enabling efficient processing of massive datasets (Berardino et al., 2002). P-SBAS, implemented on the Geohazard Exploitation Platform (GEP), offers a user-friendly interface for DInSAR analyses, facilitating the monitoring of various phenomena like earthquakes, landslides, land subsidence, and volcanic activity (Bru et al., 2021). This enhanced algorithm contributes to more robust and scalable performance in the analysis of extensive satellite data (Ikuemonisan et al., 2020).

#### 3.2. DInSAR data processing

#### 3.2.1. San Luis Potosí valley

In this study, 112 Sentinel-1 images were processed from 25 October 2014 to 28 November 2019, using the CPT with descending orbits in Interferometric Wide Swath (IWS) mode. The CPT processing involved generating 2,118 differential interferograms, selecting images with spatial baselines smaller than 100 m and temporal baseline smaller than 365 days and a multilooking of 3x15. A three arcsecond Shuttle Radar Topography Mission (SRTM) DEM was used for topographic phase removal. Coherence maps were generated to aid in pixel selection based on coherence criteria. The second stage of CPT involved processing differential interferograms to obtain deformation time-series, including linear and non-linear terms, and DEM error, here a coherence-based pixel selection criterion was applied, all the pixels with mean values lower than 0.6 and a phase standard deviation of 10° were discarded. The study used five "seeds" for integration, one within the metropolitan area and the others were selected in the mountainous area (Navarro-Hernández et al., 2020).

#### 3.2.2. Eastern Gediz River basin

In the ASSB, the Parallel Small BAseline Subset (P-SBAS) algorithm was applied to Sentinel-1 Synthetic Aperture Radar (SAR) images in both descending (June 2016 to July 2020) and ascending orbits (December 2017 to February 2021). P-SBAS processing used a coherence threshold of 0.80 for both modes and a stability threshold of ±0.7 cm/year. The study area exhibited diverse land cover, including urban areas with high coherence, agricultural zones with low coherence, and mountainous regions with sparse vegetation and high coherence. The reference point was strategically placed in the deformation far field within the mountainous region and served as a stable benchmark close to the GNSS point "KZLC." Proper reference point selection is crucial for accurate analysis, providing a fixed anchor for measuring relative motion in the study area (Navarro-Hernández, Tomás, et al., 2023). Additionally, given the availability of data for both ascending and descending orbits in this area, it was possible to perform a calculation of the vertical and horizontal components using the geometry decomposition equations previously applied in Béjar-Pizarro et al. (2017) and Cigna et al. (2019).

# 3.3. Principal and independent components analysis

As one of the objectives in the ASSB study area is to attempt to separate the displacement component related to groundwater extraction from the component associated with tectonic processes in the region, as interferograms were treated as a composite of signals, Principal Component Analysis (PCA) and Independent Component Analysis (ICA) were employed to separate spatiotemporal patterns of long-term deformation and seasonal variations (Chaussard et al., 2014). PCA, a widely-used statistical method for time series analysis, was applied to reduce the dimensionality of the dataset while preserving maximum variability (Jollife & Cadima, 2016). P-SBAS-derived displacements served as input for PCA analysis, focusing on time-series data within the sub-basin. Despite its efficiency, PCA may overlook crucial information and struggle with large datasets, necessitating pixel reduction. On the other hand, ICA, a computational signal technique, goes beyond at separating linearly mixed independent sources, offering robustness compared to PCA (Ebmeier, 2016; Gaddes et al., 2018). FastICA, utilized in this study, combines PCA for isolating independent components and data whitening. Data whitening is crucial for enhancing the suitability of the original data for ICA. The FastICA algorithm produces eigenvalues, eigenvectors, and IC score maps, revealing the spatial distribution and contribution of each component to the original matrix. Overall, this approach serves in extracting meaningful information from interferometric data, facilitating a comprehensive analysis of deformation patterns and seasonal variations (Cohen-Waeber et al., 2018).

# 3.4. Validation methodology: ValInSAR

This section describes the proposed methodology and the corresponding validation tool (Navarro-Hernández et al., 2022). It is crucial to emphasize that this validation approach is suited for regions impacted by land subsidence with negligible horizontal deformations which is the most common case when subsidence land is mainly produced by groundwater overexploitation. The application of ValInSAR involves an initial pre-processing phase during which the user prepares the input data. Following this preparatory stage, ValInSAR can be initiated, executing the validation through two distinct steps: input data (ingestion) and preprocessing.

# 3.4.1. Pre-processing

In the pre-processing phase, the initial procedure is geocoding analysis, ensuring coherence among geocoded datasets from different monitoring techniques, requiring alignment in the same geographic coordinate system. Here, it is important to note that previous studies found geocoding shifts despite corrections, with visible objects like corner reflectors serving as control points. Secondly, the selection of persistent scatterers (PS) for comparison involves two methods. Method 1 selects the most representative PSs aligned with the benchmark's surface element, demanding time and accurate

geocoding. Method 2 averages PS values within a buffer area around the benchmark, automating the process and addressing potential deviations. Buffer size selection criteria involve creating circular buffers around a benchmark, determining optimal sizes based on standard deviation trends (Figure 3.3-a). Buffer size selection involves creating circular buffers around a benchmark, gradually increasing the radius until noticeable changes in data values occur. Standard deviation of DInSAR velocity is calculated for each buffer size and plotting this against buffer size in order to identify stable dispersion values (Figure 3.3-b). The trend change in standard deviation is influenced by including persistent scatterers (PS) with varying subsidence patterns in the buffer. The selection of buffer sizes (e.g., 50, 100, 150 m) depends on DInSAR resolution and target measurement density, ensuring relevance. Additionally, applying a moving average to high-frequency time series in continuous monitoring records, which include daily or hourly measurements, enhances temporal density. This helps smooth out short-term oscillations caused by measurement noise and emphasizes general trends. In DInSAR validation, especially for continuous GNSS station datasets, the moving average provides a daily average value for each GNSS measurement, contributing to a more robust analysis (Navarro-Hernández et al., 2022).

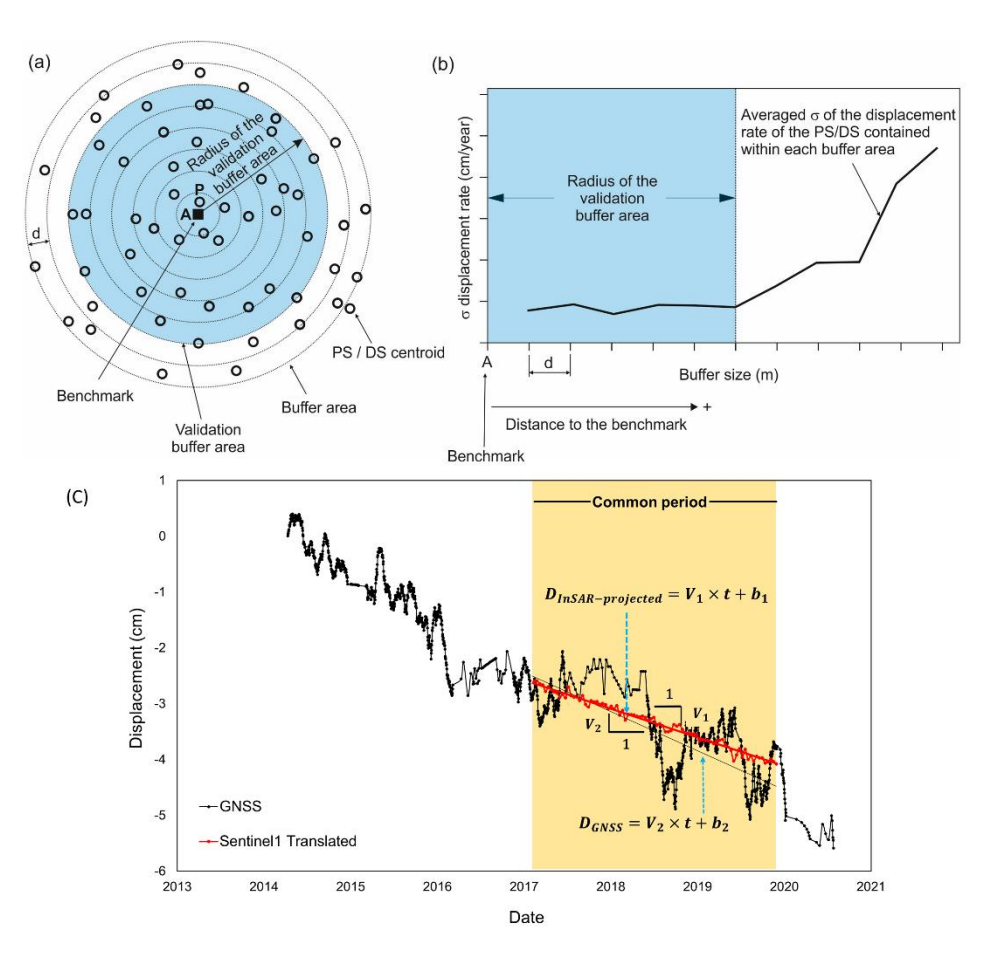


Figure 3.3 (a) Distribution of PS/DS around the in-situ benchmark A and equispaced buffer rings. (b) Dispersion analysis for different buffer sizes in order to find the optimal value. (c) . Deformation rate computation from time series.

#### 3.4.2. Step 1: Ingestion

In the first step of the validation process is divided into two procedures, the first one is related to the "File Selection and Observation Points", at this stage, ValInSAR tool automates the validation process by requiring input information in the form of temporal land subsidence series from various sources (DInSAR, levelling, GNSS, etc.). Data for each source must be organized into an Excel file, utilizing separate sheets for each technology. Each sheet, specific to one technology, includes columns for

observation date and surface movement value (positive denoting uplift). For satellite data, the incidence angle is also necessary to convert line-of-sight movement to vertical direction. The second part is about "Exploring the Data", here, the tool enables the comparison of diverse data sources, such as DInSAR versus GNSS or different DInSAR datasets from various satellites. After selecting two data sources for comparison, the code checks for common observation points within a shared time frame. Non-comparable points are excluded, and if no common data exist between the datasets, the comparison process ends. This step ensures a rigorous and relevant comparison between chosen data sources (Navarro-Hernández et al., 2022).

## 3.4.3. Step 2: Processing

In the processing phase, ValInSAR follows several crucial steps to extract meaningful information from different remote sensing sources. DInSAR, measuring line-of-sight (LOS) displacements from ascending and descending orbits, allows calculating east-west and up-down components. However, when processing both datasets is unavailable, only the vertical deformation component can be computed under the assumption of negligible horizontal deformations in widespread subsiding areas. The tool addresses uncertainties in north-south directions due to the polar orbiting geometry of SAR satellites. Velocity validation is a key aspect where VallnSAR computes mean velocities from each source, presenting the results in a figure for visual analysis. Perfect coherence would align all mean velocities along the 1:1 line, indicating agreement between technologies (Figure 3.3-c). The tool includes the identity line and a linear trend, enhancing result interpretation. Furthermore, ValInSAR analyses deformation time series validation, considering the differing revisit frequencies of technologies like DInSAR, GNSS, and levelling. The comparison involves using a 15-day moving average for GNSS data to reduce noise. The application then identifies the densest time series and interpolates data to synchronize measurement dates for accurate comparison. The final phase of processing includes the calculation of some statistical parameters such as, MD (mean difference), SD (standard deviation), Max-e (maximum difference), Min-e (minimum difference), RMSE, NRMSE1 (Normalized RMSE 1), NRMSE2 (Normalized RMSE2) and R<sup>2</sup>. These parameters are calculated in order to compare two different datasets in terms of velocity and time series, further details on all parameters are provided in Navarro-Hernández et al. (2022)

# 3.5. Flood modelling in Alto Guadalentín

# 3.5.1. Input data

In this study, DInSAR data from diverse SAR datasets spanning 1992 to 2016 were combined to create a cumulative subsidence layer dataset for the Alto Guadalentín valley. SAR images from ERS (1992-2000), ENVISAT (2003-2010), and Cosmo-SkyMED (2011-2016) were employed. DInSAR displacement data were interpolated using IDW to address measurement scatterer issues. The cumulative land subsidence for 1992-2016 revealed a maximum settlement of 2.7 m along the satellite's line of sight (LOS) (Figure 3.4).

The Spain Land Occupation Information System (Sistema de Información sobre Ocupación del Suelo de España, SIOSE, in Spanish) dataset provides a land cover map at a 1:25,000 scale, based on the 2014 version, highlighting agricultural uses in the valley and residential concentrations near mountains. Manning's roughness coefficients were assigned based on Spanish legal instructions for flood mapping (Ministerio de Medio Ambiente, 2011). The 2D boundary conditions and maximum flow rates for the primary upstream in simulations (Figure 3.4) correspond to a 100-year return period, validated by previous studies from the Hydrographic Confederation of the Segura River (CHS, 2014). Downstream conditions for the HEC-RAS model use the normal depth option for four outflows.

The 2.5 m resolution Digital Surface Model (DSM) derived from a 2009 LiDAR dataset from National Geographic Institute of Spain (IGN) was combined with DInSAR-measured cumulative ground surface changes to create the DSM for the 1992 and 2016 scenarios. The DSMs represent the actual ground surface as a consequence of cumulative land subsidence from 1992-2009 and 2009-2016. Despite aquifer overexploitation started in the 1960s and so it is expected that the subsequent subsidence phenomenon also begun at that decade, this study focuses on subsidence from 1992 to present, coinciding with the beginning of regular DInSAR observations (Navarro-Hernández et al., 2023) and so with the most contrastable period regarding land subsidence.

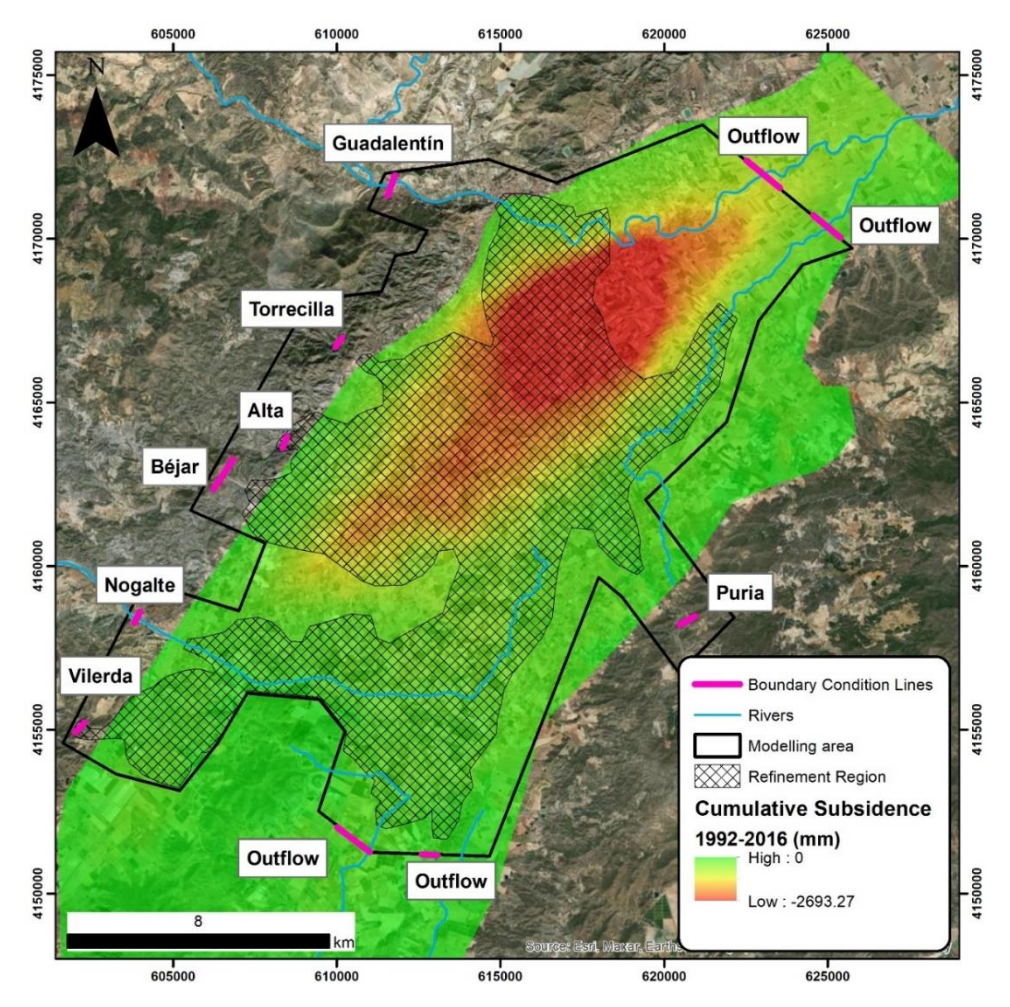


Figure 3.4 Cumulative land subsidence after the integration of all InSAR data for the 1992-2016 period. The modelling area, mesh used for the refinement region and boundary inflow and outflow sections are also plotted in the map.

#### 3.5.2. Model setup

HEC-RAS software is a versatile tool used in hydrological analysis, enabling the simulation of various river components, including steady-flow water surface profiles, unsteady flow scenarios, sediment transport computations, and water quality analysis. The model employs a hybrid 2D unsteady flow approach, integrating finite difference and finite volume methods based on mass and momentum conservation principles (Brunner, 2021).

Before initiating 2D hydraulic modelling, terrain model validation is crucial due to the precision and reliability of the results are linked to the quality and accuracy of the terrain data. The model area is discretized into grid cells, initially using a  $100 \times 100$  m grid size and subsequently refining specific areas with subgrid units of  $10 \text{ m} \times 10 \text{ m}$ . Boundary conditions for water courses in unsteady flow analysis are determined based on flow hydrographs and energy slopes obtained from the DSM. The

downstream boundary condition remains constant for the four outflows, employing the normal depth option in the HEC-RAS model. Computation intervals, hydrograph output, mapping output, and detailed output intervals are set to specific values to ensure model stability and accuracy. Addressing uncertainties related to boundary conditions, their locations are strategically placed far from the main study area in both temporal scenarios (Navarro-Hernández et al., 2023).

#### 3.5.3. Hazard and risk evaluation

The flood hazard in the Alto Guadalentín valley is evaluated using HEC-RAS software, focusing on water velocity and depth. The Ebro Basin Water Management Authority's methodology, adapted from the UK (Wallingford, 2006), calculates a hazard risk index (HR) considering water depth, velocity, and a debris flow coefficient (CHS, 2020). Simultaneously, material damage costs are estimated using the Spanish Ministry of Agriculture's approach, factoring in flooded area, unit value, and a hazard coefficient based on water depth. The methodology offers a comprehensive assessment of flood risk and associated economic impact in the region (CHS, 2020).

# 3.6. Stress-strain application

To evaluate the efficacy of the developed application, datasets from diverse aquifers globally were curated from scholarly literature, such as Madrid (Béjar-Pizarro et al., 2017), Shanghai, and Beijing (Zhang et al., 2014). The methodology applied in this section is also included in Figure 3.2. The following subsections describes the steps carried out in the stress-strain application.

## 3.6.1. Plotting the stress-strain curves

In order to acquire the data, the process involved digitizing time series plots for subsidence and piezometric measurements obtained from aquifers across different global locations. The open-source tool "WebPlotDigitizer" (Rohatgi, 2021) was used. The digitized datasets were subsequently employed to construct stress-strain curves. It's essential to highlight that the data utilized in this study might not match perfectly with the original research from it was derived.

The developed application primarily focuses on plotting stress-strain curves. The code asks to the user to upload an Excel file containing the time series of deformations and piezometric levels. The data are organized into an Excel template, allowing flexibility in terms of length and initial, intermediate, and final dates. The application automatically identifies and standardizes the data format, plots both time series, and evaluates the common period for further analysis. The representation involves plotting time series of deformation and groundwater level on the same graph with different vertical axes. The final step implies the generation of stress-strain curves. Given that data often come from different sources and field campaigns, the application analyses and identifies the densest time series during the common period. It then performs linear interpolation between consecutive values, providing data pairs for subsidence and piezometric levels at the same dates. This allows the plotting of stress-strain curves using the interpolated values calculated for the common dates.

# 3.6.2. Extraction of the $S_{ke}$ and $S_{kv}$ parameters from stress-strain curves

The developed application is focuses on automating the extraction of skeletal storage coefficients in aquifer systems and it is capable of discerning between elastic  $S_{ke}$  and inelastic  $S_{kv}$  components. This imply addressing the ins and outs of identifying elastic segments within stress-strain curves, involving user-specified parameters such as the 'Y-axis interval' and 'X-axis interval'. The computation of elastic skeletal storage ( $S_{ke}$ ) is executed by analyzing variations in piezometric level across identified elastic segments.

The user is prompted to provide subsidence and piezometric data in an Excel file. The application systematically processes these datasets using user-defined parameters to distinguish elastic and

#### **METHODOLOGY**

inelastic segments. These parameters include the 'Initial groundwater level,' representing the preconsolidation head, and the '% of maximum amplitude,' which filters out small segments in the curve. For ensure the consistency between the datasets, the application shows an error alert if discrepancies in data length are detected.

The algorithm proceeds to identify relative maximum points on the stress-strain curve, representing potential changes in aquifer behaviour or preconsolidation head values. It uses conditions related to the 'Y-axis interval' and 'X-axis interval' to classify segments as elastic, with the goal of adapting to the unique characteristics of each study area. The application provides flexibility for users to experiment with parameter values to optimize the analysis for specific cases. The initial conditions involving the 'Initial groundwater level' and the unknown maximum historical stress are considered, and the application dynamically adapts to these uncertainties. Linear regression fitting is applied to each elastic segment, generating  $S_{ke}$  values. To improve the accuracy, small loops are filtered out based on amplitude criteria, with adjustments for variations in loop sizes. This ensures that the computation of  $S_{ke}$  is focused on meaningful, representative elastic segments.

The application generates graphical outputs representing piezometric head versus cumulative displacement, displaying the differential elastic segments identified. Adjustment lines with inverse slopes are discarded as they lack physical meaning. The algorithm further generates a second graph showing the complete stress-strain curve, with elastic segments overlaid in a distinct colour. Linear regression of the complete dataset allows for the calculation of the inelastic skeletal storage  $(S_{kv})$ . The application concludes by saving the results on the last sheet of the input Excel template, including all  $S_{ke}$ ,  $S_{ke}$  weighted corresponding to each loop (both selected and discarded), and the calculated  $S_{kv}$ .

# 4. Results

# 4.1. DInSAR data for monitoring land subsidence

# 4.1.1. CPT and P-SBAS results

The application of the Coherent Pixel Technique to Sentinel-1 data in the San Luis Potosi Valley revealed significant land deformation patterns. With 33,486 pixels analysed, the study identified a high deformation rate in the north-central metropolitan zone, exhibiting an average velocity of -15 cm/year from 2014 to 2019. Stability ranges, determined by standard deviation, highlighted stable areas in green, mainly in the south and west. Positive values indicated uplift, primarily in the San Miguelito Sierra mountains, potentially linked to tectonic and isostatic processes. Conversely, negative values indicate subsidence, mainly in the valley. Deformation rates ranged from -1.5 to -3.5 cm/year in Soledad de Graciano Sánchez and -1.8 to -4.2 cm/year in more extensive in the San Luis Potosi urban area as shown Figure 4.1-a (Navarro-Hernández et al., 2020).

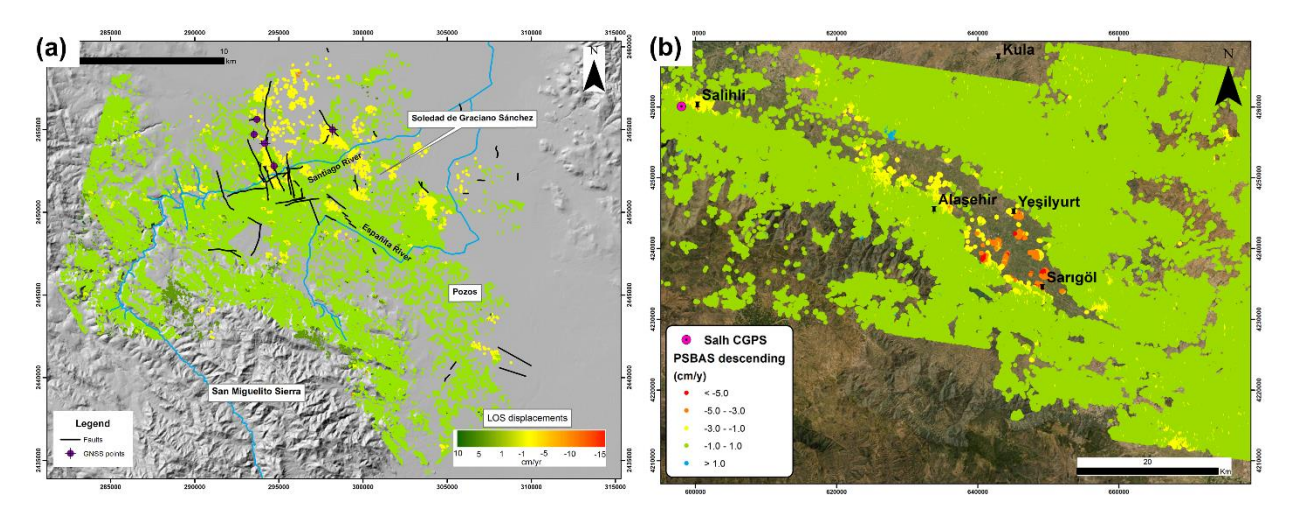


Figure 4.1 (a) LOS displacements rates for the metropolitan area of SLPV, (b) LOS displacement rates the ASSB.

P-SBAS processing generated velocity deformation maps (Figure 4.1-b), displaying descending and ascending orbits with red and blue points indicating motion away from and towards the sensor, respectively. Descending orbit images cover 13,000 km², and ascending orbit images cover 24,000 km², with pixel densities of 81 and 70 pixel/km². LOS rates range varies from -6.37 to 1.84 cm/year (descending) and -6.40 to 2.87 cm/year (ascending). The lower point density observed in the sub-basin is due to dynamic land use changes. Maximum subsidence rate is at the basin centre and the southeast graben edge, while uplifting is on the northwest basin edge, correlating with local extension dynamics. Vertical displacement maps show similar subsidence patterns, concentrated within the basin and along the southeast border. Horizontal displacement maps reveal westward movements related to continental crustal Aegean extension (red and orange points) and eastward movements confined to the graben (blue points) along dip angle faults, linked to local tectonics in the Gediz graben evolution (Navarro-Hernández, 2023).

### 4.1.2. Validation of DInSAR results

In validating the CPT results in San Luis Potosí, GNSS data for five points were compared. GNSS vertical values ranged from -3.06 to -0.12 cm/year, with negligible horizontal displacements. To facilitate a direct comparison between GNSS and Sentinel-1 displacements, GNSS vertical values were projected along the Line of Sight (LOS). The scatter plot displayed a maximum discrepancy of 2.6 cm/year, minimum of 0.07 cm/year, mean absolute discrepancies at 0.92 cm/year, and a root mean square of

1.27 cm/year (Figure 4.2-a). A high data correlation of 0.986 affirmed the strong agreement between GNSS and DInSAR measurements, validating the reliability of CPT results (Navarro-Hernández et al., 2020).

To validate the P-SBAS results, the time series of an *in-situ* CGNSS station (SALH) in Salihli, covering November 2008 to October 2020, was compared with nearby InSAR MPs. Validation utilized the ValInSAR code (Navarro-Hernández et al., 2022) by comparing descending DInSAR data with the GNSS time series. A 150 m buffer around GNSS defined a zone for averaging DInSAR data pixels. The comparison revealed strong agreement as shows Figure 4.2-b, where it can be seen a correlation plot between Sentinel-1 and CGNSS acquisitions. Statistical results indicate a good agreement between Sentinel-1 acquisitions and the SALH station. The RMSE is 0.91 cm, mean error is 0.76 cm, standard deviation of the error is 0.50 cm, maximum discrepancy is 2.33 cm, and the coefficient R2 value is 0.91, signifying good forecasting (Navarro-Hernández, 2023).

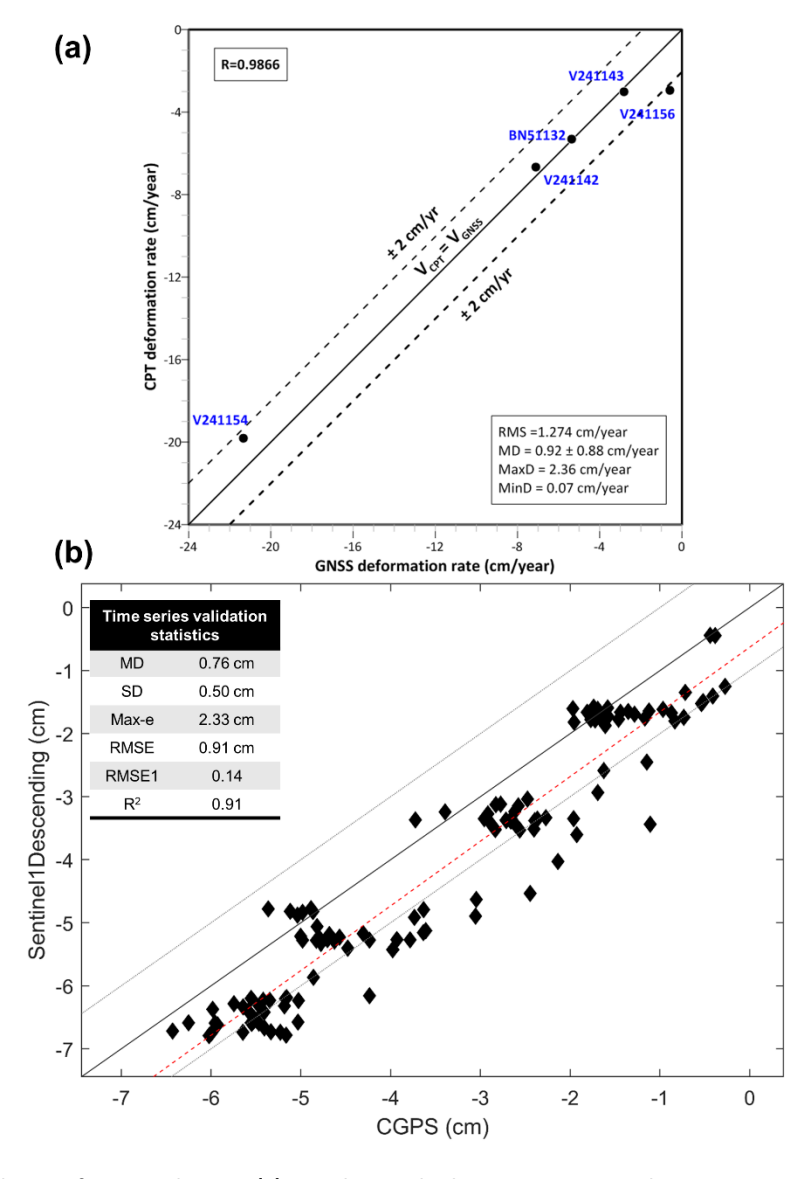


Figure 4.2 Validation of DInSAR dataset: (a) Correlation plot between CGNSS and CPT time series data in SLP. (b)

Correlation plot between SALH CGNSS and P-SBAS time series data in ASSB. Continued lines represent the 1:1 line, and dotted lines parallel to the 1:1 line represent the ± 1 cm/error

As can be observed in these two distinct case studies, in the case of San Luis Potosí, validation was conducted manually, without use a systematic validation criterion. This limitation was identified as a starting point and a research question, leading to the formulation of the second research topic. In this new line, the focus is on the development of a DInSAR data validation methodology, along with the development of an application to automate this process. Once the validation methodology was proposed and established in Navarro-Hernández et al., (2022), it was applied to validate DInSAR data in the second study area, specifically in the eastern Gediz River basin. This systematic and automated approach not only aims to improve the accuracy and reliability of the results but also represents a significant advancement in the efficiency of the DInSAR data validation process compared to unstructured manual methods.

#### 4.1.3. PCA/ICA results

The FastICA algorithm applied to P-SBAS results from eastern Gediz Basin revealed three independent components (ICs) explaining over 99 % of eigenvalues. IC1, constituting 96 % of variance, corresponds to long-term deformation with a spatial distribution similar to the mean velocity map (Figure 4.3). IC2 (2.5 % of variance) captures seasonal deformation, correlating with cumulative rainfall changes. IC3 (1 % of variance) represents extensive spatial deformation linked to seasonal patterns and surface soil moisture variations. This concise analysis highlights key deformation components and their relationships to temporal and spatial factors.

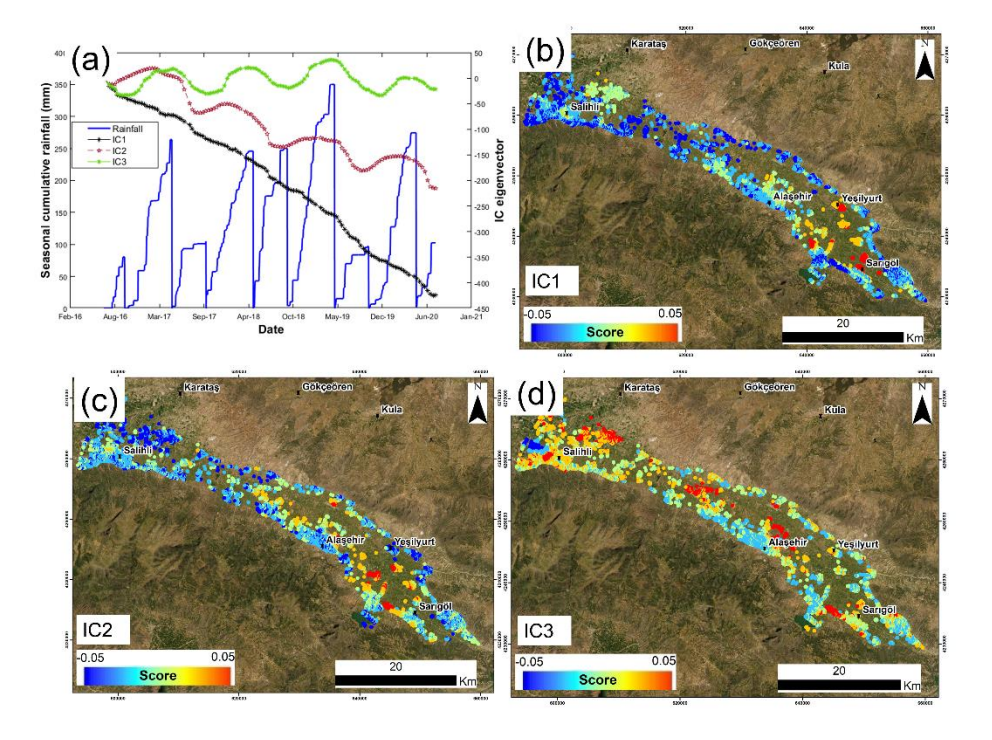


Figure 4.3 FastICA results in ASSB: (a) ICs eigenvector time series compared with seasonal cumulative rainfall (blue), (b) IC1 score map, (c) IC2 score map, (d) IC3 score map.

#### 4.2. ValInSAR results

In this section, the validation results for three selected study areas (i.e., SLPV, Alto Guadalentín and Murcia city) are presented, providing a detailed description of the code's accuracy.

# 4.2.1. Definition of buffer areas

Dispersion analysis for CSK and Sentinel-1 sensors in the Alto Guadalentín aquifer revealed optimal buffer sizes. For CSK, the range was 50 to 150 m, while for Sentinel-1, values fluctuated between 100

to 150 m due to its lower spatial resolution. In Murcia, ENVISAT data showed stable dispersion values in the range of 100 to 150 m, and in San Luis Potosí, the optimal size reached 400 m (Figure 4.4).

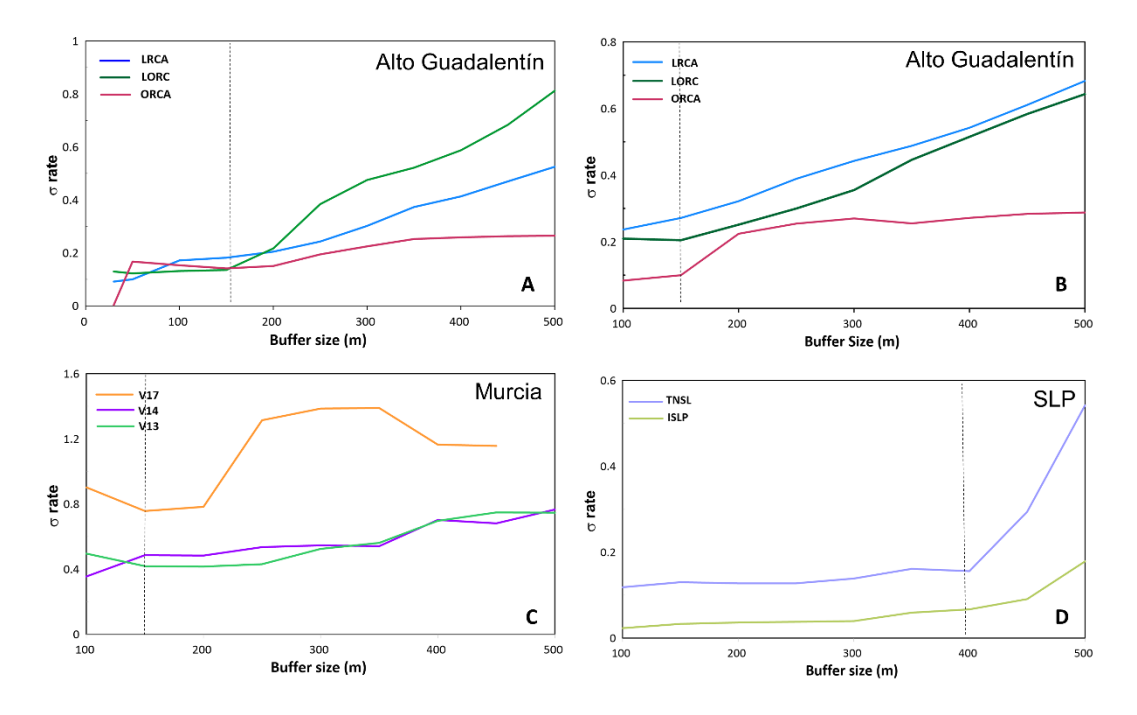


Figure 4.4 Dispersion analysis for different buffer size in order to find the optimal value. The dotted line indicates the optimal buffer size. (a) results for CSK dataset in Alto Guadalentín aquifer. (b) results for Sentinel-1 dataset in Alto Guadalentín aquifer. (c) results for ENVISAT dataset in Murcia. (d) results for Sentinel-1 dataset in San Luis Potosí.

### 4.2.2. Velocity validation

In Alto Guadalentín, levelling campaigns (2005 and 2016) and CGNSS were compared with DInSAR observations. Buffers were built around each benchmark, and mean deformation values were calculated. ENVISAT velocity results showed a very good agreement with levelling data, indicating a reliable validation. In Guadalentín Valley, ENVISAT data couldn't be validated due to a lack of temporal overlap, but CSK and Sentinel-1 sensors exhibited a good agreement with GNSS measurements. In Murcia, the velocity correlation between ENVISAT observations and extensometers displayed a good agreement, supported by statistical results (Navarro-Hernández et al., 2022). In San Luis Potosí Valley, GNSS and Sentinel-1 observations showed a good agreement over a 5-year period (Figure 4.5).

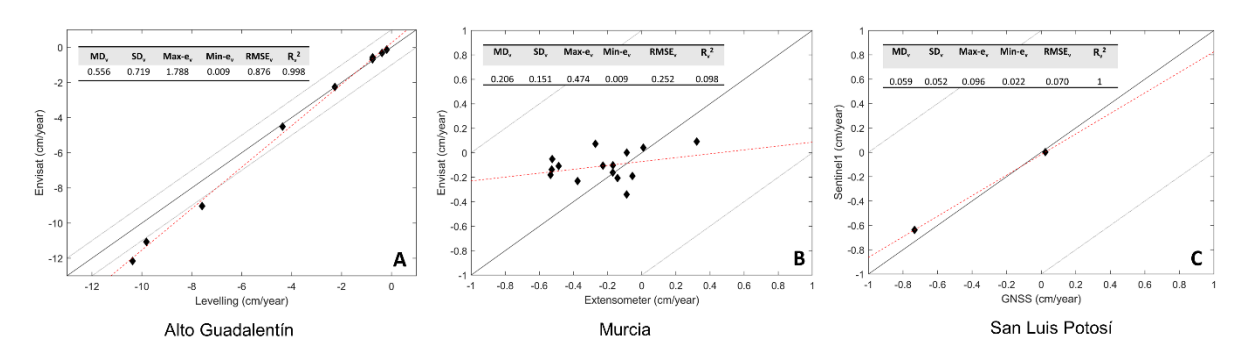


Figure 4.5 Correlation plot and statistics values (cm/year) for the velocity validation. (a) Levelling benchmark vs ENVISAT for Alto Guadalentín aquifer. (b) Extensometers vs ENVISAT for Murcia and (c) Continuous GNSS vs Sentinel-1 for San Luis Potosí Valley. Continued lines represent the 1:1 line, and dotted lines parallel to the 1:1 line represent the ± 1 cm error.

#### 4.2.3. Time series validation

Correlation between GNSS stations in Alto Guadalentín and both CSK and Sentinel-1 time series exhibited good R² values. Despite a good overall agreement, Sentinel-1 results were more dispersed than CSK, attributed to its shorter observation period and more fluctuating time series. In Murcia, time-series validation using extensometers revealed varied correlation results, with some extensometers exhibiting poor agreement. However, comparisons between ENVISAT observations and specific extensometers indicated a good agreement. Time-series correlation plots between GNSS and Sentinel-1 observations in San Luis Potosí Valley showed a good correspondence for TNSL GNSS station, while ISLP GNSS station exhibited a lower R² value, indicating a discrepancy in the seasonal deformation behaviour between DInSAR and GNSS observations (Navarro-Hernández et al., 2022).

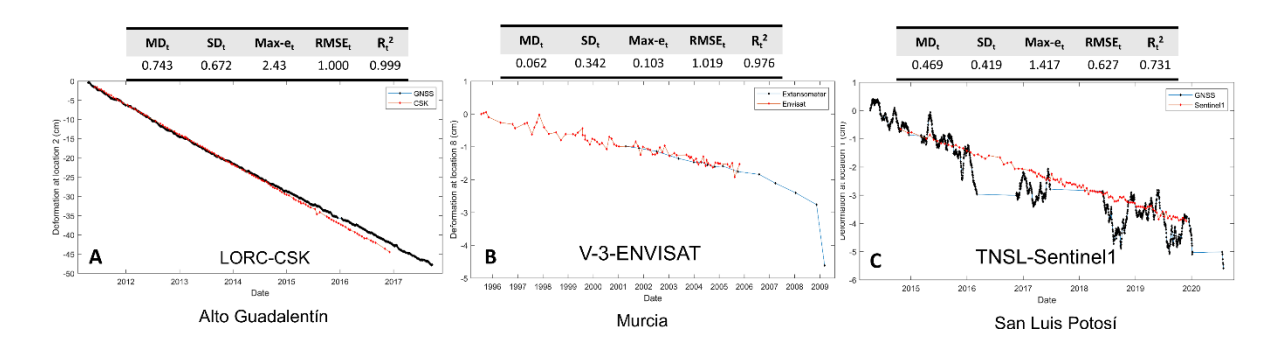


Figure 4.6 Time series validation for the comparison between DInSAR observations and in-situ techniques. (a) LORC CGNSS station with CSK observations. (b) V-3 extensometer with Envisat observations in Murcia. (c) TNSL station with Sentinel-1 observations in San Luis Potosí.

### 4.3. Flood modelling results

This section describes the results of one of the applications of DInSAR data, by modelling flood scenarios in the Alto Guadalentín valley. This section presents numerical model results for 1992 and 2016 scenarios. In 1992, water velocities range from 0.02 to 14.34 m/s, and depths vary from 0.03 to 5.18 m, resulting in a total flooded area of 101.36 km². In 2016, velocities range from 0.02 to 14.97 m/s, with depths from 0.02 to 5.06 m, resulting in a total flooded area of 103.4 km². Depths less than 0.3 m cover 55.67 km² (2016) and 55.75 km² (1992), emphasizing the dynamic nature of the hydrological system. The details about the water depth and velocity results are described below (Navarro-Hernández, et al., 2023).

### 4.3.1. Water depth results

The water depth maps presented in Figure 4.7 shows the impact of subsidence produced between 1992 and 2016 scenarios on flood risk in the Alto Guadalentín valley. Notably, the most affected regions are associated with secondary stream courses, such as Torrecilla, Bejar, and Nogalte ravines, rather than the primary watercourse, Guadalentín River. Alluvial fan structures locate at the entrance of these streams contribute to large flood areas with gradual drainage towards the northeast.

Cross sections A-A' and B-B' were created to analyse water depth changes across the valley. Figure 4.8-a highlight areas with significant changes in water depth between the 1992 to 2016 scenarios. Using a 200 m sample range, water depths under the 1992 and 2016 scenarios were compared along these cross sections (Figure 4.8). Notably, the NW direction experienced a notable increase in water depth, reaching approximately 1.5 m along A-A' and 0.8 m along B-B'. Conversely, the NE and SE directions observed decreases, indicating a migration of flood spots towards the subsidence-prone northwest centre of the basin (Navarro-Hernández, et al., 2023).

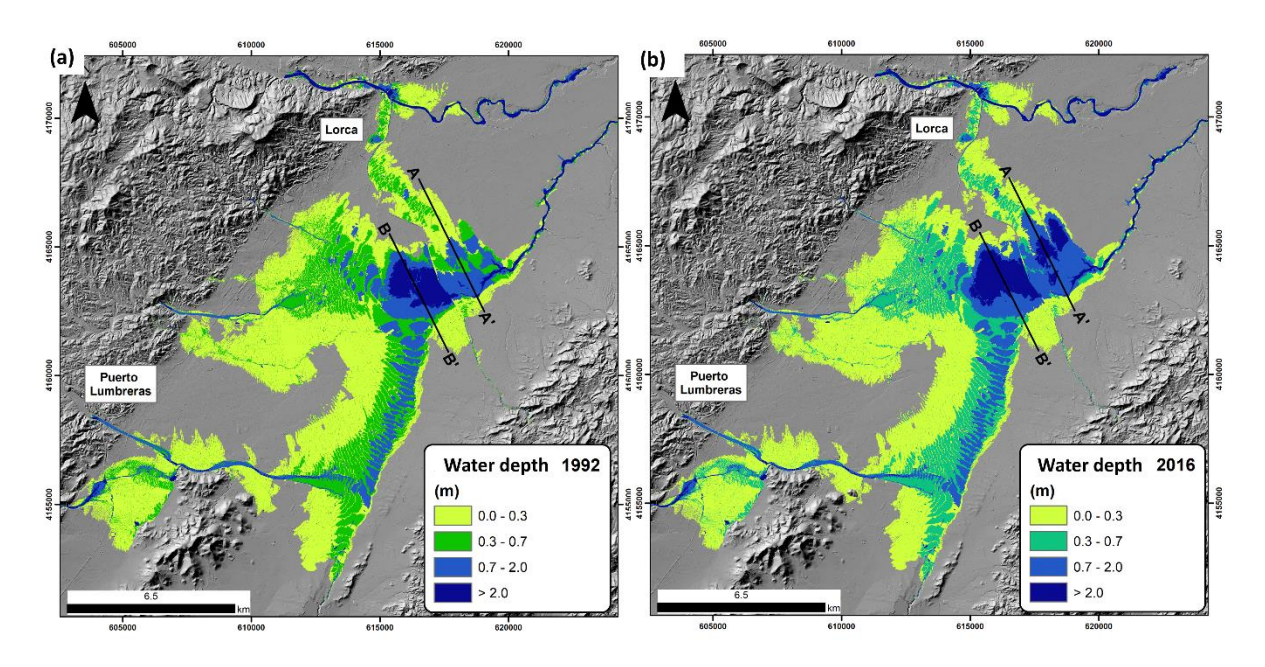


Figure 4.7 Water depth map for the (a) 1992 and (b) 2016 scenarios.

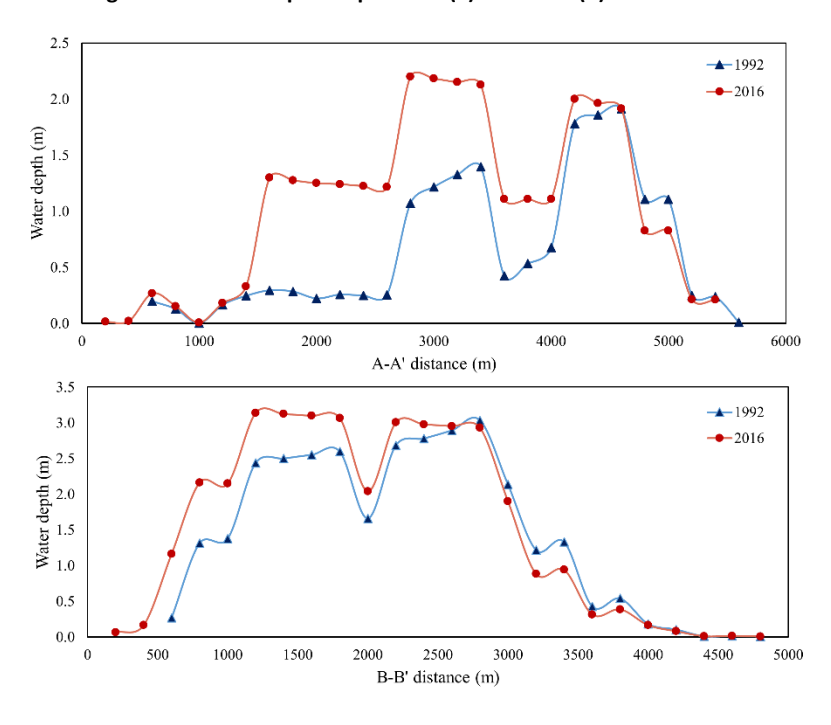


Figure 4.8 Comparison between water depths in 1992 and 2016 along cross sections A-A' and B-B'.

Urban settlements along the valley's perimeter, such as Lorca city and Puerto Lumbreras, located at higher elevations with less susceptibility to intense subsidence, remain relatively unaffected. Figure 4.7 displays the aerial extent of water depth threshold values, revealing areas prone to potential flood damage. The inundated area with water depth greater than 0.7 m increased by 15.21 %, aligning with regions experiencing higher cumulative subsidence rates. Conversely, areas with water depth less than 0.7 m decreased by 1.47 %. Considering hydrographs for a 100-year return period, water depths exceeding 2 m are observed in both scenarios along the main river channels. However, the analysis underscores changes in flood behaviour due to subsidence progression, with a 2.06 % increase in total flooded area between 1992 and 2016. These findings contribute valuable insights into the evolving flood risk in the valley over the past decades (Navarro-Hernández, et al., 2023).

## 4.3.2. Velocity results

The water velocity maps shown in Figure 4.9-a,b illustrate changes in flood extent under the 2016 scenario in the Alto Guadalentín valley. Noteworthy changes are observed at the valley centre, aligning with subsidence-prone areas. The highest velocities correspond to the river course, particularly segments near mountains with higher slopes and narrow channels. In floodplain areas like Alto Guadalentín, extended low-velocity zones indicate limited drainage capacity, producing long residence times for accumulated water. The confluence of Nogalte and Torrecilla-Bejar waterflows, impacted by subsidence, exhibits increased velocities in the 0-0.5 m/s range. Significant differences in velocity ranges are observed, with areas between 0.0 and 0.5 m/s increasing by 2.5 %, and areas between 0.5 and 1.0 m/s increasing by 2.4 % from 1992 to 2016. The velocity reduction at the centre of subsidence in 2016 indicates decelerated flow dynamics, attributed to the expansion of the flood area toward the northwest (Navarro-Hernández, et al., 2023).

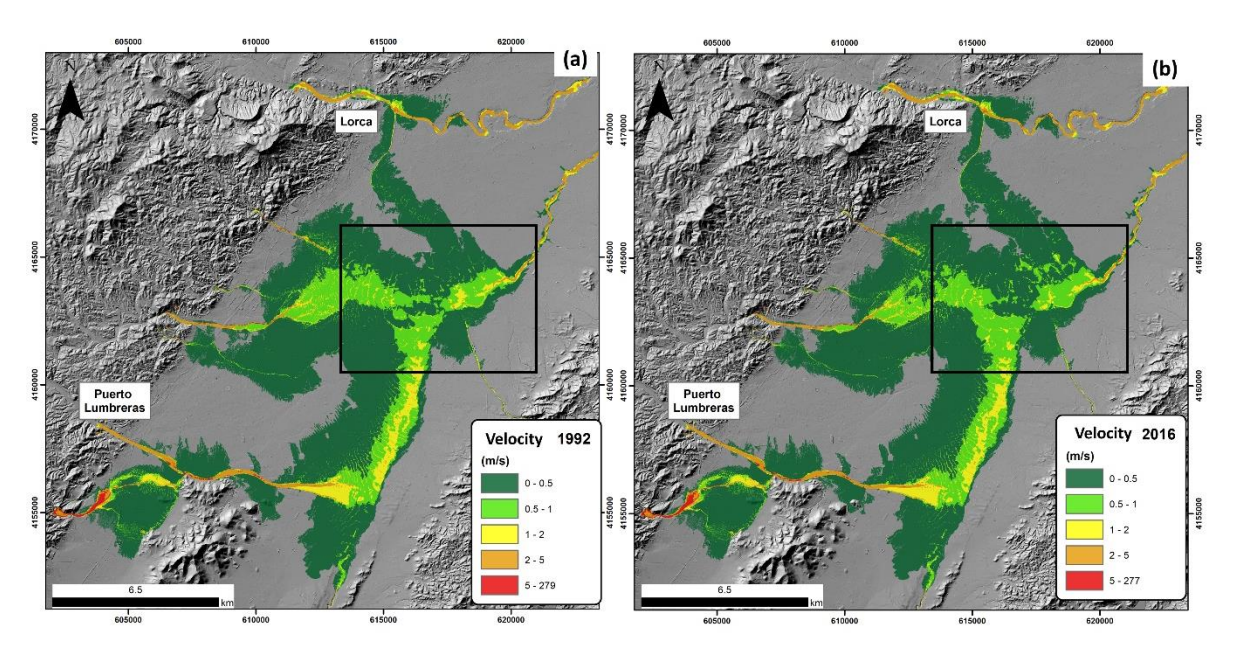


Figure 4.9 Water flow velocity map for the (a) 1992 and (b) 2016 scenarios. The black squares denote the flooded area with changes.

Figure 4.10-a, b illustrates spatial differences in water depth and velocity between 1992 and 2016. Concentrated discrepancies at the valley centre, near areas with high cumulative subsidence, reveal water depth differences of 1-2 m and velocity differences exceeding 0.35 m/s. The most impacted zone, primarily used for agriculture, contrasts with minor changes in urban and mountainous regions unaffected by subsidence. Overall, river and ravine patterns remain consistent with 1992 ground conditions in unaffected areas (Navarro-Hernández, et al., 2023).

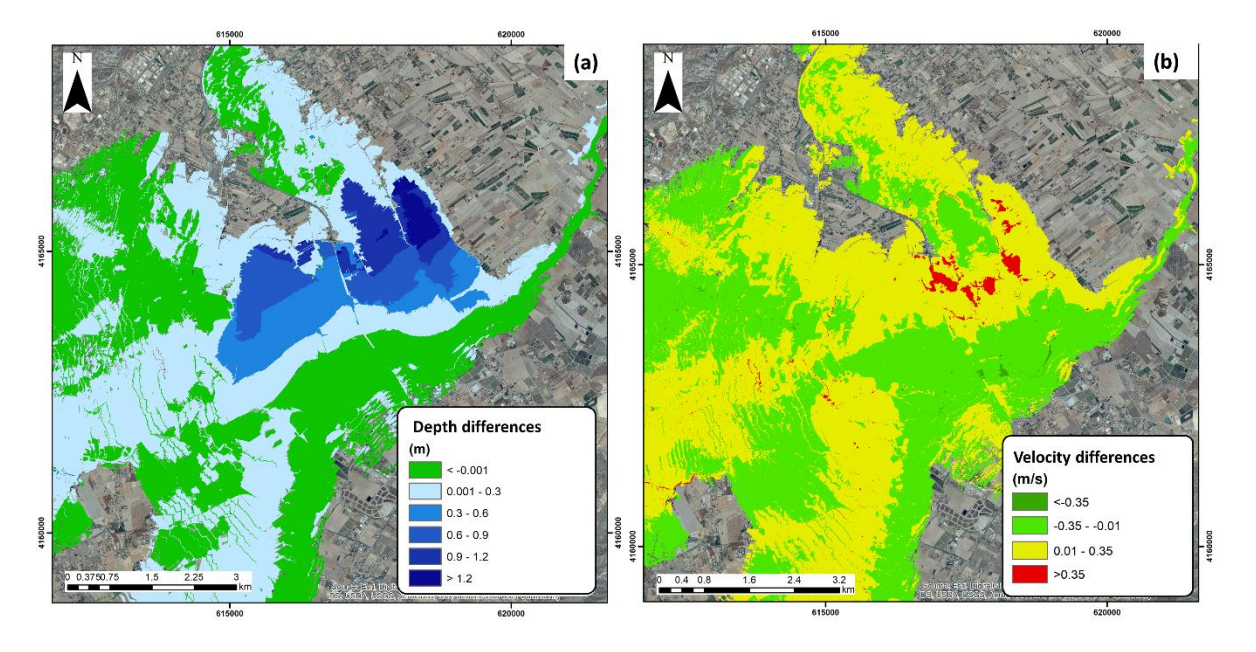


Figure 4.10 Differences in the (a) water depth and (b) velocity between the 1992 and 2016 scenarios. This corresponds to a zoom-in of the black square plotted in figure 4.9.

# 4.3.3. Flood hazard classification and economic damage estimation

Hazard risk maps in Figure 4.11-a,b, based on water depth and velocity layers, categorize areas into low, moderate, high, and extreme risks. A notable increase in hazard areas, particularly in the NW centre affected by land subsidence, is evident (Figure 4.11-a,b). Calculated differences confirm a rise in moderate (+5.04 %), high (+30.17 %), and extreme (+5.62 %) risk areas compared to 1992. Cadastral analysis (Figure 4.12-a,b) reveals a 7.08 % increase in rural buildings at low risk, 19.94 % at high risk, and 23.57 % at extreme risk. In urban areas, low-risk units increase by 3.53 %, and moderate-risk units increase by 3.76 %. The impact is more pronounced in rural constructions at the valley centre, where subsidence is prominent (Navarro-Hernández, et al., 2023).

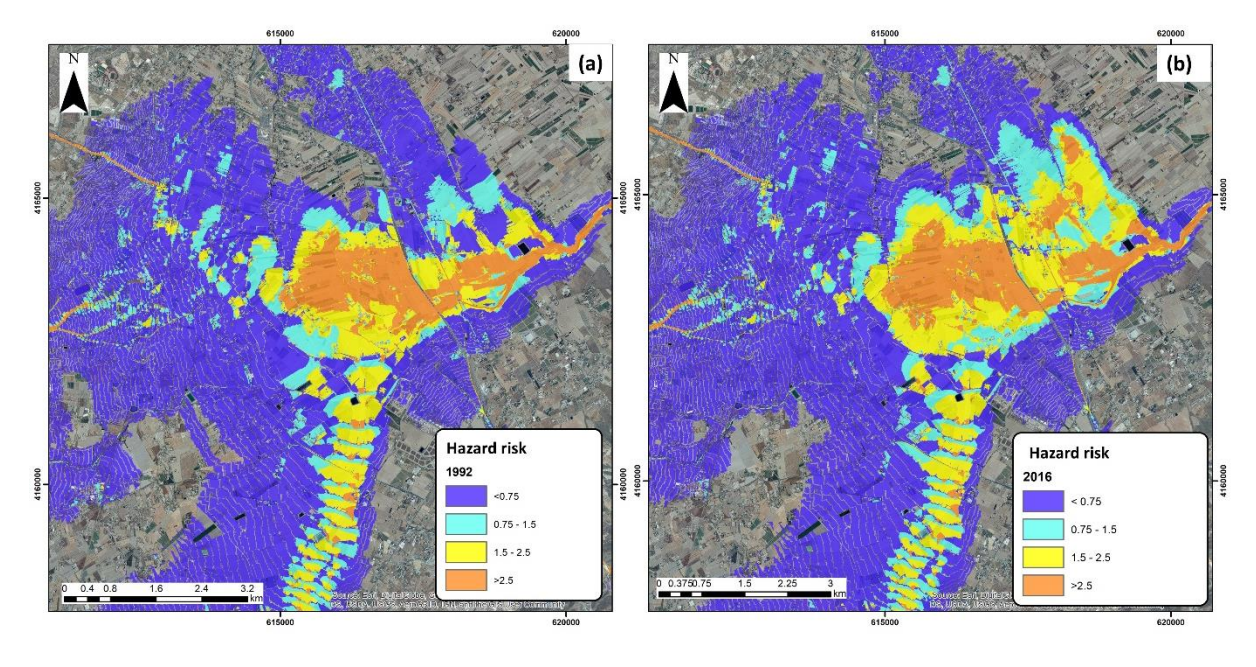


Figure 4.11 (a) Hazard risk map for the 1992 and (b) 2016 scenarios. The black squares denote the flooded area with changes.

Monetary value analysis, considering land cover and economic activity, shows a €70,172,620 increase in economic loss in the study area as a consequence of the 100-year return period event. Flood impact on agriculture contributes to 90 % of the total cost difference, with a €63,551,736 increase in economic loss. Transport networks, particularly the Lorca-Águilas highway, face a €9,473,857 increase in damage due to its passage through critical flooding areas. Commercial and community services exhibit a slight increase, primarily influenced by their urban concentration away from subsidence-prone regions. This analysis supports the assertion that land subsidence may play an important role in modifying flooding patterns, with economic losses increasing over time, especially in agriculture and critical infrastructure (Navarro-Hernández, et al., 2023).

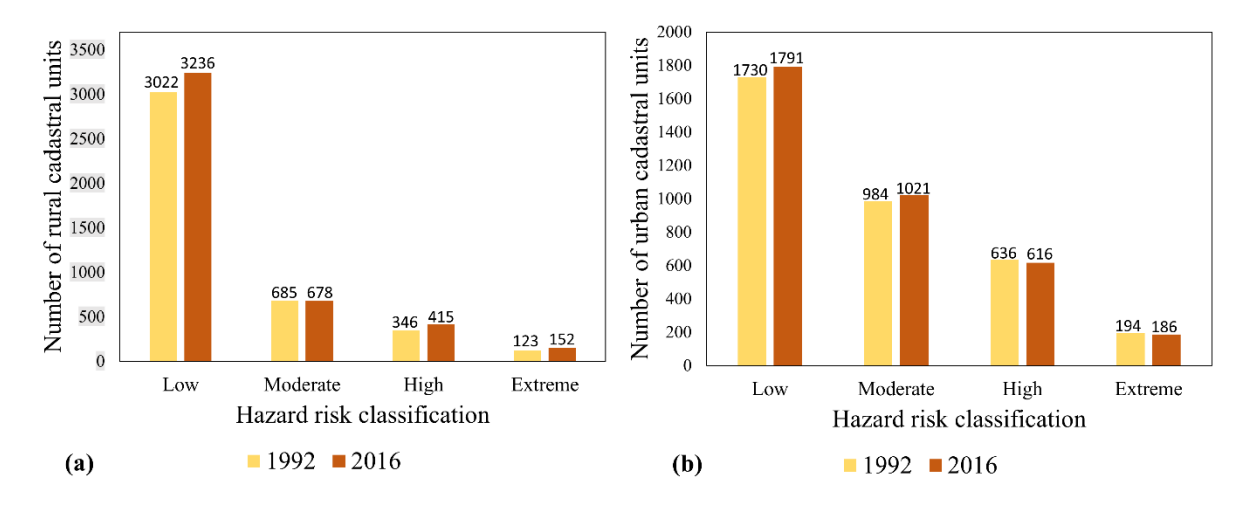


Figure 4.12 Number of (a) rural and (b) urban cadastral units affected by different flood hazard risks under the 1992 and 2016 scenarios.

# 4.4. Calculation of skeletal storage coefficient results

Five stress-strain curves from Shanghai's aquifer-system were analysed, representing different extensometers and aquifer layers. Focusing on the second confined aquifer, 34 elastic segments were used out of 35 due to a negligible loop (Figure 4.13-a). The Figure 4.13-c, corresponding to the second aquitard, displayed loading-unloading cycles tied to seasonality. Skeletal storage was calculated using 22 elastic loops, aligning well with the curve trend. The Figure 4.13-e, f, representing the third aquitard, revealed expanding loops with increased subsidence. Discarding segments with opposite slopes, 26 elastic segments were considered for calculating skeletal storage. Since the thickness of the layers (aquitards and aquifers) is known, it was possible to calculate the elastic and inelastic specific storage coefficients ( $S_{ske}$ ,  $S_{ske\_weighted}$ , and  $S_{skv}$ ). All these coefficients are listed in the supplementary material.

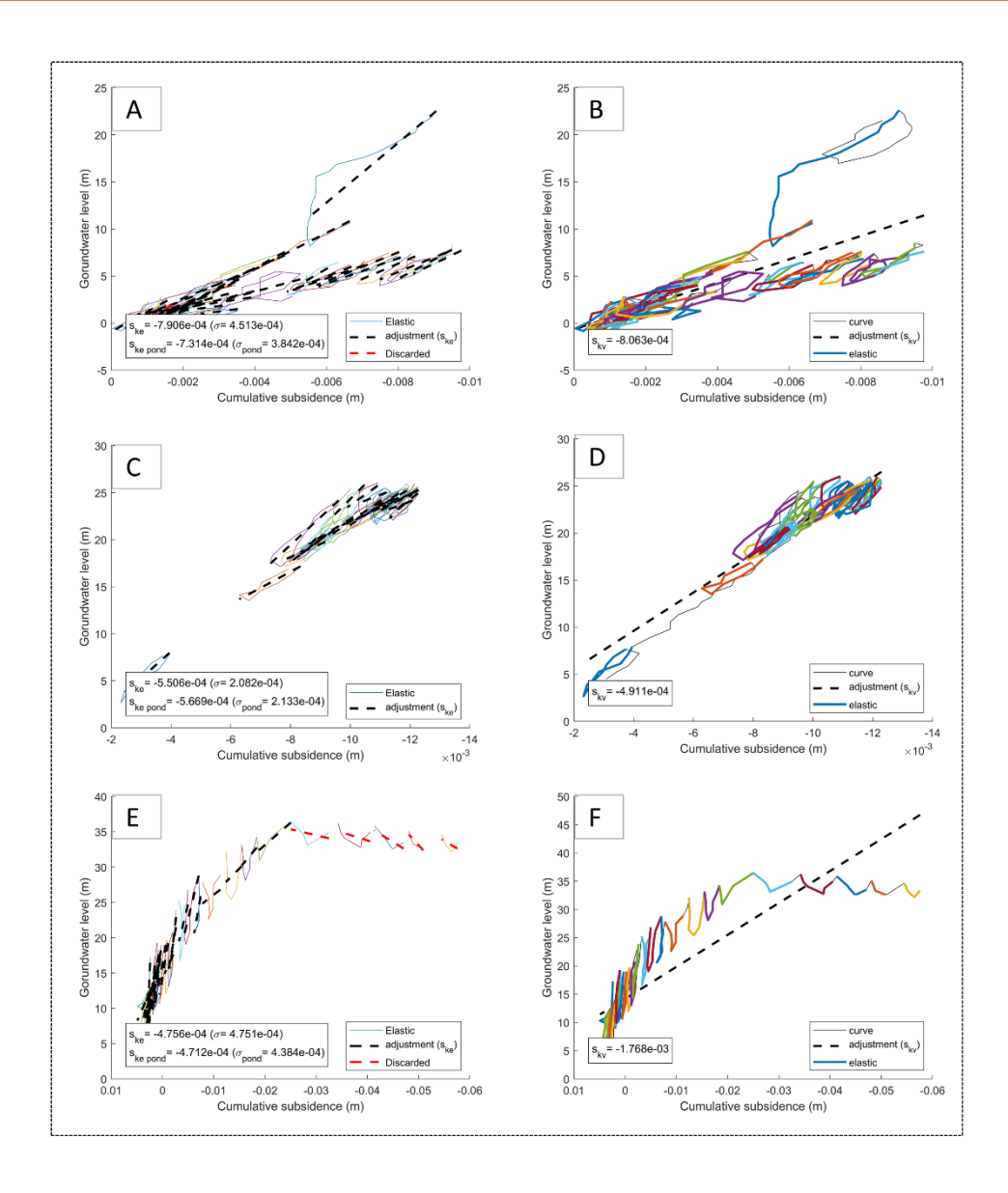


Figure 4.13 Stress-strain curves results from the Southern Yangtse Delta. (A-B) Second confined aquifer; (C-D) Second aquitard layer. (E-F) Third aquitard layer.

Seven stress-strain curves were extracted from (Zhang et al., 2014), representing various aquifer and aquitard layers. Focusing on the second aquifer level, a 35 % amplitude percentage was applied to identify seven elastic segments, excluding those with non-logical values. Notably, the orange segment significantly influenced coefficient calculations due to its size and the 97 points which compound the segment. The stress-strain curve in the blue segment was considered elastic based on the user-controlled preconsolidation head (Figure 4.14). In contrast, the deepest aquitard layer showed a clear correlation between increasing cumulative subsidence and rising piezometric head. Three elastic loops were identified, with the first discarded due to an inverse slope. Coefficient values for each layer, considering respective thicknesses, are detailed in supplementary material.

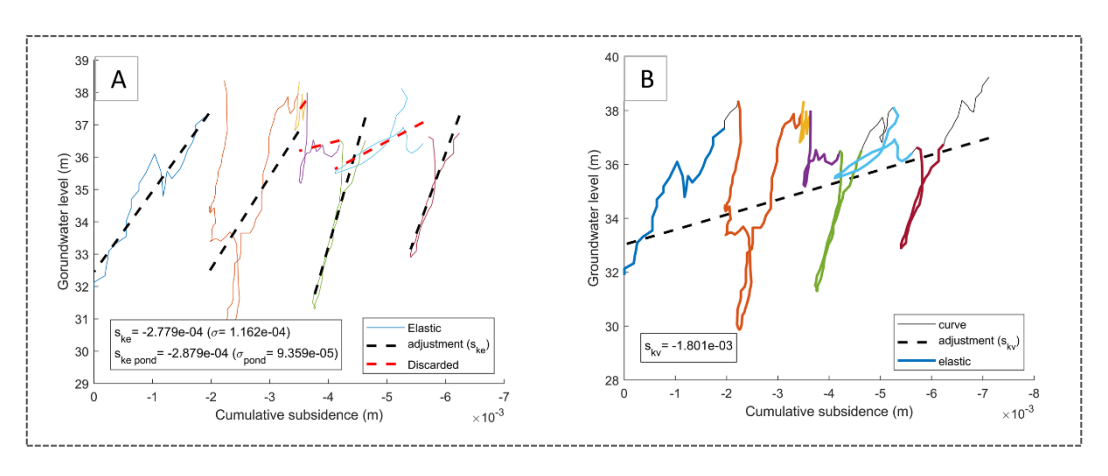


Figure 4.14 Stress-strain curves results from the Second aquifer layer of the Plain of Beijing: (A) elastic component of subsidence. (B) inelastic component of subsidence (second layer aquifer)

This section presents two stress-strain curves from Li et al., (2022) analysis. The Pinggezhuang extensometer's layer (Figure 4.15-a) identified eight elastic segments, excluding three exceeding the 35 % amplitude condition and the last loop due to an inverse slope. Calculation focused on four segments with consistent trends and minimal standard deviation. The adjustment line matched well with the overall trend of the curve. The Tianzhu extensometer's layer (Figure 4.15-c) exhibited distinct behaviour, poor cumulative subsidence recovery with decreasing piezometric level, indicating non-elastic material. Refer to supplementary material for a summary of coefficient values and layer thicknesses.

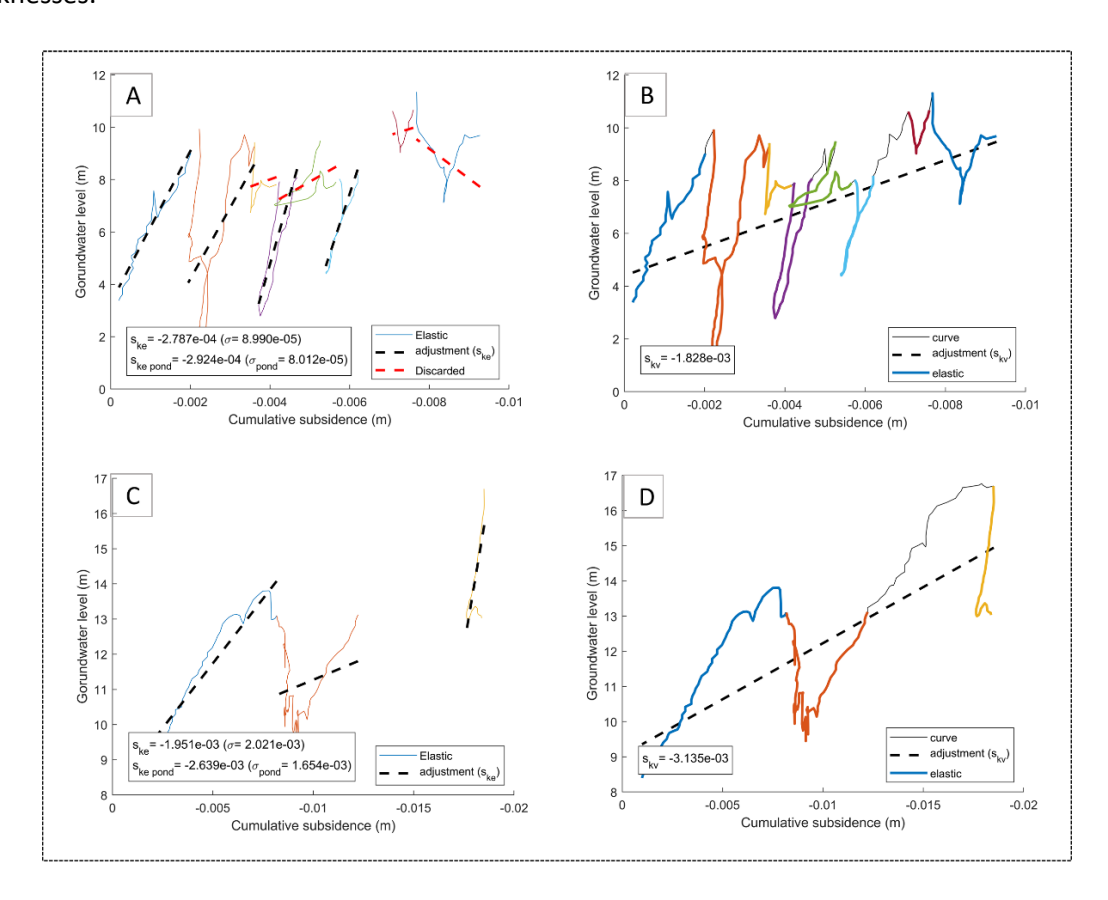


Figure 4.15 Stress-strain curves results from North China plain. (A) elastic component of subsidence in the Second layer - Pinggezhuang station; (B) inelastic component of subsidence in the Second layer - Pinggezhuang station; (C) elastic component of subsidence in the third layer - Tianzhu station; (D) inelastic component of subsidence in the third layer - Tianzhu station

In the Madrid Tertiary aquifer-system study, 17 stress-strain curves, digitized from Béjar-Pizarro, et al., (2017), were constructed using well data. Standardized at 154 m thickness, these curves, spanning 2004 to 2010, vary notably with shorter time series and distinctive single elastic loops due to material characteristics. Figure 4.16 displays representative curves, with an overall trend featuring significant elastic loops. Because the detrital material comprising the Madrid aquifer primarily exhibits elastic behaviour, there is no need to calculate the inelastic skeletal storage coefficient ( $S_{kv}$ ). Instead, the global  $S_{ke}$ , as well as the  $S_{ke}$  and  $S_{ke\_weighted}$  coefficients, have been included. These values are presented in the supplementary material.

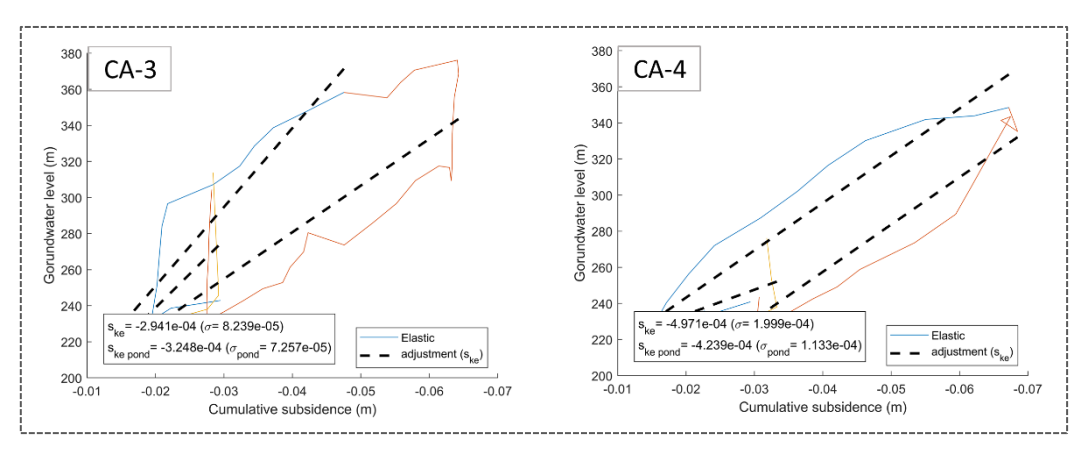


Figure 4.16 Stress-strain curves results from wells CA-3 and CA-4 placed in the Madrid Tertiary aquifer-system.

# 5. Discussion

In this section, the obtained results from all research topics comprising this thesis will be analysed and discussed. Starting with the interpretation of DInSAR results in the San Luis Potosí and Alaşehir-Sarıgöl sub-basin (ASSB) study areas, spatial distribution and magnitude of displacements are compared with triggering factors such as soft soil thickness, groundwater extraction, and active faults. Subsequently, the proposed statistical parameters for measuring the accuracy of DInSAR data are discussed. Following that, the flood modelling results in the Alto Guadalentín using DInSAR data are debated. Finally, concerning the application to automate the calculation of skeletal storage coefficients, the results are compared with those of other authors, and the efficacy of the proposed methodology is validated.

# 5.1. DInSAR data for monitoring land subsidence

# 5.1.1. Relationship between land subsidence and soft soil thickness

In geotechnical engineering, displacements  $(\delta)$  are commonly assessed by considering key parameters (Tomás et al., 2010): the thickness of potentially deformable soil (D), the variation in effective stress state expressed as an effective piezometric level drop  $(\Delta h)$ , and the soil modulus (S), dependent on stress state, representing soil deformability. This relationship is mathematically expressed as

$$\delta = S \times \Delta h \times D$$

Notably, a direct correlation is observed between subsidence and soft soil thickness, where a greater accumulation of soft soil (D) results in larger displacements. Furthermore, bedrock structure, including buried faults associated with geological features like grabens and horsts, can induce abrupt spatial variations in soft soil deposits.

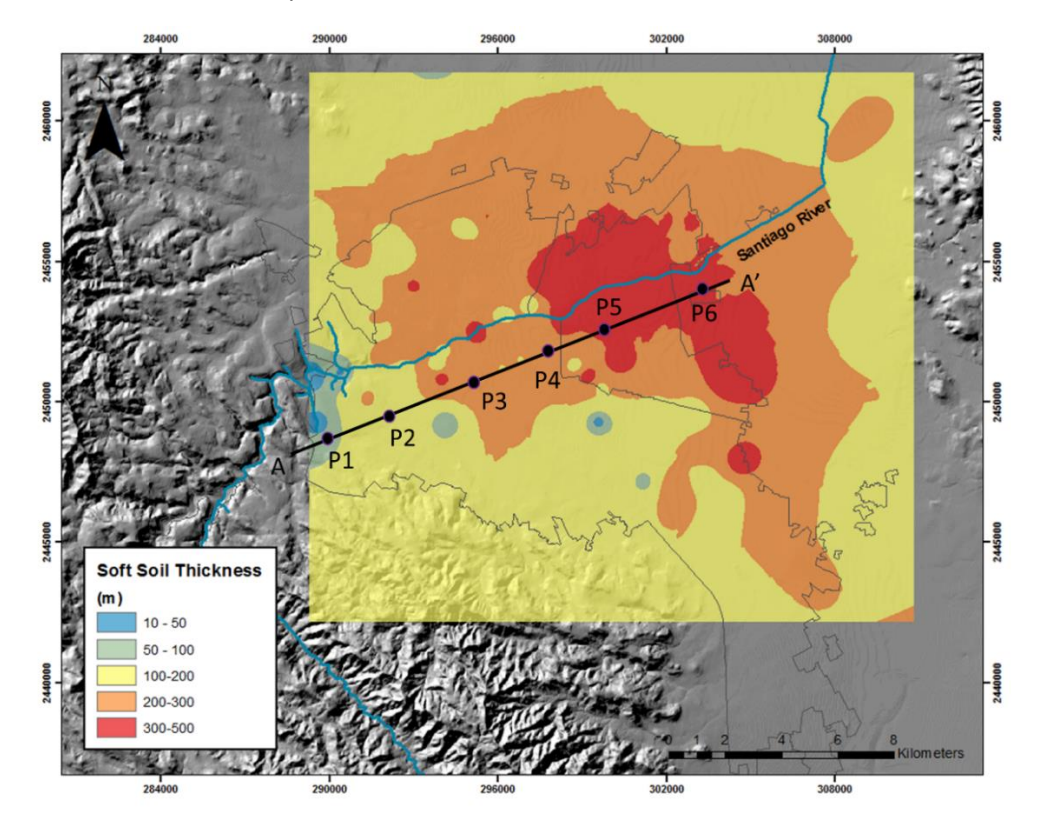


Figure 5.1 Soft soil thickness map of the San Luis Potosí valley.

Thus, the mechanical behaviour of the aquifer system, influenced by effective stress, unconsolidated soil distribution, and thickness, significantly impacts settlement magnitudes. The SLPV aquifer system, located over an extensive layer of diverse alluvial sediments with a cumulative thickness of up to 600 m, is one of the valleys/grabens monitored in this study. Soft soil thickness, obtained from borehole data, is correlated with DInSAR measured (CPT results) (Figure 4.16). The soft soil thickness distribution reveals higher values at the valley's centre, coinciding with deeper grabens and maximal sediment accumulation. Basin boundaries, bordered by competent volcanic and sedimentary rocks, contrast with the more deformable Quaternary sediments within. Comparing deformable soils with subsidence zones reveals a consistent correlation. A cross-sectional analysis (Figure 5.2) and DInSAR-derived displacement rates confirm that higher soft soil thickness corresponds to increased subsidence, validating the correlation. The study supports the interdependence of soft soil thickness and land subsidence in the San Luis Potosi Valley (Navarro-Hernández et al., 2020).

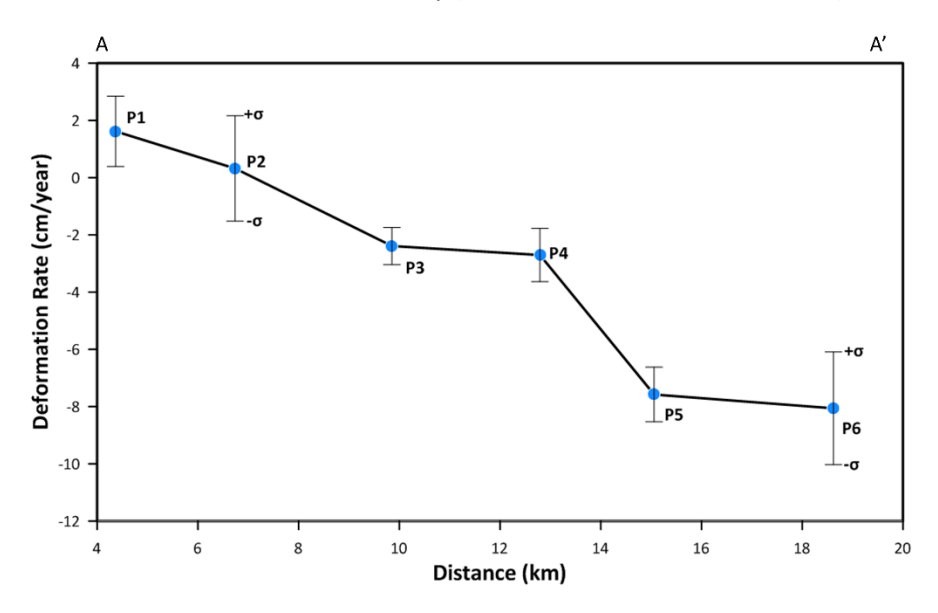


Figure 5.2 Deformation rate values along the section P1-P6 in San Luis Potosí.

Regarding to the eastern Gediz river basin analysis, the Figure 5.3-a presents the soft soil thickness map for the ASSB, constructed from lithological data obtained from 118 boreholes, mainly located in the alluvial zone. Given that aquifers with high groundwater yield are prevalent in these unconsolidated units, understanding their mechanical response to increased effective stress is crucial for comprehending displacement evolution. The distribution of soft soil thickness (Figure 5.3-a) indicates noteworthy agreements with areas exhibiting the highest displacements detected by DInSAR, particularly to the east and centre of the valley (red circle in Figure 5.3-a, b). Spatial correlation analysis, comparing borehole geological data with vertical displacement rates from P-SBAS, reveals a robust correlation (R² of 0.853) (Figure 5.3-c). This correlation illustrates that regions with maximum soft soil thickness (50 to 100 m) correspond to the highest subsidence rates, emphasizing the significant role of graben fill sediments in land subsidence within the ASSB (Navarro-Hernández et al., 2023).

Additionally, Figure 5.3-d presents the IC1 score map, explaining 96 % of the eigenvectors and correlating with the LOS deformation rate map. Positive IC1 scores align with increased clay material thickness, concentrated in the basin's centre. The comparison of P-SBAS and eigenvector time series within specific zones indicates a strong correlation between higher positive IC1 scores and elevated subsidence areas. This suggests that IC1 corresponds to the primary deformation trend attributed to

long-term land subsidence, closely linked to the compaction of soft soil material due to rising effective stress induced by groundwater over-exploitation and declining piezometric levels (Figure 5.3-e, f).

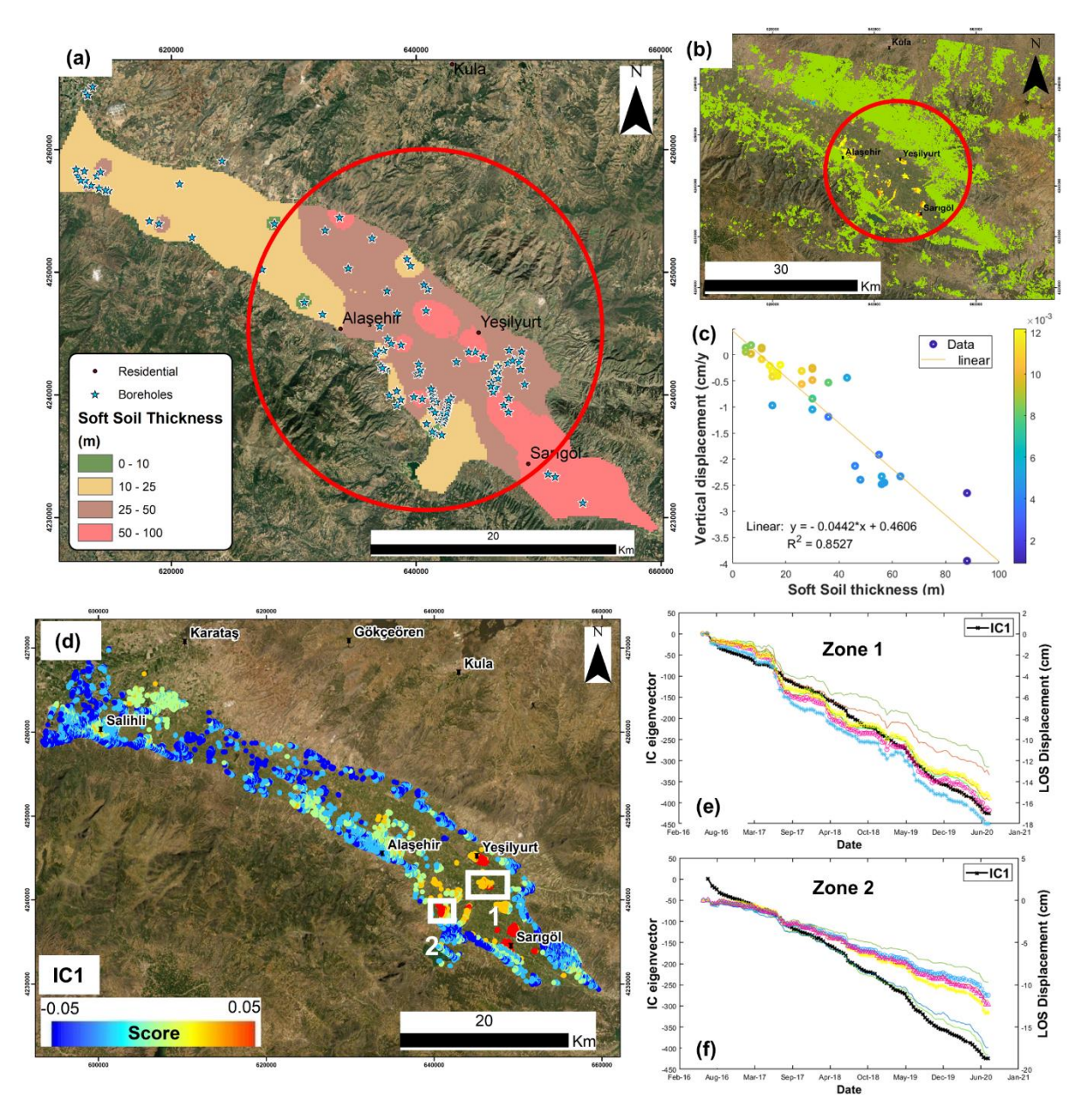


Figure 5.3 Relationship between soft soil thickness and land subsidence in Gediz basin: (a) Soft soil thickness map derived from boreholes. (b) Vertical component of LOS displacement rate. (c) Correlation plot between soft soil thickness and vertical displacement rate. (d) Comparison between IC1 and LOS displacement at two locations with high soft soil thickness and land displacements: (e) time series comparison at zone 1. (f) Time series comparison at zone 2.

### 5.1.2. Relationship between land subsidence and groundwater extraction

A comprehensive analysis utilizing data from 24 wells across the San Luis Potosi valley was conducted to understand the relationship between piezometric changes and land subsidence. Figure 5.4-a depicts a predictive map of piezometric level changes ( $\Delta h$ ) obtained through ordinary kriging and a Gaussian semivariogram model from 2007 to 2017. Higher piezometric depletion is concentrated in the central-eastern zone, matching with areas of significant soft soil thickness and higher population density. This suggests groundwater extraction as one of the primary drivers of land subsidence, correlating variations in soil stress with piezometric level fluctuations. The correlation plot (Figure 5.4-

b, c) between piezometric changes and land subsidence, as well as soft soil thickness, emphasizes the interrelated nature of these factors. Additionally, Figure 5.4 illustrates a continuous decline in piezometric levels, reaching up to 43 m in some wells over the decade (2007–2017), with associated subsidence values. Moreover, the inelastic storage coefficient ( $S_{kv}$ ) was calculated, yielding values ranging from  $1.3\times10^{-3}$  to  $4.8\times10^{-3}$ , demonstrating proportional subsidence displacements relative to water-level changes. Comparisons with values from other studies suggest a degree of consistency, emphasizing the importance of considering the entire sediment thickness and soil layering when interpreting storage coefficient values. Despite indications of elastic behaviour in aquifer systems associated with seasonal groundwater variations, a detailed evaluation was hindered by limited water table time series data (Navarro-Hernández et al., 2020).

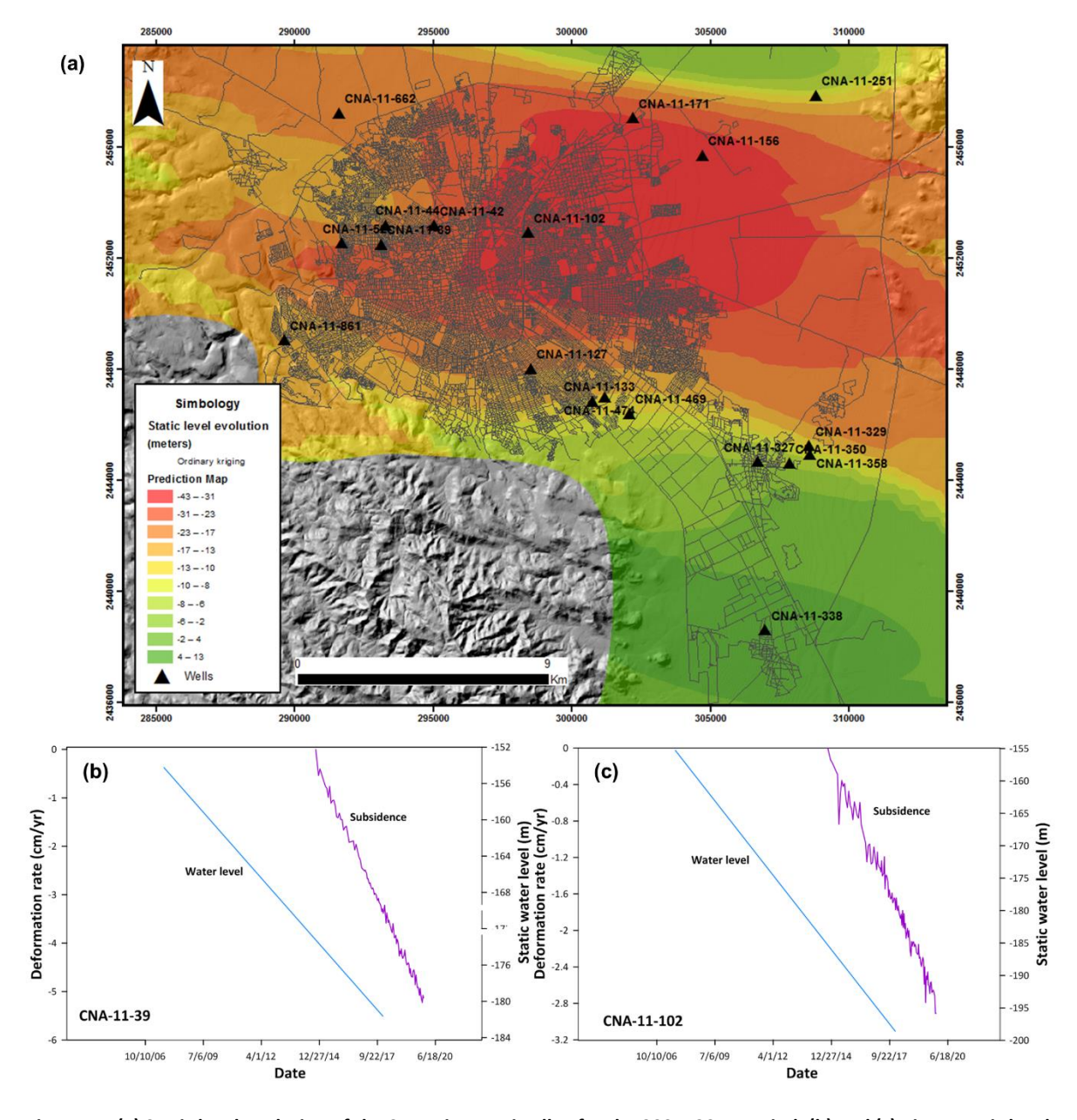


Figure 5.4 (a) Static level evolution of the San Luis Potosi valley for the 2007–2017 period. (b) and (c) Piezometric level evolution and deformation time series measured by CPT for two wells in SLPV. The location of the wells is shown in (a). Blue points and dashed blue line represent the measured values and the general trend of static water level, respectively

In the context of the ASSB, groundwater use is mainly focuses on agricultural requirements, constituting approximately 86 % of total withdrawals, while the remaining 14 % serves urban water

demand and husbandry activities, with a minor allocation for industrial purposes (GDWM, 2018). A map of piezometric level changes, derived from 11 piezometers (Figure 5.5-a), illustrates clear depletions in the plain's centre due to irrigation derived from groundwater withdrawal and along the southern border near major towns (Salihli, Alaşehir, and Sarıgöl).

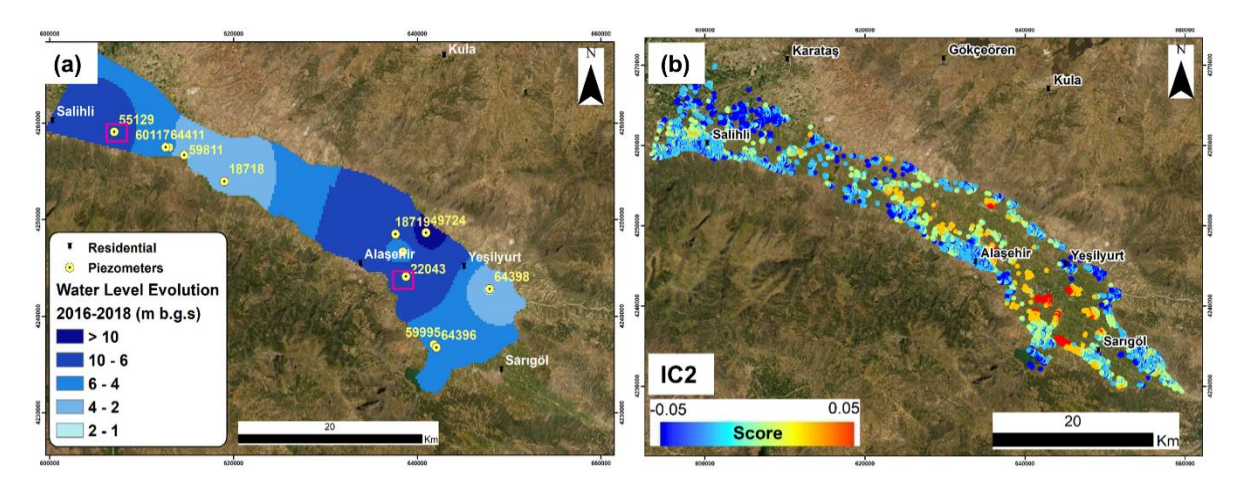


Figure 5.5 Relationship between seasonality and piezometric head evolution in Gediz basin: (a) spatial distribution of groundwater level evolution from 2016 to 2018 and (b) IC2 map score.

The correlation between the piezometric level evolution with the IC2 score map reveals overlapping extents, indicating a potential link between aquitard layer compaction and groundwater extraction (Figure 5.5-b). Further correlation analyses between IC2 eigenvectors and groundwater evolution show agreement, particularly evident in wells 55129 and 22043 from 2016 to 2018, displaying a synchronized response with minimal temporal delays. Remarkably, the IC2 time series reveals long-term subsidence with notable seasonal rebound, matching with cumulative rainfall peaks, although exhibiting monthly delays between 2016 and 2018, as can be observed in Figure 5.6-b.

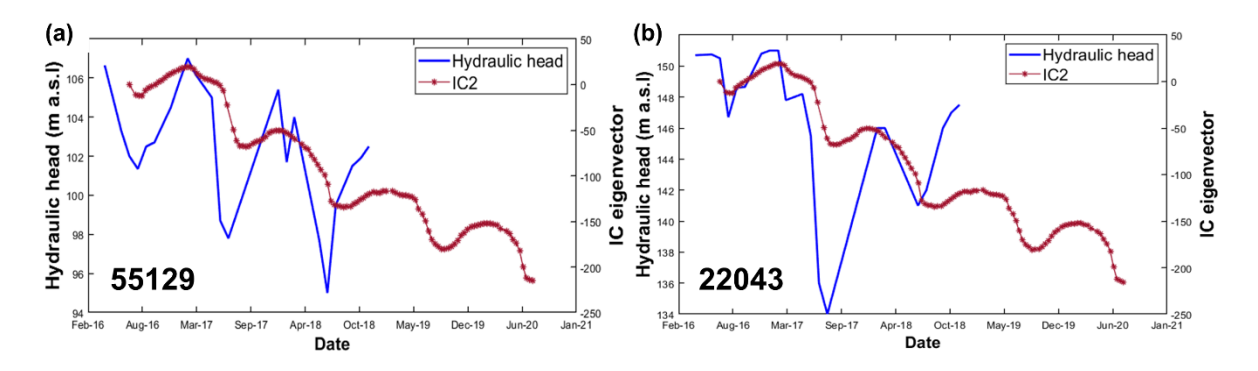


Figure 5.6 IC2 components in two selected wells of Gediz basin: (a) IC2 and piezometric head time series at the well 55129. (b) IC2 and piezometric head time series at the well 22043.

#### 5.1.3. Relationship between land subsidence and active faults

In the San Luis Potosi Valley, the active north-south striking normal faults, which area concentrated in the centre-north regions, impact structures and roads. Stress and subsidence structures by extension are evident, possibly linked to water level decay and land subsidence. Surface fault movement, often along preexisting blind faults, results in differential subsidence and tensional stresses, causing earth fissures (Conway, 2015). CPT displacement maps show spatial correlation with major faults, suggesting their continued activity. CPT results also reveal fault traces, such as the San José del Terremoto and Aeropuerto faults, highlighting structural damage and subsidence patterns (Figure 5.7). This information aids in mapping fault lines and monitoring at-risk areas for urban planning and damage

prevention. The obtained data aligns with a Subsidence-Creep-Fault Processes model, emphasizing the importance of DInSAR in geological mapping and risk assessment (Navarro-Hernández et al., 2020).

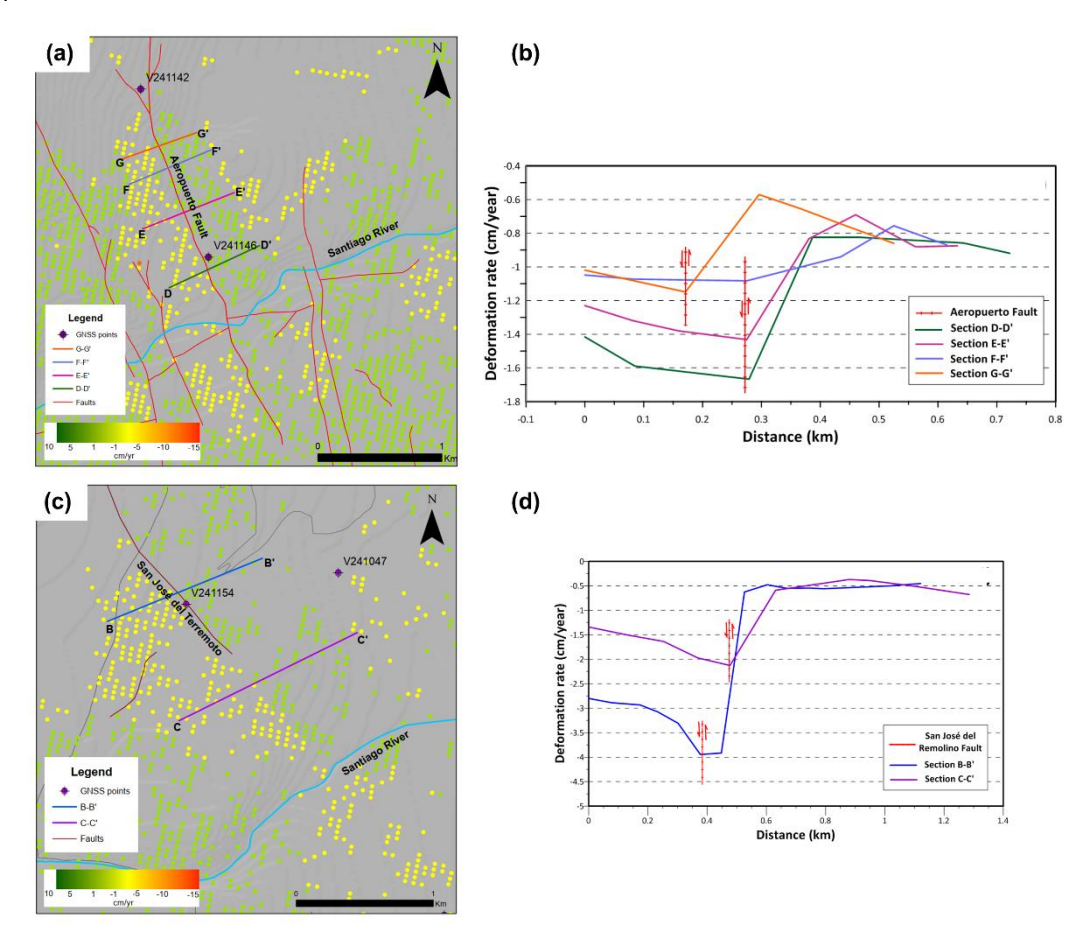


Figure 5.7 Deformation rate map derived by CPT covering (a) the Aeropuerto fault zone, coloured lines represent sections across the trace fault. (b) Land subsidence sections D-D', E-E', F-F', and G-G' along the Aeropuerto fault. (c) the San José del terremoto fault.

Unfortunately, in the ASSB it was not possible to distinguish multi-year deformation rates using Independent Component Analysis (ICA), due to it was not feasible the isolation of tectonic-induced deformation from that caused by groundwater withdrawal and soft soil compaction. Differential ground subsidence, associated with groundwater withdrawal is in agreement with mapped active faults, like the Sarıgöl fault, detected by Sentinel-1 satellite data (Figure 5.8-a). Cross-sections across the Sarıgöl fault reveal a significant change in deformation velocity on both sides, attributed to differential compaction related to varying clay and silty material thickness (Figure 5.8-b). In this area, the amount of clay and silty material varies significantly on either side of the fault, influenced by the bedrock's topography. This causes irregular settlements, resulting in major structural damage in the towns. The study establishes a connection between tectonic structures, sediment distribution, and differential subsidence, emphasizing the role of bedrock faults in influencing aquifer layers and subsurface deformation in the Sarıgöl region (Navarro-Hernández et al., 2023).

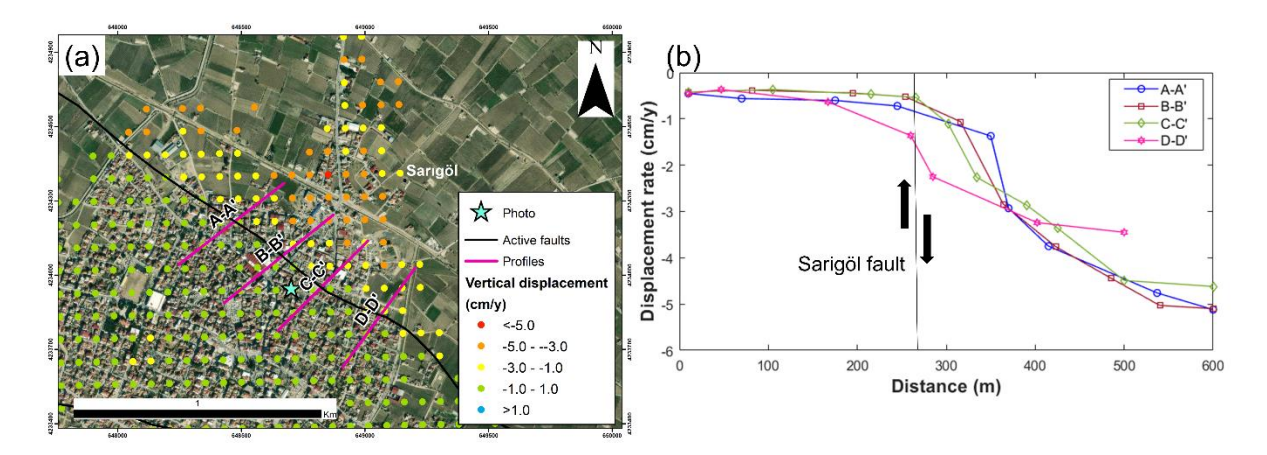


Figure 5.8 Relationship between active faults and land subsidence: (a) Rate displacement map covering Sarıgöl fault influence area in Gediz basin. (b) Analysis of vertical displacement sections A-A', B-B', C-C' and D-D' along the Sarıgöl fault trace.

### 5.2. Recommended accuracies for validation of DInSAR data

The accuracy of DInSAR results depend on the temporal overlap between datasets used for validation. Taking into account the extension of the records, ENVISAT outperforms CSK and Sentinel-1 in the Alto Guadalentín case, supporting from a longer temporal overlap with levelling data. In Murcia, where extensometers (rod type) are used for validation, limitations arise due to fixed points, potentially impacting accuracy, especially in areas with shallow anchors. Discrepancies in the extensometer measurements are observed and attributed to their shallow depth. Dispersion analysis indicates no universal optimal buffer size, emphasizing the need for consideration of subsidence spatial distribution. The study suggests a minimum buffer of 50 m and a maximum of 400 m, with variations influenced by geological factors. Geological knowledge is crucial in the interpretation of buffer distances. Further investigations could explore relationships between standard deviation fluctuations, different sensors, spatial resolution, processing algorithms, subsurface lithology, and other factors across various study areas (Navarro-Hernández et al., 2022).

For recommended accuracies thresholds for assessing the reliability of DInSAR measurements using the ValInSAR code, two types of RMSE are calculated:  $RMSE_v$  for velocity discrepancies and  $RMSE_t$  for displacement time series errors. These metrics, while dependent on the magnitude of measured displacements, may not be directly comparable between different study areas due to variations in subsidence magnitude. To address this, normalized RMSE metrics ( $NRMSE_1$  and  $NRMSE_2$ ) are proposed.  $NRMSE_1$ , normalized using the dynamic range of *in-situ* deformation values, is generally recommended for assessing accuracy, while  $NRMSE_2$ , normalized using the average deformation values, is suitable when the range of *in-situ* deformation values is close to zero (Navarro-Hernández et al., 2022).

A classification scheme based on  $R^2$  and  $NRMSE_1$  is introduced to categorize accuracy. The "High Accuracy" category, denoted in green, signifies  $R^2 > 0.8$  and  $NRMSE_1 < 0.3$ . The "Good Accuracy" category, in yellow, includes results with  $R^2$  between 0.8 and 0.4, and  $NRMSE_1 < 0.3$ , or results with  $R^2 > 0.8$  and  $NRMSE_1$  between 0.3 and 0.6. The "Reasonable Accuracy" category encompasses  $R^2$  values between 0.8 and 0.4 and  $NRMSE_1$  values between 0.3 and 0.6. Lastly, the "Inaccurate" category pertains to results with low  $R^2$  and/or high  $NRMSE_1$  values (Navarro-Hernández et al., 2022).

Figure 5.9 and Figure 5.10 illustrate the application of the proposed accuracy classification to various validation scenarios, highlighting the categorization of results for different study areas and measurement techniques. The analysis emphasizes the importance of considering sample size

limitations, as demonstrated in the San Luis Potosí validation, where small sample sizes may lead to inconsistencies in assessing linear dependence. The categorization scheme offers a comprehensive approach to evaluating the accuracy of DInSAR measurements in diverse settings (Navarro-Hernández et al., 2022).

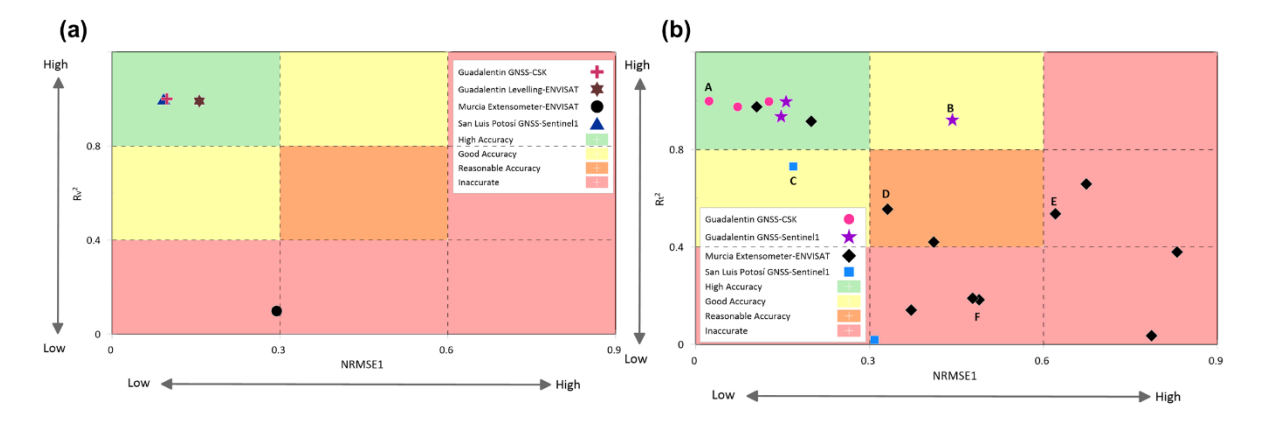


Figure 5.9 (a) Thresholds proposed for DInSAR validation using velocity values. (b) Accuracy thresholds proposed for DInSAR validation using displacement time series. Letters from A to F correspond to the scatterplots in Figure 5.10.

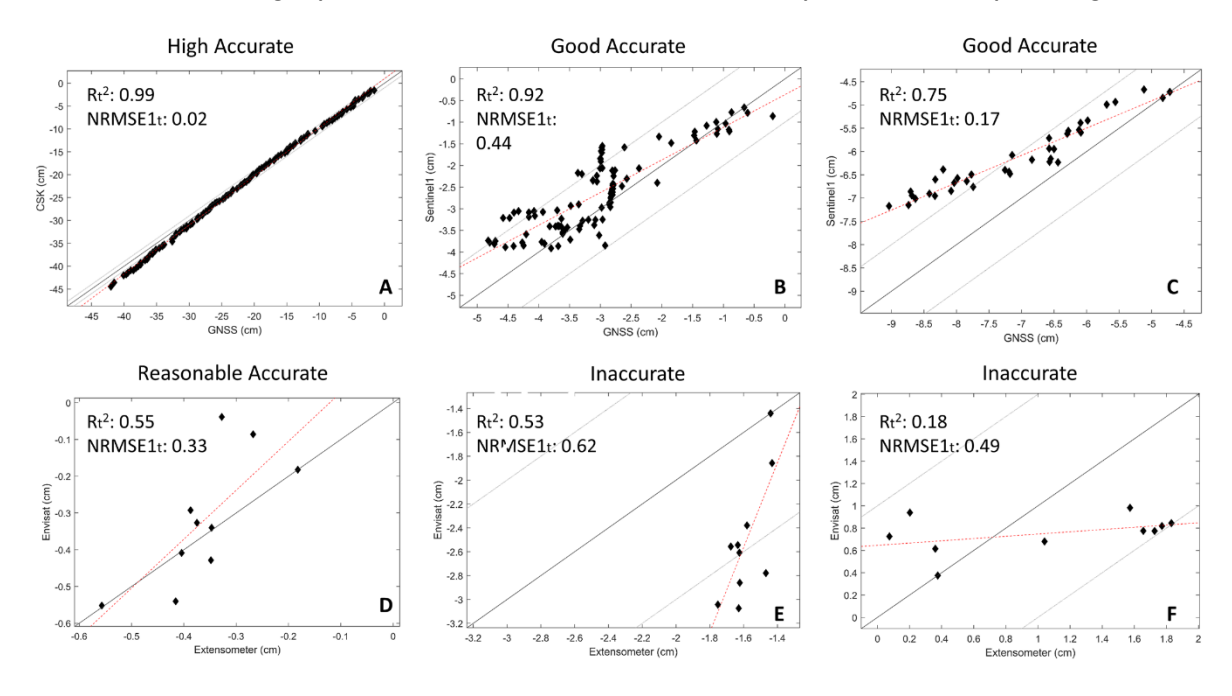


Figure 5.10 Correlation plot for time series validation due to accuracy categorization in Figure 5.9. (a) correlation between LORC station and CSK observations in Alto Guadalentín. (b) Correlation between LRCA station and Sentinel-1 observations in Alto Guadalentín. (c) Correlation between TNSL station and Sentinel-1 in San Luis Potosí. (d) Correlation between Ei-6 extensometer and ENVISAT observations in Murcia. (e) Correlation between Ei-1 extensometer and ENVISAT observations in Murcia. (f) Correlation between extensometer and ENVISAT observations in Murcia. Continued lines represent the 1:1 line, and dotted lines parallel to the 1:1 line represent the ± 1 cm error.

# 5.3. Flood modelling in Alto Guadalentín

The choice of 2D models over 1D models in the study area, Alto Guadalentín valley, is driven by the distinctive geomorphological features, particularly the prevalence of detrital aquifers in flat or valley locations. Unlike 1D models, inadequate for this valley due to the absence of well-defined channels and different water flow directions, 2D models is applied for horizontal components in the water velocity vector, which is crucial for accurately representing the valley's complex water flow patterns. Land subsidence resulting from groundwater overexploitation takes place gradually over extended

time scales, therefore impacting infrastructures economically. The developed study integrates both land subsidence and flood risk assessments, revealing how their convergence can modify or exacerbate flood risks. Hydraulic modelling of a 100-year return period flood event in 2016, incorporating DInSAR-derived ground surface lowering, demonstrates an important increase in maximum flood depth and inundation area compared to 1992 levels (Navarro-Hernández et al., 2023).

Spatial changes in flood propagation, evidenced by water velocity maps and cross-sectional profiles, indicate a change in inundation patterns toward the NW direction, marching with areas which experience the highest cumulative land subsidence. The modification in flooding dynamics caused by subsidence has repercussions on the capability of drainage of the valley, potentially leading to prolonged water retention periods and influencing the economic impacts associated with floods. The results integrate flood hazard maps with cadastral data and identify significant increments in risk for rural units. In the 2016 scenario, extreme and high flood risk categories exhibit a notable increase, impacting approximately 152 rural cadastral units. These findings are in agreement with recorded damage from the 2012 flood, emphasizing the importance of accurate hazard assessment for effective local authorities' management strategies and cost evaluations. The flood, velocity, and hazard risk maps contribute essential insights for local authorities in identifying high-risk flooding zones, formulating management strategies, evaluating hazards and monetary costs, and designing drainage plans for the highway. The study also highlights the importance of considering potential future movements of flood risks if the subsidence process persists (Navarro-Hernández et al., 2023).

# 5.4. Calculation of skeletal storage coefficient discussion

In this section, MATLAB results are validated by comparing them with digitized time series, employing coefficients calculated by the methodology developed by Riley (1969).

In the Southern Yangtse Delta, stress-strain curves demonstrate elasto-plastic behaviour, including both recoverable and non-recoverable deformations. The slopes calculated match closely with those determined by Zhang et al. (2007). Notably, the  $S_{ke}$  values from Zhang et al. (2007) fall within the range of maximum and minimum slopes identified by the developed application, indicating correspondence with an elastic loop. Discrepancies occur primarily due to Zhang et al. (2007) consider a single elastic loop, whereas the application considers all loops, enhancing accuracy and minimizing subjectivity. Figure 5.11 illustrates the comparison of  $S_{ke}$  values, emphasizing capability of the application to consider multiple elastic loops, improving accuracy. It is essential to note that the digitization process introduces some uncertainties in the exact original values used in this study.

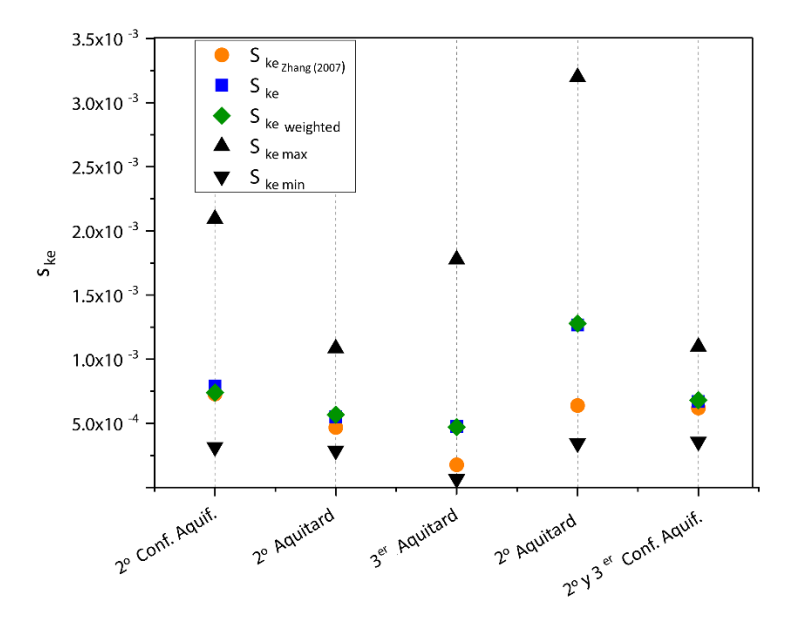


Figure 5.11. Comparison graphic of the different storage coefficients calculated in the Southern Yangtse Delta.

In the Beijing plain, only the initial confined aquifer layer displays elastic behaviour, while subsequent layers exhibit elasto-plastic characteristics. The application calculates elastic and inelastic skeletal storage coefficients, detailed in the supplementary material. For the shallow aquifer layer with elastic behaviour in the Beijing plain, the developed application produces similar storage coefficients ( $S_{ke}$ ) compared to  $S_{ke\_Zhang(2014)}$  2.250  $\times$  10<sup>-4</sup> and 2.72  $\times$  10<sup>-4</sup> respectively. Notably,  $S_{ke\_Zhang(2014)}$  derived from linear fitting shows discrepancies, it tends to have numerically smaller values than  $S_{ke}$  and  $S_{ke\_weighted}$  due to asymmetrical behaviour in elastic loops. The discrepancy is attributed to single-line approach for estimating elastic storage coefficients in Zhang et al. (2014), contrasting with our methodology, which considers multiple elastic segments for computing averages ( $S_{ke}$  and  $S_{ke\_weighted}$ ). In summary,  $S_{kv}$  coefficients are generally in agreement in magnitude with Zhang et al. (2014), with minor discrepancies attributed to the digitization process of input data.

In the North China Plain, specifically at Pinggezhuang and Tianzhu stations, the study identifies three curve behaviours: elastic, elastoplastic, and primarily plastic. Storage coefficients ( $S_{ke}$ ,  $S_{ke\_weighted}$  and  $S_{kv}$ ) closely are in agreement with Li et al. (2022) as shown in Table S17. After analyse the Pinggezhuang extensometer, the first curve exhibits elastic behaviour, with  $S_{ke}$  and  $S_{ke\_weighted}$  values near  $S_{ke\_Li(2022)}$  (6.864  $\times$  10<sup>-4</sup>), the value consistently falls within the range of mean  $S_{ke\_max}$  and  $S_{ke\_min}$  values for identified elastic segments. In the second layer of Pinggezhuang,  $S_{ke\_Li(2022)}$  values don't match precisely with maximum and minimum slopes but share similar numerical values. Despite the absence of elastic behaviour, the Tianzhu extensometer's layer was analysed, emphasizing the need for continuous supervision, especially when interpreting results. As deformation doesn't rebound with rising groundwater levels, only inelastic storage coefficients are presented (Figure 5.12).

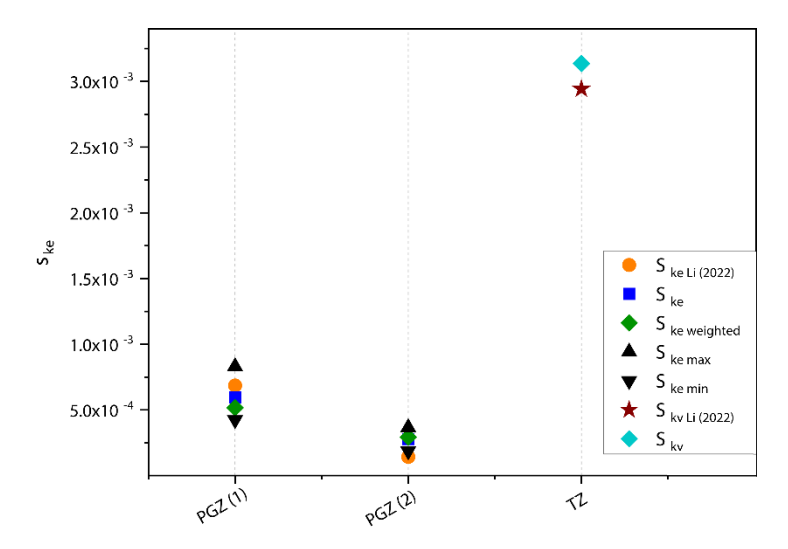


Figure 5.12 Comparison graphic of the different storage coefficients calculated in the North China Plain.

The study of the Madrid aquifer integrates DInSAR data and groundwater level measurements, producing stress-strain curves reflecting elastic behaviour across the multi-layer aquifer system. Unlike single-layer-focused research, this study assesses the aquifer system's general behaviour. Among 17 analysed curves, the average elastic storage coefficients align closely with Béjar-Pizarro et at. (2017), as it can be observed in the Figure 5.13.  $S_{ke\_B\acute{e}jar(2017)}$  consistently falls within the range defined by mean  $S_{ke\_min}$  and  $S_{ke\_max}$  values. Well-specific analysis reveals variable results with no clear pattern, demonstrating the application's adaptability. This study demonstrates the application's capability to analyse stress-strain curves effectively, providing consistent elastic storage coefficients within an order of magnitude of  $10^{-4}$  in all cases.

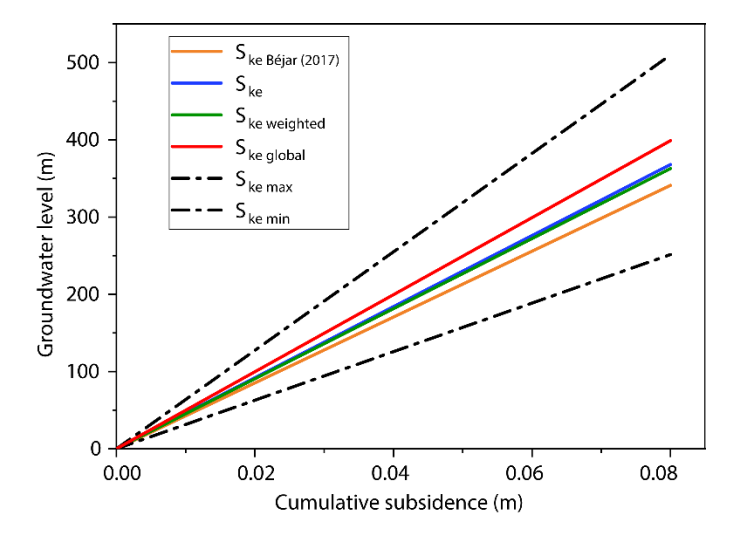


Figure 5.13 Comparison between the elastic storage coefficients calculated by the MATLAB application and the coefficients calculated by Béjar-Pizarro et al. (2017)

This study demonstrates the capability of the application to analyse stress-strain curves, validating its use in hydrogeological parameter estimation despite slight magnitude differences, presumably caused by data digitization. Emphasizing the significance of storage coefficients in assessing aquifer reserves and groundwater extraction potential, the application enhances and partially automates the estimation of the coefficients using data from DInSAR, currently obtained in land subsidence studies due to groundwater extraction. It includes broad applicability, enabling hydrogeological parameter estimation for entire aquifer systems or specific layers, essential for effective water resource management. With increasing water demand and potential land subsidence impacts on a vast

# DISCUSSION

population, stress-strain studies offer valuable insights for risk mitigation in urban and non-urban areas. The proposed methodology, supported by the application, could be a key in the aquifer storage coefficient determination, offering a time-efficient, cost-effective, and global approach. Future developments may extend applicability to terrains with visco-elastoplastic behaviour, providing a comprehensive understanding of aquifer dynamics. Additionally, the comparisons with traditional pumping tests could validate the methodology's real-world accuracy.

# 6. Conclusions

This last section aims to collect and summarize all conclusions from the five JCR contributions that constitutes the core of the present doctoral dissertation.

#### Research topic 1: DInSAR for monitoring land subsidence in overexploited aquifers.

The first part of this doctoral dissertation goes in details on the comprehensive analysis of land subsidence in two distinct regions, the San Luis Potosi Valley (SLPV) and the Alaşehir-Sarıgöl sub-basin (ASSB) of the Gediz River Basin (GRB). Applying advanced DInSAR techniques, such as CPT and P-SBAS processing to Sentinel-1 SAR images, the research provides valuable insights into the complex dynamics of subsidence.

The analysis of land subsidence in the San Luis Potosi Valley (SLPV) was conducted utilizing Coherent Pixel Technique (CPT) on a dataset comprising 112 Sentinel-1 images spanning from 2014 to 2019. The outcomes of this method delineated deformation patterns, particularly notable towards the centre-east region, within the municipality of Soledad de Graciano Sánchez, exhibiting rates predominantly ranging from –1.5 to –3.5 cm/year. In the northern central portion of the valley, subsidence rates were observed between –1.8 and –4.2 cm/year, with maximum Line-of-Sight (LOS) deformation estimated up to –15 cm/year in the metropolitan area. The validation of CPT results was achieved through comparison with five Global Navigation Satellite System (GNSS) measurements, yielding a high correlation coefficient of 0.986, thus affirming the efficacy of this advanced DInSAR technique in settlement detection and monitoring.

This study establishes a direct correlation between groundwater extraction activities in the San Luis Potosi valley and the drawdown of the aquifer systems piezometric level. The consequent reduction in pore pressure amplifies the effective stress applied by unconsolidated Quaternary sediments, leading to increased consolidation in areas with greater sediment accumulation. Consequently, ground surface settlements occur, conducting detrimental effects on urban infrastructures. The analysis underscores a positive relationship between the thickness of accumulated Quaternary sediments and the magnitude of settlements observed.

Moreover, in the SLPV, pronounced settlements associated with subsurface faults, caused by the tectonic configuration of the graben, have been identified. This localized phenomenon manifests abruptly, resulting in significant structural damage to buildings and infrastructure. Concurrently, generalized subsidence is attributed to groundwater extraction, leading to a slower subsidence process, particularly evident in the northern and north-eastern sectors of the SLPV. These regions correspond to areas characterized by thicker soft soils and more substantial piezometric declines. It is proposed that the SLPV exhibits a structurally governed subsidence pattern, influenced by buried tectonic faults impacting the underlying bedrock. Faults within the horst-graben structure have fostered basin formation with variable sediment thicknesses and compositions. Additionally, groundwater abstraction has induced fault-related subsidence, aligning with the distribution of buried structural faults.

In summary, the findings of this study underscore the persistent and irreversible land subsidence within the Quaternary aquifer system of the SLPV, attributed to excessive groundwater extraction. The significant influence of soft soil thickness and groundwater depletion on subsidence magnitude has been validated. Furthermore, a substantial structural control over subsidence patterns by faults affecting the bedrock has been elucidated. Future integration of insights garnered from this research

with numerical models will empower local water management authorities to anticipate land subsidence under diverse scenarios and devise corresponding mitigation strategies.

Similarly, In the Alaşehir-Sarıgöl sub-basin of the Gediz River Basin (GRB), Turkey, the application of Persistent Small Baseline Subset (P-SBAS) processing to Sentinel-1 Synthetic Aperture Radar (SAR) imagery spanning from 2016 to 2020 has unveiled significant subsidence phenomena, primarily concentrated in agricultural and urban sectors. Analysis of Interferometric Synthetic Aperture Radar (DInSAR) results has delineated a direct correlation between subsidence rates and the thickness of soft soil layers, where regions with greater soft soil thickness exhibit higher rates of subsidence. Furthermore, a discernible association has been observed between piezometric decline and subsidence occurrences, particularly in areas characterized by substantial groundwater depletion coinciding with thick soft soil layers.

Utilizing Independent Component Analysis (ICA) on DInSAR datasets has facilitated the identification of distinct spatiotemporal deformation trends embedded within the first two components. Component 1 (IC1) signifies long-term, quasi-linear deformation attributed to aquitard compaction, while Component 2 (IC2) represents long-term deformations accompanied by seasonal fluctuations attributed to water level variations. Collectively, these two principal components account for approximately 98 % of the variance in deformation patterns.

The outcomes underscore a heightened compaction of basin sediments resulting from extensive groundwater extraction and subsequent piezometric decline, predominantly influenced by the structural configuration of the graben. Notably, differential compaction rates along fault lines at the southern periphery of the basin have induced earth fissures, exemplified in Sarigöl city, contributing to significant structural damage in urban locales.

As a general conclusion of the topic research, the findings emphasize the human-intensified compaction of basin fillings in both study areas due to groundwater withdrawal, with structural implications. Decision-makers worldwide can take advantages of these feasible insights for effective groundwater management, land-use planning, and infrastructure resilience. The integration of these results into subsidence modelling enables authorities to predict and mitigate future scenarios, offering a crucial tool for sustainable resource management. This research holds global relevance, offering a template for regions facing similar challenges, and the integration of its outcomes into predictive models can significantly contribute to informed decision-making in the face of increasing groundwater depletion and land subsidence.

#### Research topic 2: Validation of DInSAR data applied in land subsidence areas.

In the second part of the thesis, this research topic presents a validation methodology customized for assessing land subsidence monitoring data derived from Differential Interferometric Synthetic Aperture Radar (DInSAR) observations, specifically applicable to regions experiencing land subsidence without significant horizontal deformations. The proposed methodology is encapsulated within a MATLAB-based tool named ValInSAR, designed to automate the validation process and establish a standardized protocol for evaluating DInSAR data reliability. Additionally, we introduce a criterion for accepting or rejecting DInSAR datasets for further analysis based on statistical metrics computed by the ValInSAR tool.

Through the utilization of an Excel template for data organization (accessible in the supplementary materials), ValInSAR facilitates rapid computation of velocity correlation graphs, time-series validation plots, and the generation of various statistical metrics pertaining to velocity and displacement time series. The efficacy of the code has been validated across three distinct land subsidence-affected

regions: the Alto Guadalentín aquifer, Murcia city, and the San Luis Potosí valley. Each site was monitored utilizing diverse Synthetic Aperture Radar (SAR) sensors (e.g., ENVISAT, CSK, and Sentinel-1), with corresponding in-situ datasets available to facilitate validation.

It is imperative to underscore that while the proposed validation methodology is well-suited for areas experiencing land subsidence without horizontal deformations, the open-source nature of the code allows for customization to accommodate varying user requirements, including the incorporation of horizontal displacement calculations for more comprehensive investigations. All DInSAR observations are vertically projected to enable comparison with in-situ techniques, particularly in regions where vertical deformation predominates.

During pre-processing, several key considerations emerge. Firstly, the selection of DInSAR points for validation is contingent upon the resolution of the SAR sensor, often necessitating the averaging of Persistent Scatterer (PS) values within a buffer area due to the absence of a PS directly coinciding with the in-situ point. Secondly, the analysis of standard deviation (SD) suggests that optimal buffer size lacks an absolute value and is contingent upon the spatial distribution of land subsidence. For instance, areas characterized by homogeneous subsidence patterns may warrant larger buffer sizes, while regions exhibiting structurally controlled subsidence favour smaller buffers to minimize dispersion around the in-situ point.

ValInSAR provides an array of statistical parameters, including Mean Difference (MD), standard deviation (SD) of error, correlation coefficient, and Root Mean Square Error (RMSE), pertinent for evaluating DInSAR performance across different sensors and in-situ techniques within the same study area. However, these metrics may not facilitate relative comparisons between DInSAR results obtained in disparate study areas due to their dependency on subsidence magnitude. To address this limitation, we propose a normalization scheme for RMSE parameters, yielding Normalized RMSE<sub>1</sub> (NRMSE<sub>1</sub>) and Normalized RMSE<sub>2</sub> (NRMSE<sub>2</sub>) metrics, which, when combined with the R-squared (R<sup>2</sup>) coefficient, enable a classification scheme to assess DInSAR accuracy. This systematic approach aids in discerning the reliability of DInSAR data across diverse study areas.

# • Research topic 3: Applications of DInSAR data

Finally, expanding on the application of DInSAR, in the first investigation, two-dimensional (2D) HEC-RAS hydraulic models were constructed for the Alto Guadalentín valley (SE Spain), representing terrain scenarios corresponding to 1992 and 2016. These scenarios were delineated based on cumulative land subsidence data acquired via Differential Interferometric Synthetic Aperture Radar (DInSAR) observations spanning the aforementioned timeframe. Noteworthy considerations included the incorporation of geomorphological characteristics to guide the modelling approach, leading to the preference for 2D models over one-dimensional (1D) counterparts. This preference arises from the prevalence of land subsidence phenomena in detrital aquifers within flat terrain, rendering 1D models unsuitable for ephemeral rivers and multidirectional water flow scenarios characteristic of the Alto Guadalentín valley during flash flood events.

The primary finding of this research underscores the imperative of accounting for subsidence dynamics when assessing flood risk in impacted regions. Importantly, the extent of this impact is contingent upon both the geological context of the study area and the magnitude of land subsidence. Exemplifying this interplay, the Alto Guadalentín valley exhibits cumulative land subsidence reaching up to 2.7 m over a 14-year period, thereby exemplifying the cumulative influence of subsidence in inland basins. Furthermore, the potential amplification of this impact is underscored if land subsidence commenced concurrently with the beginning of overexploitation dating back to the 1960s.

Land subsidence phenomena drive profound morphological alterations within basins, leading to the creation of new flood-prone areas while simultaneously affecting the characteristics of existing ones. Notably, alterations in maximum water depth and velocity during flood events are evident consequences. Specifically, this study reveals an expansion of the modelled flood-affected area with a 100-year return period, increasing by up to 2.04 km². Crucially, areas experiencing water depths exceeding 0.7 m witnessed a 15.21 % increase between 1992 and 2016. Spatial analyses further indicate a migration of inundation areas towards the northwest, aligning with the observed spatial distribution of land subsidence.

Moreover, velocity emerges as a hydraulic parameter significantly impacted by the land subsidence process. Ground surface depressions resulting from subsidence induce hydraulic bottlenecks, diminishing flow velocities, exacerbating drainage inefficiencies, and prolonging inundation durations in low-lying areas. In regions susceptible to land subsidence, both inland and coastal, diminished drainage capacities heighten the economic vulnerability associated with potential flood events. In light of these findings, flood risk management strategies necessitate a comprehensive consideration of subsidence-induced risks. Strategies and protective measures must be designed with foresight into the potential mobility of flooded areas resultant from gradual ground surface lowering. Hazard mapping derived from this study furnishes valuable insights for identifying flood-prone areas and facilitating the evaluation of prospective flooding scenarios in regions affected by land subsidence.

Finally, the findings underscore the utility of DInSAR techniques in monitoring complex natural-anthropogenic phenomena and their integration into flood hazard estimation frameworks. The synergistic utilization of DInSAR data alongside high-resolution Digital Surface Models (DSMs), land cover maps, and cadastral information enhances the accuracy and efficacy of flood hazard management initiatives.

The second study related to DInSAR data application, introduces a MATLAB-supported methodology for stress-strain curve analysis in aquifer systems affected by land subsidence. As underscored within this study, the deformation dynamics exhibited by aquifer systems in response to the temporal evolution of piezometric head, influenced by various anthropogenic and/or natural factors, represent a profoundly intricate phenomenon. Consequently, the analysis of stress-strain relationships necessitates rigorous scientific scrutiny and objectivity. However, the absence of an objective methodology characterized by universally applicable criteria, independent of subjective factors or analyst interpretations, served as the primary impetus for designing the methodology developed herewith and its subsequent integration into an open-source software framework.

The proposed methodology for investigating stress-strain curves, implemented through MATLAB software, accommodates the study of aquifers exhibiting both elastic and elastoplastic behaviour. Validation outcomes based on diverse case studies affirm the consistency of results, thereby rendering the methodology adaptable across various behaviour types. Anchored upon a protocol governed by discernible criteria and parameters, this methodology offers versatility for adaptation to a considerable amount of case studies and geotechnical contexts, while simultaneously expediting processes, automating tasks, and mitigating subjectivity in outcomes. It merits acknowledgment that proficient utilization of the application and judicious parameter control necessitate antecedent comprehension of subsidence magnitude pertinent to the specific case study under examination.

This methodological framework facilitates the automated derivation of aquifer storage coefficients from stress-strain curves, thereby supporting the quick and efficacious implementation of groundwater resource management measures. Furthermore, insights derived from the utilization of this methodology and its implementation in computational form prove invaluable for groundwater resource managers, empowering them to enact measures conducive to enhanced groundwater resource management in a manner characterized by swiftness, effectiveness, and sustainability in relation to water resource factors. Moreover, parameters derived from stress-strain curves engender the development of hydrogeological models conducive to informed and adaptive management practices.

As a general conclusion, all these research topics findings highlight the significance of validating DInSAR data, incorporating subsidence in flood risk assessments, and employing a standardized methodology for stress-strain curve analysis. The published results of the proposed MATLAB codes, ValInSAR, hydraulic models, and stress-strain curve methodology collectively contribute to advancing the understanding and management of land subsidence in diverse hydrogeological settings.

#### • Final Conclusions and Contributions of the Doctoral Thesis

As highlighted in the five JCR articles constituting the core of this doctoral thesis, the application of advanced DInSAR techniques and spatial analysis provides an efficient and effective platform for monitoring, analysing, and identifying predisposing factors of land subsidence in affected regions. Specifically, the integration of DInSAR data, LiDAR-derived terrain surface models, and 2D hydraulic models enhances understanding of underlying mechanisms and enables a more precise assessment of associated risks.

The findings of this research carry significant implications for the management and mitigation of land subsidence in affected regions. The identification and characterization of predisposing factors contributing to land subsidence establish a solid foundation for the development of effective management and mitigation strategies. In particular, pinpointing areas at high risk of land subsidence allows for targeted implementation of preventive and corrective measures to reduce associated risks and alleviate negative impacts on infrastructure, the environment, and society.

Furthermore, the results of this research contribute to advancing knowledge in the field of land subsidence and offer valuable insights for future research in related areas. Specifically, the application of advanced DInSAR techniques and spatial analysis provides new perspectives on the underlying mechanisms of land subsidence and facilitates a better understanding of the predisposing factors driving this phenomenon. Additionally, the integration of DInSAR data, 2D hydraulic models, and algorithms for DInSAR validation and coefficient automation offers an efficient and effective methodology for identifying and characterizing predisposing factors of land subsidence in affected regions.

In conclusion, this doctoral thesis makes a significant contribution to the field of land subsidence and provides a solid foundation for future research in related areas. The findings of this research carry important implications for the management and mitigation of land subsidence in affected regions, while also offering valuable insights for the development of effective management and mitigation strategies. Moreover, the application of advanced DInSAR techniques and spatial analysis provides new perspectives on the underlying mechanisms of land subsidence, leading to a better understanding of the predisposing factors driving this phenomenon.

# Conclusiones

Esta última sección tiene como objetivo recopilar y resumir todas las conclusiones de las cinco contribuciones JCR que constituyen el núcleo de la presente tesis doctoral.

• Tema de investigación 1: DInSAR para el monitoreo de la subsidencia del suelo en acuíferos sobreexplotados.

La primera parte de esta tesis doctoral detalla el análisis exhaustivo de la subsidencia del suelo en dos regiones distintas, el Valle de San Luis Potosí (SLPV) y la subcuenca Alaşehir-Sarıgöl (ASSB) de la Cuenca del Río Gediz (GRB). Aplicando técnicas avanzadas de DInSAR, como el procesamiento CPT y P-SBAS a imágenes SAR Sentinel-1, la investigación proporciona valiosas perspectivas sobre la dinámica compleja de la subsidencia.

El análisis de la subsidencia del suelo en el Valle de San Luis Potosí (SLPV) se realizó utilizando la Técnica de Píxel Coherente (CPT) en un conjunto de datos que comprende 112 imágenes Sentinel-1 desde 2014 hasta 2019. Los resultados de este método delimitaron patrones de deformación, especialmente notables hacia la región centro-este, dentro del municipio de Soledad de Graciano Sánchez, con tasas predominantemente en el rango de –1.5 a –3.5 cm/año. En la parte central norte del valle, se observaron tasas de subsidencia entre –1.8 y –4.2 cm/año, con una deformación máxima de línea de visión del satélite (LOS) estimada de hasta –15 cm/año en el área metropolitana. La validación de los resultados de CPT se logró mediante la comparación con cinco mediciones del Sistema Global de Navegación por Satélite (GNSS), lo que arrojó un alto coeficiente de correlación de 0.986, confirmando así la eficacia de esta técnica avanzada de DInSAR en la detección y monitoreo de asentamientos.

Este estudio establece una correlación directa entre las actividades de extracción de agua subterránea en el valle de San Luis Potosí y la disminución del nivel piezométrico de los sistemas acuíferos. La reducción consiguiente de la presión de poro amplifica el estrés efectivo aplicado por los sedimentos cuaternarios no consolidados, lo que lleva a un aumento de la consolidación en áreas con mayor acumulación de sedimentos. Como resultado, se producen asentamientos en la superficie del suelo, con efectos perjudiciales en las infraestructuras urbanas. El análisis subraya una relación positiva entre el espesor de los sedimentos cuaternarios acumulados y la magnitud de los asentamientos observados.

Además, en el valle de San Luis Potosí, se han identificado asentamientos pronunciados asociados con fallas subsuperficiales, causadas por la configuración tectónica del graben. Este fenómeno localizado se manifiesta abruptamente, provocando daños estructurales significativos en edificios e infraestructuras. Simultáneamente, se atribuye la subsidencia generalizada a la extracción de agua subterránea, lo que conduce a un proceso de subsidencia más lento, especialmente evidente en los sectores norte y noreste del valle de San Luis Potosí. Estas regiones corresponden a áreas caracterizadas por suelos blandos más gruesos y mayores declinaciones piezométricas. Se propone que el valle de San Luis Potosí exhibe un patrón de subsidencia gobernado estructuralmente, influenciado por fallas tectónicas enterradas que impactan el lecho rocoso subyacente. Las fallas dentro de la estructura de horst-graben han favorecido la formación de cuencas con espesores y composiciones de sedimentos variables. Además, la extracción de agua subterránea ha inducido la subsidencia relacionada con fallas, alineándose con la distribución de fallas estructurales enterradas.

En resumen, los resultados de este estudio subrayan la persistente e irreversible subsidencia del suelo dentro del sistema acuífero cuaternario del valle de San Luis Potosí, atribuida a la extracción excesiva

de agua subterránea. Se ha validado la influencia significativa del espesor de los suelos blandos y la disminución del agua subterránea en la magnitud de la subsidencia. Además, se ha elucidado un control estructural sustancial sobre los patrones de subsidencia por fallas que afectan el lecho rocoso. Una futura integración de conocimientos derivados de esta investigación con modelos numéricos capacitará a las autoridades locales de gestión del agua para anticipar la subsidencia del suelo bajo diversos escenarios y diseñar estrategias de mitigación correspondientes.

Del mismo modo, en la subcuenca Alaşehir-Sarıgöl de la Cuenca del Río Gediz (GRB), Turquía, la aplicación del procesamiento P-SBAS a imágenes SAR Sentinel-1 que abarcan desde 2016 hasta 2020 ha revelado fenómenos significativos de subsidencia, principalmente concentrados en sectores agrícolas y urbanos. El análisis de los resultados de Interferometría SAR (DInSAR) ha delimitado una correlación directa entre las tasas de subsidencia y el espesor de las capas de suelo blando, donde las regiones con un mayor espesor de suelo blando exhiben tasas más altas de subsidencia. Además, se ha observado una asociación discernible entre la disminución piezométrica y los eventos de subsidencia, especialmente en áreas caracterizadas por una disminución sustancial del agua subterránea que coincide con capas gruesas de suelo blando.

La utilización del Análisis de Componentes Independientes (ICA) en conjuntos de datos de DInSAR ha facilitado la identificación de tendencias distintas de deformación espacio-temporal incrustadas dentro de los dos primeros componentes. El Componente 1 (IC1) significa deformación a largo plazo y cuasi lineal atribuida a la compactación del acuitardo, mientras que el Componente 2 (IC2) representa deformaciones a largo plazo acompañadas de fluctuaciones estacionales atribuidas a variaciones en el nivel del agua. En conjunto, estos dos componentes principales representan aproximadamente el 98 % de la varianza en los patrones de deformación.

Los resultados subrayan una mayor compactación de los sedimentos de la cuenca como resultado de la extensa extracción de agua subterránea y la subsiguiente disminución piezométrica, predominantemente influenciada por la configuración estructural del graben. Específicamente, las tasas de compactación diferencial a lo largo de las líneas de falla en el perímetro sur de la cuenca han inducido fisuras en la tierra, ejemplificadas en la ciudad de Sarigöl, contribuyendo a daños estructurales significativos en áreas urbanas.

Como conclusión general de la investigación del tema, los resultados enfatizan la compactación intensificada de los rellenos de la cuenca en ambas áreas de estudio debido a la extracción de agua subterránea inducida por las actividades de naturaleza antrópica, con implicaciones estructurales. Los encargados de la toma de decisiones en todo el mundo pueden aprovechar estos conocimientos factibles para una gestión efectiva del agua subterránea, la planificación del uso del suelo y la resiliencia de la infraestructura. La integración de estos resultados en la modelización de la subsidencia permite a las autoridades predecir y mitigar escenarios futuros, ofreciendo una herramienta crucial para la gestión sostenible de los recursos. Esta investigación tiene relevancia global, ofreciendo un molde para regiones que enfrentan desafíos similares, y la integración de sus resultados en modelos predictivos puede contribuir significativamente a la toma de decisiones informadas frente a la creciente disminución del agua subterránea y la subsidencia del suelo.

### • Tema de investigación 2: Validación de datos DInSAR aplicados en áreas de subsidencia del suelo.

En la segunda parte de la tesis, este tema de investigación presenta una metodología de validación personalizada para evaluar datos de monitoreo de subsidencia del suelo derivados de observaciones diferenciales de radar de apertura sintética (DInSAR), específicamente aplicable a regiones que experimentan subsidencia del suelo sin deformaciones horizontales significativas. La metodología

propuesta está embebida dentro de una herramienta basada en MATLAB llamada ValInSAR, diseñada para automatizar el proceso de validación y establecer un protocolo estandarizado para evaluar la confiabilidad de los datos de DInSAR. Además, presentamos un criterio para aceptar o rechazar conjuntos de datos de DInSAR para un análisis adicional basado en métricas estadísticas calculadas por la herramienta ValInSAR.

A través de la utilización de una plantilla de Excel para la organización de datos (accesible en los materiales suplementarios), ValInSAR facilita la rápida computación de gráficos de correlación de velocidad, gráficos de validación de series temporales y la generación de diversas métricas estadísticas relacionadas con series temporales de velocidad y desplazamiento. La eficacia del código ha sido validada en tres regiones distintas afectadas por la subsidencia del suelo: el acuífero Alto Guadalentín, la ciudad de Murcia y el valle de San Luis Potosí. Cada sitio fue monitoreado utilizando diversos sensores de Radar de Apertura Sintética (SAR) (por ejemplo, ENVISAT, CSK y Sentinel-1), con conjuntos de datos correspondientes disponibles in situ para facilitar la validación.

Es importante destacar que, si bien la metodología de validación propuesta es adecuada para áreas que experimentan subsidencia del suelo sin deformaciones horizontales, la naturaleza de código abierto del código permite la personalización para adaptarse a diferentes requisitos de los usuarios, incluida la incorporación de cálculos de desplazamiento horizontal para investigaciones más completas. Todas las observaciones de DInSAR se proyectan verticalmente para permitir la comparación con técnicas in situ, particularmente en regiones donde predomina la deformación vertical.

Durante el preprocesamiento, surgen varias consideraciones clave. En primer lugar, la selección de puntos de DInSAR para validación depende de la resolución del sensor SAR, lo que a menudo requiere el promedio de valores de Puntos Persistentes (PS) dentro de un área de amortiguación debido a la ausencia de un PS que coincida directamente con el punto in situ. En segundo lugar, el análisis de la desviación estándar (SD) sugiere que el tamaño óptimo del búfer carece de un valor absoluto y depende de la distribución espacial de la subsidencia del suelo. Por ejemplo, las áreas caracterizadas por patrones de subsidencia homogéneos pueden requerir tamaños de búfer más grandes, mientras que las regiones que exhiben subsidencia controlada estructuralmente favorecen búferes más pequeños para minimizar la dispersión alrededor del punto in situ.

ValInSAR proporciona una variedad de parámetros estadísticos, incluyendo Diferencia Media (MD), desviación estándar (SD) del error, coeficiente de correlación y Error Cuadrático Medio (RMSE), pertinentes para evaluar el rendimiento de DInSAR a través de diferentes sensores y técnicas in situ dentro de la misma área de estudio. Sin embargo, estas métricas pueden no facilitar comparaciones relativas entre resultados de DInSAR obtenidos en áreas de estudio dispares debido a su dependencia de la magnitud de la subsidencia. Para abordar esta limitación, proponemos un esquema de normalización para los parámetros RMSE, que produce las métricas de Error Cuadrático Medio Normalizado (NRMSE<sub>1</sub>) y Error Cuadrático Medio Normalizado 2 (NRMSE<sub>2</sub>), que, combinadas con el coeficiente R-cuadrado (R²), permiten un esquema de clasificación para evaluar la precisión de DInSAR. Este enfoque sistemático ayuda a discernir la confiabilidad de los datos de DInSAR en diversas áreas de estudio.

### • Tema de investigación 3: Aplicaciones de datos DInSAR

Finalmente, ampliando sobre la aplicación de DInSAR, en la primera investigación, se construyeron modelos hidráulicos HEC-RAS bidimensionales (2D) para el valle de Alto Guadalentín (SE de España), representando escenarios topográficos correspondientes a 1992 y 2016. Estos escenarios se

delinearon en base a datos acumulados de subsidencia del suelo adquiridos mediante observaciones DInSAR que abarcaron el período mencionado. Consideraciones destacables incluyeron la incorporación de características geomorfológicas para guiar el enfoque de modelado, lo que llevó a la preferencia por los modelos 2D sobre los unidimensionales (1D). Esta preferencia surge de la prevalencia de fenómenos de subsidencia del suelo en acuíferos detríticos dentro de terrenos planos, lo que hace que los modelos 1D sean inadecuados para ríos efímeros y escenarios de flujo de agua multidireccional característicos del valle de Alto Guadalentín durante eventos de inundación repentina.

El hallazgo principal de esta investigación subraya la importancia de tener en cuenta la dinámica de la subsidencia al evaluar el riesgo de inundación en regiones afectadas. Es importante destacar que la magnitud de este impacto depende tanto del contexto geológico del área de estudio como de la magnitud de la subsidencia del suelo. Ejemplificando esta interacción, el valle de Alto Guadalentín muestra una subsidencia del suelo acumulada de hasta 2.7 m en un período de 14 años, ejemplificando así la influencia acumulativa de la subsidencia en las cuencas interiores. Además, se destaca la posible amplificación de este impacto si la subsidencia del suelo comenzó simultáneamente con el inicio de la sobreexplotación desde la década de 1960.

Los fenómenos de subsidencia del suelo impulsan alteraciones morfológicas profundas dentro de las cuencas, lo que conduce a la creación de nuevas áreas propensas a inundaciones y afecta simultáneamente las características de las existentes. Es importante destacar que las alteraciones en la profundidad y la velocidad máxima del agua durante los eventos de inundación son consecuencias evidentes. Específicamente, este estudio revela una expansión del área afectada por inundaciones modeladas con un período de retorno de 100 años, que aumenta hasta 2.04 km². Es crucial destacar que las áreas que experimentan profundidades de agua superiores a 0.7 m presenciaron un aumento del 15.21 % entre 1992 y 2016. Los análisis espaciales indican además una migración de las áreas de inundación hacia el noroeste, alineándose con la distribución espacial observada de la subsidencia del suelo.

Además, la velocidad emerge como un parámetro hidráulico significativamente impactado por el proceso de subsidencia del suelo. Las depresiones en la superficie del suelo resultantes de la subsidencia inducen cuellos de botella hidráulicos, disminuyendo las velocidades de flujo, exacerbando las ineficiencias de drenaje y prolongando las duraciones de inundación en áreas bajas. En regiones susceptibles a la subsidencia del suelo, tanto interiores como costeras, las capacidades de drenaje disminuidas aumentan la vulnerabilidad económica asociada con posibles eventos de inundación. A la luz de estos hallazgos, las estrategias de gestión del riesgo de inundación requieren una consideración integral de los riesgos inducidos por la subsidencia. Las estrategias y medidas protectoras deben diseñarse teniendo en cuenta la movilidad potencial de las áreas inundadas resultante de la disminución gradual de la superficie del suelo. Los mapas de riesgos derivado de este estudio proporcionan información valiosa para identificar áreas propensas a inundaciones y facilitar la evaluación de escenarios de inundación prospectivos en regiones afectadas por la subsidencia del suelo.

Finalmente, los hallazgos subrayan la utilidad de las técnicas DInSAR en la monitorización de fenómenos naturales-antrópicos complejos y su integración en marcos de estimación del riesgo de inundación. La utilización sinérgica de datos DInSAR junto con Modelos Digitales de Superficie (DSM) de alta resolución, mapas de cobertura terrestre e información catastral mejora la precisión y la eficacia de las iniciativas de gestión del riesgo de inundación.

El segundo estudio relacionado con la aplicación de datos DInSAR, introduce una metodología desarrollada para MATLAB cuyo objetivo es el análisis de curvas de esfuerzo-deformación en sistemas acuíferos afectados por la subsidencia del suelo. Como se destaca en este estudio, la dinámica de deformación exhibida por los sistemas acuíferos en respuesta a la evolución temporal de la carga piezométrica, influenciada por varios factores antropogénicos y/o naturales, representa un fenómeno profundamente intrincado. En consecuencia, el análisis de las relaciones esfuerzo-deformación requiere un escrutinio científico riguroso y objetividad. Sin embargo, la ausencia de una metodología objetiva caracterizada por criterios universalmente aplicables, independientes de factores subjetivos o interpretaciones del analista, sirvió como principal impulso para diseñar la metodología desarrollada aquí y su posterior integración en un marco de software de código abierto.

La metodología propuesta para investigar las curvas esfuerzo-deformación, implementada a través del software MATLAB, se aplica al estudio de acuíferos que exhiben tanto comportamiento elástico como elastoplástico. Los resultados de validación basados en diversos estudios de caso afirman la consistencia de los resultados, lo que hace que la metodología sea adaptable a través de varios tipos de comportamiento. Anclada en un protocolo gobernado por criterios y parámetros discernibles, esta metodología ofrece versatilidad para la adaptación a una cantidad considerable de estudios de caso y contextos geotécnicos, al tiempo que agiliza procesos, automatiza tareas y mitiga la subjetividad en los resultados. Es importante reconocer que la utilización competente de la aplicación y el control adecuado de los parámetros requieren una comprensión previa de la magnitud de la subsidencia pertinente al estudio de caso específico bajo investigación.

Este marco metodológico facilita la obtención automatizada de coeficientes de almacenamiento de acuíferos a partir de curvas esfuerzo-deformación, lo que respalda la implementación rápida y eficaz de medidas de gestión de recursos hídricos subterráneos. Además, los conocimientos derivados del uso de esta metodología y su implementación en forma computacional resultan invaluables para los gestores de recursos hídricos subterráneos, capacitándolos para promulgar medidas propicias para una gestión mejorada de los recursos hídricos subterráneos de manera caracterizada por la rapidez, la eficacia y la sostenibilidad en relación con los factores de tiempo y costo.

### • Conclusiones finales y contribuciones de la tesis doctoral.

Como se destaca en los cinco artículos JCR que constituyen el núcleo de la presente tesis doctoral, la aplicación de técnicas avanzadas de DInSAR y análisis espaciales ofrece una plataforma eficiente y efectiva para el monitoreo, análisis e identificación de factores predisponentes de la subsidencia del suelo en regiones afectadas. Específicamente, la integración de datos DInSAR, modelos de superficie del terreno obtenidos con LiDAR y modelos hidráulicos en 2D permite una mejor comprensión de los mecanismos subyacentes y una evaluación más precisa del riesgo asociado.

Los resultados de esta investigación tienen importantes implicaciones para la gestión y mitigación de la subsidencia del suelo en regiones afectadas. La identificación y caracterización de factores predisponentes que desencadenan la subsidencia del suelo proporciona una base sólida para el desarrollo de estrategias de gestión y mitigación efectivas. Específicamente, la identificación de áreas con un alto riesgo de subsidencia del suelo permite la implementación de medidas preventivas y correctivas dirigidas para reducir el riesgo asociado y mitigar los impactos negativos en la infraestructura, el medio ambiente y la sociedad.

Además, los resultados de esta investigación contribuyen al avance del conocimiento en el campo de la subsidencia del suelo y proporcionan información valiosa para futuras investigaciones en áreas relacionadas. Específicamente, la aplicación de técnicas avanzadas de DInSAR y análisis espaciales

### **CONCLUSIONS**

ofrece nuevas perspectivas sobre los mecanismos subyacentes de la subsidencia del suelo y permite una mejor comprensión de los factores predisponentes que desencadenan este fenómeno. Además, la integración de datos DInSAR, modelos hidráulicos 2D y algoritmos para validación de DInSAR y automatización de coeficientes para la caracterización de acuíferos ofrece una metodología eficiente y efectiva para la identificación y caracterización de factores predisponentes de la subsidencia del suelo en regiones afectadas.

En conclusión, la presente tesis doctoral proporciona una contribución significativa al campo de la subsidencia del suelo y ofrece una base sólida para futuras investigaciones en áreas relacionadas. Los resultados de esta investigación tienen importantes implicaciones para la gestión y mitigación de la subsidencia del suelo en regiones afectadas, y proporcionan información valiosa para el desarrollo de estrategias de gestión y mitigación efectivas. Además, la aplicación de técnicas avanzadas de DInSAR y análisis espaciales ofrece nuevas perspectivas sobre los mecanismos subyacentes de la subsidencia del suelo y permite una mejor comprensión de los factores predisponentes que desencadenan este fenómeno.

### 7. Future research

The present doctoral thesis has revealed various lines of research that will be explored in the coming years, thus marking the beginning of a new stage of inquiry and discovery. The newly identified lines are:

- a. Application of machine learning in DInSAR studies for the prediction of temporal series, utilizing diverse information derived from different sources in addition to the series obtained through DInSAR. This includes the integration of other temporal series such as precipitation, piezometry, etc.
- b. Development of improvements in the ValInSAR code so that it is not limited to validating data only corresponding to areas affected by subsidence but can also validate temporal series related to studies of other phenomena such as landslides, earthquakes, volcanoes, etc.
- c. Process new areas affected by subsidence since this phenomenon is on the rise at present, and more cities around the world are experiencing sinking issues due to the increasing demand for groundwater globally.
- d. Conduct more detailed studies on damages and effects on structures resulting from subsidence, as well as on the flooding associated with this phenomenon.
- e. Apply other methods for separating mixed signals to attempt to discriminate the contribution of tectonic effects from the subsidence caused by the compaction of soft soils due to groundwater extraction.
- f. Develop a holistic analysis frame of subsidence phenomenon and its socio-economical implications that include economic impacts of reducing groundwater exploitation, social impacts of potential restructuration of high-water demand agents, and finally economical cost of the flood risk increase derived from the changes in the flooding trends as a consequence of land subsidence.

### 8. References

- Amighpey, M., & Arabi, S. (2016). Studying land subsidence in Yazd province, Iran, by integration of InSAR and levelling measurements. *Remote Sensing Applications: Society and Environment*, 4, 1–8. https://doi.org/10.1016/j.rsase.2016.04.001
- Aobpaet, A., Cuenca, M. C., Hooper, A., & Trisirisatayawong, I. (2010). *Land subsidence evaluation usin InSAR time series analysis in Bankok metropolitan area.* 2009(March).
- Awange, J. L. (2018). GNSS Environmental Sensing: Revolutionizing Environmental Monitoring. In *Environmental Science and Engineering (Subseries: Environmental Science)* (Issue 9783540882558). https://doi.org/10.1007/978-3-540-88256-5\_2
- Béjar-Pizarro, M., Ezquerro, P., Herrera, G., Tomás, R., Guardiola-Albert, C., Ruiz Hernández, J. M., Fernández Merodo, J. A., Marchamalo, M., & Martínez, R. (2017). Mapping groundwater level and aquifer storage variations from InSAR measurements in the Madrid aquifer, Central Spain. *Journal of Hydrology*, *547*, 678–689. https://doi.org/10.1016/j.jhydrol.2017.02.011
- Béjar-Pizarro, M., Notti, D., Mateos, R. M., Ezquerro, P., Centolanza, G., Herrera, G., Bru, G., Sanabria, M., Solari, L., Duro, J., & Fernández, J. (2017). Mapping vulnerable urban areas affected by slow-moving landslides using Sentinel-1InSAR data. *Remote Sensing*, *9*(9), 1–17. https://doi.org/10.3390/rs9090876
- Berardino, P., Fornaro, G., Lanari, R., & Sansosti, E. (2002). A new algorithm for surface deformation monitoring based on small baseline differential SAR interferograms. *IEEE Transactions on Geoscience and Remote Sensing*, 40(11), 2375–2383. https://doi.org/10.1109/TGRS.2002.803792
- Blanco-Sánchez, P. (2009). SAR Differential Interferometry for deformation monitoring under a multi-frequency approach. *Universidad Politécnica de Cataluña, November*, 216.
- Blanco-Sánchez, P., Mallorquí, J., Duque, S., & Monells, D. (2008). The Coherent Pixels Technique (CPT): An Advanced DInSAR Technique for Nonlinear Deformation Monitoring. *Pure and Applied Geophysycs*, 165, 1167–1193. https://doi.org/10.1007/s00024-008-0352-6
- Bolger, B. L., Park, Y., Unger, A. J. A., & Sudicky, E. A. (2011). Simulating the pre-development hydrologic conditions in the San Joaquin. *Journal of Hydrology*, *411*(3–4), 322–330. https://doi.org/10.1016/j.jhydrol.2011.10.013
- Bonì, R., Herrera, G., Meisina, C., Notti, D., Béjar-Pizarro, M., Zucca, F., González, P. J., Palano, M., Tomás, R., Fernández, J., Fernández-Merodo, J. A., Mulas, J., Aragón, R., Guardiola-Albert, C., & Mora, O. (2015). Twenty-year advanced DInSAR analysis of severe land subsidence: The Alto Guadalentín Basin (Spain) case study. *Engineering Geology*, *198*, 40–52. https://doi.org/10.1016/j.enggeo.2015.08.014
- Bru, G., Ezquerro, P., Guardiola-Albert, C., Béjar-Pizarro, M., Herrera, G., Tomás, R., Navarro-Hernández, M. I., López-Sanchez, J. M., Ören, A. H., Çaylak, B., Elçi, A., Shatanawi, K., Mohammad, A. H., Abu Hajar, H. A., Bonì, R., & Meisina, C. (2021). *Land Subsidence Analysis Caused By Aquifer Overexploitation Using Gep Tools: a-Dinsar on the Cloud*. 7–8. https://doi.org/10.4995/cigeo2021.2021.12722

- Bru, G., Herrera, G., Tomás, R., Duro, J., de la Vega, R., & Mulas, J. (2013). Control of deformation of buildings affected by subsidence using persistent scatterer interferometry. *Structure and Infrastructure Engineering*, *9*(2), 188–200. https://doi.org/10.1080/15732479.2010.519710
- Burbey, T. J. (2001). Stress-strain analyses for aquifer-system characterization. *Ground Water*, *39*(1), 128–136. https://doi.org/10.1111/j.1745-6584.2001.tb00358.x
- Castellazzi, P., Arroyo-Domínguez, N., Martel, R., Calderhead, A., Normand, J., Gárfias, J., & Rivera, A. (2016). Land subsidence in major cities of Central Mexico: Interpreting InSAR-derived land subsidence mapping with hydrogeological data. *International Journal of Applied Earth Observations and Geoinformation*, 47, 102–111. https://doi.org/10.1016/j.jag.2015.12.002
- Cerri, M. (2017). Flood simulation using HEC-RAS model calibrated with remotely sensed water mask: a case study of Mulde River, Germany [Technical University of Munich].

  https://www.researchgate.net/profile/Marco\_Cerri/publication/320977695\_Flood\_simulation
  \_using\_HECRAS\_model\_calibrated\_with\_remotely\_sensed\_water\_mask\_a\_case\_study\_of\_Mulde\_River\_G
  ermany/links/5f3f9fa5a6fdcccc43dfbeba/Flood-simulation-using-HEC-RAS-model-
- Chaussard, E., Bürgmann, R., Shirzaei, M., Fielding, E. J., & Baker, B. (2014). Predictability of hydraulic head changes and characterization of aquifer-system and fault properties from InSAR-derived ground deformation. *AGU: Journal of Geophysical Research, Solid Earth, 119*, 3076–3095. https://doi.org/10.1002/2014JB011266.Received
- CHS. (2014). Sistema Nacional de Cartografía de Zonas Inundables: Demarcacion Hidrográfica del Segura, Mapas de Peligrosidad y Riesgo de Inundación.
- CHS. (2020). Revisión y Actualización de los Mapas de Peligrosidad y Riesgo por Inundación de las Áreas con Riesgo Potencial Significativo de Inundación 2º Ciclo.
- Cigna, F., Tapete, D., Garduño-Monroy, V. H., Muñiz-Jauregui, J. A., García-Hernández, O. H., & Jiménez-Haro, A. (2019). Wide-area InSAR survey of surface deformation in urban areas and geothermal fields in the eastern Trans-Mexican Volcanic Belt, Mexico. *Remote Sensing*, *11*(20), 1–33. https://doi.org/10.3390/rs11202341
- Cohen-Waeber, J., Bürgmann, R., Chaussard, E., Giannico, C., & Ferretti, A. (2018). Spatiotemporal Patterns of Precipitation-Modulated Landslide Deformation From Independent Component Analysis of InSAR Time Series. *Geophysical Research Letters*, 45(4), 1878–1887. https://doi.org/10.1002/2017GL075950
- CONAGUA. (2015). Actualización de la disponibilidad media anual de agua en el acuífero San Luis Potosí (2411) Estado de San Luis Potosí.
- Conway, B. D. (2015). Land subsidence and earth fissures in south-central and southern Arizona, USA. *Hydrogeology Journal*, *24*(3), 649–655. https://doi.org/10.1007/s10040-015-1329-z
- Copernicus. (2018). *Corine land cover*. https://land.copernicus.eu/pan-european/corine-land-cover/clc2018
- Darini, G. (2007). Land subsidence due to groundwater withdrawal: the case of Bologna.
- De Luca, C., Bonano, M., Casu, F., Manunta, M., Manzo, M., Onorato, G., Zinno, I., & Lanari, R. (2018). The parallel SBAS-DINSAR processing chain for the generation of national scale sentinel-

- 1 deformation time-series. *Procedia Computer Science*, *138*, 326–331. https://doi.org/10.1016/j.procs.2018.10.046
- Declercq, P., Gerard, P., Pirard, E., Perissin, D., Walstra, J., & Devleeschouwer, X. (2017). Subsidence related to groundwater pumping for breweries in Merchtem area (Belgium), highlighted by Persistent Scaterrer Interferometry. *Int J Appl Earth Obs Geoinformation*, *63*(July), 178–185. https://doi.org/10.1016/j.jag.2017.07.012
- Duque, S., Mallorqui, J. J., Blanco, P., & Monells, D. (2007). Application of the Coherent Pixels Technique ( CPT ) to urban monitoring. *IEEE*.
- Duru, B., Yargıcı, A. F., Topçu, C., Çakmak, Ö., Gültekin, O. Ş., Bulut, O. F., Dilek, F. B., & Yetiş, Ü. (2018). Management of Groundwater Quality and Quantity: Gediz River Basin Pilot Study. *Turkish Journal of Water Science and Management*, *2*(2), 84–109. https://doi.org/10.31807/tjwsm.423465
- Ebmeier, S. K. (2016). Application of independent component analysis to multitemporal InSAR data with volcanic case studies. *Journal of Geophysical Research: Solid Earth*, *121*(12), 8970–8986. https://doi.org/10.1002/2016JB013765
- Ezquerro, P., Herrera, G., Marchamalo, M., Tomás, R., Béjar-Pizarro, M., & Martínez, R. (2014). A quasi-elastic aquifer deformational behavior: Madrid aquifer case study. *Journal of Hydrology*, 519(PA), 1192–1204. https://doi.org/10.1016/j.jhydrol.2014.08.040
- Ezquerro, P., Tomás, R., Béjar-Pizarro, M., Fernández-Merodo, J. A., Guardiola-Albert, C., Staller, A., Sánchez-Sobrino, J. A., & Herrera, G. (2020). Improving multi-technique monitoring using Sentinel-1 and Cosmo-SkyMed data and upgrading groundwater model capabilities. *Science of the Total Environment*, 703, 134757. https://doi.org/10.1016/j.scitotenv.2019.134757
- Fernandez, J., Prieto, J. F., Escayo, J., Camacho, A. G., Luzón, F., Tiampo, K. F., Palano, M., Abajo, T., Pérez, E., Velasco, J., Herrero, T., Bru, G., Molina, I., López, J., Rodríguez-Velasco, G., Gómez, I., & Mallorquí, J. J. (2018). Modeling the two- and three-dimensional displacement field in Lorca, Spain, subsidence and the global implications. *Scientific Reports*, 8(1), 1–15. https://doi.org/10.1038/s41598-018-33128-0
- Foroughnia, F., Nemati, S., Maghsoudi, Y., & Perissin, D. (2019). An iterative PS-InSAR method for the analysis of large spatio-temporal baseline data stacks for land subsidence estimation. *Int J Appl Earth Obs Geoinformation*, 74(October 2018), 248–258. https://doi.org/10.1016/j.jag.2018.09.018
- Fuller, M. L. (1908). Summary of the controlling factors of artesian flows.
- Gaddes, M. E., Hooper, A., Bagnardi, M., Inman, H., & Albino, F. (2018). Blind Signal Separation Methods for InSAR: The Potential to Automatically Detect and Monitor Signals of Volcanic Deformation. *Journal of Geophysical Research: Solid Earth*, 123(11), 10,226-10,251. https://doi.org/10.1029/2018JB016210
- Galloway, D., Jones, D. R., & Ingebritsen, S. E. (1999). Land subsidence in the United States. In *Geological Survey Circular* (U.S.Geolog).
- Galloway, D. L., & Burbey, T. J. (2011). Review: Regional land subsidence accompanying groundwater extraction. *Hydrogeology Journal*, *19*(8), 1459–1486. https://doi.org/10.1007/s10040-011-0775-5

- Galloway, D. L., & Hoffmann, J. (2007). The application of satellite differential SAR interferometry-derived ground displacements in hydrogeology. *Hydrogeology Journal*, *15*(1), 133–154. https://doi.org/10.1007/s10040-006-0121-5
- Garzón, J. C. (2011). EVALUACIÓN DE ASENTAMIENTOS POR CONSOLIDACIÓN GENERADA POR DESCENSO DEL NIVEL FREÁTICO. Universidad Nacional de Colombia.
- Gil-Meseguer, E., Pérez-Morales, A., & Gómez-Espín, J. (2012). Precipitaciones y avenidas del 28 de septiembre del 2012 en el cuadrante suroccidental de la cuenca del Segura, (Municipios de Lorca, Puerto Lumbreras y Pulpí). *Papeles de Geografía*, 55(56), 75–94.
- Hergt, T., Castro-Larragoitia, J., Cardona-Benavides, A., & Carrillo-Rivera, J. J. (2009). Análisis multivariado en la definición de sistemas de flujo de agua subterránea en San Luis Potosí, México. *Ingenieria Hidraulica En Mexico*, 24(4), 37–54.
- Hernández-García, M. E., & Custodio, E. (2004). Natural baseline quality of Madrid Tertiaty Detrital Aquifer groundwater (Spain): a basis for aquifer management. *Environmental Geology, 46*, 173–188.
- Herrera, G., Tomás, R., Monells, D., Centolanza, G., Mallorquí, J. J., Vicente, F., Navarro, V. D., Lopez-Sanchez, J. M., Sanabria, M., Cano, M., & Mulas, J. (2010). Analysis of subsidence using TerraSAR-X data: Murcia case study. *Engineering Geology*, *116*(3–4), 284–295. https://doi.org/10.1016/j.enggeo.2010.09.010
- Herrera-García, G., Ezquerro, P., Tomas, R., Béjar-Pizarro, M., López-Vinielles, J., Rossi, M., Mateos, R. M., Carreón-Freyre, D., Lambert, J., Teatini, P., Cabral-Cano, E., Erkens, G., Galloway, D., Hung, W. C., Kakar, N., Sneed, M., Tosi, L., Wang, H., & Ye, S. (2021). Mapping the global threat of land subsidence. *Science*, *371*(6524), 34–36. https://doi.org/10.1126/science.abb8549
- Hooper, A. J. (2008). A multi-temporal InSAR method incorporating both persistent scatterer and small baseline approaches. *Geophysical Research Letters*, *35*(16), 1–5. https://doi.org/10.1029/2008GL034654
- Horst, T. Van Der, Rutten, M. M., Giesen, N. C. Van De, & Hanssen, R. F. (2018). Monitoring land subsidence in Yangon, Myanmar using Sentinel-1 persistent scatterer interferometry and assessment of driving mechanisms. *Remote Sensing of Environment*, *217*(July), 101–110. https://doi.org/10.1016/j.rse.2018.08.004
- Hu, B., Chen, J., & Zhang, X. (2019). Monitoring the land subsidence area in a coastal urban area with InSAR and GNSS. *Sensors (Switzerland)*, 19(14), 1–19. https://doi.org/10.3390/s19143181
- Hu, L., Dai, K., Xing, C., Li, Z., Tomás, R., Clark, B., Shi, X., Chen, M., Zhang, R., Qiu, Q., & Lu, Y. (2019). Land subsidence in Beijing and its relationship with geological faults revealed by Sentinel-1 InSAR observations. *International Journal of Applied Earth Observation and Geoinformation*, 82(June), 101886. https://doi.org/10.1016/j.jag.2019.05.019
- Hu, R. L., Yue, Z. Q., Wang, L. C., & Wang, S. J. (2004). Review on current status and challenging issues of land subsidence in China. 76, 65–77. https://doi.org/10.1016/j.enggeo.2004.06.006
- Ikuemonisan, F. E., Ozebo, V. C., & Olatinsu, O. B. (2020). Geostatistical evaluation of spatial variability of land subsidence rates in Lagos, Nigeria. *Geodesy and Geodynamics*, xxxx, 1–12. https://doi.org/10.1016/j.geog.2020.04.001

- Imamoglu, M., Balik Sanli, F., Cakir, Z., & Kahraman, F. (2022). Rapid ground subsidence in the Küçük Menderes Graben (W. Turkey) captured by Sentinel-1 SAR data. *Environmental Earth Sciences*, 81(7), 1–14. https://doi.org/10.1007/s12665-022-10339-3
- Jollife, I. T., & Cadima, J. (2016). Principal component analysis: A review and recent developments. Philosophical Transactions of the Royal Society A: Mathematical, Physical and Engineering Sciences, 374(2065). https://doi.org/10.1098/rsta.2015.0202
- Koca, M. Y., Sözbilir, H., & Uzel, B. (2011). Sarıgöl Fay Zonu Boyunca Meydana Gelen Deformasyonların Nedenleri Üzerine Bir Araştırma. *Jeoloji Muhendisligi Dergisi*, 35(2), 151–174.
- Li, J., Zhu, L., Gong, H., Zhou, J., Dai, Z., Li, X., Wang, H., Zoccarato, C., & Teatini, P. (2022). Unraveling elastic and inelastic storage of aquifer systems by integrating fast independent component analysis and a variable preconsolidation head decomposition method. *Journal of Hydrology*, 606. https://doi.org/10.1016/j.jhydrol.2021.127420
- Llamas, R., Villarroya, F., & Hernández-García, M. E. (1996). Causes and effects of water restrictions in Madrid during the drought of 1990/93. *Annual Meeting, American Institute of Hydrology: Hydrology and Hydrogeologyof Urban and Urbanizing Areas.*
- Mahmoudpour, M., Khamehchiyan, M., Nikudel, M. R., & Ghassemi, M. R. (2013). *Characterization of regional land subsidence induced by groundwater withdrawals in Tehran*, *Iran.* 3(2), 49–62.
- Maliva, R. G. (2004). Aquifer Characterization Techniques. In *Schlumberger Water Services* (Issue 4). Springer. https://doi.org/10.2110/pec.04.80
- Marchi, L., Borga, M., Preciso, E., & Gaume, E. (2010). Characterisation of selected extreme flash floods in Europe and implications for flood risk management. *Journal of Hydrology*, *394*(1–2), 118–133. https://doi.org/10.1016/j.jhydrol.2010.07.017
- Mihu-Pintilie, A., Cîmpianu, I., Stoleriu, C. C., & Paveluc, L. E. (2019). Using High-Density LiDAR Data and 2D Streamflow Hydraulic Modeling to Improve Urban Flood Hazard. *Water*, *11*(1832), 1–24.
- Minh, D. H. T., Hanssen, R., & Rocca, F. (2020). Radar interferometry: 20 years of development in time series techniques and future perspectives. *Remote Sensing*, *12*(9). https://doi.org/10.3390/RS12091364
- Ministerio de Medio Ambiente, y M. R. y M. (2011). *Guía Metodológica para el desarrollo del Sistema Nacional de Cartografía de Zonas Inundables*.
- Mora, O. (2003). Advanced differential SAR techniques for detection of terrain and building displacements. *Uninversidad Politécnica de Cataluña*, 182.
- Navarro-Hernández, M. I., Tomás, R., Lopez-Sanchez, J. M., Cárdenas-Tristán, A., & Mallorquí, J. J. (2020). Spatial analysis of land subsidence in the San Luis potosi valley induced by aquifer overexploitation using the coherent pixels technique (CPT) and sentinel-1 insar observation. *Remote Sensing*, 12(22), 1–23. https://doi.org/10.3390/rs12223822
- Navarro-Hernández, M. I., Tomás, R., Valdes-Abellan, J., Bru, G., Ezquerro, P., Guardiola-Albert, C., Elçi, A., Batkan, E. A., Caylak, B., Ören, A. H., Meisina, C., Pedretti, L., & Rygus, M. (2023). Monitoring land subsidence induced by tectonic activity and groundwater extraction in the eastern Gediz River Basin (Türkiye) using Sentinel-1 observations. *Engineering Geology*, 327. https://doi.org/10.1016/j.enggeo.2023.107343

- Navarro-Hernández, M. I., Valdes-Abellan, J., Tomás, R., Lopez-Sanchez, J. M., Ezquerro, P., Bru, G., Boni, R., Meisina, C., & Herrera, G. (2022). VallnSAR: A systematic approach for the validation of Differential SAR Interferometry in land subsidence areas. *IEEE Journal of Selected Topics in Applied Earth Observations and Remote Sensing*, *15*, 3650–3671. https://doi.org/10.1109/JSTARS.2022.3171517
- Navarro-Hernández, M. I., Valdes-Abellan, J., Tomás, R., Tessitore, S., Ezquerro, P., & Herrera, G. (2023). Analysing the Impact of Land Subsidence on the Flooding Risk: Evaluation Through InSAR and Modelling. *Water Resources Management*, *37*(11), 4363–4383. https://doi.org/10.1007/s11269-023-03561-6
- Noyola-Medrano, M. C., Ramos-Leal, J. A., Domínguez-Mariani, E., Pineda-Martínez, L. F., López-Loera, H., & Carbajal, N. (2009). Factores que dan origen al minado de acuíferos en ambientes áridos: Caso Valle de San Luis Potosí. *Revista Mexicana de Ciencias Geologicas*, 26(2), 395–410.
- Pardo, J. M., Lozano, A., Herrera, G., Mulas, J., & Rodríguez, Á. (2013). Instrumental monitoring of the subsidence due to groundwater withdrawal in the city of Murcia (Spain). *Environmental Earth Sciences*, 70(5), 1957–1963. https://doi.org/10.1007/s12665-013-2710-7
- Poland, J. F. (1984). *Guidebook to studies of land subsidence due to groundwater withdrawal* (J. F. Poland, Ed.). UNESCO.
- Poland, J. F., Lofgren, B. E., Ireland, R. L., & Pugh, R. G. (1984). Land subsidence in the San Joaquin Valley, California, as of 1972. *Geological Survey Professional Paper*, 437 I. https://doi.org/10.3133/pp437I
- Poyraz, F., & Hastaoğlu, K. Ö. (2020). Monitoring of tectonic movements of the Gediz Graben by the PSInSAR method and validation with GNSS results. *Arabian Journal of Geosciences*, *13*(17), 1–11. https://doi.org/10.1007/s12517-020-05834-5
- Poyraz, F., Hastaoğlu, K. O., Koçbulut, F., Tiryakioğlu, I., Tatar, O., Demirel, M., Duman, H., Aydın, C., Ciğer, A. F., Gursoy, O., Turk, T., & Sıgırcı, R. (2019). Determination of the block movements in the eastern section of the Gediz Graben (Turkey) from GNSS measurements. *Journal of Geodynamics*, 123(November 2018), 38–48. https://doi.org/10.1016/j.jog.2018.11.001
- Prati, C., Ferretti, A., & Perissin, D. (2010). Recent advances on surface ground deformation measurement by means of repeated space-borne SAR observations. *Journal of Geodynamics*, 49(3–4), 161–170. https://doi.org/10.1016/j.jog.2009.10.011
- Pujadas Ferrer, J. (2002). Las inundaciones en España: Impacto económico y gestión del riesgo. In *Riesgos Naturales* (pp. 879–888). Ariel.
- Raspini, F., Loupasakis, C., Rozos, D., Adam, N., & Moretti, S. (2014). Ground subsidence phenomena in the Delta municipality region (Northern Greece): Geotechnical modeling and validation with Persistent Scatterer Interferometry. *International Journal of Applied Earth Observations and Geoinformation*, 28, 78–89. https://doi.org/10.1016/j.jag.2013.11.010
- Rigo, A., Béjar-Pizarro, M., & Martínez-Díaz, J. (2013). Monitoring of Guadalentín valley (southern Spain) through a fast SAR Interferometry method. *Journal of Applied Geophysics*, *91*, 39–48. https://doi.org/10.1016/j.jappgeo.2013.02.001
- Riley, F. S. (1969). Analysis of Borehole Extensometer Data from Central California. In *Land Subsidence, Volume 2* (pp. 423–431). International Association of Scientific Hydrology.

- Rohatgi, A. (2021). WebPlotDigitizer (4.5). https://automeris.io/WebPlotDigitizer/index.html
- Schumann, A. H. (2011). Flood Risk Assessment and Management. In *Flood Risk Assessment and Management: How to Specify Hydrological Loads, Their Consequences and Uncertainties*. Springer. https://doi.org/10.1007/978-90-481-9917-4\_11
- Tatar, O., Poyraz, F., Gürsoy, H., Cakir, Z., Ergintav, S., Akpinar, Z., Koçbulut, F., Sezen, F., Türk, T., Hastaoğlu, K. Ö., Polat, A., Mesci, B. L., Gürsoy, Ö., Ayazli, I. E., Çakmak, R., Belgen, A., & Yavaşoğlu, H. (2012). Crustal deformation and kinematics of the Eastern Part of the North Anatolian Fault Zone (Turkey) from GPS measurements. *Tectonophysics*, *518–521*, 55–62. https://doi.org/10.1016/j.tecto.2011.11.010
- Tessitore, S., Fernández-Merodo, J. A., Herrera, G., Tomás, R., Ramondini, M., Sanabria, M., Duro, J., Mulas, J., & Calcaterra, D. (2016). Comparison of water-level, extensometric, DInSAR and simulation data for quantification of subsidence in Murcia City (SE Spain). *Hydrogeology Journal*, *24*(3), 727–747. https://doi.org/10.1007/s10040-015-1349-8
- Tomas, R., Herrera, G., Cooksley, G., & Mulas, J. (2011). Persistent Scatterer Interferometry subsidence data exploitation using spatial tools: The Vega Media of the Segura River Basin case study. *Journal of Hydrology*, 400(3–4), 411–428. https://doi.org/10.1016/j.jhydrol.2011.01.057
- Tomás, R., Herrera, G., Delgado, J., Lopez-Sanchez, J. M., Mallorquí, J. J., & Mulas, J. (2010). A ground subsidence study based on DInSAR data: Calibration of soil parameters and subsidence prediction in Murcia City (Spain). *Engineering Geology*, *111*(1–4), 19–30. https://doi.org/10.1016/j.enggeo.2009.11.004
- Tomás, R., Romero, R., Mulas, J., Marturià, J. J., Mallorquí, J. J., Lopez-Sanchez, J. M., Herrera, G., Gutiérrez, F., González, P. J., Fernández, J., Duque, S., Concha-Dimas, A., Cocksley, G., Castañeda, C., Carrasco, D., & Blanco, P. (2014). Radar interferometry techniques for the study of ground subsidence phenomena: A review of practical issues through cases in Spain. *Environmental Earth Sciences*, 71(1), 163–181. https://doi.org/10.1007/s12665-013-2422-z
- Tonkul, S., Baba, A., Şimşek, C., Durukan, S., Demirkesen, A. C., & Tayfur, G. (2019). Groundwater recharge estimation using HYDRUS 1D model in Alaşehir sub-basin of Gediz Basin in Turkey. *Environmental Monitoring and Assessment*, 191(10). https://doi.org/10.1007/s10661-019-7792-6
- Tristán, A. C., García, M. D. R., Cárdenas, O. R., Ovalle, A. G. C., & Putri, R. F. (2020). Analysis of sinking incidence in the San Luis Potosí Valley, México. *IOP Conference Series: Earth and Environmental Science*, 451(1). https://doi.org/10.1088/1755-1315/451/1/012009
- Üner, S., & Dogan, D. D. (2021). An integrated geophysical, hydrological, thermal approach to finite volume modelling of fault-controlled geothermal fluid circulation in Gediz Graben. *Geothermics*, 90(December 2020), 102004.

  https://doi.org/10.1016/j.geothermics.2020.102004
- W. Brunner, G. (2021). *HEC-RAS, River Analysis System, 2D Modeling Users Manual Version 6.0 Beta* (p. 289).
- Wallingford, H. R. (2006). *R&D Outputs: Flood risk to people: Phase 2 FD2321/TR1*. www.defra.gov.uk/environ/fcd

- Xue, Y. Q., Wu, J. C., Zhang, Y., Ye, S. J., Shi, X. Q., Wei, Z. X., Li, Q. F., & Yu, J. (2008). Simulation of regional land subsidence in the southern Yangtze Delta. *Science in China, Series D: Earth Sciences*, *51*(6), 808–825. https://doi.org/10.1007/s11430-008-0062-z
- Zermeña, M., Esquivel, R., Hernandez, A., Mendoza, E., & Arellano, J. (2005). Influencia De La Extraccion Del Agua En La Subsidencia YAgrietamiento de la ciudad de Aguascalientes. *Investigación y Ciencia de La Universidad Autónoma de Aguascalientes*, 15–22.
- Zhang, Y., Gong, H., Gu, Z., Wang, R., Li, X., & Zhao, W. (2014). Characterization of land subsidence induced by groundwater withdrawals in the plain of Beijing city, China. *Hydrogeology Journal*, 22(2), 397–409. https://doi.org/10.1007/s10040-013-1069-x
- Zhang, Y., Xue, Y.-Q., Wu, J.-C., Ye, S.-J., Wei, Z.-X., Li, Q.-F., & Yu, J. (2007). Characteristics of aquifer system deformation in the Southern Yangtse Delta, China. *Engineering Geology*, *90*(3–4), 160–173. https://doi.org/10.1016/j.enggeo.2007.01.004
- Zhu, L., Gong, H., Chen, Y., Wang, S., Ke, Y., Guo, G., Li, X., Chen, B., Wang, H., & Teatini, P. (2020). Effects of Water Diversion Project on groundwater system and land subsidence in Beijing, China. *Engineering Geology*, *276*. https://doi.org/10.1016/j.enggeo.2020.105763

## II. SECOND PART Compendium



# Spatial Analysis of Land Subsidence in the San Luis Potosi Valley Induced by Aquifer Overexploitation Using the Coherent Pixels Technique (CPT) and Sentinel-1 InSAR Observation

by María Inés Navarro-Hernández 1, Roberto Tomás 27, Juan M. Lopez-Sanchez 3, Abraham Cárdenas-Tristán 1 and Jordi J. Mallorquí 4

### Abstract

The San Luis Potosi metropolitan area has suffered considerable damage from land subsidence over the past decades, which has become visible since 1990. This paper seeks to evaluate the effects of groundwater withdrawal on land subsidence in the San Luis Potosi Valley and the development of surface faults due to the differential compaction of sediments. For this purpose, we applied the Coherent Pixels Technique (CPT), a Persistent Scatterer Interferometry (PSI) technique, using 112 Sentinel-1 acquisitions from October 2014 to November 2019 to estimate the deformation rate. The results revealed that the deformation areas in the municipality of Soledad de Graciano Sánchez mostly exhibit subsidence values between -1.5 and -3.5 cm/year; whereas in San Luis Potosi these values are between -1.8 and -4.2 cm/year. The PSI results were validated by five Global Navigation Satellite System (GNSS) benchmarks available, providing a data correlation between the results obtained with both techniques of 0.986. This validation suggests that interferometric derived deformations agree well with results obtained from GNSS data. The strong relationship between trace fault, land subsidence,e and groundwater extraction suggests that groundwater withdrawal is resulting in subsidence induced faulting, which follows the pattern of structural faults buried by sediments.

*Cited as:* Navarro-Hernández, M.I.; Tomás, R.; Lopez-Sanchez, J.M.; Cárdenas-Tristán, A.; Mallorquí, J.J. Spatial Analysis of Land Subsidence in the San Luis Potosi Valley Induced by Aquifer Overexploitation Using the Coherent Pixels Technique (CPT) and Sentinel-1 InSAR Observation. *Remote Sens.* **2020**, *12*, 3822. https://doi.org/10.3390/rs12223822

Remote Sens. 2020, 12(22), 3822; https://doi.org/10.3390/rs12223822

Submission received: 23 October 2020 / Revised: 17 November 2020 / Accepted: 17 November

2020 / Published: 21 November 2020

(This article belongs to the Special Issue <u>Earth Observations for Land Subsidence Identification</u>, Monitoring and Their Contribute to Modeling)



### ValInSAR: A Systematic Approach for the Validation of Differential SAR Interferometry in Land Subsidence Areas

by María I. Navarro-Hernández, Javier Valdes-Abellan, Roberto Tomás, Juan M. Lopez-Sanchez, Pablo Ezquerro, Guadalupe Bru, Roberta Bonì, Claudia Meisina and Gerardo Herrera

### Abstract

Land subsidence is a natural or anthropogenic process triggering the settlement of the Earth's surface. When this phenomenon is induced by groundwater withdrawal, compaction of unconsolidated sediments causes land displacement. Differential interferometric synthetic aperture radar (DInSAR) is widely used nowadays to monitor subsidence over extensive areas. However, validation of DInSAR measurements with in-situ techniques is lacking in many case studies, reducing the reliability of further analyses. The aim of this article is to propose a systematic methodology to validate DInSAR measurements with in-situ techniques to obtain reliable subsidence measurements. The article provides a literature review of the most common approaches to validate DInSAR measurements and a description of the proposed systematic methodology, which is supported by a MATLAB open-source code. The methodology allows the analysis of both DInSAR-based velocity and displacement time series. We propose a set of statistics to assess the accuracy of the DInSAR estimates. For this purpose, RMSE parameters have been normalized with the range and the average of the in-situ deformation values. Moreover, combining these normalized parameters with the Pearson correlation coefficient (R2), a classification scheme is recommended for accepting/rejecting the DInSAR data for further analyses. This methodology has been applied in three study areas characterized by very well-documented subsidence processes: The Alto Guadalentín Valley and Murcia City in Spain, and San Luis Potosí in Mexico.

*Cited as:* Navarro-Hernández, M. I., Valdes-Abellan, J., Tomás, R., Lopez-Sanchez, J. M., Ezquerro, P., Bru, G., Boni, R., Meisina, C., & Herrera, G. (2022). VallnSAR: A systematic approach for the validation of Differential SAR Interferometry in land subsidence areas. IEEE Journal of Selected Topics in Applied Earth Observations and Remote Sensing, 15, 3650–3671. https://doi.org/10.1109/JSTARS.2022.3171517

IEEE JOURNAL OF SELECTED TOPICS IN APPLIED EARTH OBSERVATIONS AND REMOTE SENSING, VOL. 15, 2022 DOI: 10.1109/JSTARS.2022.3171517

Manuscript received January 14, 2022; revised March 9, 2022; accepted April 22, 2022. Date of publication May 3, 2022; date of current version May 18, 2022



### Analysing the Impact of Land Subsidence on the Flooding Risk: Evaluation Through InSAR and Modelling

by María I. Navarro-Hernández, Javier Valdes-Abellan, Roberto Tomás, Serena Tessitore, Pablo Ezquerro and Gerardo Herrera

### **Abstract**

Floods greatly impact human settlements in flood risk areas, such as floodplains and coastal lowlands, following heavy rainfall. The Alto Guadalentin valley, an orogenic tectonic depression, experiences extreme flash floods and land subsidence due to groundwater withdrawal, rendering it one of Europe's fastest subsiding regions. In this study, we compared two 2D flood event models representing different land subsidence scenarios for 1992 and 2016. To determine the flooded area and water depth variations due to land subsidence, the Hydrologic Engineering Centre River Analysis System 2D (HEC-RAS 2D) model was used to simulate flood inundation by the Alto Guadalentin River and its tributaries. Synthetic aperture radar (SAR) satellite (ERS, ENVISAT, and Cosmo-SkyMED) images were employed, along with the interferometric SAR (InSAR) technique, to calculate the magnitude and spatial distribution of land subsidence. By analysing the accumulated subsidence distributions obtained from InSAR, the original topography of the valley in 1992 and 2016 was reconstructed. These digital surface models (DSMs) were then used to generate 2D hydraulic models, simulating flood scenarios in the unsteady mode. The results demonstrated significant changes in the water surface elevation over the 14-year period, with a 2.04 km<sup>2</sup> increase in areas with water depths exceeding 0.7 m. These findings were utilized to create a flood risk map and assess the economic flood risk. The data highlight the crucial role of land subsidence in determining the inundation risk in the Alto Guadalentin valley, providing valuable insights for emergency management and civil protection against future potential flooding events.

*Cited as:* Navarro-Hernández, M.I., Valdes-Abellan, J., Tomás, R. et al. Analysing the Impact of Land Subsidence on the Flooding Risk: Evaluation Through InSAR and Modelling. Water Resour Manage 37, 4363–4383 (2023). https://doi.org/10.1007/s11269-023-03561-6

Water Resources Management (2023) 37:4363–4383 https://doi.org/10.1007/s11269-023-03561-6

Received: 30 August 2022 / Accepted: 14 July 2023 / Published online: 2 August 2023





# Monitoring land subsidence induced by tectonic activity and groundwater extraction in the eastern Gediz River Basin (Türkiye) using Sentinel-1 observations

by María I. Navarro-Hernández, Roberto Tomás, Javier Valdes-Abellan, Guadalupe Bru, Pablo Ezquerro, Carolina Guardiola-Albert, Alper Elçi, Elif Aysu Batkan, Baris Caylak, Ali Hakan Ören, Claudia Meisina, Laura Pedretti, and Michelle Rygus

### **Abstract**

Alaşehir-Sarıgöl sub-basin (ASSB) in Türkiye faces severe water stress mainly due to intensive agricultural irrigation. This has led to declining groundwater levels, aquifer compaction, and subsequent land subsidence. This study aims to evaluate the roles of tectonic activity and groundwater withdrawal in land-subsidence and investigate additional factors like faults and soft soil thickness. The P-SBAS algorithm was applied, using 98 and 123 Sentinel-1 SAR images in ascending and descending orbits, respectively, from 2016 to 2020. Independent Component Analysis separated long-term displacements from seasonal variations in the InSAR time series data. InSAR analysis showed displacement rates up to -6.40 cm/year. Results reveal a direct correlation between InSAR displacement and soft soil thickness, highlighting aquitard layer compaction due to groundwater withdrawal and piezometric head depletion as the primary causes of land subsidence. It was not possible to disentangle the multi-year displacements with different rates, i.e., to isolate the displacements caused by tectonic activity from displacements due to the soft soil compaction induced by groundwater withdrawal. Nonetheless, the analysis identified two spatiotemporal displacement trends: one linked to long-term, linear plastic compaction of the aquitard due to groundwater withdrawal and the other involving long-term displacements with seasonal rebounds caused by yearly water level fluctuations.

*Cited as:* Navarro-Hernández, M. I., Tomás, R., Valdes-Abellan, J., Bru, G., Ezquerro, P., Guardiola-Albert, C., Elçi, A., Batkan, E. A., Caylak, B., Ören, A. H., Meisina, C., Pedretti, L., & Rygus, M. (2023). Monitoring land subsidence induced by tectonic activity and groundwater extraction in the eastern Gediz River Basin (Türkiye) using Sentinel-1 observations. Engineering Geology, 107343. https://doi.org/10.1016/j.enggeo.2023.107343

Engineering Geology Volume 327, 20 December 2023, 107343 https://doi.org/10.1016/j.enggeo.2023.107343

Received 7 November 2022; Received in revised form 24 October 2023; Accepted 30 October 2023 Available online 2 November 2023

### III. THIRD PART Other publications

1

2

### A New Stress-Strain Analysis Application for Aquifer Systems Characterization in Land Subsidence Affected Areas

3 4 5

María I. Navarro-Hernández 1, Sergio García-Pozo 1, Javier Valdes-Abellan 1 and Roberto Tomás 1

7 8

6

<sup>1</sup>Department of Civil Engineering, Polytechnic School, University of Alicante, Alicante, Spain mainnahe@ua.es, sgp107@alu.ua.es, javier.valdes@ua.es, roberto.tomas@ua.es

9 10

11

12

13

14

15

16

17

18

19

20

21

22

23

24

25

26

27

28

29

30

31

32

33

### **Abstract**

Anthropogenic land subsidence is caused by over-extraction of groundwater resources. In most cases, recharge and withdrawal of groundwater in aquifer- systems produce changes in the thickness of the aquifer-system layers, which consequently leads to ground deformations. Pore pressure reduction due to groundwater withdrawal is the main external cause, while soil compressibility is the main internal cause of land subsidence. The relationship between stress and strain of an aquifer-system (or of specific layers of an aquifer-system) are usually expressed through stress-strain curves. These curves represent hydrograph data (stress due to piezometric level variations) against land subsidence compaction records (strain). These curves consist in linear or semi-linear diagrams that provide very useful information about the geomechanical behaviour of the aquifer-system (e.g., elastic, plastic, elasto-plastic or visco-elasto-plastic) and even can be used to estimate hydrological parameters as the storage coefficients of the aquifer-system. The determination of storage coefficients has traditionally relied on visual assessment conducted by skilled researchers, thus involving a notably subjective methodology. In this work, we present a MATLAB© application to automatize and streamline the analysis of land subsidence datasets, their potential correlation with piezometric levels, and the estimation of the storage coefficients, reducing the analysis time-cost and the potential presence of human-interpretation errors. The developed application integrates temporal series of groundwater level usually obtained from observation wells, and ground deformation measured by in-situ (e.g., borehole extensometer, levelling survey, etc.) or remote sensing (e.g., interferometric synthetic aperture radar, InSAR) techniques to automatically build the stress-strain curves. Different aguifer-systems in the world exhibiting typical geomechanical behaviours are used in this work to illustrate the performance of the proposed application.

34

35

36

**Keywords**: aquifer-system deformation; stress-strain curve; groundwater extraction; storage coefficient; land subsidence; MATLAB.

37

### 1. Introduction

Land subsidence induced by intensive groundwater withdrawal from detrital aquifers is a worldwide issue affecting many important cities worldwide. The expanding urban population is exacerbating this issue, thereby intensifying the strain on already limited and occasionally scarce freshwater resources (D. Galloway et al., 1999; D. L. Galloway & Burbey, 2011; Herrera-García et al., 2021).

The use of stress-strain curves is a graphical way to describe the relationship between ground displacement due to aquifer-system compaction and groundwater level evolution over time. The mechanical behaviour of an aquifer-system or of a specific layer of the aquifer system can be interpreted through the information contained in the stress-strain curves. Furthermore, the value of some hydrogeological variables such as the storage coefficient can be estimated from this relationship. Nevertheless, despite the advantages and information offered by the stress-strain relationship, the analysis of these curves is typically conducted manually without a clear, objective protocol. This process is tedious and time-consuming, leading to subjective results highly reliant on the researcher's ability and expertise to interpret graphical information.

In light of the preceding discussion, this manuscript introduces a newly developed application designed to automate the analysis of stress-strain curves, with the goal of enhancing objectivity and expediting the analytical process. This application has been tested with real data from different aquifers affected by land subsidence throughout the world.

### 1.1. Stress-strain curves

The preconsolidation pressure is the maximum effective stress ( $\sigma_{e(max)}$ ) experienced by a soil throughout its geological history. This pressure distinguishes between elastic (recoverable) and inelastic (irreversible) deformations of the soil. This concept is fundamental for understanding the mechanisms of land subsidence caused by fluctuations in the piezometric level (Poland, 1984). In soils affected by groundwater withdrawal, the preconsolidation pressure indicates the maximum stresses induced by the decline in the piezometric level. This value suggests the depth at which deformations become irreversible. In other words, once the preconsolidation pressure is reached, a portion of the displacement cannot be recovered (Hoffmann, 2003; Tomás et al., 2007).

In 1925, Terzagui defined the poroelasticity theory which related the water level fluctuation (hydraulic head) and the effective stress in the aquifer skeleton (D. L. Galloway & Hoffmann, 2007; Hoffmann et al., 2001):

$$\Delta \sigma_e = \sigma_T - \gamma \Delta h \tag{1}$$

Where  $\Delta \sigma_e$  is stress effective changes,  $\sigma_T$  is the total stress,  $\gamma$  is the water density and  $\Delta h$  is the piezometric level (fluid pressure) changes. From this equation, when the total stress remains

constant ( $\sigma_T=0$ ), changes in the piezometric level is equivalent to changes in the effective stress, this can result in either the compression or expansion of the aquifer skeleton, depending on the new load (Galloway et al., 1998). When the effective stress decreases due to an increasing in the fluid pressure (i.e., piezometric level increases) the aquifer expands elastically. When the effective stress increases due to a fluid pressure decrease and the effective stress do not exceed the maximum past value, then the aquifer system compresses elastically. However, if the maximum past effective stress is exceeded, then the deformation is inelastic and the reduction of pore volume results in compaction (D. L. Galloway et al., 1998; Hoffmann et al., 2001).

Stress-strain curves of aquifer-systems represent the relationship between ground deformation measurements (land subsidence in this case) and piezometric level fluctuations during a common observation period. This method was developed by Riley (F. S. Riley, 1969), who proposed to plot the stress (i.e., groundwater level variations) against the strain (i.e., deformations) of an aquifer-system or a specific layer of an aquifer, in order to estimate the skeletal storage coefficient of the compressible strata (Burbey, 2001).

In the hydrogeologic characterization of aquifers, the skeletal specific storage is crucial in the compressibility estimation. The compressibility can be elastic or inelastic for aquifers and aquitard in an aquifer system and it can be expressed in skeletal specific storage ( $S_{sk}$ ) terms (Galloway et al., 1998):

$$\begin{cases} S_{sk} = S_{ske} = \alpha_{ke}\rho g & when \sigma_e < \sigma_{e(max)} \\ S_{sk} = S_{skv} = \alpha_{kv}\rho g & when \sigma_e > \sigma_{e(max)} \end{cases}$$
 [2]

Where, the subscript e and v correspond to elastic and virgin (inelastic) respectively,  $\rho$  is the fluid density and g is the acceleration of the gravity. The specific storage coefficient ( $S_s$ ) is the volume of water released from the aquifer system per unit changes in piezometric level (Galloway & Hoffmann, 2007), this means the capacity of an aquifer to store and release water in respond se to changes in fluid pressure. Furthermore, under confined conditions, the specific storage is composed by two elements shown in Eq. [3] where  $S_{sk}$  is a component due to compressibility of the skeletal unit and  $S_{sw}$  is a component due to the compressibility of the water (F. S. Riley, 1969).

$$S_{\rm S} = S_{\rm Sk} + S_{\rm SW} \tag{3}$$

However, for compacting aquifer systems aquifers  $S_{sk} \gg S_w$ , and the changes in the storages caused by changes in the piezometric level are meanly determinate by the skeletal compressibility (Galloway & Hoffmann, 2007). Thus, equation [3] can be rewritten as:

$$S_{S} = S_{Sk}$$
 [4]

Taking into account that the product of the elastic or inelastic skeletal specific storage and aggregate thickness of the aquitards or aquifers  $\sum b$ , the skeletal storage coefficient  $S_k$  can be defined as (D. L. Galloway et al., 1998):

$$\begin{cases} S_k = S_{ke} = S_{ske}(\sum b) & when \ \sigma_e < \sigma_{e(\max)} \\ S_k = S_{kv} = S_{skv}(\sum b) & when \ \sigma_e > \sigma_{e(\max)} \end{cases}$$
 [5]

Furthermore, Riley (1969) demonstrated that when effective stress changes gradually over time while the total stress remains constant,  $S_k$  can be calculated from paired time-series of piezometric changes and displacements (Galloway & Hoffmann, 2007) by:

$$S_{k} = \frac{\Delta b}{\Delta h}$$
 [6]

Replacing  $S_{sk}$  in the definition of the specific storage coefficient  $(S_s)$  and combining the concepts in equation [5] and [6], from the stress-strain curves, the elastic skeletal specific storage  $(S_{ske})$  and the inelastic skeletal specific storage  $(S_{skv})$  can be estimated replacing as:

$$S_{sk} = \frac{S_k}{b} = \frac{\Delta b}{b \cdot \Delta h} \tag{7}$$

Equation [6] will be the formula applied throughout this study, where the result is dimensionless. As is known, interstitial pressure dissipates slowly in clays and silts (confined layers) due to the small size and limited connectivity of their pores. Interesting information about the time lag in interstitial pressure dissipation between the aquifer and the confining layers can be obtained from the width of the hysteresis cycles in the diagrams (Riley, 1984).

### 1.2. Mechanical behaviour of aquifers

Taking into consideration the different variables participating in the phenomenon, such as the stratigraphy features of the aquifer system, the pumping conditions, the climate setup and particularly the precipitation trend and the past groundwater levels which will defined the preconsolidation head), aquifers can exhibit different mechanical behaviours, and even more, the same aquifer can show different behaviours at different periods of time. From the analysis of previous studies about the relationship between subsidence and groundwater level evolution using stress-strain curves, three main behaviour types can be identified: elastic, elastoplastic and visco-elastoplastic.

When the stress state in a layer of an aquifer-system does not exceed the pre-consolidation stress (i.e., the previous maximum effective stress that has sustained in the past), or the water level is always above its minimum historical level, the system exhibits a fully recoverable elastic deformation. This is the typical case of aquifer-systems exhibiting seasonal variations of groundwater level, with an annual periodicity and normally without an important affection caused by human exploitation. Deformation is associated with both compaction and expansion, resulting in curves that exhibit synchronized or consistently delayed deformation in response to groundwater level fluctuations. However, in natural environments, the aquifers do not often exhibit a perfect elastic behaviour since there is usually a small plastic non-recoverable deformation component when two consecutive and theoretically elastic loops are compared. Despite this, it is possible to say that an aquifer has mainly an elastic behaviour (Youquan Zhang et al., 2014).

In the elasto-plastic behaviour, even that the stress remains in the limits of elastics behaviour (i.e., the water level fluctuations are always above the minimum historical observed groundwater level), the aquifer exhibit non-recoverable plastic deformation. In those cases, the stress-strain plot shows

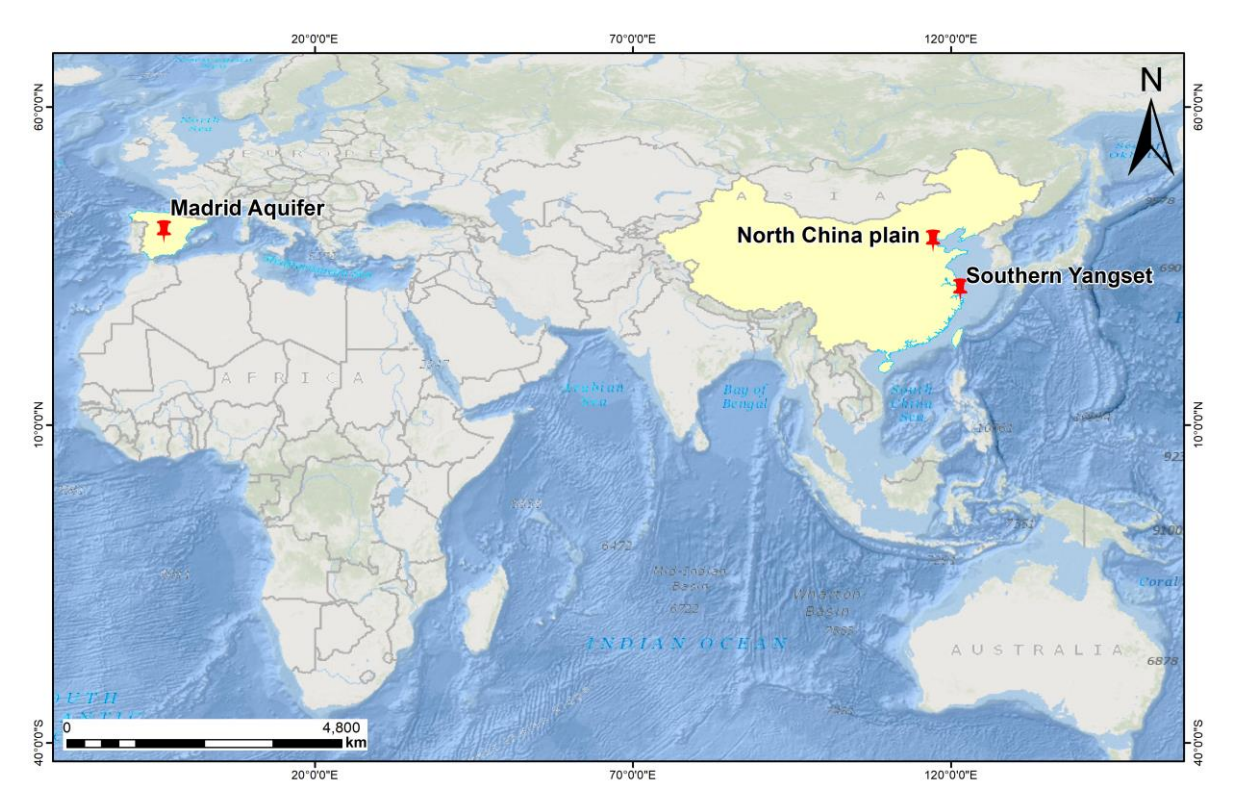
a combination of elastic loops with recoverable deformation, followed by non-recovery deformations (Burbey, 2001; Zhang et al., 2014; Zhang et al., 2007).

Once the pre-consolidation stress limit is exceeded, the aquifer materials can show an irrecoverable deformation, typically observed in intensively exploited aquifers over extended periods, resulting in a significant drop in groundwater levels. Stress-strain plots in such cases reveal a clear temporal evolution of aquifer material deformation and compaction, even with slight stress level increases. In this plastic domain, the aquifer responds with greater deformation to a unit stress increase compared to the elastic domain. These deformations persist even after pumping ceases, continuing until a new stress equilibrium is established(Burbey, 2001; Zhang et al., 2014; Zhang et al., 2007).

However, it's important to note that the specific behaviour of aquifers can vary widely based on geological and hydrogeological conditions. Additionally, further research and field data are often needed to fully characterize and understand the behaviour of a particular aquifer system.

### 2. Description of the study areas

This section provides a concise description of the geographical, geological, and hydrogeological characteristics of the four study areas (2 in China and 1 in Spain) used in this paper (see Figure 1) to evaluate the novel application. The main aim is to provide a hydrogeological environmental background of the dataset and results used to validate the outcomes obtained from the MATLAB application.



### 2.1. Southern Yangtse Delta, China

The southern Yangtse Delta, characterized by its extensive flat terrain, is located within three economically significant provinces in China. The notable economic and industrial advancement in this region has generated an augmented demand for groundwater, subsequently leading to substantial subsidence measured in metric units(Zhang et al., 2007). The region hosts a highly complex aquifer system comprising Quaternary materials derived from fluvial, lacustrine, and oceanic environments. These materials include gravel, sand, silty sand, silty clay, and clay. The depth of the aquifer system varies from 250 to 310 m beneath Shanghai, but in certain areas, it can exceed 360 m (Zhang et al., 2007). The system comprises five aquifer layers primarily composed of granular materials like gravel and sand. The topmost aquifer is unconfined, whereas the remaining four aquifers are confined. These aquifers are separated by lower-permeability materials such as silt and clay, corresponding to aquitard layers.

In this aquifer, land subsidence was first reported 1921 in Shanghai, first displacement due to the groundwater extraction were about 24 mm/year. However, after 1949, when groundwater pumping significantly increased, displacements reached values of up to 110 mm per year. Authorities implemented measures to mitigate land subsidence, including increasing artificial recharge and relocating groundwater extraction to deeper confined aquifer layers. Despite these efforts, the declining trend in piezometric levels did not cease until the end of 1999. As a results, three cones of depression from three different important cities were joined, forming a regional cone of depression covering an area of 7,000 km², with water levels dropping by 87.7 m in the centre of the cone. By the year 2000 the maximum cumulative subsidence in the area had reached to 2.8 m (Xue et al., 2008).

### 2.2. North China Plain (Beijing city) / North China plain (Pinggezhuang and Tianzhu stations)

Beijing is renowned as one of the most densely populated cities in the world and is also classified as having one of the highest subsidence risk deltas in China (Syvitski et al., 2009). This vast plain covers an area of almost 6,400 km² and is delimited by the Taihang and Jundu Mountains. The sediments constituting this plain originated from fluvial and alluvial processes. These deposits have led to the development of a distinct aquifer system with well-defined units. Overlying the bedrock, which consists of Cambrian-Permian rocks and forms the lateral and lower boundaries of the aquifer, are volcanic rocks from the Paleogene-Neogene period. The sediments that fill this rock geometry display varying granulometry and date back to the Pliocene and Quaternary periods, corresponding to the fluvial deposits of the delta(Zhang et al., 2014). The aquifer-system is a multi-layer system consisting of five confined aquifers separated by low-permeability layers. Currently, the three uppermost aquifers are the most heavily exploited, serving as sources of water supply for domestic and industrial purposes.

The extensometer stations at Pinggezhuang and Tianzhu are located to the south of Beijing. The

Tianzhu extensometer is situated in an area that has experienced significant groundwater extraction since 2004. It is positioned at the confluence of two alluvial fans from the Wenyu and Chaobai rivers. Meanwhile, the Pinggezhuang extensometer is installed in one of the five areas in Beijing with the highest subsidence rates (up to 24 mm/year). This area is also situated over the alluvial fan of the Chaobai River. Both extensometers are positioned within sedimentary deposits that have been accumulating through fluvial and alluvial processes since the Paleogene to the Quaternary period. The Pinggezhuang station records 380 m of Quaternary material characterized by heterogeneous granulometry. In contrast, the Tianzhu station spans over 500 m of aquifer thickness, owing to the intersection of two alluvial fans with a higher cumulative sedimentary deposition. In this location, the aquifer is further characterized as a multi-layer system composed of fine-grained deposits (Li et al., 2022).

Long-term over-exploitation of groundwater has caused a drastic decline in piezometric levels, with a maximum lowering of about 30 meters in both phreatic and confined aquifer systems from 2004 to 2010 (Zhu et al., 2015). This significant reduction in water levels resulted in sediment compaction and extensive land subsidence. The most important cumulative land subsidence in the region, reached up to 600 mm from 1955 to 2009, to monitoring these displacement borehole extensometers were set up in 2004 and 2008 in a couple of sites, with the deepest monitoring reaching around 250 meters, and a reference point established at a bedrock depth of 900 meters. Furthermore, from June 2003 to January 2010, PSI (Permanent Scatterer Interferometry) study measured the largest annual land subsidence up to 52 mm/year, with a maximum cumulative subsidence of 342 mm (Zhu et al., 2020).

### 2.3. Madrid aquifer, central Spain

The Madrid Tertiary aquifer system is a sedimentary basin covering an area of approximately 600 km². This basin presents a triangular shape and is surrounded by various mountain ranges, including the Toledo, Altamira, and the Central System Ranges. The aquifer in this region corresponds to an unconfined aquifer system comprising materials from continental environments dating from the early Cenozoic to the upper Miocene. It represents the primary freshwater reservoir in the Community of Madrid. While the mean thickness of the aquifer typically measures around 1,000 m, in certain locations, it can extend to a potential depth of 3,000 m. The aquifer's multilayer structure consists of different levels of sand lenses embedded within a low-permeability clay matrix (Béjar-Pizarro et al., 2017).

### 3. Data and methodology

To assess the effectiveness of the developed application, datasets from various aquifers around the world were chosen from scientific literature, including those from Madrid (Béjar-Pizarro et al., 2017), Shanghai and Beijing (Zhang et al., 2014) Certain criteria were applied when selecting these papers.

Figure 2 summarizes the methodology applied in this paper. As shown in the figure, two steps are

carried out in the MATLAB software. The first step, detailed in Section 3.2, focuses on the automation of constructing and plotting stress-strain curves. The second step, described in Section 3.3, has been developed to automate the extraction and calculation of the  $S_{ke}$  and  $S_{kv}$  parameters from the stress-strain curves.

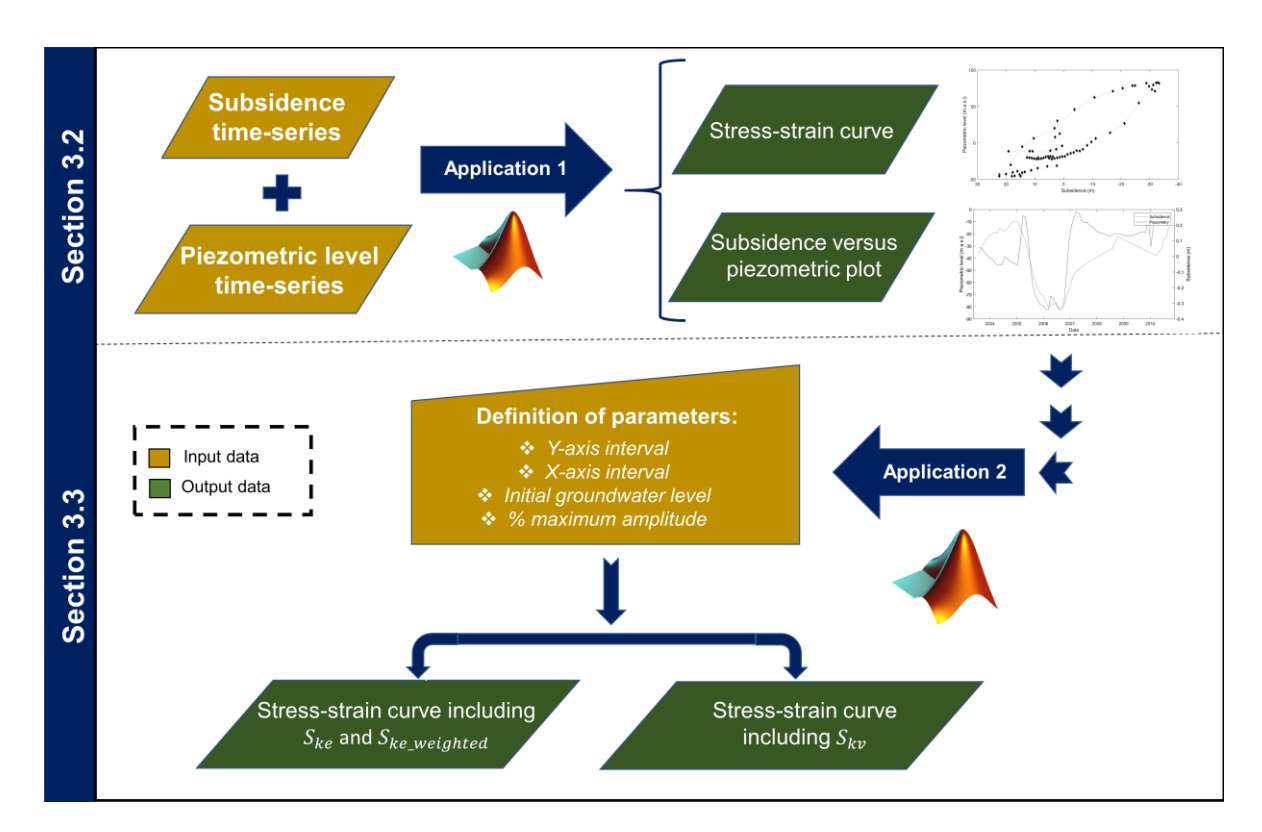


**Figure 2**. Flowchart used in the stress-strain curves and the calculation of the  $S_{ke}$  and  $S_{kv}$  parameters performed by the developed application.

### 3.1. Data collection and digitalization

To acquire the data utilized in this paper, it was essential to digitize time series plots for subsidence and piezometric measurements from aquifers in diverse global locations. To this aim, the open-source software "WebPlotDigitizer" (Rohatgi, 2021), a web-based tool adept at extracting information from graphics, images, and maps, was used. The digitized datasets were subsequently employed to create stress-strain curves It is noteworthy to emphasize this fact because it demonstrates that the data used in the current study may not be identical to that used in the original research from which it was obtained. Table 1 summarizes the information pertaining to the digitized time series data gathered from previous scientific studies conducted in various regions worldwide which have been described in section 2.

 Table 1. Summary of digitized time series. E: Elastic; EP: Elastoplastic; Ex: Extensometer.

Reference	Location	Nº of SS curves	Instrumentation	Behaviour
Zhang, et al., 2007a	Shanghai, China	3	Ex	EP
Zhang et al., 2007b	Shanghai, China	2	Ex	EP
Zhang et al., 2014	North China plain	7	InSAR	E and EP
Béjar-Pizarro et al., 2017	Madrid, Spain	17	InSAR	E
(Li et al., 2022)	North China plain	3	Ex	E and EP

### 

### 3.2. Plotting the stress-strain curves using a MATLAB application

The first application developed is focus on the plotting of the stress-strain curves, the complete application can be found in the supplementary material S1 and is accessible through Zenodo repository (www.xxxx). In the first step, the program prompts the user to upload an Excel file containing: a) pre-listed time series of deformations  $(t_i, s_i)$ , where  $s_i$  represents the deformation measured at time  $t_i$ , with j varying from 1 to m, and m representing the number of subsidence measurements; b) and piezometric levels time series  $(t_i, h_i)$ , where  $h_i$  represents the piezometric level measured at time  $t_i$ , with 'i' varying from 1 to 'n', and 'n' representing the number of piezometric samples. These data are organized in four columns (a pair of columns accounting for date  $t_i$  and ground deformation  $s_i$  values and an equivalent pair of columns for the date  $t_i$  and the piezometric level  $h_i$  into an Excel template. It is not required for the user to input time series with the same length or the same initial, intermediate and final dates. The program automatically identifies and assigns a uniform data format, then plots both time series accordingly. Furthermore, the application identifies the common period from both time series, and evaluates if the common period is long enough to continue with further analysis. The time series of deformation and groundwater level are then represented in the same plot, using different vertical axes (piezometric level in the left vertical axis and land subsidence in the secondary right vertical axis).

The final step involves generating the stress-strain curves. To develop this plot, it is required to have common data from both piezometric  $(t_i,\ h_i)$  and land subsidence  $(t_j,\ s_j)$  time series. Since the information usually comes from different sources and field campaigns the data from both time series typically have a distinct sampling date (i.e., "ij" for the common time period) and data acquisition frequency. To address this issue, the developed application first analyses and identifies the densest time series during the common period. Then, it extracts data from the densest time series using the dates from the other time series and performs linear interpolation between consecutive values. For example, considering that  $n_c$  and  $m_c$  are the number of data points in the common period for the piezometry and the land subsidence, respectively, if  $n_c < m_c$ , then the time series of subsidence present a denser sampling than the piezometric time series and, therefore, new

values of subsidence will be obtained by interpolation at the same dates when piezometric data exist. Once the interpolation process has finished, the application provides the data pairs of subsidence and piezometric level at the same dates, and then the stress-strain curves can be plotted using the interpolated pairs of  $s_i$  and  $h_i$  values calculated for the common dates.

### 3.3. Extraction of the $S_{ke}$ and $S_{kv}$ parameters from stress-strain curves using a MATLAB application

The second application (available in the supplementary material S2) is focused on extracting the skeletal storage coefficients of an aquifer system (elastic or inelastic). This automation involves the most complex step in the development of the application. The elastic skeletal storage ( $S_{ke}$ ) can be calculated from the slope of the elastic segments identified in the stress-strain curve, as indicated in eq. (6). In case that the stress-strain plot reveals the existence of more than one elastic segment, the application will identify all of them, and will obtain the  $S_{ke}$  for each cycle. It allows for the computation of a mean  $S_{ke}$  value considering all  $S_{ke}$  values across cycles. This mean  $S_{ke}$  value can be considered as the characteristic value for the aquifer system.

Similarly, the inelastic skeletal storage  $(S_{kv})$  can be calculated from the slope of the line that best fits all the piezometry-subsidence data using eq. (6). Lastly, by knowing the thickness of the aquifer or the analysed layer, it is possible to estimate the specific storage coefficient due to the compressibility of the solid skeleton  $(S_{sk})$  (Equation 7.).

In detail, the software starts by prompting the user to provide an Excel file containing the necessary data for generating the stress-strain curve described in section 3.2. The first column should contain subsidence data as input, while the second column should contain piezometric data (Figure 3a.). Both datasets should be in the same length units (e.g., meters). The application has been designed to identify any discrepancies in the amount of data between the two columns. In such cases, an error alert will appear on the screen.

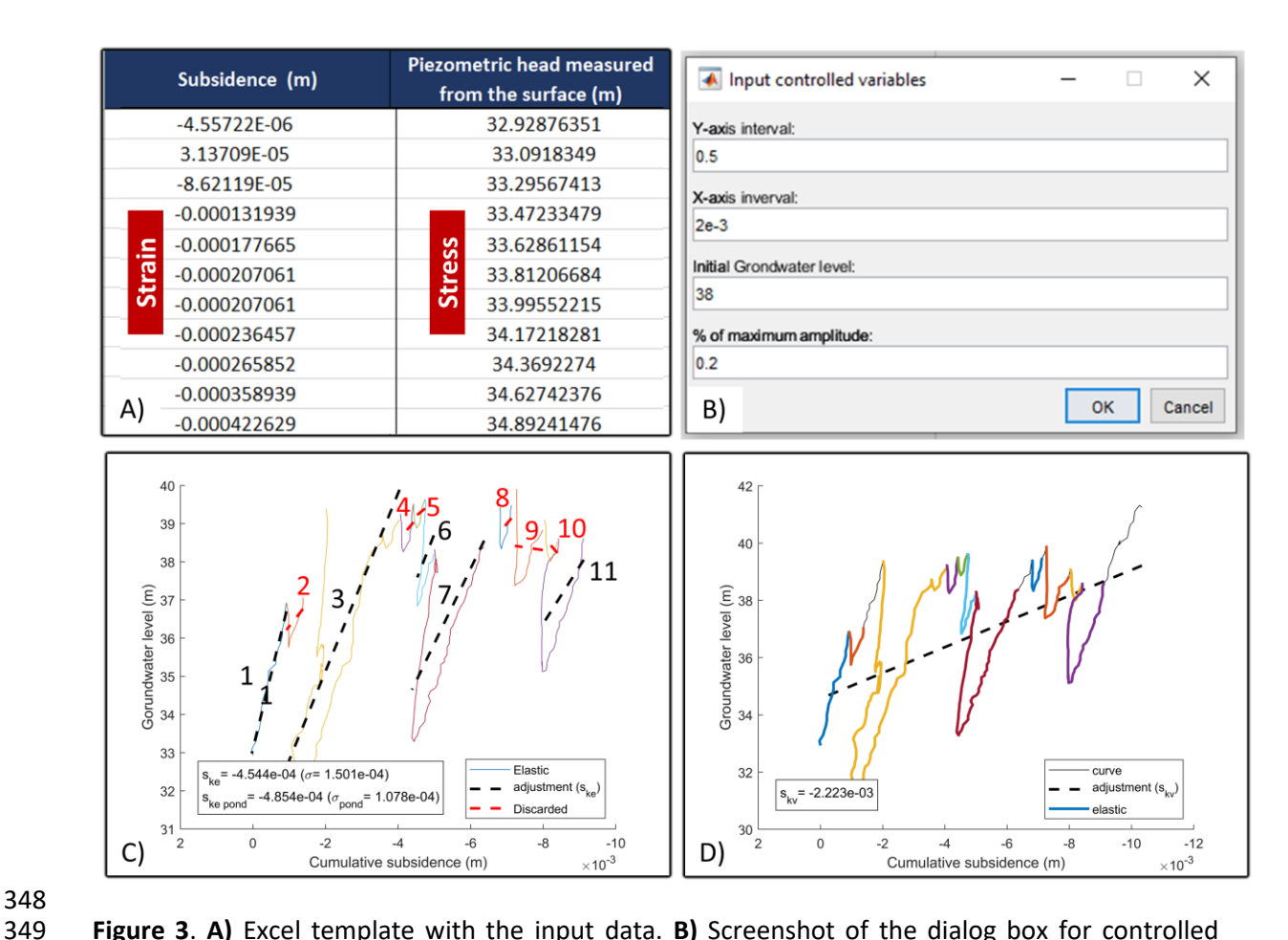


**Figure 3. A)** Excel template with the input data. **B)** Screenshot of the dialog box for controlled variable input in MALAB. **C)** Elastic cycles generated by the application (plotted in different colours). The valid elastic segments utilized in the analysis are denoted by 1, 3, 6, 7, and 11. Segments 2, 4, 5, and 8 were discarded due to their small amplitude, while segments 9 and 10 were discarded due to their inverse slope. **D)** Plot of the stress-strain curve including all the elastic loops. The dashed line represents the linear regression of the entire dataset.

### 3.1.1. Defining the user-input parameters.

To perform the analysis effectively, the application requires four specific input parameters to be defined by the user (through a prompt window, Figure 3b). These variables are as follows: a) the 'Y-axis interval' (minimum variation of piezometric level to accept the existence of an elastic cycle); b) the 'X-axis interval'; c) The 'Initial groundwater level' corresponds to the preconsolidation head, which indicates the minimum piezometric head (I.e. the maximum effective stress) recorded in the aquifer system throughout its history, expressed in terms of piezometric head; and d) the '% of maximum amplitude', which enables the filtering out of very small elastic or inelastic segments in the curve which in turns may not be representative of the aquifer system.

Once the input data is correctly processed by the application, the application automatically begins to distinguish between elastic and inelastic segments. These user-defined parameters play a crucial

role in identifying the segments and signals related to different mechanical behaviours. Their primary function is to enable the application's adaptation to any study case, considering the unique characteristics of each site, which may vary significantly (S2). It is worth noting that properly applying and defining these parameters implies prior knowledge of the magnitude of subsidence and piezometric heads in each study area. However, the use of the application let the user to try several values of the parameters and check the suitability of them to the specific study case. To distinguish elastic from inelastic segments, the application proceeds to identify the relative maximum and minimum points on the stress-strain curve. The maximum points can potentially represent changes in aquifer behaviour or even preconsolidation head values. However, not all maximum points separate the elastic and inelastic segments. Therefore, it is essential to select those maximum values that genuinely mark the beginning of an elastic segment in the curve. The first condition required to classify a segment as elastic is that the difference in piezometric head between consecutive maximum and minimum points must exceed the value of the 'Y-axis interval' previously set by the user. When this condition is met, the relative maximum is saved by the application. This process is repeated for all relative maxima found in the curve, and the resulting values are stored in a matrix of maximum values.

After identifying the first relative maximum, two different situations may arise when defining an elastic segment:

A. If the subsequent maximum point (which also satisfies the 'Y-axis interval' condition) has a lower piezometric value than the originally defined 'initial groundwater level' value, that maximum will mark the end of the initial elastic segment. In this scenario, the preconsolidation head (I.e., the 'Initial groundwater level') has not yet been exceeded, and the aquifer exhibits elastic behaviour as the piezometric head does not exceed the preconsolidation head.

B. Conversely, in the opposite situation, if the subsequent point has a higher piezometric value than that defined for the 'Initial groundwater level', the elastic segment will finish when the piezometric head reaches the value of the first maximum registered piezometric head until this time (I.e., the 'Initial groundwater level'). Following this, the application will then proceed to sequentially search for the subsequent point that exceeds the piezometric head of the previous maximum, indicating that the preconsolidation pressure has been surpassed. This situation can lead to irreversible deformations.

The previously described logic operator will be sequentially applied to all the maximum points that meet the 'Y-axis interval' condition. It is important to note that the application prompts the user beforehand to specify the piezometric head changes they wish to consider for discretizing the elastic and inelastic segments.

The second controlled condition involves setting a specific 'X-axis interval' value, which enables the mitigation of potential issues arising from the inherent distribution of data noise. This condition specifies that in order for a point to be recognized as a maximum, there must be a minimum horizontal gap between two consecutive maxima. Typically, the value of the X-axis interval is quite small (e.g., 0.0001, 0.0002 or 0.005 m). The objective is to eliminate relative maxima that may arise

due to factors such as digitization, instrument accuracy (e.g., piezometers, extensometers, InSAR, etc.), or even noise in the time series signal. Moreover, this condition allows to discard minor trends that might interfere with broader trends, which are the primary focus of this study.

Another crucial aspect to consider is the maximum historical stress preceding the analysed time series represented by the 'Initial groundwater level'. In most of the cases, this value is unknown in advance and is adopted as the first minimum value of the piezometric head of the time series. Consequently, if the initial data points of the stress-strain curve do not exceed this preconsolidation head value, they will be considered as elastic segments. When the initial preconsolidation head value is unknown, the application will consider that this preconsolidation head equals the first registered value of piezometric level of the time series. Then, the first segment of the graph, if it shows an increase in the pressure value, will be considered as belonging to an inelastic domain until the curve reaches its first maximum that satisfies the first two conditions mentioned above. This maximum will then replace the previous preconsolidation pressure value and it will be considered as the starting point of the first elastic segment.

After delineating the various segments, the application will perform a linear regression fitting for each elastic segment or loop. The inverse of the slope of each of these j-segments (subsidence/piezometric head) will provide the skeletal storage  $(S_{kej})$ , specifically the elastic component. The mean value of  $S_{kej}$  across all loops will enable the determination of an average  $S_{ke}$  value for each stress-strain curve (Figure 3c). Since the sizes of the loops can vary depending on the amount of data, it is also possible to estimate a weighted elastic skeletal storage  $(S_{ke\_weighted})$  by considering the total elastic points and the number of points composing each loop.

When examining the segmented stress-strain curves, it is common to observe elastic loops of considerable size alongside others that are relatively small in comparison. This situation can impact the final results. Even though we consider the weighted value mentioned earlier, it is advisable to exclude very small loops from the calculation of  $S_{ke}$ . This is because linear fitting is much more likely to produce inaccurate estimations of  $S_{ke}$  from small loops. To address this issue, the application identifies the loop with a higher amplitude in the Y-axis (I.e., with the difference between the maximum and minimum piezometric head). Then, using the value of '% of maximum amplitude' small loops are eliminated. In practical terms, the application applies an amplitude percentage of the largest loop to all identified small loops to determine which ones to discard. For example, if the largest elastic loop has an amplitude of 10 m and the user-defined amplitude percentage is 20%, all loops with an amplitude less than 2 m will not be considered in the calculation of  $S_{ke}$ . Additionally, adjustment lines with an inverse slope will be discarded, as they do not make physical sense (see Figure 3c).

The algorithm produces an initial graph showing piezometric head versus cumulative subsidence as output. This graph encompasses all the differential elastic segments defined by considering the first three user-controlled variables: the 'Y-axis interval', the 'X-axis interval', and the 'Initial groundwater level' (i.e., the preconsolidation head) prior to the analysed time series. Each loop is represented by its best-fit line for the data, indicated by a dotted line. The black adjustment lines represent the

slopes used to calculate the elastic skeletal storage. Conversely, the red lines indicate segments that have been discarded either because they don't meet the '% of maximum amplitude' criterion and/or the slope of the line is inverse (see Figure 3c). Afterward, the algorithm generates a second graph displaying the complete stress-strain curve data in black. Overlaying this data in a different colour are the elastic segments defined earlier. As a result, the inelastic segment is presented in black dashed line. Finally, the linear regression of the complete dataset allows for the calculation of the inelastic skeletal storage ( $S_{kv}$ ) by determining the inverse slope of the adjustment line (see Figure 3d).

In addition to generating the graphics mentioned above, the application also saves on the last sheet of the input excel templated all  $S_{ke}$ ,  $S_{ke\_weighted}$  corresponding to each loop (both selected and discarded) as well as the  $S_{kv}$ . Complete

### 4. Results

This section details the results for each study area described in the section 2. The parameters used for the calculation of the coefficients are listed in the supplementary material (S1).

### 4.1. Southern Yangtse Delta, China

Five stress-strain curves from the aquifer beneath Shanghai city have been analysed, each corresponding to different extensometers and/or different aquifer layers (see S2). From the information provided in Zhang et al. (2007a), three stress-strain curves were constructed. The first curve analysed corresponds to the second confined aquifer. In this curve, the application identified 35 elastic segments; however, for the calculation of  $S_{ke}$ , 34 of these segments were used. One elastic loop was discarded because it did not exceed the established amplitude percentage (10%), as shown in Figure 4a. The second stress-strain curve corresponds to the second aquitard, and it exhibits loading and unloading cycles due to seasonality (Figure 4c). The elastic skeletal storage was calculated using 22 elastic loops, and the adjustment curve that encompasses all the data aligns well with the general trend of the stress-strain curve (Figure 4d). The last curve corresponds to the third aquitard (Figures 4e-f). In this curve, it is evident how the loops widen as subsidence increases, leading to a progressive increase in the slope of the line. However, the last five elastic segments exhibit opposite slopes, which is the reason these segments were discarded. For the calculation of  $S_{ke}$  and  $S_{ke}$  weighted, 26 elastic segments were considered (Figure 4e).

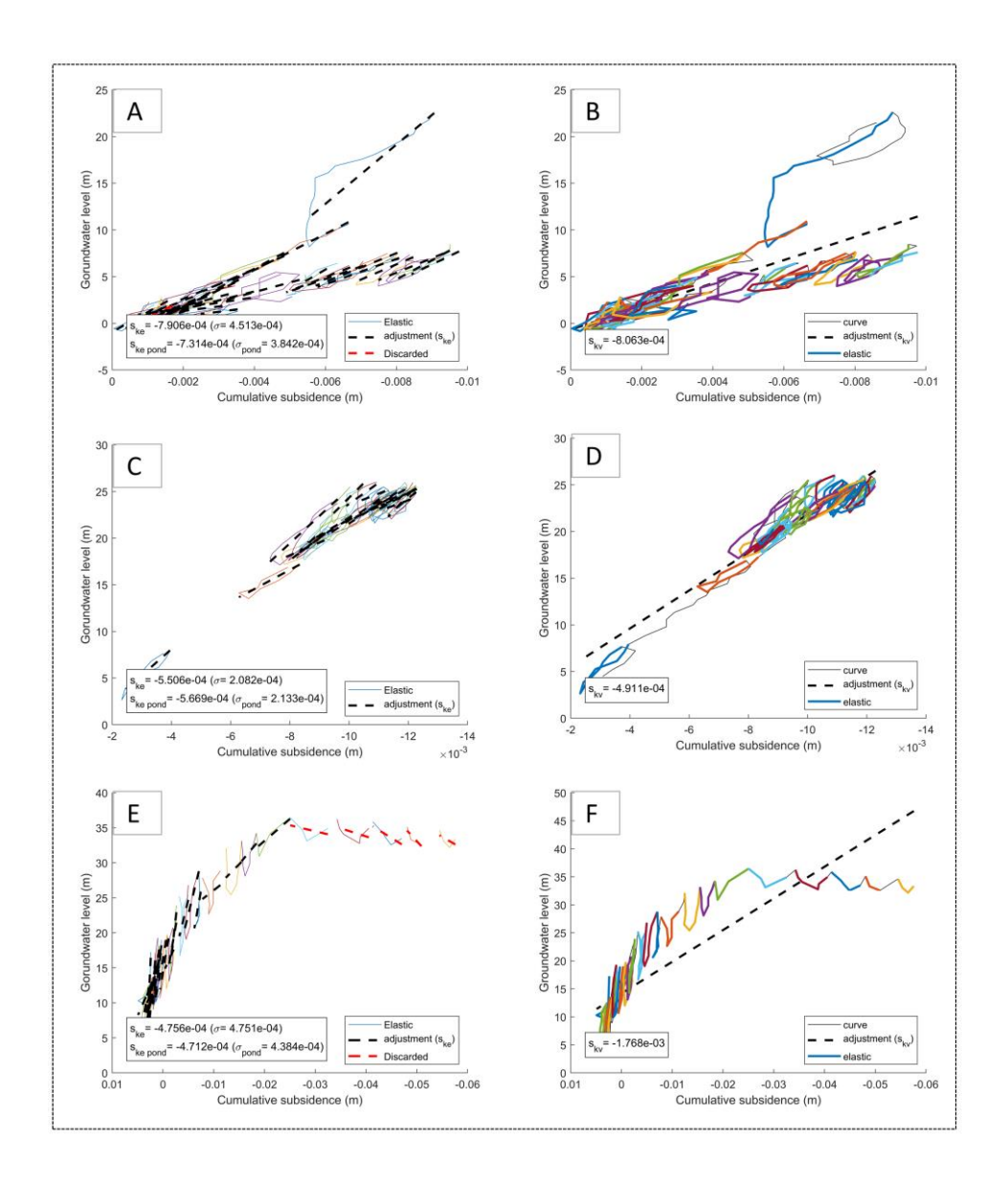


**Figure 4.** Stress-strain curves results from the Southern Yangtse Delta. (A-B) Second confined aquifer; (C-D) Second aquitard layer. (E-F) Third aquitard layer.

Since the thickness of the layers (aquitards and aquifers) is known, it was possible to calculate the elastic and inelastic specific storage coefficients ( $S_{ske}$ ,  $S_{ske\_weighted}$ , and  $S_{skv}$ ). All of these coefficients are listed in the supplementary material (S4).

### 4.2. North China Plain (Beijing city)

Seven stress-strain curves were obtained from Zhang et al. (2014). These curves correspond to three aquifer levels and four aquitard levels; information about the thickness of these layers is provided in S5. In the present section, we will select and describe only one aquifer and one aquitard layer. Stress-strain curves for the remaining layers are presented in the supplementary material S6-7.

In the second aquifer level, seven elastic segments were identified by the application (Figure 5a). In this case, a 35% amplitude percentage was applied, which represents the highest value used in this case study. This higher percentage was necessary to exclude segments shown in blue and purple in Figure 5a. These segments had adjustment lines that did not correspond to logical values for the calculation. As a result, the standard deviation of the data exhibited small magnitudes, on the order of 10<sup>-5</sup> and 10<sup>-4</sup>. It is important to note that the second segment in orange had a significant influence on the coefficient calculation. This segment comprised 97 data points, whereas the other segments had fewer data points, specifically 31, 40, and 48 points. Concerning the first segment of the stress-strain curve in blue, it was considered as an elastic segment. This classification was based on the third variable controlled by the user, which is the initial preconsolidation head. Finally, Figure 5b displays the adjustment line for all the data, illustrating that the global trend aligns well with the entire set of elastic loops.

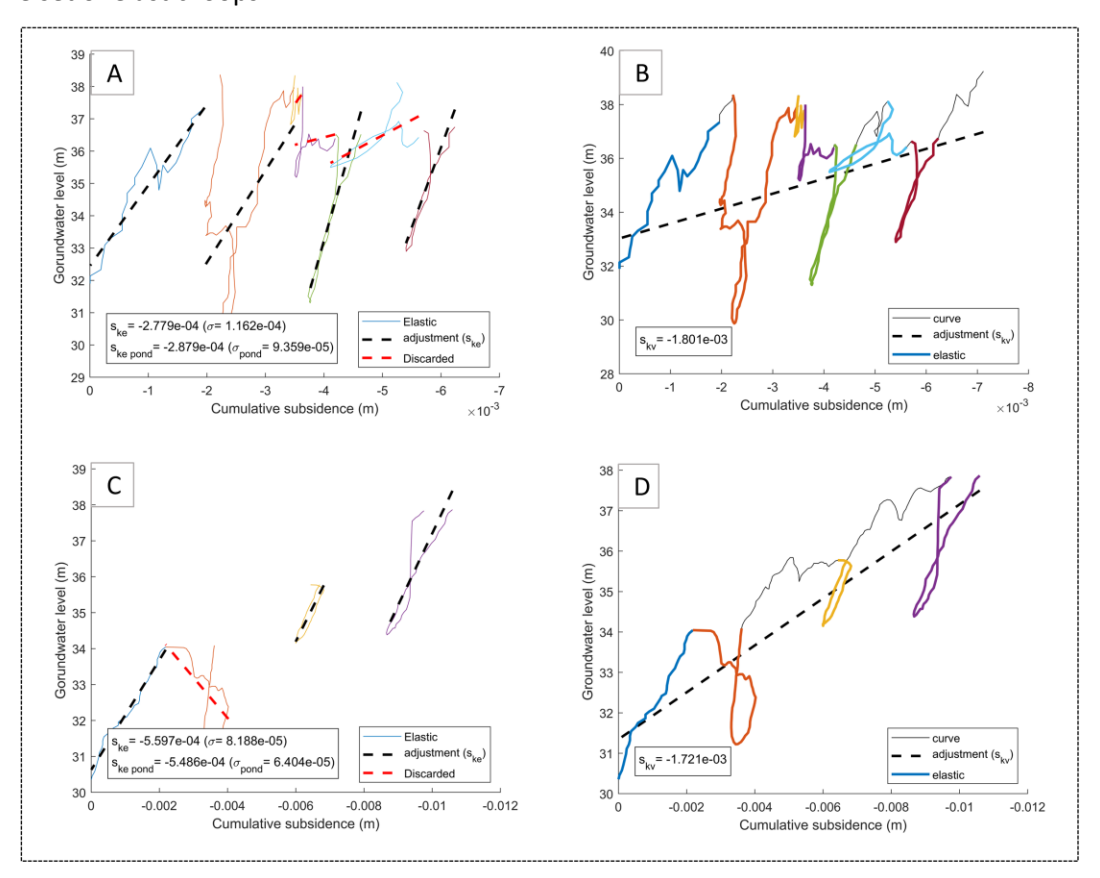


**Figure 5.** Stress-strain curves results from the Plain of Beijing. (A-B) Second aquifer layer; (C-D) last aquitard layer.

The last aquitard layer corresponds to the maximum depth of the system, and this layer exhibits a clear increasing trend in cumulative subsidence as the piezometric head increases. Figure 5c illustrates the presence of three elastic loops; the first one was discarded because its adjustment line had an inverse slope. However, the other two loops displayed similar values of the adjustment lines, resulting in low standard deviation values. Notably, the adjustment line for all the data points closely matches the general trend of the stress-strain curve (refer to Figure 5d).

The values of all the calculated coefficients for each aquifer layer, taking into account their respective thicknesses, are summarized in the supplementary material S8.

#### 4.3. North China Plain (Pinggezhuang and Tianzhu stations)

In this section, two of the six stress-strain curves analysed by Li et al. (2022) are presented. A table containing information on the thickness of each layer can be found in the supplementary material S9.

One of the layers analysed by the Pinggezhuang extensometer is depicted in Figure 6a. In this stress-strain curve, eight elastic segments were initially identified. However, three of them were excluded because they did not meet the percentage of amplitude condition, with values exceeding 35%. Additionally, the last loop was disregarded due to its inverse slope. Consequently, only four segments were considered for calculating the hydrogeological coefficient. These four segments exhibited similar trends, resulting in a small standard deviation value. Similar to previous stress-strain curves, the adjustment line for all the data conformed well to the overall trend of the curve, passing through all the larger elastic loops (refer to Figure 6b).

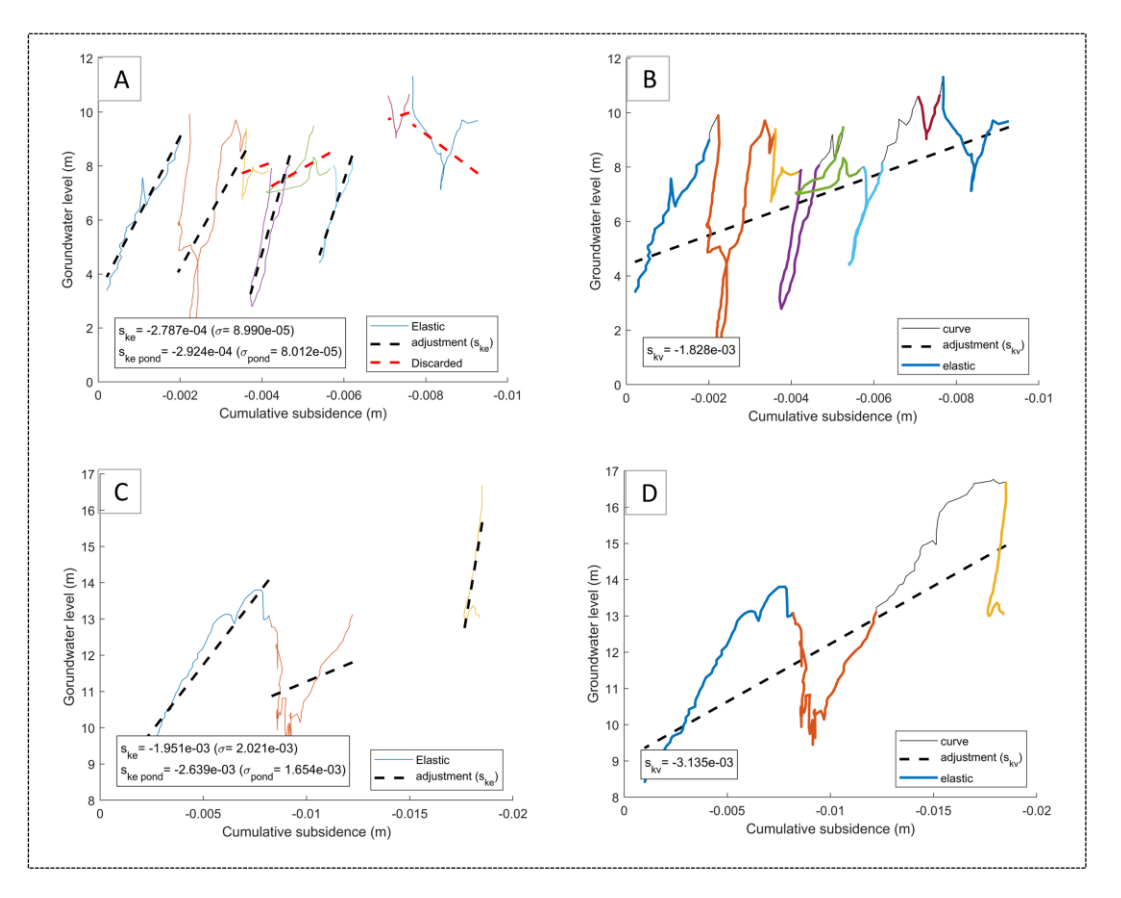


**Figure 6.** Stress-strain curves results from North China plain. (A-B) Second layer - Pinggezhuang station; (C-D) Third layer - Tianzhu station.

The layer studied by the Tianzhu extensometer exhibits a stress-strain curve that is notably different from the others in the study area. As shown in Figure 7c, this layer does not display a recovery of cumulative subsidence when the piezometric level decreases. This indicates that the materials in this layer are not demonstrating elastic behaviour. While a  $S_{ke}$  coefficient value is presented in Figure 6c, it does not accurately reflect reality, and the elastic value is not considered for validation. In this case, for validation purposes, the  $S_{kv}$  value shown in Figure 6d is used for the validation analysis in the section 5.

To summarize the coefficient values for all the stress-strain curves constructed in this study area, accounting for the thickness of the studied layers, please refer to Table S11 in the supplementary material.

#### 4.4. Madrid aquifer, central Spain

In this study area, 17 stress-strain curves digitized from the supplementary material of the paper published by Béjar-Pizarro et al. (2017) have been built based on the different wells distributed in the Madrid Tertiary aquifer-system. To obtain the global hydrogeological parameters the thickness of the layers has been standardized at 154 m.

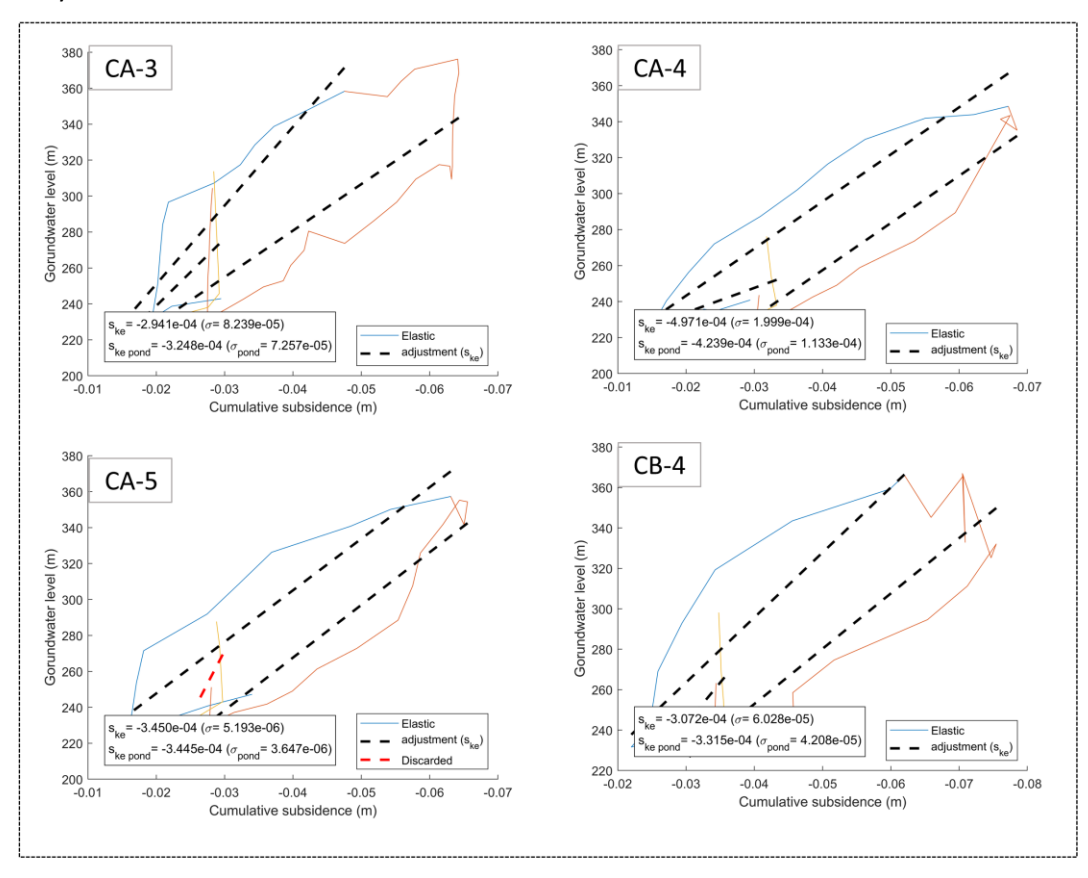


**Figure 7.** Stress-strain curves results from the Madrid Tertiary aguifer-system.

These curves exhibit notable differences compared to those previously analysed. In this case, the time series are relatively shorter, spanning from 2004 to 2010. Additionally, the intrinsic characteristics of the materials result in a single, distinctive elastic loop in the majority of cases without the observation of a plastic deformation. Consequently, the focus of the analysis in this study area is on distinguishing between segments exhibiting elastic behaviour rather than identifying complete elastic loops. Figure 7. illustrates some of the stress-strain curves generated by the MATLAB application. All the others curves appear in the Figure S12-13.

A similar overall trend is observed in the majority of the stress-strain curves, with the presence of an important elastic loop. Across all the curves, two primary segments can be identified. One of these segments is associated with the loading and unloading branches of the main loop. Furthermore, in cases where curves exhibit smaller loops, they typically consist of more than two larger elastic segments. These smaller loops tend to appear at the edges of the largest loop (see Figure 7).

Because the detrital material comprising the Madrid aquifer primarily exhibits elastic behaviour, there is no need to calculate the inelastic skeletal storage coefficient ( $S_{kv}$ ). Instead, the global  $S_{ke}$ , as well as the  $S_{ke}$  and  $S_{ke\_weighted}$  coefficients, have been included. These values are presented in Table S14.

### 5. Discussion

In this section, the results obtained using the MATLAB application are validated by comparing them with the digitized time series, for which coefficients have been calculated using the methodology proposed by Riley (1969).

In the Southern Yangtse Delta, all the stress-strain curves exhibit elasto-plastic behaviour, involving both recoverable and non-recoverable deformations. The calculated slopes are very similar to those calculated by Zhang et al. (2007a & 2007b). Furthermore, in all the curves, the  $S_{ke}$  value calculated by Zhang et al. (2007a & 2007b) falls within the range of maximum and minimum slopes identified by the application and relatively close to the average  $S_{ke}$ . This indicates that the  $S_{ke\_Zhang}(2007)$  corresponds to one of the elastic loops considered by the application (see Figure 8). It's important to note that the discrepancies are primarily related to the fact that Zhang et al. (2007a & 2007b) calculated the coefficients based on only one elastic loop, while the application is capable of considering all the elastic loops and subsequently calculating statistical parameters such as the mean and weighted mean of the  $S_{ke}$ . This approach aims to enhance accuracy and reduce subjectivity.

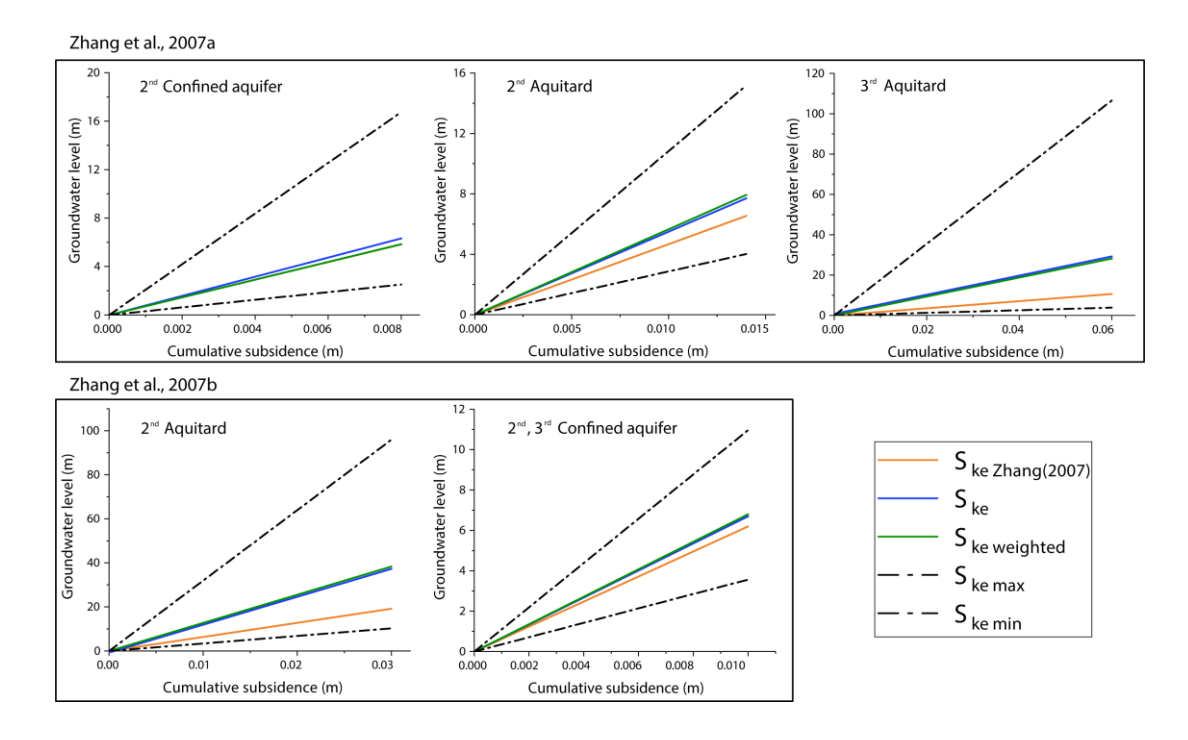


**Figure 8.** Comparison between the elastic storage coefficients calculated by the MATLAB application and the coefficients calculated by Zhang et al. (2007a & 2007b).

 Regarding the  $S_{kv}$  values, all of them also closely resemble those calculated by Zhang et al. (2007a & 2007b). These values are presented in Table S15, which displays all the coefficients calculated by the application alongside those computed by Zhang et al. (2007a & 2007b) for each aquifer and aquitard layer. The comparison between the  $S_{ke}$  values is depicted in Figure 9. This figure illustrates the discrepancies between the original and the calculated  $S_{ke}$  coefficients. It is crucial to highlight that in the presents paper, it was not possible to utilize the exact values considered as originals because they were derived from a digitization process, which could introduce some inaccuracies.

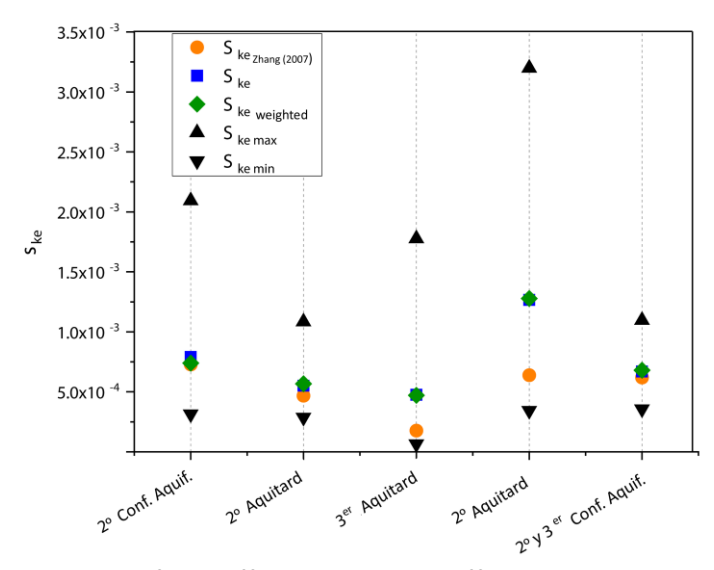


Figure 9. Comparison graphic of the different storage coefficients in the Southern Yangtse Delta.

In the plain of Beijing, only the first confined aquifer layer has an elastic behaviour, the rest of the layers present an elasto-plastic behaviour. All the elastic and inelastic skeletal storage coefficients obtained by the application of the developed application appear in the Table S16.

In the case of the shallow aquifer layer exhibiting elastic behaviour of the plain of Beijing, similar storage coefficients ( $S_{ke}$ ) were obtained with the developed application as compared to  $S_{ke\_Zhang(2014)}$  2.250 x 10<sup>-4</sup> and 2.72 x 10<sup>-4</sup> respectively. It's important to highlight that  $S_{ke\_Zhang(2014)}$  was derived from a linear fitting to all the data, which might not be entirely suitable for this type of terrain. The resulting  $S_{ke}$  (global) obtained from fitting all the data was (2.70 x 10<sup>-4</sup>). It was observed that  $S_{ke\_Zhang(2014)}$  did not consistently fall within the range defined by the maximum and minimum slopes of the other coefficients, indicating discrepancies (Figure S17). Moreover,  $S_{ke\_Zhang(2014)}$  tended to have numerically smaller values than  $S_{ke}$  and  $S_{ke\_weighted}$ , which was due to the asymmetrical behaviour of elastic loops in the curves (Figure 10.). Another important factor contributing to differences in the results was the number of segments considered to estimate the elastic storage coefficient. While Zhang et al. (2014) calculated this parameter using a single line, our methodology, as proposed in this study, involved multiple elastic segments for computing the averages ( $S_{ke}$  and  $S_{ke\_weighted}$ ) of the coefficients.

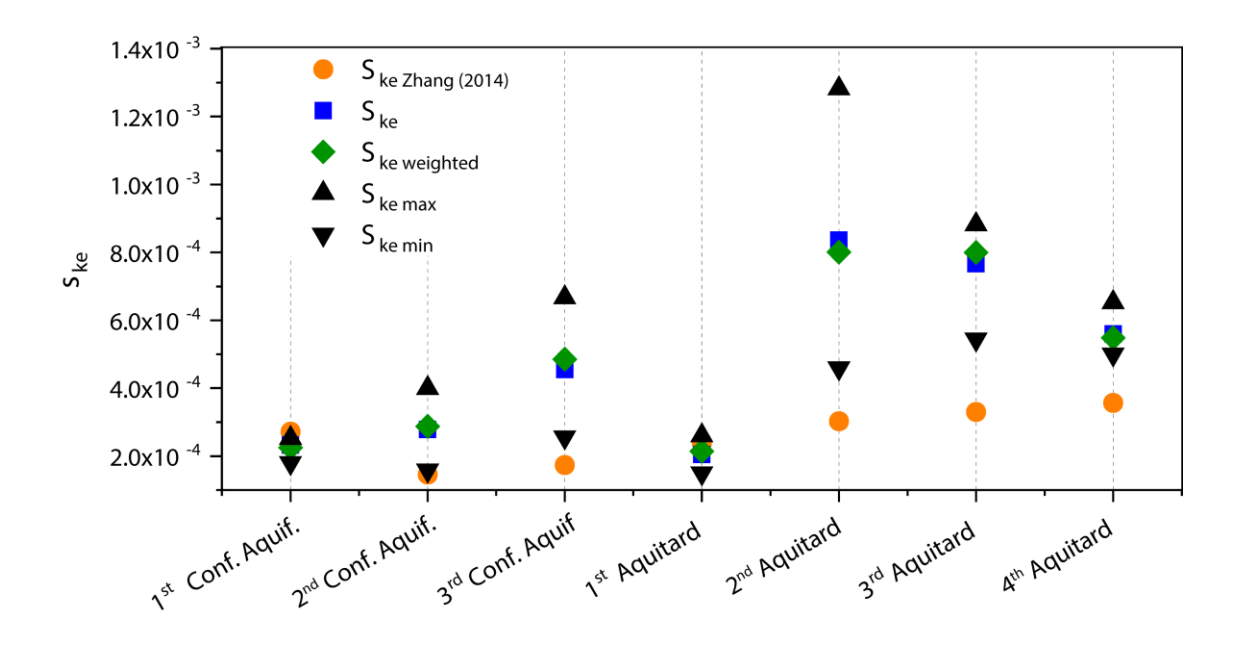


Figure 10. Comparison graphic of the different storage coefficients in the plain of Beijing.

In summary, the  $S_{kv}$  coefficients in the curves generally exhibited a similar order of magnitude to those in Zhang et al.(2014) (Table S16). Any minor variations could be attributed to the digitization process of the results from Zhang et al, which were used in the present study as input data for the developed application. Notably, the second aquitard level was the only one that displayed a slightly distinct global fitting line compared to the 2014 study, being somewhat more vertical.

Regarding to Pinggezhuang and Tianzhu stations in the North China Plain, the study reveals three distinct curve behaviours: elastic, elastoplastic, and primarily plastic. In Table S17. it can be seen that storage coefficients  $S_{ke}$  and  $S_{ke\_weighted}$ , and  $S_{kv}$ , closely align with those reported in Li et al. (2022).

In the Pinggezhuang extensometer, the first curve demonstrates elastic behaviour, four identified elastic segments exhibit similar trends, producing  $S_{ke}$  and  $S_{ke\_weighted}$  values near  $S_{ke\_Li(2022)}$  (6.864  $\times$  10<sup>-4</sup>). Notably,  $S_{ke\_Li(2022)}$  consistently falls within the range defined by the mean  $S_{ke\_max}$  and  $S_{ke\_min}$  values of these segments (Figure S19). In the second layer in the Pinggezhuang extensometer,  $S_{ke\_Li(2022)}$  does not align with the maximum and minimum slopes from the analysis (Figure S19). Nevertheless, numerical values are strikingly similar, with all  $S_{ke}$  values falling within the same order of magnitude (Table S17; Figure 11).

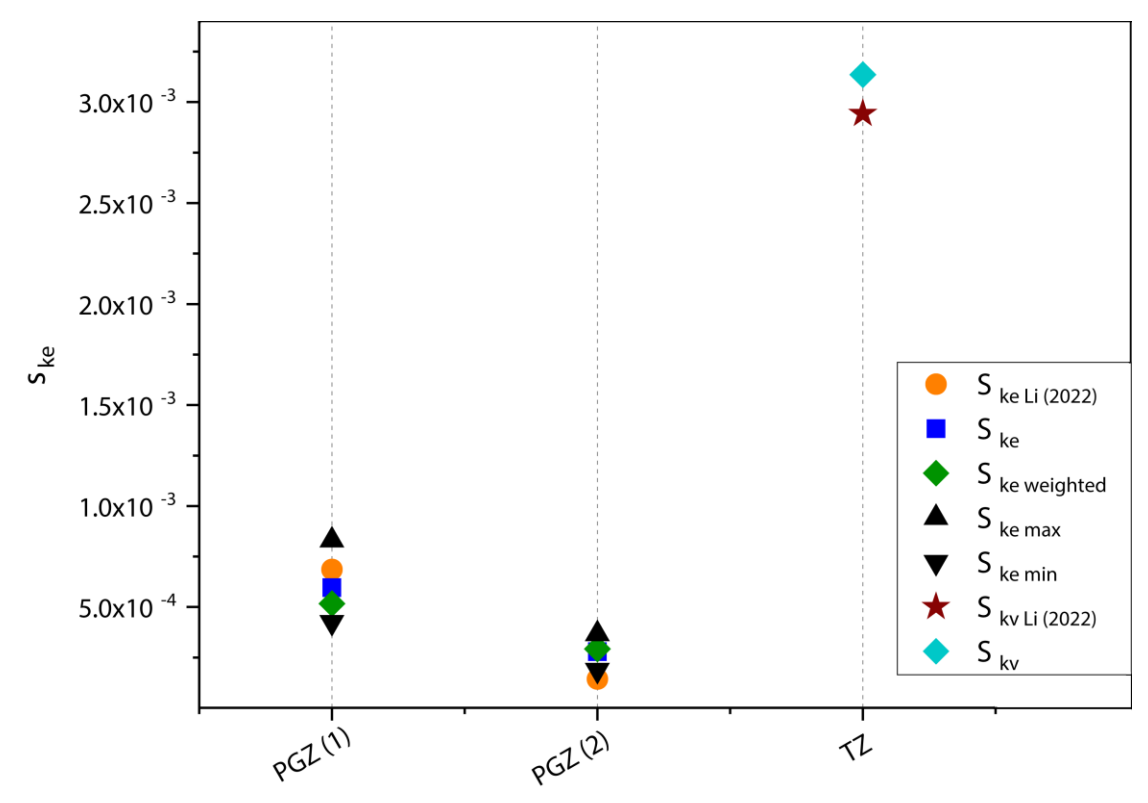
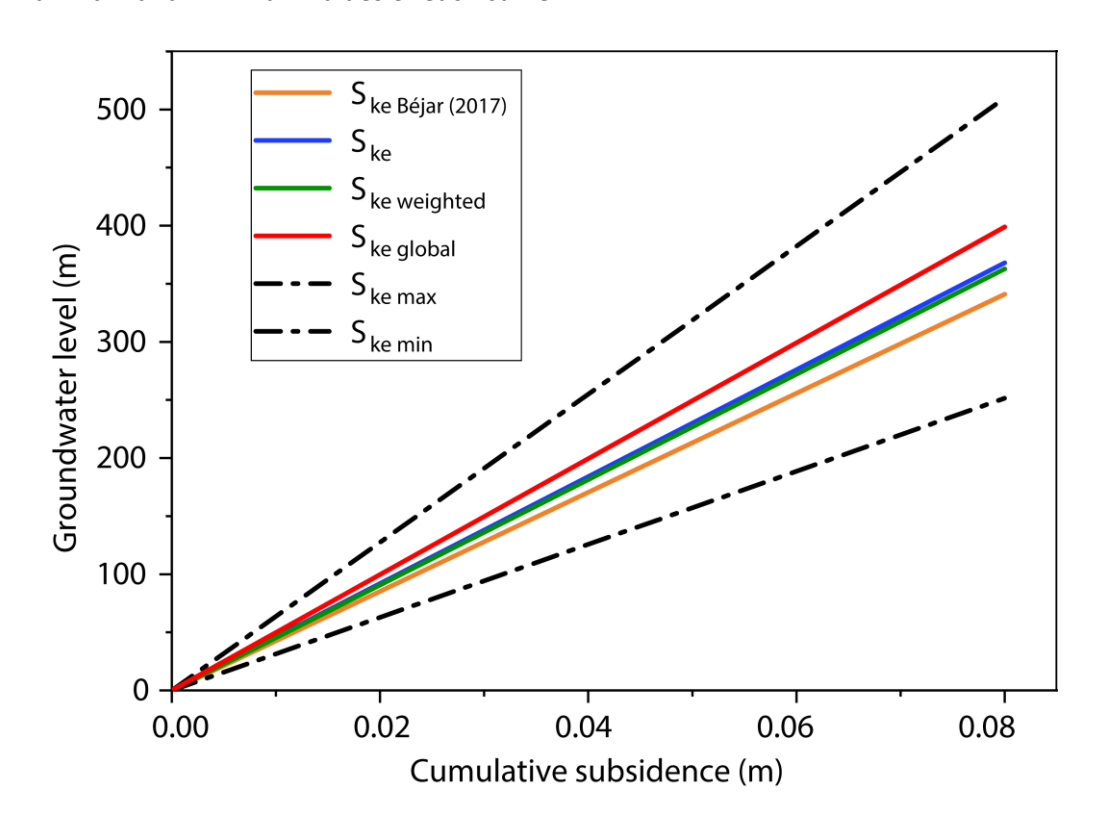


Figure 11. Comparison graphic of the different storage coefficients in the North China Plain.

Finally, despite the absence of elastic behaviour, the layer studied by the Tianzhu extensometer was also analysed using the MATLAB application. This emphasizes the significance of continuous oversight by a qualified researcher throughout the analysis, especially when inputting controlled variables and interpreting results. In this scenario, as deformation does not rebound as the water level increases, it does not distinguish elastic segments. Instead, it identifies periods where deformation halts or slows down without recovery. As a result, only inelastic storage coefficients are presented in the graphs, as elastic parameters are not applicable (Figure S19 and Figure 11).

For the Madrid aquifer case, that study combined InSAR data and water level measurements to obtain stress-strain curves which exhibit an elastic behaviour. Unlike other study areas that focus on specific aquifer layers, this research aims to assess the overall behaviour of the mulit-layer aquifer system. Among 17 curves analyses, the average of all elastic storage coefficients and the mean values taken from Béjar-Pizarro et al. (2017) are presented (Figure 12). The application-derived values with the novel application closely resemble the Béjar-Pizarro et al. (2017) average. Additionally,  $S_{ke\_B\acute{e}jar(2017)}$  consistently falls within the range defined by mean  $S_{ke\_min}$  and  $S_{ke\_max}$  values (Figure 12). Detailed analysis of each well reveals variable results with no clear pattern (Figure 13). In most cases, despite slight differences between the coefficients estimated by Béjar-Pizarro et al. (2017) and those obtained through this methodology,  $S_{ke\_B\acute{e}jar(2017)}$  falls within the maximum and minimum values of each curve.



**Figure 12.** Comparison between the elastic storage coefficients calculated by the MATLAB application and the coefficients calculated by Béjar-Pizarro et al. (2017)

Is worthy to highlight that this work does not aim to replicate the exact article results but rather demonstrates the application capability to analyse stress-strain curves with elastic and plastic behaviour, it is demonstrated that the application effectively successes such analysis. The obtained elastic storage coefficients, alongside  $S_{ke\_B\acute{e}jar(2017)}$ , reveal consistent results, falling within an order of magnitude of  $10^{-4}$  in all cases (Table S20; Figure 13).

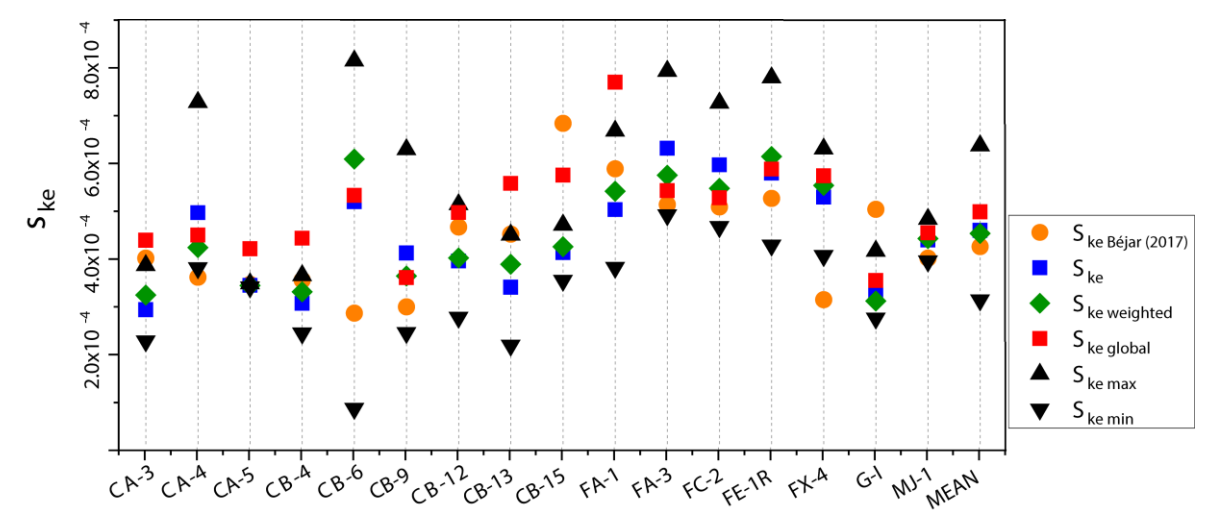


Figure 13. Comparison graphic of the different storage coefficients in the Madrid Aquifer.

In general, the results presented in this study show small differences in magnitude from values reported in the papers based on, with most hydrogeological parameters fitting into the same order of magnitude as is shown in the most of the figures above. It is important to point out that the use of data digitized from images, rather than original data, increases the data volume compared to the articles. This leads to variations in the least-squares fitting performed by the application and can explain the slight differences in results. Nevertheless, it has been demonstrated that the application performs a good analysis of the elastic and elastoplastic stress-strain curves, validating the proposed methodology for future studies in this field. In this section is also significant to highlight the differences between the characteristics of the  $S_{ke}$  (obtained through the arithmetic mean) and the  $S_{ke\_weighted}$  coefficient (calculated by considering the total elastic points and the number of points in each elastic segment) for the analysed curves. Despite these values are often similar, the  $S_{ke\_weighted}$  has an advantage as it assigns greater weight to larger loops, resulting in a more coherent final result.

In summary, the developed application enhances and partly automates studies related to land subsidence due to groundwater extraction from aquifers. It has broad temporal and spatial applicability, allowing for the estimation of hydrogeological parameters for entire aquifer systems or specific layers (aquitard or aquifer). These parameters play a crucial role in water resource management. In the context of addressing the critical role of hydrogeological parameters in water resource management, it can be considered how this paper discusses the significance of storage coefficients in assessing aquifer reserves and the volume of water that can be extracted from them (i.e., storage capacity and loss of an aquifer). With increasing water demand and the potential impact of land subsidence due to aquifer exploitation on over 600 million people, it is vital to quantify and analyse land behaviour through stress-strain studies. These studies can provide valuable insights for developing risk mitigation strategies in both urban and non-urban areas, potentially reducing infrastructure damage and saving significant costs.

At present, aquifer storage coefficients are determined through pumping tests at specific locations within the aquifer. However, the proposed methodology, supported by the novel developed

application, could estimate the storage coefficient for the entire aquifer system if deformation data for the entire aquifer surface, obtained through InSAR or other measurement systems, were available. This approach would reduce the economic costs associated with well construction and pumping tests, it would also provide global hydrogeological parameters for the entire aquifer system (which can also be valuable for subsidence modelling purposes) and it would produce those advantages with a much time-efficient methodology

Furthermore, potential application modifications and updates could enable the study of terrains with visco-elastoplastic behaviour and the identification of segments in stress-strain curves with viscous behaviour (where deformation continues despite water level recovery or stabilization). This would encompass a wide range of possible terrain behaviours. In future research, an interesting way to evaluate whether the results obtained with this methodology correspond to the reality of aquifers would be to conduct a study comparing the hydrogeological parameters obtained through pumping tests with those obtained through the application.

#### 6. Conclusions

As highlighted in this work, the deformation behaviour of an aquifer-system due to the temporal evolution of its piezometric head, influenced by multiple anthropogenic and/or natural factors, is a highly complex phenomenon. Therefore, the stress-strain relationships must be conducted with scientific rigor and as objectively as possible. However, the absence of an objective methodology based on universally applicable criteria for all case studies and independent of subjective factors or interpretations by the analyst, was the main motivation for developing the methodology proposed in this work and implementing it in an open-source software.

The methodology proposed for the study of stress-strain curves, codified using MATLAB software, allows for the study of aquifers with elastic or elastoplastic behaviour. The results obtained during the validation process using information from several case studies are consistent, making the methodology applicable to all behaviour types. The application is based on a protocol that relies on criteria and parameters that allow for the adaptation of this methodology to a wide variety of case studies and geotechnical contexts. Similarly, it streamlines, automates, and reduces the subjectivity of the results. It should be noted that the proper use of the application and user-controlled parameters requires prior knowledge of the magnitude of the subsidence phenomenon for the specific case study being analysed.

This methodology facilitates the automatic derivation of aquifer storage coefficients from stress-strain curves. This could support the implementation of measures for the management of groundwater resources quickly and more effectively. Moreover, the information derived from the use of this methodology and its computer application is of great utility for groundwater resource managers, as it enables the implementation of measures for the proper management of groundwater resources in a faster, more effective, and sustainable manner from a water resource perspective. Additionally, the parameters derived from stress-strain curves allow for the

development of hydrogeological models that are applicable to such management.

774775

## **Acknowledgements**

776777778

779

780

This research was funded by the ESA-MOST China DRAGON-5 project (ref. 59339) and by the PRIMA programme supported by the European Union under grant agreement No 1924, project RESERVOIR integrated to PRIMA Programme and supported by the European Union's Framework Programme for Research and Innovation.

781 782

783

#### References

784 785

789

790

791

792

793

794

795

796

797

798

799

800

801

802

803

804

- Abidin, H. Z., Andreas, H., Gumilar, I., Sidiq, T., & Gamal, M. (2015). Environmental Impacts of Land Subsidence in Urban Areas of Indonesia. *FIG Working Week 2015, June*. https://www.researchgate.net/publication/277667741
  - Béjar-Pizarro, M., Ezquerro, P., Herrera, G., Tomás, R., Guardiola-Albert, C., Ruiz Hernández, J. M., Fernández Merodo, J. A., Marchamalo, M., & Martínez, R. (2017). Mapping groundwater level and aquifer storage variations from InSAR measurements in the Madrid aquifer, Central Spain. *Journal of Hydrology*, 547, 678–689. https://doi.org/10.1016/j.jhydrol.2017.02.011
  - Bonì, R., Herrera, G., Meisina, C., Notti, D., Béjar-Pizarro, M., Zucca, F., González, P. J., Palano, M., Tomás, R., Fernández, J., Fernández-Merodo, J. A., Mulas, J., Aragón, R., Guardiola-Albert, C., & Mora, O. (2015). Twenty-year advanced DInSAR analysis of severe land subsidence: The Alto Guadalentín Basin (Spain) case study. *Engineering Geology*, 198, 40–52. https://doi.org/10.1016/j.enggeo.2015.08.014
  - Burbey, T. J. (2001). Stress-strain analyses for aquifer-system characterization. *Ground Water*, *39*(1), 128–136. https://doi.org/10.1111/j.1745-6584.2001.tb00358.x
    - Cigna, F., & Tapete, D. (2021). Present-day land subsidence rates, surface faulting hazard and risk in Mexico City with 2014–2020 Sentinel-1 IW InSAR. *Remote Sensing of Environment, 253*(February 2020). https://doi.org/10.1016/j.rse.2020.112161
    - Dai, K., Shi, X., Gou, J., Hu, L., Chen, M., Zhao, L., Dong, X., & Li, Z. (2020). Diagnosing subsidence geohazard at beijing capital international airport, from high-resolution SAR interferometry. Sustainability (Switzerland), 12(6), 1–16. https://doi.org/10.3390/su12062269
- Galloway, D., Jones, D. R., & Ingebritsen, S. E. (1999). Land subsidence in the United States. In Geological Survey Circular (U.S.Geolog).
- Galloway, D. L., & Burbey, T. J. (2011). Review: Regional land subsidence accompanying groundwater
   extraction. *Hydrogeology Journal*, *19*(8), 1459–1486. https://doi.org/10.1007/s10040-011 0775-5
- 6311 Galloway, D. L., & Hoffmann, J. (2007). The application of satellite differential SAR interferometryderived ground displacements in hydrogeology. *Hydrogeology Journal*, *15*(1), 133–154. https://doi.org/10.1007/s10040-006-0121-5
- Galloway, D. L., Hudnut, K. W., Ingebritsen, S. E., Phillips, S. P., Peltzer, G., Rogez, F., & Rosen, P. A. (1998). Detection of aquifer system compaction and land subsidence using interferometric

- synthetic aperture radar, Antelope Valley, Mojave Desert, California. *Water Resources Research*, *34*(10), 2573–2585. https://doi.org/10.1029/98WR01285
- Hernandez-Marin, M., Pacheco-Martinez, J., Ramirez-Cortes, A., Burbey, T. J., Ortiz-Lozano, J. A.,
  Zermeño-de-Leon, M. E., Guinzberg-Velmont, J., & Pinto-Aceves, G. (2014). Evaluation and
  analysis of surface deformation in west Chapala basin, central Mexico. *Environmental Earth*Sciences, 72(5), 1491–1501. https://doi.org/10.1007/s12665-014-3054-7
- Herrera-García, G., Ezquerro, P., Tomas, R., Béjar-Pizarro, M., López-Vinielles, J., Rossi, M., Mateos, R. M., Carreón-Freyre, D., Lambert, J., Teatini, P., Cabral-Cano, E., Erkens, G., Galloway, D., Hung, W. C., Kakar, N., Sneed, M., Tosi, L., Wang, H., & Ye, S. (2021). Mapping the global threat of land subsidence. *Science*, *371*(6524), 34–36. https://doi.org/10.1126/science.abb8549
- Hoffmann, J. (2003). THE APPLICATION OF SATELLITE RADAR INTERFEROMETRY. Stanford University.
- Hoffmann, J., Zebker, H. A., Galloway, D. L., & Amelung, F. (2001). Seasonal subsidence and rebound in Las Vegas Valley, Nevada, observed by synthetic aperture radar interferometry. *Water Resources Research*, *37*(6), 1551–1566. https://doi.org/10.1029/2000WR900404
- Li, J., Zhu, L., Gong, H., Zhou, J., Dai, Z., Li, X., Wang, H., Zoccarato, C., & Teatini, P. (2022). Unraveling elastic and inelastic storage of aquifer systems by integrating fast independent component analysis and a variable preconsolidation head decomposition method. *Journal of Hydrology*, 606. https://doi.org/10.1016/j.jhydrol.2021.127420
- Motagh, M., Djamour, Y., Walter, T. R., Wetzel, H. U., Zschau, J., & Arabi, S. (2007). Land subsidence in Mashhad Valley, northeast Iran: Results from InSAR, levelling and GPS. *Geophysical Journal International*, *168*(2), 518–526. https://doi.org/10.1111/j.1365-246X.2006.03246.x
- Poland, J. F. (1984). *Guidebook to studies of land subsidence due to groundwater withdrawal* (J. F. Poland, Ed.). UNESCO.
- Riley, F. S. (1969). Analysis of Borehole Extensometer Data from Central California. In *Land Subsidence, Volume 2* (pp. 423–431). International Association of Scientific Hydrology.
- Riley, R. S. (1984). Developments in borehole extensometry. In L. Johnson, L. Carbognin, & L. Ubertini (Eds.), *Land subsidence: Proceedings of the Third International Symposium on Land Subsindece held in Venice, Italy* (pp. 169–186). International Association of Hydrological Sciences.
- 844 Rohatgi, A. (2021). WebPlotDigitizer (4.5). https://automeris.io/WebPlotDigitizer/index.html
- Syvitski, J. P. M., Kettner, A. J., Overeem, I., Hutton, E. W. H., Hannon, M. T., Brakenridge, G. R., Day,
  J., Vörösmarty, C., Saito, Y., Giosan, L., & Nicholls, R. J. (2009). Sinking deltas due to human
  activities. *Nature Geoscience*, *2*(10), 681–686. https://doi.org/10.1038/ngeo629
- Tomás, R., Domenech, C., Mira, A., Cuenca, A., & Delgado, J. (2007). Preconsolidation stress in the Vega Baja and Media areas of the River Segura (SE Spain): Causes and relationship with piezometric level changes. *Engineering Geology*, 91(2–4), 135–151. https://doi.org/10.1016/j.enggeo.2007.01.006
- Xue, Y. Q., Wu, J. C., Zhang, Y., Ye, S. J., Shi, X. Q., Wei, Z. X., Li, Q. F., & Yu, J. (2008). Simulation of regional land subsidence in the southern Yangtze Delta. *Science in China, Series D: Earth Sciences*, *51*(6), 808–825. https://doi.org/10.1007/s11430-008-0062-z
- Zhang, Y., Gong, H., Gu, Z., Wang, R., Li, X., & Zhao, W. (2014). Characterization of land subsidence induced by groundwater withdrawals in the plain of Beijing city, China. *Hydrogeology Journal*, 22(2), 397–409. https://doi.org/10.1007/s10040-013-1069-x
- Zhang, Y., Xue, Y.-Q., Wu, J.-C., & Ye, S.-J. (2007). Stress-Strain Measurements of Deforming Aquifer Systems that Underlie Shanghai, China. *Geological Society of America*, 8(3), 217–228.

860	Zhang, Y., Xue, YQ., Wu, JC., Ye, SJ., Wei, ZX., Li, QF., & Yu, J. (2007). Characteristics of aquifer
861	system deformation in the Southern Yangtse Delta, China. Engineering Geology, 90(3–4), 160–
862	173. https://doi.org/10.1016/j.enggeo.2007.01.004
863	Zhu, L., Gong, H., Chen, Y., Wang, S., Ke, Y., Guo, G., Li, X., Chen, B., Wang, H., & Teatini, P. (2020).
864	Effects of Water Diversion Project on groundwater system and land subsidence in Beijing,
865	China. Engineering Geology, 276. https://doi.org/10.1016/j.enggeo.2020.105763
866	Zhu, L., Gong, H., Li, X., Wang, R., Chen, B., Dai, Z., & Teatini, P. (2015). Land subsidence due to
867	groundwater withdrawal in the northern Beijing plain, China. Engineering Geology, 193, 243-
868	255. https://doi.org/10.1016/j.enggeo.2015.04.020
869	
970	
870	
871	

## A New Stress-Strain Analysis Application for Aquifer Systems Characterization in Land Subsidence Affected Areas

María I. Navarro-Hernández <sup>1</sup>, Sergio García-Pozo <sup>1</sup>, Javier Valdes-Abellan <sup>1</sup> and Roberto Tomás <sup>1</sup>

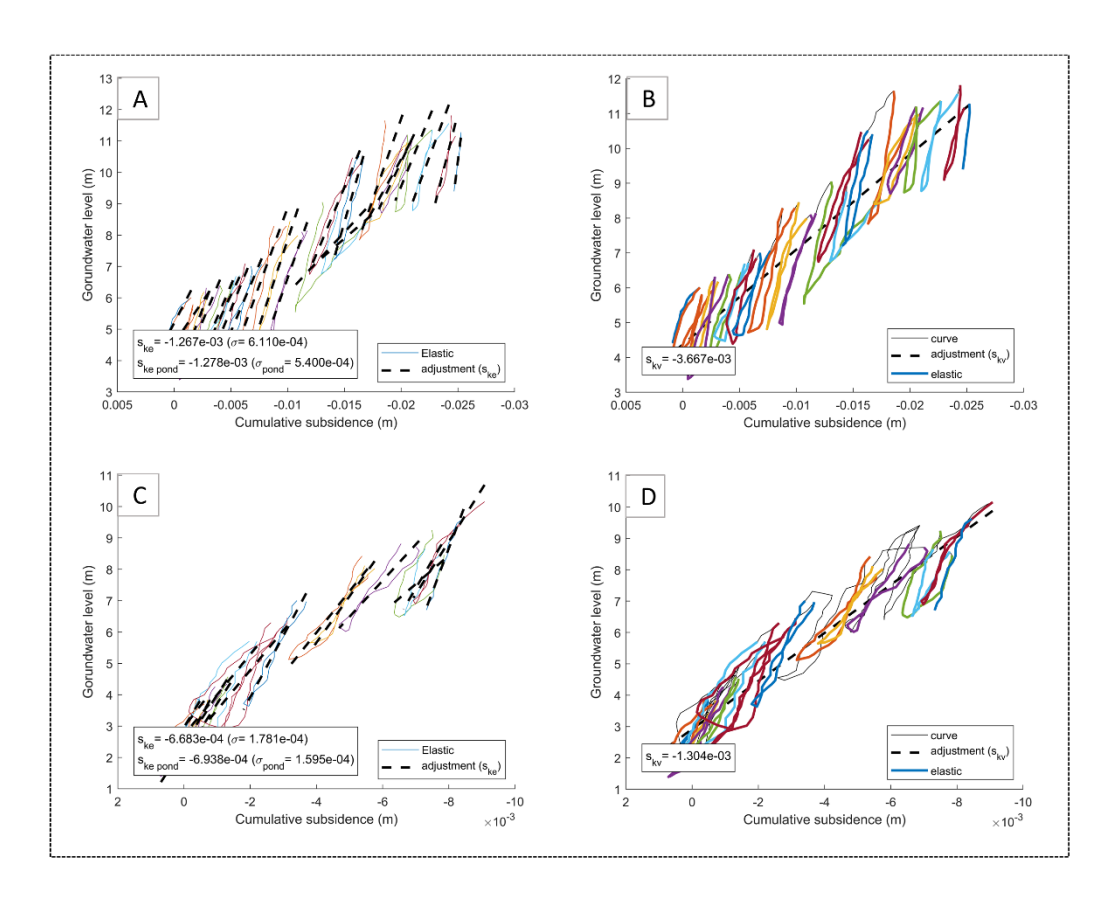
# SUPLEMENTARY MATERIAL

**S1**. Summary of the numerical values of all the parameters considered for the analysis of each of the stress-strain curves.

			User	-controlled variables					
Nº Curve	Extensometer / well	Y-axis interval (m)	X-axis interval (m)	Initial groundwater level (m)	% Maximum amplitude				
Zhang et al., 2007a									
1	F004	1	2 · 10-4	0	10				
2	F003	1	2 · 10-4	0	10				
3	F003	1	2 · 10-4	0	10				
		Zl	nang et al., 20	07b					
4	-	1	2 · 10-4	6	10				
5	-	1	2 · 10-4	6	10				
		Z	hang et al., 20	014					
6	MLC3	0.5	2 · 10-4	36	20				
7	MLC3	1.5	1 · 10-4	37	35				
8	MLC3	0.5	2 · 10-4	38	20				
9	MLC3	1	1 · 10-4	37	25				
10	MLC3	1.6	5 · 10 <sup>-3</sup>	37	20				
11	MLC3	1.2	1 · 10-3	39	20				
12	MLC3	0.8	2 · 10-3	34	20				
		Béjar	-Pizarro et a	l., 2017					
13	CA-3	30	1 · 10-4	370	20				
14	CA-4	10	1 · 10-4	345	20				
15	CA-5	20	1 · 10-4	360	50				
16	CB-4	40	1 · 10-4	360	20				
17	CB-5	10	1 · 10-4	345	20				
18	CB-6	10	1 · 10 <sup>-4</sup>	345	20				
19	CB-9	10	1 · 10-4	380	20				
20	CB-12	10	1 · 10-4	330	20				
21	CB-13	10	1 · 10 <sup>-4</sup>	330	20				
22	CB-15	10	1 · 10-2	335	20				
23	FA-1	40	1 · 10-4	325	20				
24	FA-3	20	1 · 10-2	340	30				
25	FC-2	10	1 · 10-2	340	30				
26	FX-4	30	1 · 10-4	340	20				
27	G-I	40	1 · 10-2	350	20				
28	FE-1R	20	1 · 10-2	370	20				
29	MJ-1	40	$1 \cdot 10^{-2}$	330	20				
			Li et al., 202	2					
30	PGZ	1	$1 \cdot 10^{-4}$	20.6	20				
31	PGZ	1.5	2 · 10-4	9	35				
32	TZ	1.3	1 · 10-4	13.8	20				

**S2.** Analysed layers of the aquifer located in the southeast of the Yangtze Delta (Shanghai). Data obtained from Zhang et al. (2007a y 2007b)

Nº Curve	Aquifer layer	Extensometer	Thickness (m)						
Zhang et al., 2007a									
1 <sup>a</sup>	Second confined aquifer	F004	76.70 m						
2ª	Second aquitard	F003	27.04 m						
3ª	Third aquitard	F003	29.26 m						
	Zhang et al.,	2007b							
4 <sup>a</sup>	Second aquitard	-	40.00 m						
5ª	Second and third confined aquifer	-	70.00 m						



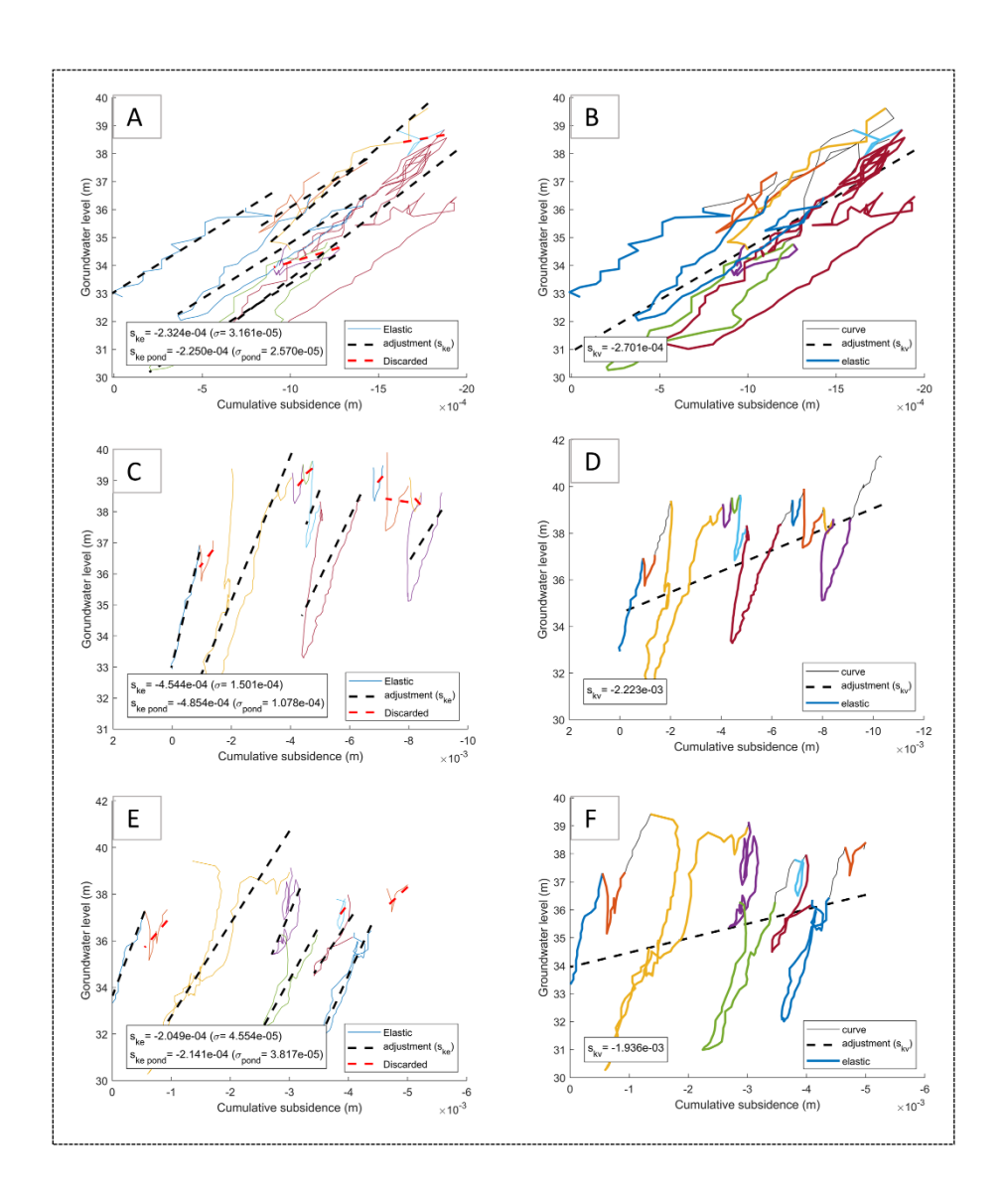
**S3.** Stress-strain curves results from the Southern Yangtse Delta. (A-B) Second aquitard level; (C-D) Second and third confined aquifer.

**S4.** Compilation of the specific elastic and inelastic storage coefficients for the analysed layers of the aquifer beneath Shanghai.

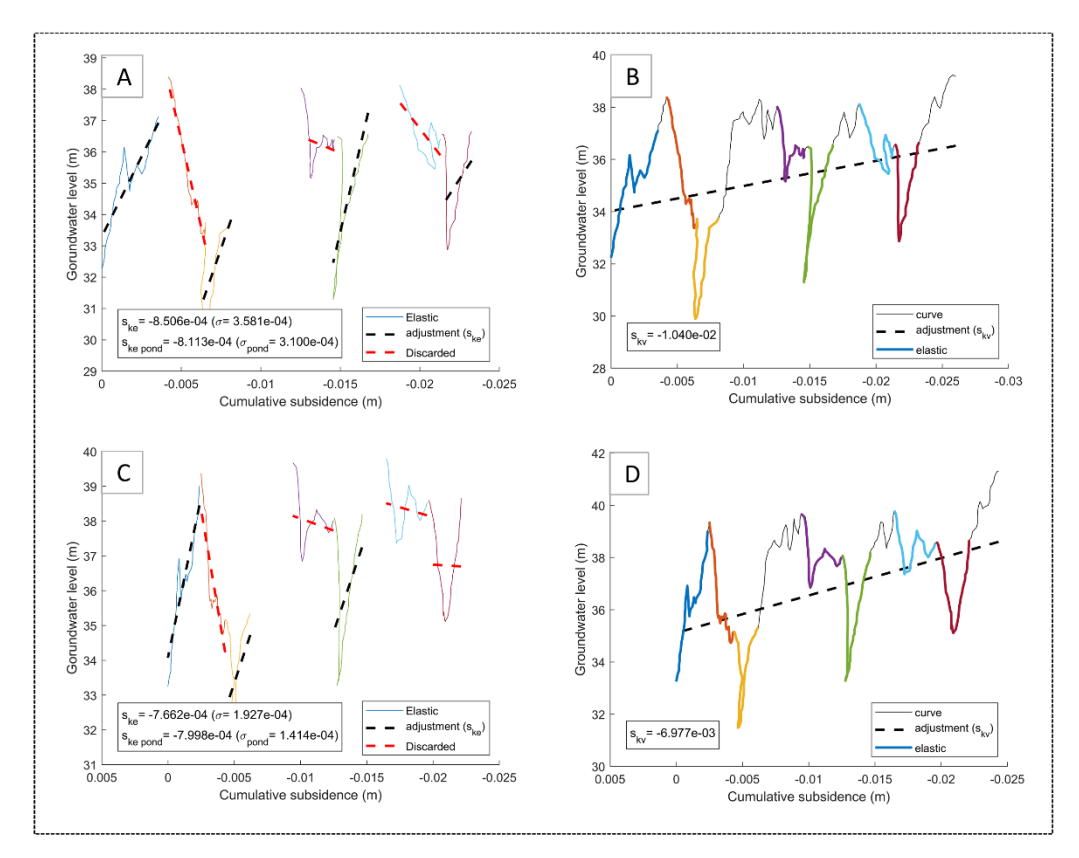
Nº Curve	Aquifer layer	$S_{ske} \ (m^{-1})$	$S_{ske\ weighted} \ (m^{-1})$	$S_{skv} \ (m^{-1})$
		Zhang et al., 2007a	a	
1ª	Second confined aquifer	1.031 · 10 <sup>-5</sup>	9.535 · 10 <sup>-6</sup>	1.05 · 10-5
2ª	Second aquitard	$2.036 \cdot 10^{-5}$	$2.096 \cdot 10^{-5}$	1.816 · 10 <sup>-5</sup>
3ª	Third aquitard	$1.625 \cdot 10^{-5}$	$1.610 \cdot 10^{-5}$	$6.044 \cdot 10^{-5}$
	:	Zhang et al., 2007l	)	
4 <sup>a</sup>	Second aquitard	$3.166 \cdot 10^{-5}$	$3.196 \cdot 10^{-5}$	9.166 · 10 <sup>-5</sup>
5ª	Second and third confined aquifer	9.570 · 10 <sup>-6</sup>	9.714 · 10 <sup>-6</sup>	1.862 · 10-5

**S5**. Analysed layers of the aquifer located in the Beijing Plain (China). Data obtained from Zhang et al. (2014).

Nº Curve	Aquifer layer	Extensometer	Thickness (m)
6ª	First confined aquifer	MLC3	16.0 m
7ª	Second confined aquifer	MLC3	19.7 m
8ª	Third confined aquifer	MLC3	31.0 m
9ª	First aquitard	MLC3	14.0 m
10ª	Second aquitard	MLC3	17.8 m
11ª	Third aquitard	MLC3	15.0 m
12ª	Fourth aquitard	MLC3	70.0 m



 ${\bf S6.}$  Stress-strain curves results from the Plain of Beijing. (A-B) First confined aquifer; (C-D) Third confined aquifer. (E-F) First aquitard layer.



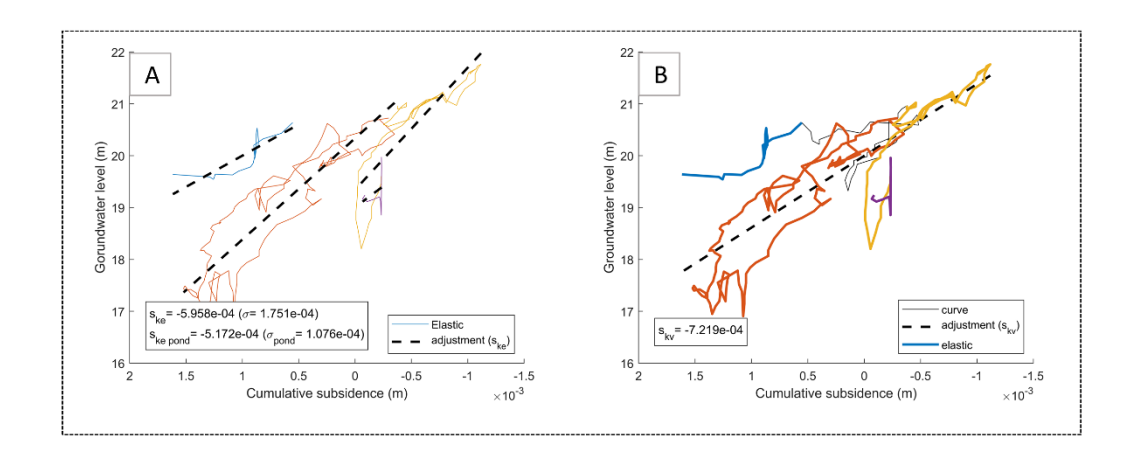
**S7.** Stress-strain curves results from the Plain of Beijing. (A-B) Second aquitard layer; (C-D) Third aquitard layer.

**S8**. Compilation of the specific elastic and inelastic storage coefficients for the analysed layers of the aquifer beneath the Beijing Plain. Parameters that do not apply are indicated with '-'.

Nº Curve	Aquifer layer	$S_{ske}$ $(m^{-1})$	$S_{ske\ weighted}$ $(m^{-1})$	$S_{skv}$ $(m^{-1})$
6ª	First confined aquifer	1.453 · 10-5	$1.406 \cdot 10^{-5}$	-
7ª	Second confined aquifer	1.411 · 10-5	$1.461 \cdot 10^{-5}$	$9.143 \cdot 10^{-5}$
8ª	Third confined aquifer	1.466 · 10-5	1.566 · 10 <sup>-5</sup>	$7.171 \cdot 10^{-5}$
9ª	First aquitard	1.463 · 10-5	1.529 · 10-5	1.383 · 10-4
10ª	Second aquitard	4.696 · 10-5	$4.498 \cdot 10^{-5}$	5.845 · 10-4
11ª	Third aquitard	5.108 · 10-5	5.332 · 10-5	4.651 · 10-4
12ª	Fourth aquitard	$7.995 \cdot 10^{-6}$	$7.838 \cdot 10^{-6}$	2.458 · 10-5

**S9**. Analysed layers of the aquifer located beneath the Northern China Plain. Data obtained from Li et al. (2022).

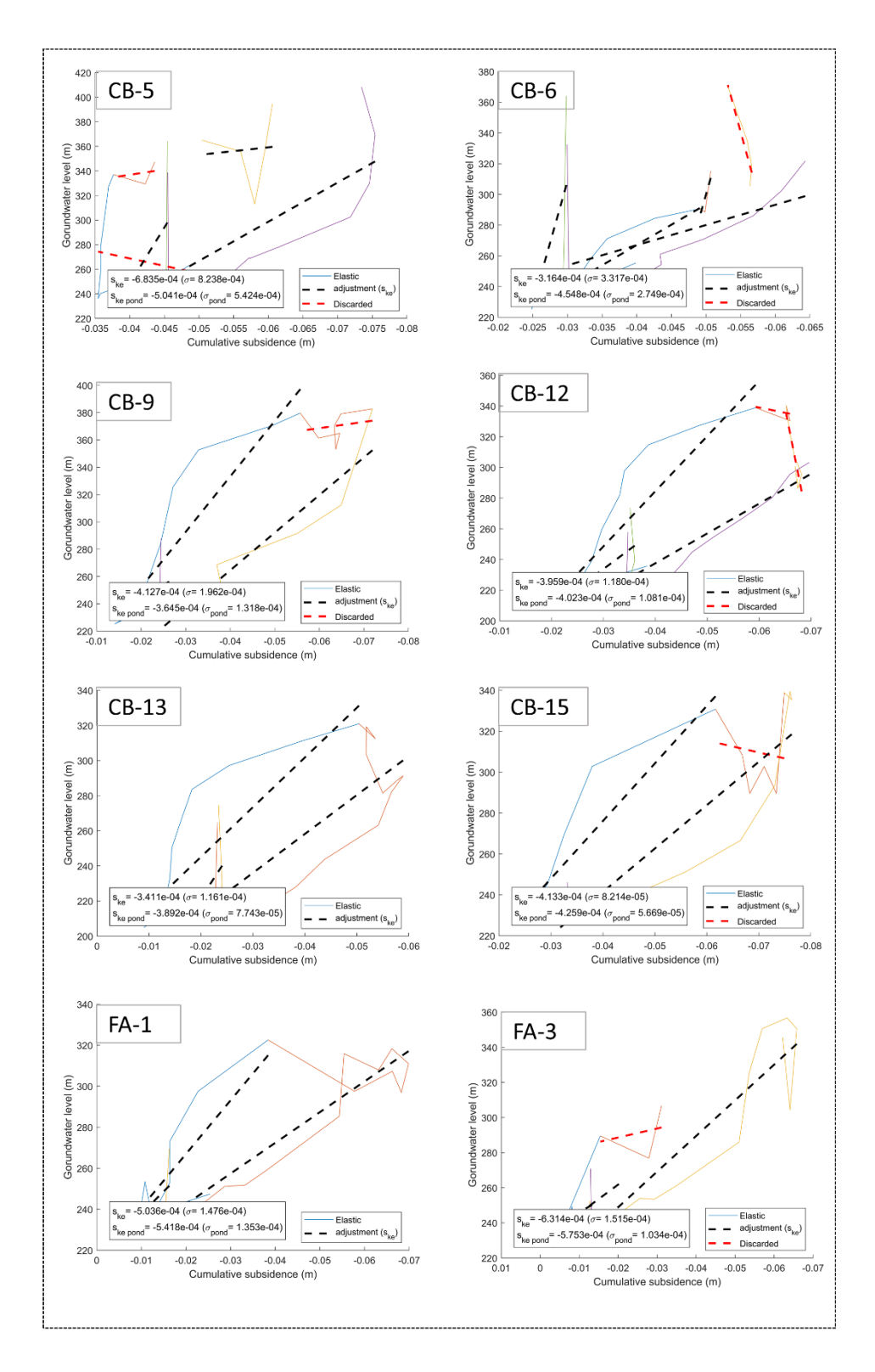
Nº Curve	Aquifer layer	Extensometer	Thickness (m)
30ª	-	PGZ	31.2 m
31ª	-	PGZ	89.16 m
32ª	-	TZ	19.70 m



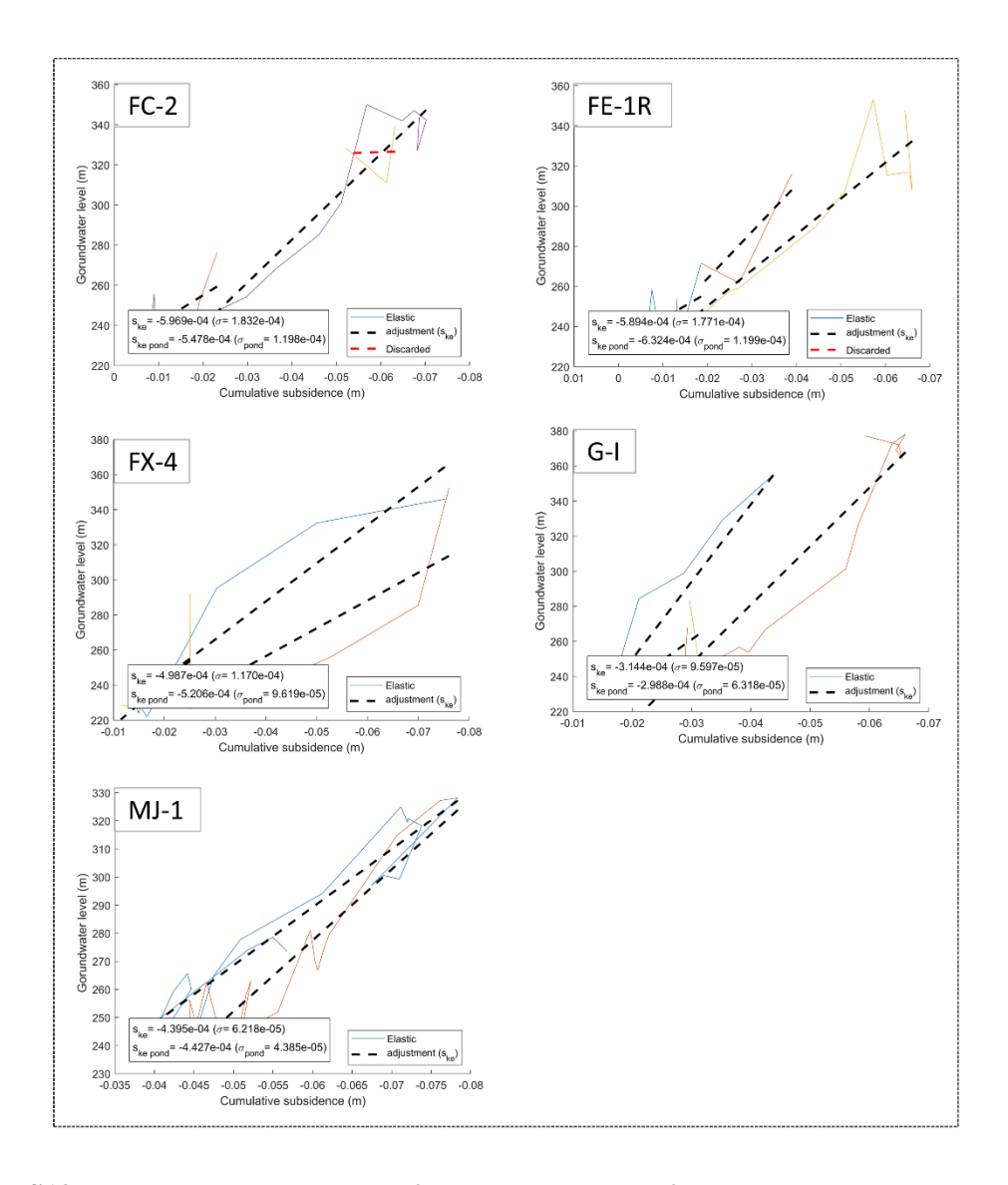
**S10.** Stress strain curves results from North China plain. (A-B) First layer.

**S11**. Compilation of the specific elastic and inelastic solid skeleton storage coefficients for the analysed layers of the aquifer beneath the Northern China Plain. Parameters that do not apply are indicated with '-'

Nº curve	$S_{ske} \ (m^{-1})$	$S_{ske\ weighted}$ $(m^{-1})$	$S_{skv} \ (m^{-1})$
30 <sup>a</sup>	1.910 · 10-5	1.658 · 10-5	-
31ª	1.415 · 10-5	1.484 · 10 <sup>-5</sup>	9.279 · 10 <sup>-5</sup>
32ª	-	-	$3.517 \cdot 10^{-5}$



S12. Stress-strain curves results from the Madrid aquifer.



 $\boldsymbol{S13}.$  Stress-strain curves results from the Madrid aquifer.

**S14**. Compilation of the specific elastic storage coefficients from the analysed curves of the aquifer in the Madrid Basin.

Nº curve	$S_{ke}$	$S_{ke\;weighted}$	$S_{ke\;global}$
CA-3	$2.941 \cdot 10^{-4}$	$3.248 \cdot 10^{-4}$	$4.394 \cdot 10^{-4}$
CA-4	$4.971 \cdot 10^{-4}$	$4.239 \cdot 10^{-4}$	$4.503 \cdot 10^{-4}$
CA-5	$3.450 \cdot 10^{-4}$	$3.445 \cdot 10^{-4}$	$4.216 \cdot 10^{-4}$
CB-4	$3.072 \cdot 10^{-4}$	$3.315 \cdot 10^{-4}$	$4.435 \cdot 10^{-4}$
CB-5	$6.835 \cdot 10^{-4}$	$5.041 \cdot 10^{-4}$	$3.828 \cdot 10^{-4}$
CB-6	$5.196 \cdot 10^{-4}$	$6.091 \cdot 10^{-4}$	$5.331 \cdot 10^{-4}$
CB-9	$4.127 \cdot 10^{-4}$	$3.646 \cdot 10^{-4}$	$3.615 \cdot 10^{-4}$
CB-12	$3.959 \cdot 10^{-4}$	$4.023 \cdot 10^{-4}$	$4.972 \cdot 10^{-4}$
CB-13	$3.411 \cdot 10^{-4}$	$3.892 \cdot 10^{-4}$	$5.582 \cdot 10^{-4}$

CB-15	$4.133 \cdot 10^{-4}$	$4.260 \cdot 10^{-4}$	$5.753 \cdot 10^{-4}$
FA-1	$5.036 \cdot 10^{-4}$	$5.418 \cdot 10^{-4}$	$7.697 \cdot 10^{-4}$
FA-3	$6.314 \cdot 10^{-4}$	$5.753 \cdot 10^{-4}$	$5.434 \cdot 10^{-4}$
FC-2	$5.970 \cdot 10^{-4}$	$5.478 \cdot 10^{-4}$	$5.283 \cdot 10^{-4}$
FX-4	$5.799 \cdot 10^{-4}$	$6.146 \cdot 10^{-4}$	5.882 · 10-4
G-I	$5.294 \cdot 10^{-4}$	$5.539 \cdot 10^{-4}$	$5.739 \cdot 10^{-4}$
FE-1R	$3.309 \cdot 10^{-4}$	$3.124 \cdot 10^{-4}$	$3.553 \cdot 10^{-4}$
MJ-1	$4.395 \cdot 10^{-4}$	$4.427 \cdot 10^{-4}$	$4.545 \cdot 10^{-4}$
MEAN	4.600 · 10-4	$4.534 \cdot 10^{-4}$	$4.986 \cdot 10^{-4}$

**S15.** Summary of the  $S_{ke}$  and  $S_{kv}$  coefficients obtained through the software and the results from articles in the southeast of the Yangtze Delta (Shanghai)."

Aquifer layer	$S_{ke}$	$S_{ke\ weighted}$	S <sub>ke article</sub>	$S_{kv}$	S <sub>kv artícle</sub>	
		Zhang et al., 2	2007a			
2° Conf Aquif.	7.906 · 10 <sup>-4</sup>	$7.314 \cdot 10^{-4}$	7.287 · 10 <sup>-4</sup>	8.063 · 10-4	$1.825 \cdot 10^{-3}$	
2° Aquitard	5.506 · 10-4	5.669 · 10-4	4.678 · 10-4	$4.911 \cdot 10^{-4}$	$1.338 \cdot 10^{-3}$	
3 <sup>er</sup> Aquitard	$4.756 \cdot 10^{-4}$	$4.712 \cdot 10^{-4}$	$1.770 \cdot 10^{-4}$	$1.768 \cdot 10^{-3}$	$2.130 \cdot 10^{-3}$	
	Zhang et al., 2007b					
2° Aquitard	1.267 · 10-3	1.278 · 10-3	6.394 · 10 <sup>-4</sup>	$3.667 \cdot 10^{-3}$	$3.566 \cdot 10^{-3}$	
2° y 3 <sup>er</sup> Conf Aquif.	6.800 · 10-4	6.800 · 10-4	6.199 · 10 <sup>-4</sup>	1.304 · 10 <sup>-3</sup>	$1.332 \cdot 10^{-3}$	

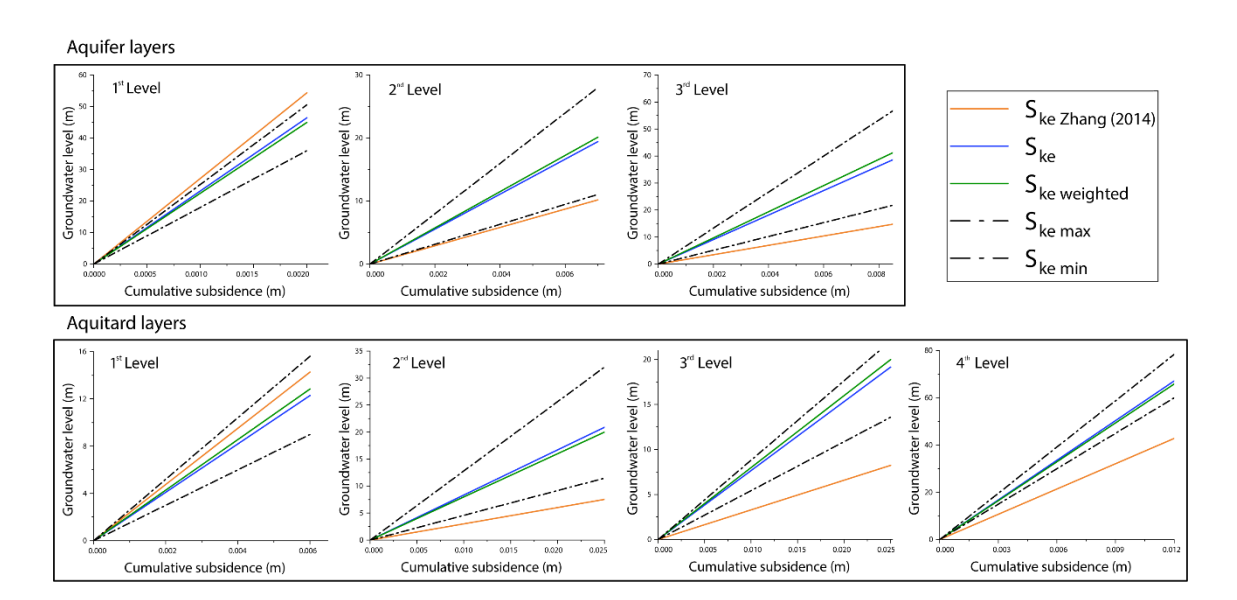
**S16.** Summary of the  $S_{ke}$  and  $S_{kv}$  coefficients obtained through the software and the results from article of the Beijing Plain. Parameters that do not apply are indicated with '-'.

Aquifer layer	$S_{ke}$	$S_{ke\ weighted}$	S <sub>ke article</sub>	$S_{kv}$	S <sub>kv article</sub>		
	Aquifer layers						
1er Conf Aquif	$2.325 \cdot 10^{-4}$	$2.250 \cdot 10^{-4}$	$2.720 \cdot 10^{-4}$	-	-		
2° Conf Aquif.	$2.779 \cdot 10^{-4}$	$2.879 \cdot 10^{-4}$	$1.458 \cdot 10^{-4}$	$1.801 \cdot 10^{-3}$	$2.561 \cdot 10^{-3}$		
3er Conf Aquif.	4.544 · 10-4	4.854 · 10-4	1.736 · 10-4	2.223 · 10-3	1.860 · 10-3		
		Aquitar	d layers				
1er Aquitard	$2.049 \cdot 10^{-4}$	$2.141 \cdot 10^{-4}$	2.380 · 10-4	$1.936 \cdot 10^{-3}$	$1.680 \cdot 10^{-3}$		
2° Aquitard	8.359 · 10-4	8.006 · 10-4	3.026 · 10-4	1.040 · 10-2	$6.408 \cdot 10^{-3}$		
3er Aquitard	7.662 · 10-4	$7.998 \cdot 10^{-4}$	3.300 · 10-4	$6.977 \cdot 10^{-3}$	$7.050 \cdot 10^{-3}$		
4° Aquitard	$5.597 \cdot 10^{-4}$	$5.486 \cdot 10^{-4}$	$3.570 \cdot 10^{-4}$	$1.721 \cdot 10^{-3}$	$1.960 \cdot 10^{-3}$		

**S17.** Summary of the  $S_{ke}$  and  $S_{kv}$  coefficients obtained through the software and the results from Li et al.

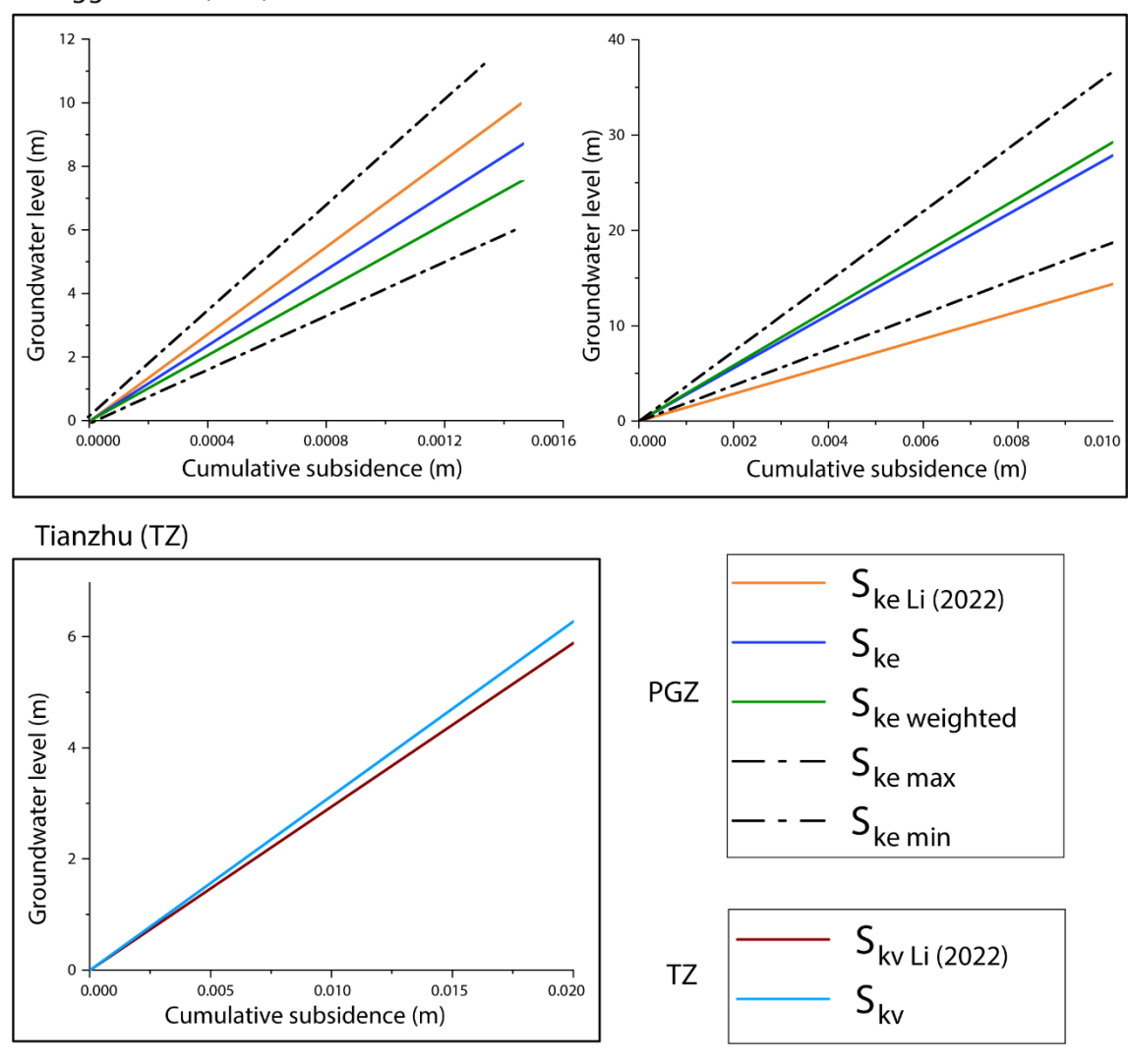
(2022). Parameters that are not applicable are indicated with "-"

Aquifer layer	$S_{ke}$	$S_{ke\ weigthed}$	$S_{keLi(2022)}$	$S_{kv}$	$S_{kvLi(2022)}$
PGZ (1)	$5.958 \cdot 10^{-4}$	5.172 · 10 <sup>-4</sup>	6.864 · 10-4	-	-
PGZ (2)	$2.787 \cdot 10^{-4}$	$2.924 \cdot 10^{-4}$	1.438 · 10-4	$1.828 \cdot 10^{-3}$	$2.955 \cdot 10^{-3}$
TZ	-	-	-	3.135 · 10-3	2.942 · 10 <sup>-3</sup>



**S18.** Comparative charts of the elastic storage coefficients obtained in the analyses with the values presented in the Beijing article.

## Pinggezhuan (PGZ)



**S19.** Comparison between the elastic storage coefficients calculated by the MATLAB application and the coefficients calculated by Li et al. (2022).

**S20**. Summary of the  $S_{ke}$  coefficients obtained through the software and the results from the detrital aquifer article of Madrid.

Well	$S_{ke}$	$S_{ke\ weighted}$	S <sub>ke global</sub>	$S_{ke\ article}$
CA-3	$2.941 \cdot 10^{-4}$	$3.248 \cdot 10^{-4}$	$4.394 \cdot 10^{-4}$	$4.02 \cdot 10^{-4}$
CA-4	4.971 · 10 <sup>-4</sup>	4.239 · 10-4	4.503 · 10 <sup>-4</sup>	3.62 · 10 <sup>-4</sup>
CA-5	3.450 · 10-4	3.445 · 10-4	4.216 · 10-4	3.47 · 10 <sup>-4</sup>
CB-4	3.072 · 10 <sup>-4</sup>	3.315 · 10-4	4.435 · 10 <sup>-4</sup>	3.56 · 10 <sup>-4</sup>
CB-5	$6.835 \cdot 10^{-4}$	5.041 · 10-4	3.829 · 10 <sup>-4</sup>	$2.29 \cdot 10^{-4}$
CB-6	5.196 · 10-4	6.091 · 10-4	5.331 · 10-4	2.87 · 10 <sup>-4</sup>
CB-9	4.127 · 10-4	3.645 · 10-4	3.615 · 10-4	3.00 · 10 <sup>-4</sup>
CB-12	3.959 · 10 <sup>-4</sup>	4.023 · 10-4	4.972 · 10-4	4.67 · 10-4

CB-13	3.411 · 10-4	$3.892 \cdot 10^{-4}$	5.582 · 10-4	$4.52 \cdot 10^{-4}$
CB-15	4.133 · 10-4	4.259 · 10-4	5.754 · 10-4	6.84 · 10 <sup>-4</sup>
FA-1	5.036 · 10-4	5.418 · 10-4	7.697 · 10-4	5.89 · 10 <sup>-4</sup>
FA-3	$6.314 \cdot 10^{-4}$	$5.753 \cdot 10^{-4}$	5.434 · 10-4	5.14 · 10 <sup>-4</sup>
FC-2	$5.970 \cdot 10^{-4}$	5.478 · 10-4	5.284 · 10-4	5.09 · 10 <sup>-4</sup>
FE-1R	$5.799 \cdot 10^{-4}$	$6.146 \cdot 10^{-4}$	5.882 · 10-4	$5.27 \cdot 10^{-4}$
FX-4	$5.294 \cdot 10^{-4}$	5.539 · 10 <sup>-4</sup>	5.739 · 10-4	3.15 · 10-4
G-I	3.309 · 10-4	$3.124 \cdot 10^{-4}$	3.554 · 10-4	5.04 · 10 <sup>-4</sup>
MJ-1	$4.395 \cdot 10^{-4}$	$4.427 \cdot 10^{-4}$	$4.546 \cdot 10^{-4}$	4.02 · 10 <sup>-4</sup>
MEAN	$4.600 \cdot 10^{-4}$	$4.534 \cdot 10^{-4}$	$4.986 \cdot 10^{-4}$	$4.262 \cdot 10^{-4}$